ISSN 0288-4534
CODEN: KONAE7

KONA

POWDER AND PARTICLE

No. 12(1994)

Published by The Council of Powder Technology (JAPAN)

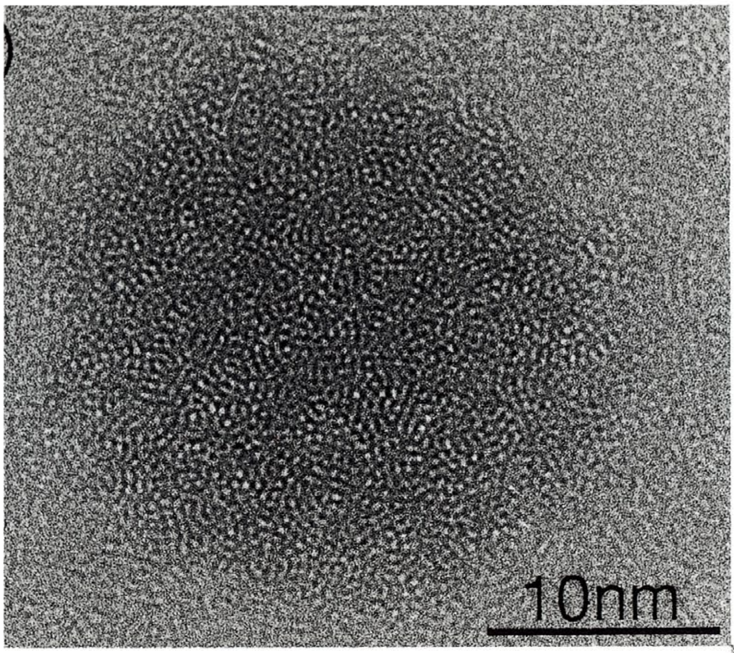

Image of an amorphous Sb cluster (a) and an $AuSb_2$ cluster (b) by high resolution electron microscopy (HREM)

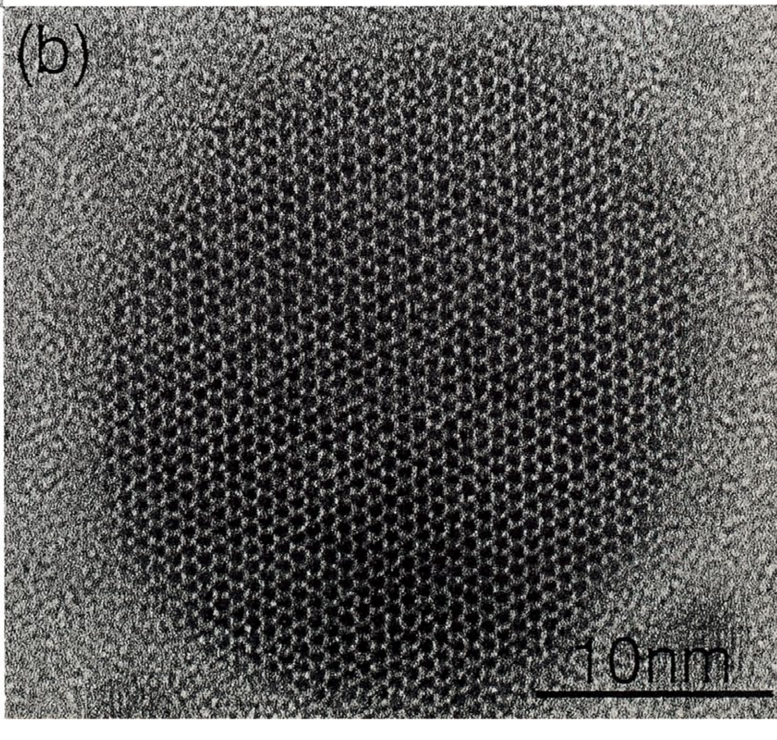

KONA

POWDER AND PARTICLE

KONA, issued annually since 1983 by the Council of Powder Technology, Japan, is a refereed journal publishing the articles on powder sciences and technology, and is distributed to the interested persons and institutions throughout the world.

About the Cover of Journal "KONA"

The chinese character "粉" is pronounced as "KONA" in Japanese, and means "Powder". The hand written "粉" is after the late Mr. Eiichi Hosokawa, the founder of Hosokawa Micron Corporation.

Hosokawa Micron Corporation and its R&D Center

Editorial Board

K. Miyanami	Editor in Chief (Univ. of Osaka Prefecture, JAPAN)
Asian Block	
Y. Kousaka	Block Vice Chairman (Univ. of Osaka Prefecture, JAPAN)
N. Yoshioka	(Professor Emeritus of Kyoto Univ., JAPAN)
G. Jimbo	(Chubu Powtech Plaza Lab., JAPAN)
M. Arakawa	(Former Kyoto Institute of Tech., JAPAN)
T. Oshima	(Himeji Institute of Tech., JAPAN)
Y. Morikawa	(Osaka Sangyo Univ., JAPAN)
H. Masuda	(Kyoto Univ., JAPAN)
Y. Tsuji	(Osaka Univ., JAPAN)
H. Emi	(Kanazawa Univ., JAPAN)
Y. Kuwahara	(National Industrial Research Institute of Nagoya, JAPAN)
P. Arnold	(Univ. of Wollongong, AUSTRALIA)
S. H. Kang	(Yeugnam Univ., KOREA)
W. Tanthapanichakoon	(Chulalongkorn Univ., THAILAND)
T. Yoshida	(Professor Emeritus of Osaka Prefecture JAPAN)
T. Yokoyama	(Former Hosokawa Micron Corp., JAPAN)
Secretariat	
T. Yokoyama	(Hosokawa Micron Corp., JAPAN)
F. Nakagawa	(Hosokawa Micron Corp., JAPAN)
European Block	
J. Schwedes	Block Chairman (Univ. Braunschweig, GERMANY)
B. Scarlett	Block Vice Chairman (Delft Univ. of Technology, THE NETHERLANDS)
K. Schönert	(Technische Univ. Clausthal, GERMANY)
F. Löffler	(Univ.Karlsruhe, GERMANY)
H. Schubert	(Bergakademie Freiberg, GERMANY)
E. Forssberg	(Univ. Lulea, SWEDEN)
S. R. de Silva	(Postec-Research A/S, NORWAY)
D. Ocepek	(Univ. Ljubljana, SLOVENIA)
J. F. Davidson	(Univ. of Cambridge, UNITED KINGDOM)
G. F. Ferrara	(Univ. di Trieste, ITALY)
J. F. Large	(Univ. de Tech. de Compiégne, FRANCE)
Secretariat	
W. Peukert	(Hosokawa Mikropul, GERMANY)
Americas Block	
M. McLaren	Block Chairman (Rutgers Univ., U.S.A.)
T. P. Meloy	Block Vice Chairman (West Virginia Univ., U.S.A.)
R. K. Rajamani	(Univ. of Utah, U.S.A.)
B. H. Kaye	(Laurentian Univ., CANADA)
P. S. Santos	(Univ. of Sãu Paulo, BRAZIL)
D. Fuerstenau	(Univ. California)
L. Hixon	(Hosokawa Micron Inter., U.S.A.)
W. Gregg	(Hosokawa Micron Inter., U.S.A.)
Secretariat	
D. A. Scott	(Hosokawa Micron Inter., U.S.A.)

■ Publication Office

The Council of Powder Technology (Japan)
in **Hosokawa Micron Corporation**
No. 9, 1-chome, Shoudai Tajika, Hirakata-shi, Osaka 573 Japan

■ Notes

○ Sponsored by Hosokawa Powder Technology Foundation

(Complimentary Copy)

Printed in Japan

The Letter from the Editor

The Mile High City has experienced quite a big congress on Particle Technology in last summer. Four hundred and sixty participants from over 25 countries have got together at The First Particle Technology Forum in Denver, Colorado, U.S.A. According to its program, about 360 papers including poster sessions have been presented and it has been essentially the 3rd World Congress on Particle Technology.

On this occasion, the KONA meeting has been held at the place very close to the conference site. Prof. M. McLaren, the chairman of the American Block KONA committee, extended a warm welcome to the 12 international attendees from the Asian, European and American Blocks, and expressed the gratitude of the scientific community for the generosity and important work of the KONA efforts worldwide. Many constructive and sound suggestions were proposed for the advancement of our KONA efforts. All committee members are committed to keeping the prestige associated with the journal and its contents. I do hope that we can do our best for further improvement of the KONA and its editorial procedures. Many thanks are due to Ms.D.A. Scott for her taking care of the meeting this time.

It has been noted that the 1998 formal international KONA meeting will be held in Birmingham, U.K., on the occasion (13-15 July 1998) of (4th) World Congress on Particle Technology.

Kei Miyanami

Kei Miyanami,
Editor-in-Chief

KONA

GENERAL INFORMATION

HISTORY OF THE JOURNAL

The Council of Power Technology (CPT), Japan, has been established in 1969 as a non-profit organization to enhance the activities of research and development on powder science and technology in Japan under the sponsorship of Hosokawa Micron Corporation. In 1983, the CPT has decided to issue an international journal named "KONA", which publishes the excellent articles appeared in Japanese Journals concerning with powder science and technology, translated into English, throughout the world. After the seventh volume issued in 1989, the CPT has changed its policy to internationalize the "KONA" from the 8th issue (1990) on by incorporating the monographs originally written in English from the authors throughout the world.

AIMS AND SCOPE OF THE JOURNAL

KONA Journal is to publish the papers in a broad field of powder sciences and technology, ranging from fundamental principles to practical applications. The papers discussing technological experiences and critical reviews of existing knowledge in specialized areas will be welcome.

These papers will be published only when they are judged, by the Editor, to be suitable for the progress of powder sciences and technology, and are approved by each Block Editorial Committee. The paper submitted to the Editorial Secretariat should not have been previously published except the translated papers which would be selected by the Block Editorial Committees.

CATEGORY OF PAPERS

- Invited papers
  Original research and review papers invited by the Block KONA Editorial committees.
- Contributed papers
  Original research and review papers submitted to the Block KONA Editorial Committees, and refereed by the Editors.
- Translated papers
  Papers translated into English, previously published in other languages, selected by the Block KONA Editorial Committees with the permission of the authors and/or the copyright holder.

SUBMISSION OF PAPERS

Papers should be sent to each Block KONA Editorial Secretariat.

- Asian Block Editorial Secretariat
  T. Yokoyama or F. Nakagawa
  Hosokawa Micron Corporation Micromeritics Laboratory
  1-9, Shoudai Tajika, Hirakata, 573 JAPAN
- European Block Editorial Secretariat
  Dr. W. Peukert
  Hosokawa Mikropul
  Welserstr. 9-11, 51149 Köln
  Postfach 900749, 51117 Köln
  GERMANY
- American Block Editorial Secretariat
  D.A. Scott
  10 Chatham Road, Summit, NJ 07901 USA

FREQUENCY

KONA will be issued once each calendar year.

SUBSCRIPTION

KONA is distributed free of charge to senior researchers at universities and laboratories as well as to institutions and libraries in the field throughout the world. The publisher is always glad to consider the addition of names of those who wish to obtain this journal regularly to the mailing list. Distribution of KONA is made by each Block Secretariat.

INSTRUCTIONS TO AUTHORS

(1) Manuscript format

- Two copies should be submitted to the Editorial Secretariat, in double-spaces typing on pages of uniform size.
- Authorship is to give author's names, and the mailing address where the work has been carried out on the title page.
- Abstract of 100-180 words should be given at the beginning of the paper.
- Nomenclature should appear at the end of each paper. Symbols and units are listed in alphabetical order with their definitions and dimensions in SI units.
- Literature references should be numbered and listed together at the end of paper, not in footnotes. Alphabetical order is accepted. Please give information as in the following examples:
  1) Carslaw, H.C. and J.C. Jaeger: "Conduction of Heat in Solids", 2nd ed., Clarendon Press, Oxford, England (1960).
  2) Howell, P.A.: US Patent, 3,334,603 (1963).
  3) Rushton, J.H., S. Nagata and D.L. Engle: AlChE J., 10. 298 (1964).
  4) Seborg, D.E.: Ph. D. Dissertation, Princeton Univ., N.J., U.S.A (1969).
- Original figures with each single copy should be submitted, on separate sheets. Authors' names and figure numbers are marked in the corner.
- Figure numbers and captions are listed on a separate sheet.
- Place of figure insertion is to be indicated in the margin of the manuscript.
- Tables should be typed on separated sheets.

(2) Reprints

- The authors shall receive 50 free reprints. Additional reprints will be furnished when ordered with return of galley proofs.

(3) Publication policy

- All papers submitted for publication become immediately the property of the CPT and remain so unless withdrawn by the author prior to acceptance for publication or unless released by the Editor. Papers are not to be reproduced or published in any form without the written permission of the CPT.

KONA Powder and Particle No. 12 (1994)

Contents

<**Review**>

<**Original Research Paper**>

<**Translated Research Paper**>

Explanation of the cover Photograph

An atomistic scale observation of spontaneous alloying

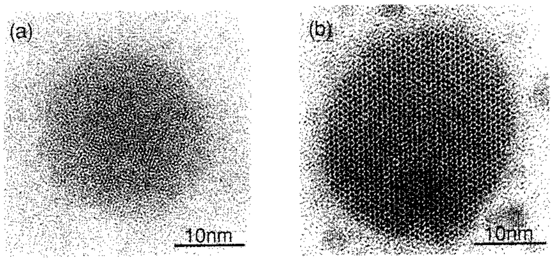

Ultrafine particles in the size range of a few to ten nm often exhibit physical and chemical properties that are significantly different from those of bulk solids. Such ultrafine particles are designated as atom clusters or simply clusters. Recently it was found that extremely rapid dissolution of solute atoms takes place in such nm-sized atom clusters. This phenomenon is called as the spontaneous alloying in atom clusters.

An atomistic scale observation of spontaneous alloying has been carried out by high resolution electron microscopy (HREM). **Figure (a)** shows an HREM image of an as-produced amorphous Sb cluster on a supporting carbon film. The cluster shows contrast similar to the ''salt and pepper'' contrast characteristic of an amorphous structure. **Figure (b)** shows an HREM image of an AuSb$_2$ cluster formed after gold deposition. During the deposition, the supporting film was kept at ambient temperature. It has been confirmed by an optical diffraction experiment of the cluster image that the incident beam direction is [111] of the AuSb$_2$ cluster. Small clusters of approximately 4 nm in the mean diameter, dispersed on the supporting carbon film, are gold.

Through the HREM experiment, it becomes evident that when gold is evaporated onto amorphous Sb clusters, gold atoms which come in contact with Sb clusters quickly dissolve into the clusters and Ausb$_2$ compound clusters are formed even at ambient temperature. It is also known that the ease with which such rapid spontaneous alloying takes place decreases with increasing size of original amorphous Sb clusters.

Review

The Necessity for Establishment of International Standards for Powders †

Malcolm G. McLaren*
*Institute for Engineered Materials Department of Ceramics, Rutgers-the State University of New Jersey**

1. Introduction

It is felt that the proper instrument for establishing standards, preferably international, is the International Organization for Standardization (ISO) based in Geneva. ISO is the specialized international agency for standardization. Its members are standards bodies of some 103 countries representing more than 95% of the world's industrial production. ISO is a non-governmental organization established in 1947 for the purpose of developing world-wide standards to improve international communication and collaboration, and to promote the smooth and equitable growth of international trade. ISO work results in international technical agreements which are published as international standards.

Common standards for measuring and expressing quantities of time, linear dimensions, weight, and energy have been hallmarks of cultural achievement throughout recorded history. In the present century, common standards for ensuring quality, compatibility, safety and reliability are the logical consequence of continuing industrial and social development.

Standardization is both the process of coming to agreement on common solutions to recurring technical problems, and the result of having put those agreements into practice. The process and the practice are inseparable and dynamic, as are the technological societies they serve.

International standardization is a natural consequence of the development of international trade and technical collaboration. Remarkable achievements of international standardization have been made possible through the collaborative efforts of national standards organizations and with the cooperation and support of producers, consumers, and governments from all over the world.

There are, of course, many important international standardization problems left to be solved, and others are sure to follow new technological developments and expanded international trade.

International standardization is an investment based on confidence in the rational application of technology for the benefit of all people.

Smoothing the Hurdles of International Trade

Trading partners throughout the world have grown to appreciate the importance of internationally agreed standards for transport vehicles and cargo containers; for storage and handling requirements of perishable products; and for compatible world-wide facilities and administrative procedures to ease the movement of goods, people, and services internationally.

Equally important to the smooth functioning of trade are internationally agreed standards for specifying and testing traded products, such as for grading of rubber, for testing safety aspects of gas cylinders, or for achieving interchangeability and compatibility of components for machine tools and earth-moving machinery.

A primary objective of ISO is to replace the often divergent standards of its member countries with international standards. Interest in ISO work has developed over the years to the extent that today ISO is the world's largest international organization for technical and industrial collaboration. Concurrent with the growth of ISO, the importance of multinational cooperative efforts to achieve international agreement on standards and technical regulations has been recognized and reinforced by more than 30 government signatories to a special Standards Code as part of the General Agreement on Tariffs and Trade (GATT).

International standards developed by ISO cover a wide variety of needs which are designed to remove unnecessary impediments to international communication, collaboration and trade. This is the common thread in all ISO work.

---

* Piscataway, New Jersey 08855-0909 U.S.A

† Received Sep. 20, 1994
An Editorial prepared by Malcolm G. McLaren as chairman of the Americas Block of KONA and primarily excerpted from ISBN 9267 100866 (1984).

Making the Most of Raw Materials

Iron ore, crude oil, latex, starch, bauxite, wood and clay are never purchased from any source without question as to their quality or condition. Further along the industrial chain these same materials yield steels, polymers rubber, paper, aluminum, sawn timber and ceramic frits, all graded according to various process requirements and refinement techniques.

Standards underlie the whole process of assessing raw materials and getting them into usable condition. Purity levels are determined and other physical and chemical properties are characterized at many stages using standardized test methods and grading systems to specify quality and performance.

Because basic raw materials are of major importance in international trade, international standardization in this field continues to be of vital concern in industrialized as well as developing economies. This explains why ISO has published more than one thousand international standards covering basic commodities such as steel, zinc, copper, aluminum, petroleum, petrochemicals, and natural fibers.

The above examples serve to show the need for standardization in the technological areas of powder preparation and utilization and that ISO standards are the preferable means to accomplish freedom of use and trade in these materials. There are currently 62 existing standards which are related to powder metallurgy which could be used as examples for other powder preparation methods and products.

It would seem that a separate ISO Technical Committee (TC) should be established in order to deal with the wide range of new powders that are being developed for commercialization. It is up to the technical community which makes use of this KONA Journal to help establish such a committee.

Author's short biography

Malcolm G. McLaren

Director, Institure for Engineered Materials, Professor, Department of Ceramics Rutgers-The State University of New Jersey Piscataway, New Jersey 08855-0909, Tel. 908-445-5700
Telefax: 908-445-5595

Areas of Expertise:
Whiteware ceramics, refractories, electronic ceramics, ceramic materials, ceramic processing, education, technical innovations, industry/university/government research, administration.

Education:
Rutgers Unviersity Ph.D. In Ceramics, 1962, M.S. In Ceramic, 1951, B.S. In Ceramics, 1950

Experience:
1954-1955
Paper Makers Importing Co., Inc., Easton, PA Chief Ceramist and Assistant Secretary-Treasurer
1955-1957
USAF, Wright-Patterson Air Force Base, Ohio 1/Lt., Metallurgy and Ceramics Branch of Aeronautical Res. Labs.
1957-1962
Paper Makers Importing Co., Inc., Easton, PA Vice-President
Rutgers University, New Brunswick, NJ
1962-1994
Professor and Chair, Department of Ceramics
1987-present
Director, Institute for Engineered Materials

Review

Liquid Bridge Adhesion Force and Dispersion of Aggregate Particles†

Yasuo Kousaka and Yoshiyuki Endo
*Dept. of Chem. Engineering, University of Osaka Pref.**

Abstract

Many studies have been made on liquid bridges between particles, but the mechanism of liquid bridge formation and its adhesion force when the bridge is in an equibrium condition with the surrounding humidity has not been theoretically clarified. A study has been made on this subject and a new theory is introduced in this paper. Next, a mechanism to disperse aggregate particles down to primary particles by the acceleration of an air stream is explained and a discussion is made on the dispersion force applied to aggregate particles and the adhesion force between particles (van der Waals force and liquid bridge force).

1. Introduction

Among the adhesion forces which act between particles or between particles and walls in air, the adhesion force arising from a liquid bridge is the greatest. This liquid bridge often makes handling of powdery materials difficult. In describing the liquid bridge, Laplace Young's equation[1,2] may be important. This equation gives the internal pressure inside a liquid surrounded by convex and concave surface. Many theoretical studies on liquid bridges use this equation to obtain the liquid bridge shape and the adhesion force of liquid bridges but these studies have not quantitatively related liquid bridge shapes and the adhesion forces to surrounding humidities. Another important equation in this connection is Kelvin's equation[3] which is used to explain the formation of liquid bridges by capillary condensation. However, this theoretical equation is erroneously used as explained later. Here, to simplify the discussion, the liquid bridge shape and the adhesion force acting between particles in an equilibrium condition with the surrounding humidity is explained for a liquid bridge formed between two spheres of identical size with 0° contact angle between the liquid and the particle. The equilibrium moisture contents in a powdery material and the strength of a powder bed are explained in relation with liquid bridges.

Next, a method and experimental results of the dispersion of aggregate particles into primary particles by acceleration of an air stream are introduced, and the mechanism of dispersion, the dispersion force acting on particles, and the adhesion force between particles are discussed.

2. Liquid Bridge Formation and Adhesion Force between Particles

2.1 Liquid Bridge Formation by Ideal Pure Water

As shown in **Fig. 1**, the negative pressure (capillary pressure) P_L (taking negative pressure as a positive value) is obtained from the following Laplace-Young Equation.

$$p_L = \sigma\left[\frac{1}{r_1{}'} - \frac{1}{r_2{}'}\right] \tag{1}$$

Where σ is the surface tension of the liquid and $r_1{}'$, $r_2{}'$ are radii shown in **Fig. 1**. The capillary pressure p_L is constant in a bridge and therefore the shape of the liquid bridge becomes a symmetry of rotation which satisfies Equation (1) with p_L as a constant. The capital letters in **Fig. 1** indicate the dimensionless values which are obtained on the basis of the particle radius r_0. On the other hand, the partial pressure of vapor at the surface of a liquid bridge is obtained using the following Kelvin equation[4].

$$\frac{P_d}{P_{s0}} = \exp -\left[\frac{M_\sigma}{RT_{\varrho L}} \cdot \frac{\mathrm{d}s}{\mathrm{d}v}\right] \equiv P_{Kel} \tag{2}$$

Where P_{s0} is the saturation vapor pressure, M the molecular weight of the liquid, R the gas constant, T the absolute temperature, ϱ_L the density of the liquid, s the vapor liquid interface surface area of the liquid bridge, and v the volume. P_{Kel} is explained

---

* Gakuen-cho, Sakai, Osaka 593-01, Japan

† Received May 26, 1994

later. For water P_d/P_{s0} is equivalent to the surrounding relative humidity of the liquid bridge. A liquid bridge at a certain humidity satisfies Equation (2). Therefore ds/dv for a liquid bridge which satisfies Equation (1) is obtained as the following approximate equation[4)].

$$r_0 \frac{ds}{dv} \doteqdot \frac{1.5}{R_2} \text{ or } \frac{ds}{dv} \doteqdot \frac{1.5}{r_2},\ (R_2 = r_2/r_0) \qquad (3)$$

Where R_2 is the dimensionless neck radius shown in **Fig. 1**, and r_0 the particle radius. The relation of Equation (3) is valid not only for a liquid bridge between two identical spheres but also for a liquid bridge between different size spheres, and between a sphere and a flat plate[5)]. In this case, r_0 is the radius of the smaller sphere.

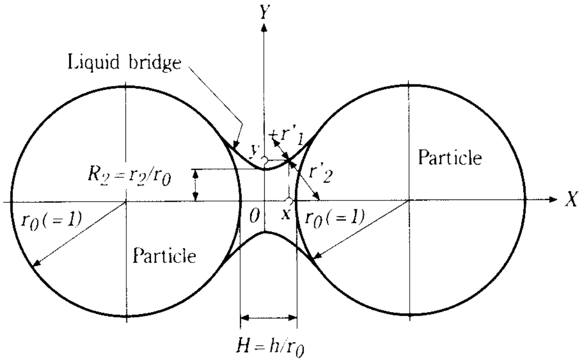

Fig. 1 Dimensions of a liquid bridge between two spheres

When Equations (2) and (3) are used, the size of a liquid bridge (represented by r_2 in **Fig. 1**) in an equilibrium condition with humidity can be obtained as the solid curve in **Fig. 2**, and under a room temperature and atmospheric pressure, the neck radius r_2 of the pure water bridge reaches about 0.15 nm (radius of water molecule) – 100 nm, regardless of the particle radius r_0[4, 5)]. In the past, the liquid bridge shape was assumed to be a circular arc having a radius r_1' shown in **Fig. 1** as constant $(=r_1)$ and Equation (3) was expressed as follows[6-9)].

$$\frac{ds}{dv} = \frac{1}{r_1} - \frac{1}{r_2} \qquad (4)$$

When the separation distance between two spheres as shown in **Fig. 1** is approximated to $h = 0$, this equation takes the following form.

$$\frac{ds}{dv} = \frac{2r_0 - 3r_2}{{r_2}^2} \qquad (5)$$

The dashed curve of **Fig. 2** shows the relation of Equation (5) when the particle radius r_0 is given as 1 μm and the value differs from the solid curve of Equation (3). In past studies, the bridge shape was approximated by a circular arc and therefore, the difference in **Fig. 2** shows that Kelvin's equation was not correctly used. When r_0 becomes larger than 1 μm, the difference between Equation (3) and Equation (5) becomes much greater.

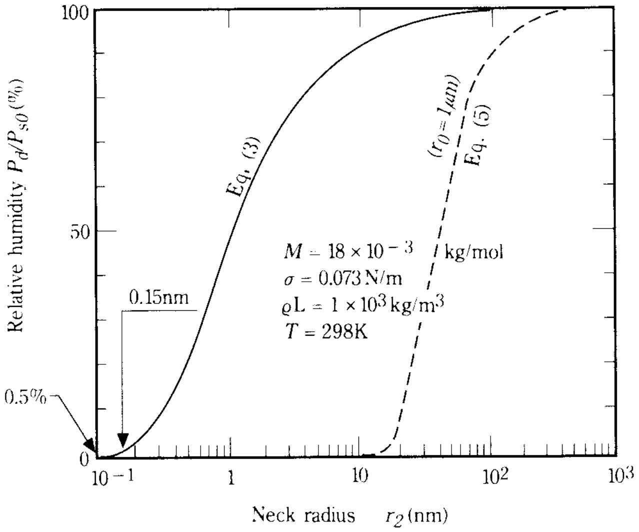

Fig. 2 Change in neck radius of liquid bridge with relative humidity

Figure 3 shows the observation results of a liquid bridge between glass beads with diameters of 1 mm, with an optical microscope. **Figure 3(a)** shows a photomicrograph of ultra-pure water used for a bridge liquid, left for 24 hours at a humidity of 90%. **Figure 3(b)** shows tap water used for a bridge liquid left for 24 hours at a humidity of 40%[4)]. In **Fig. 3(a)**, the existence of a liquid bridge could not be confirmed with a microscope, which supports the theory in **Fig. 2**. **Figure 3(b)** indicates that the inclusion of a small amount of soluble impurities in the tap water affects the formation of a liquid bridge. The reason for this is explained in detail in the next section. In past studies in which ultra-pure water was not available, liquid bridges which had grown large like the one shown in **Fig. 3(b)** were observed and it is thought that the results were compared with Equation (4).

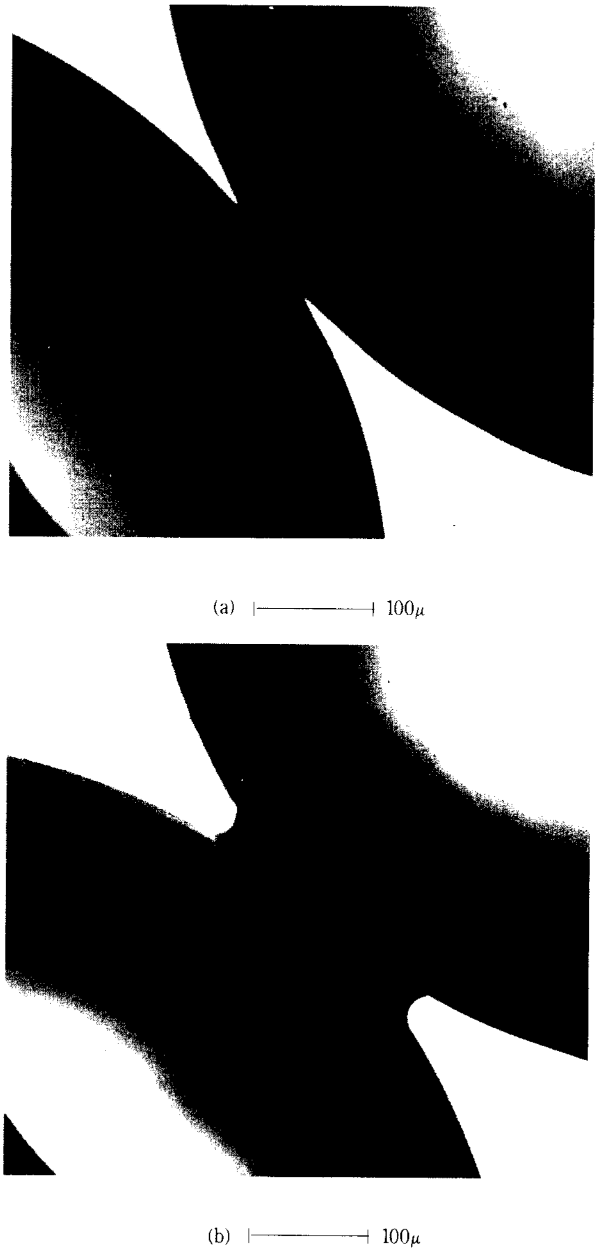

Fig. 3 Photomicrographs of liquid bridge
((a) liquid: ultra-pure water, at 90% relative humidity,
(b) liquid: tap water, at 40% relative humidity)

2.2 Liquid Bridge Formation by Water Containing Soluble Impurities

Once particles produced in water are dried, soluble impurities contained in water remain on the particles' surfaces as residue and if they are hygroscopic, they absorb the moisture contained in the air and form liquid bridges. Even in cases where soluble impurities are contained in a bridge liquid such as this, the following modified Kelvin equation can be applied10,11).

$$\frac{P_d}{P_{s0}} = (1-\gamma)\,P_{Kel} \qquad (6)$$

Where P_{Kel} indicates the right side of Equation (2) and ds/dv in the equation is obtained from Equation (3). $\gamma \equiv in_S/(n_W + in_S)$, where n is the number of molecules, subscript W represents pure water, and s stands for the solute. Furthermore, i is van't Hoff factor and differs depending on the type and concentration of the solute but with NaCl, H_2SO_4 etc., it is about 2. P_d/P_{s0} is the ambient relative humidity. γ in equation (6) becomes as follows when the number of solute molecules, n_S, divided by the single particle volume v_p is defined as N_S10).

$$\gamma = \frac{iM_W}{\varrho_W}\Bigg/\left(\frac{v}{v_pN_S} - \frac{M_S}{\varrho_S} + \frac{iM_W}{\varrho_W}\right) \qquad (7)$$

Where M is the molecular weight, ϱ is the density, v is the volume of the liquid bridge, subscript w represents pure water, and s the solute. The liquid bridge volume can be approximated by the following equation when particles of **Fig. 1** come into contact with each other ($H = 0$)10).

$$v = (\pi/2)\,r_0^{\;3}R_2^{\;4} \qquad (8)$$

Figure 4(b) and **(c)** show the Kelvin effect (P_{Kel}) on a liquid bridge and the effect of the solute concentration ($1-\gamma$)10) for a $CaCl_2$ water solution. The Kelvin effect shown in **Fig. 4(c)** satisfies the same relation as that of the solid curve of **Fig. 2.** The effect of solute concentration shown in **Fig. 4(b)** makes the liquid bridge (R_2) larger with an increase in solute contents N_S. The dashed curve in **Fig. 4(b)** shows the range within which the solute (salts) recrystallizes with a decrease in humidity. Also, nearly the same results as those of **Fig. 4(b)** are obtained with solutes other than $CaCl_2$10). The adhesion force between particles shown in **Fig. 4(a)** is explained later.

If the particle radius r_0, the type of the solute and its N_S content are known, the size of the liquid bridge (R_2) can be determined so that the ordinate product $(1-\gamma)\,P_{Kel}$ of **Fig. 4(b)** and **(c)** becomes equal to the atmospheric humidity. When absolutely no solute is contained in the liquid, then $\gamma = 0$, and R_2 is determined by **Fig. 4(c)** only. On the other hand, when the particle radius r_0 is large and the solute amount N_s is large, the effect of the solute concentration becomes dominant and Kelvin's effect becomes neglibile ($P_{Kel} \fallingdotseq 1$). Thus the size of the liquid bridge (R_2) is determined only by the effect of the solute concentration shown in **Fig. 4(b)**. Most fine particles used in industrial processes satisfy this condition[12].

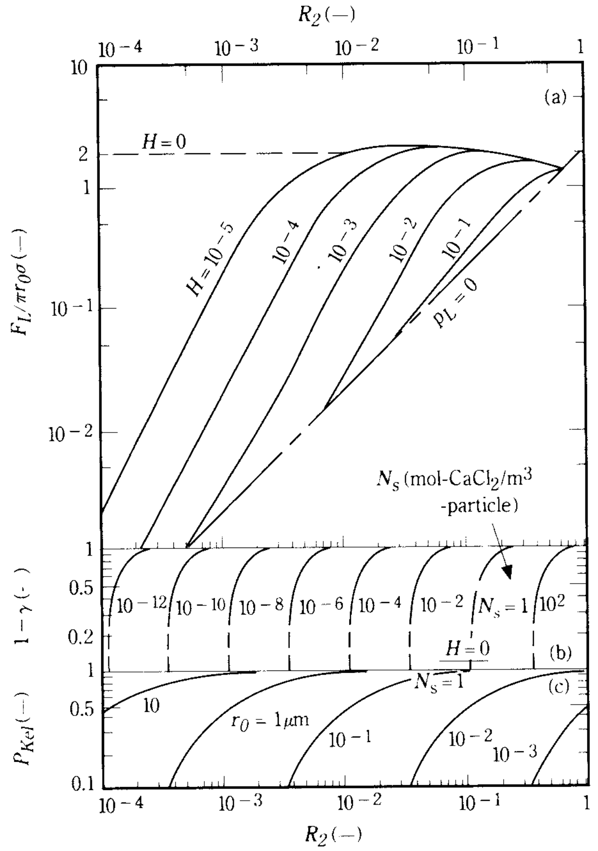

Fig. 4 Change in liquid bridge force F_L and neck radius R_2 with relative humidity $(1-\gamma)\cdot P_{Kel}$

2.3 Equilibrium Moisture Contents in Powdery Materials

If it is to be assumed that all moisture contents in powdery materials form liquid bridges between particles and that the bridges are of a consistent size with uniform distribution, the equilibrium moisture contents (dry basis) M_f can be expressed by the following equation.

$$M_f = \frac{k_p \varrho_L v}{2\varrho_p v_p} \tag{9}$$

Where ϱ_p is the density of a particle, v_p is the volume of a particle, k_p is the coordination number of particles in the powder bed and can be calculated from the porosity ε of the powder bed by using Ridgway-Tarbuck's equation[13] $(k_p = 13.8(1-\sqrt{1.21\varepsilon - 0.297}))$. v is the volume of one liquid bridge and if the separation distance between particles in the powder bed is $h \fallingdotseq 0$, v can be approximated by Equation (8). From Equation (9), the volume of one liquid bridge v and the moisture contents M_f in a powder bed can be mutually converted. The equilibrium moisture contents for various packed beds of submicron particles were observed, and a relation between Equation (7) and Equation (9) was found to be valid[12]. **Figure 5** gives one of the examples. In this figure, after immersing a certain amount of iron oxide particles in CaCl$_2$ water solution, it was left at various humidities until equilibrium was reached and the equilibrium moisture contents M_f was measured. The abscissa of **Fig. 5** indicates the normalized volume of one liquid bridge converted by Equation (9) from the equilibrium moisture content M_f. The results roughly coincide with the theoretical line of Equation (9) in which CaCl$_2$ concentration was high and Kelvin's effect was neglected. When ultra-pure water without CaCl$_2$ was used (⦶ mark), a liquid bridge of about same size when 1.3×10^2 mol/m^3 of CaCl$_2$ is added was formed. This is presumed that some kinds of soluble impurities corresponding to this were attached to the particle from the beginning.

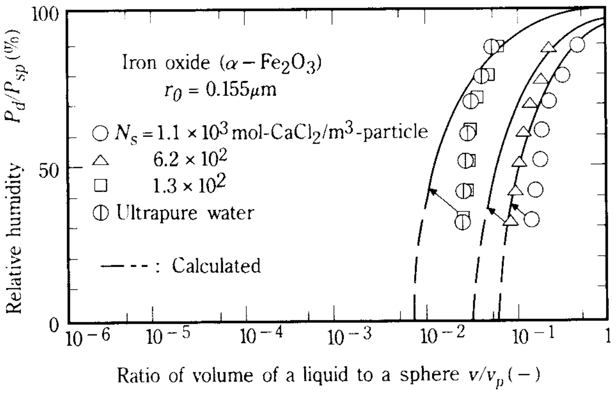

Fig. 5 Relation between volume of a liquid bridge in powdery materials and relative humidity

Small amounts of soluble impurities are usually attached to fine particles which are used in industrial processes and this is often the cause of the formation of liquid bridges. By sufficiently washing the particles and eliminating soluble impurities as much as possible, the moisture content of a particle bed and the adhesion force of liquid bridges can be reduced.

2.4 Adhesion Force Arising from a Liquid Bridge

The liquid bridge adhesion force F_L can be obtained as follows by integrating Laplace-Young's equation[14, 15].

$$F_L = \pi r_2{}^2 P_L + 2\pi\sigma r_2 = \pi y^2 P_L + \frac{2\pi\sigma y}{\sqrt{1+\left(\frac{dy}{dx}\right)^2}} \tag{10}$$

Where the right side first term is the capillary force of an arbitrary cross section πy^2 vertical to the x axis of the liquid bridge shown in **Fig. 1**, the second term expresses the component of x axis direction of surface tension at the vapor liquid interface of the same cross section, and it is shown that the sum of the two forces is constant $(= F_L)$ regardless of the position of the x axis. Equation (10) is not limited to a liquid bridge between two identical spheres but is valid between two different size spheres or between spheres and plates. Besides this, equations expressing the adhesion force of liquid bridges include Pietsh's equation16) and Fisher's equation17) for two identical spheres, and McFarlane's equation18) for spheres and plates but Pietsh's equation does not accurately express the adhesion force because it approximates a liquid bridge shape to a circular arc. Also the results obtained in the two latter equations are equivalent to the result of Equation (10) but in a strict sense, their derivation is not accurate.

Fig. 4(a) shows the relation of Equation (10) for liquid bridges between two identical spheres14). As mentioned before, when a liquid bridge size (R_2) in equilibrium with the surrounding humidity is obtained from **Figs. 4(b)** and **(c)**, adhesion force F_L between particles can be obtained from **Fig. 4(a)** for each distance between particles $H\ (\equiv h/r_0)$. In a condition where there are no other external forces other than the liquid bridge adhesion force, the separation distance between particles approaches $h \fallingdotseq 0.4\ nm$ under the effect of the adhesion force of the liquid bridge and the surface free energy of the liquid bridge19).

2.5 Strength of a Powder Bed

It is assumed that the powder bed tensile strength σ_t can be expressed by the following Rumpf's equation20).

$$\sigma_t = \frac{k_p\,(1-\varepsilon)}{\pi d_p{}^2} F_L \tag{11}$$

Where ε is the porosity, $d_p\ (\equiv 2\,r_0)$ is the diameter of particles composing the powder bed, and F_L is the liquid bridge force acting between two particles. Using this equation, the adhesion force F_L acting between two particles shown in **Fig. 4(a)** can be converted into powder bed strength σ_t. If values other than the particle diameter d_p are constant, the liquid bridge adhesion force F_L is proportional to d_p as shown in **Fig. 4(a)**. Therefore the powder bed strength σ_t is inversely proportional to d_p and as the particle diameter becomes smaller, σ_t becomes larger. Therefore as the particle size becomes smaller, handling of powdery materials becomes more difficult.

3. Dispersion of Aggregate Particles by Acceleration in an Air Stream

3.1 Theoretical Considerations

When an aggregate consisting of two particles, one large and one small, is placed in a high-speed air stream, a separation force arises during acceleration because the drag force and the inertial force acting on the respective particles are different21). The dispersion of aggregate particles into primary particles by acceleration in an air stream utilizes this mechanism and as a disperser, an ejector structured to rapidly accelerate an air stream is used.

Using a model aggregate consisting of one large and one small particle as shown in **Fig. 6**, the dispersion force F_d can be derived as follows when the aggregate is instantaneously introduced into an uniform fluid flow22).

$$\begin{aligned} F_d = \{&0.119\,\varrho_f u_r{}^2 d_{VB}{}^2 D_V{}^2\,(\varkappa_A - D_V \varkappa_B \varrho_{pA}/\varrho_{pB}) \\ &+ 2.07\,(\eta \varrho_f u_r{}^3 d_{VB}{}^3 D_V{}^3)^{1/2} (\varkappa_A - D_V{}^{3/2} \varkappa_B \varrho_{pA}/\varrho_{pB}) \\ &+ 9.05\,\eta u_r d_{VB} D_V\,(\varkappa_A - D_V{}^2 \varkappa_B \varrho_{pA}/\varrho_{pB})\} \\ &/(D_V{}^3 \varrho_{pA}/\varrho_{pB} + 1) \end{aligned} \tag{12}$$

Where subscripts A and B relate to the two particles composing the aggregate shown in **Fig. 6**, ϱ_f is the density of the fluid, η is the viscosity of the fluid, u_r is the relative velocity between the particle and the fluid, $D_V \equiv d_{VA}/d_{VB}$, d_V is the volume equivalent diameter, ϱ_p is the particle density, and $\varkappa$ is the dynamic shape factor which is described later. The fluid density is related to this equation and therefore, even though the fluid velocity u_r reaches the critical velocity (sound velocity), a further large dispersion force can be obtained by increasing the fluid density by applying a high pressure.

The case when aggregate particles are composed of spherical primary particles of the same density ($\varrho_{pA} = \varrho_{pB}$ of Equation (12)) was considered. Here, the volume equivalent diameter d_V of the aggregate particle is obtained using the following equation.

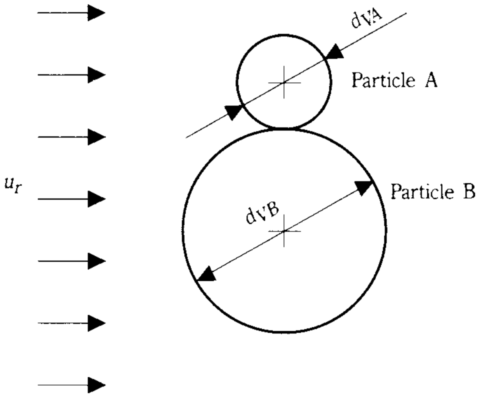

Fig. 6 A model aggregate

$$d_V = N^{1/3} d_{p1} \tag{13}$$

Where N is the number of primary particles composing the aggregate particle and d_{p1} is the primary particle diameter. The dynamic shape factor $\varkappa$ can be obtained approximately, within the range where N is small, using the following equation[23].

$$\varkappa = 0.862\ N^{1/3}\ (2 \leq N \leq 10) \tag{14}$$

With aggregates composed of a large number N of primary particles, d_{VB} is large and therefore the dispersion force F_d of Equation (12) the particles are more easily dispersed. With doublets consisting of two identical spheres, $\varkappa_A = \varkappa_B = 1$, $D_V = d_{VA}/d_{VB} = 1$ and the dispersion force of Equation (12) becomes $F_d = 0$. This means that the dispersion is not initiated by acceleration. Therefore, attention was focused on triplets composed of 3 primary particles and their dispersion force and adhesion force between particles were considered. **Figure 7** shows the dispersion force F_d (solid curve in the Figure) obtained using Equation (12) when triplets disperse into one primary particle and one doublet. P_1 in the Figure is the air pressure supplied by an ejector mentioned later, ϱ_f is the density of air which has reached critical pressure at the throat section of the ejector and u_r is the flow velocity (critical velocity) at the throat section. On the other hand, the dashed line in the Figure indicates van der Waals force as the adhesion force F_a between the particles when dry PSL (polystyrene latex) particles are used. This F_a becomes larger in proportion to the number of contact points between the primary particles in separation (namely F_{a1}, F_{a2} in the Figure). By comparing the adhesion force between the particles in this Figure with the dispersion force, for particles of primary particle diameter of 5 μm and 2 μm can be estimated that almost all particles will be dispersed under the pressure of $P_1 = 1$ MPa and 5 MPa respectively. The alternate long and short dash line in the Figure indicates the liquid bridge adhesion force obtained from the previous **Fig. 4(a)** and this will be explained later.

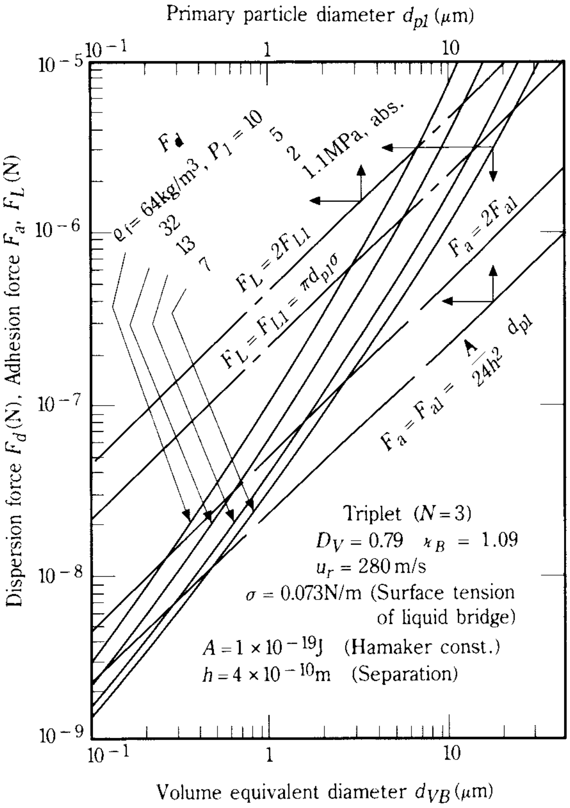

Fig. 7 Calculated results of dispersion and adhesion forces

3.2 Experimental Results

Aggregate particles composed of freeze-dried monodispersed PSL particles were dispersed by an ejector (made by Nisshin Flour Milling Co., Ltd.) shown in **Fig. 8**, allowed to settle on a slide glass placed at the bottom of the sampling chamber shown in **Fig. 8** by gravitational settling, then observed through an optical microscope as shown in **Fig. 9**. The results are given in **Fig. 10**[22,24]. The ordinate in **Fig. 10** shows the ratio of the number of aggregate particles consisting of N primary particles (including $N = 1$) to the total number of aggregates and primary particles after dispersion. P_1 denotes the pressure of nitrogen gas supplied to the ejector. In **Fig. 10**, the results predicted in **Fig. 7** were obtained, such

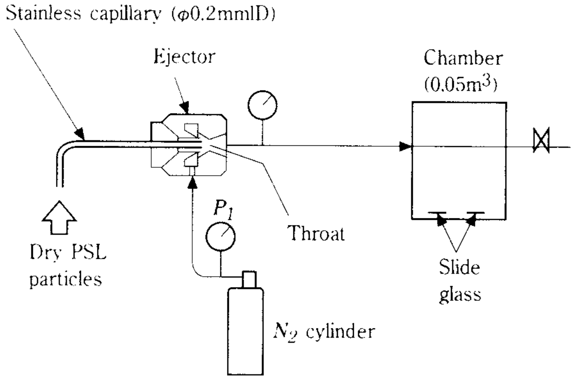

Fig. 8 Experimental set-up for dispersion of aggregate particles

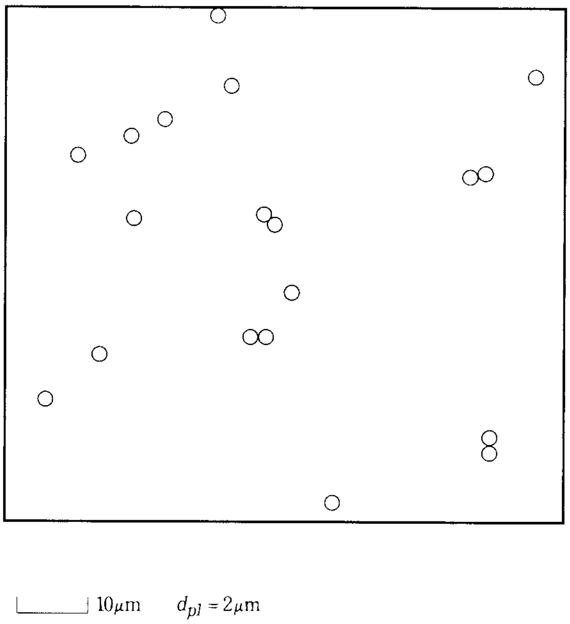

Fig. 9 Photomicrograph of dispersed PSL particles

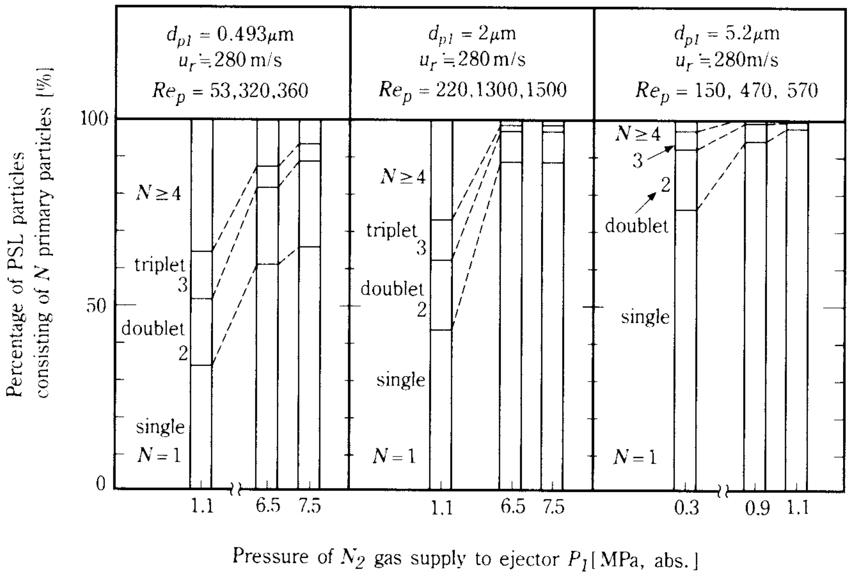

Fig. 10 Experimental results of dispersion of dry PSL aggregate particles

as doublets do not disperse much, and with an increase in nitrogen gas pressure or when the primary particle diameter becomes large, dispersion readily takes place. In this way, by raising the critical pressure of the air stream and increasing the gas density, it became possible to disperse aggregate particles composed of submicron particles with diameters of around 1 μm in air which was believed to be difficult in the past.

Another method to improve the dispersion process is shown in the following[25]. Submicron particles (PSL particles) to be dispersed were mixed with larger dispersing media (glass beads with a diameter of about 100 μm) so as the PSL particles to coat on the glass bead surfaces, and then they were fed to the ejector shown in **Fig. 8**. As shown in **Fig. 11(a)**, the PSL particles were attached thinly to the surface of the glass beads prior to dispersion. As shown in **Fig. 11(b)**, the PSL particles were separated from the glass beads which have passed through the ejector. **Figure 12** shows the experimental results. With PSL particles having a particle diameter of about 0.5 μm, singlets (primary particles) were obtained of 85% of the particles. As expressed by Equation (12), when the particle diameter d_{VB} of particles B, and the particle density ϱ_{pB} become

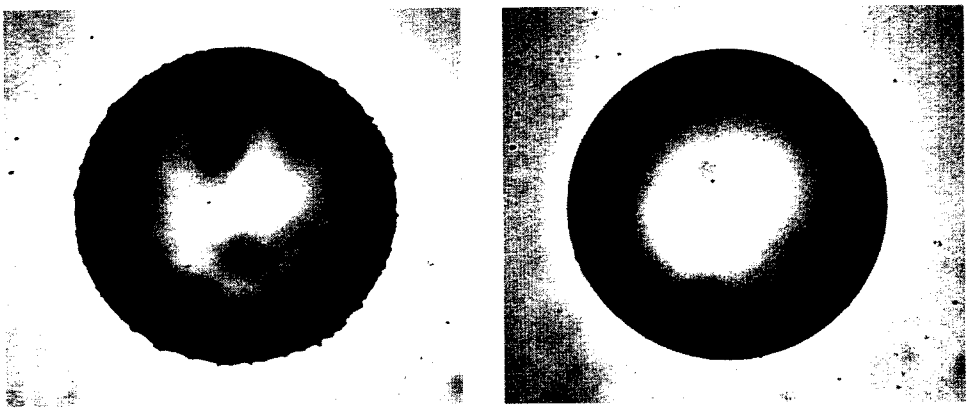

(a) Before

(b) After

Fig. 11 Photomicrographs of glass beads (d_{p2} ≒ $100\ \mu m$) coated with PSL particles ($d_{p1} = 0.493\ \mu m$) before and after dispersion

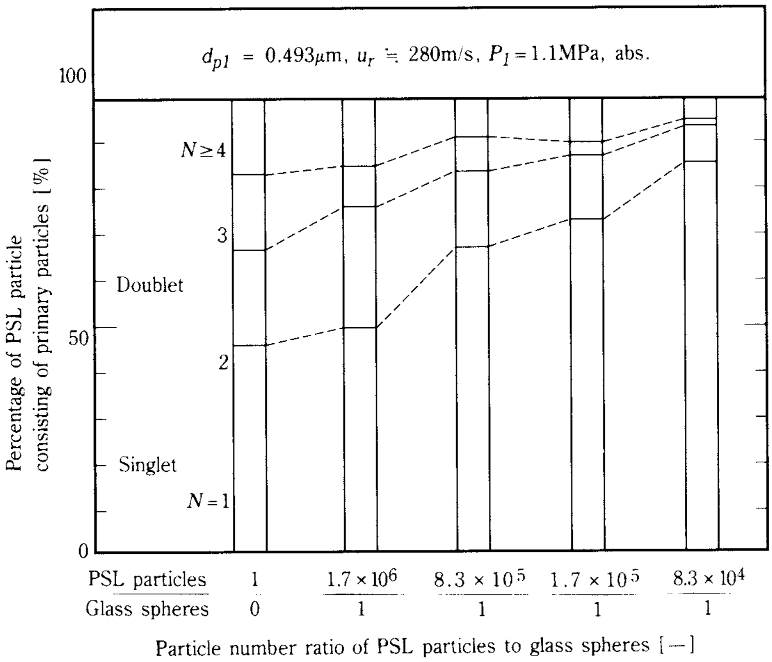

Fig. 12 Experimental results of dispersion of PSL aggregate particles ($d_{p1} = 0.493\ \mu m$)

large, dispersion force F_d increases. This method utilizes this fact. The mixture of PSL particles and 100 μm glass beads has good flowability and therefore a stable feed is possible. Since the terminal settling velocity of 100 μm glass beads is high (0.5 m/s), separation of beads from PSL particles is easy after passing through the ejector.

3.3 Evaluation of Adhesion Forces between Particles in Air

The above concerns the dispersion of particles coagulated by van der Waal's force but when particles coagulate together due to the liquid bridge adhesion force, the adhesion force between particles becomes stronger by about one order of magnitude than the van der Waals force as shown by the alternate long and short dash line in **Fig. 7** and therefore it becomes difficult for aggregate particles to disperse. **Figure 13** shows the experimental results. The experimental setup is the same as that of **Fig. 8** and the feed gas pressure P_1 to the ejector is 10 MPa. The ordinate of **Fig. 13** is the same as that

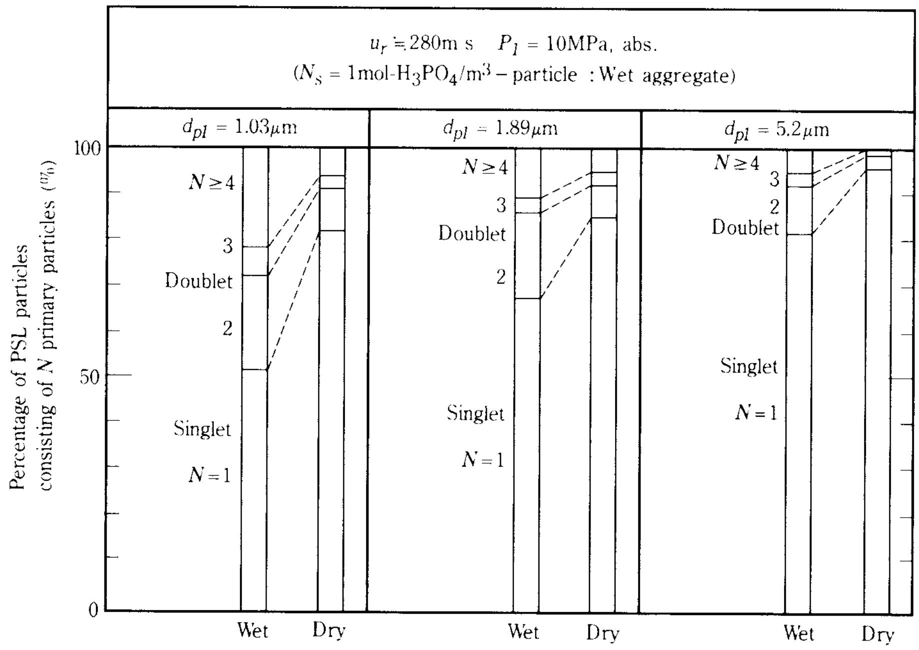

Fig. 13 Experimental results of dispersion of dry and wet PSL aggregate particles

of **Fig. 9**. Since the dispersion force applied to the aggregate particles is the same, the wet aggregate particles which form the liquid bridge do not disperse so much compared with dry aggregate particles. In this way, when the adhesion force between particles becomes strong, it becomes difficult for particles to disperse but depending on the magnitude of the dispersion force.

Figure 14 is a plot of the dispersion results obtained using an ejector, of PSL aggregate particles for both adhesion forces between particles of van der Waal force and liquid bridge adhesion force. The abscissa of the figure represents the percentage of singlets against the total number of aggregates and singlets after dispersion while the ordinate of the figure represents the ratio of the dispersion force to the adhesion force between particles when triplets are dispersed. The number of contact points n_k of primary particles in separation of triplets is one or two but the adhesion force value between particles in the figure was assumed to be $n_k = 1$. The ○ mark in the figure shows the case of van der Waal's force while the Δ mark shows the case of liquid bridge adhesion force which correlate well with the ratio of the dispersion force to the adhesion force between particles. In this figure, the slope of the line has a smaller gradient up to a point where the line bends and the value of the ordinate is unity and this shows that when the dispersion force becomes smaller than the adhesion force between particles, particle dispersion becomes difficult. If a dispersion experiment is conducted using an ejector with a known dispersion force applicable to aggregate particles and the results are plotted as shown in **Fig. 14**, then the adhesion force between the primary particles which compose the aggregate can be roughly estimated.

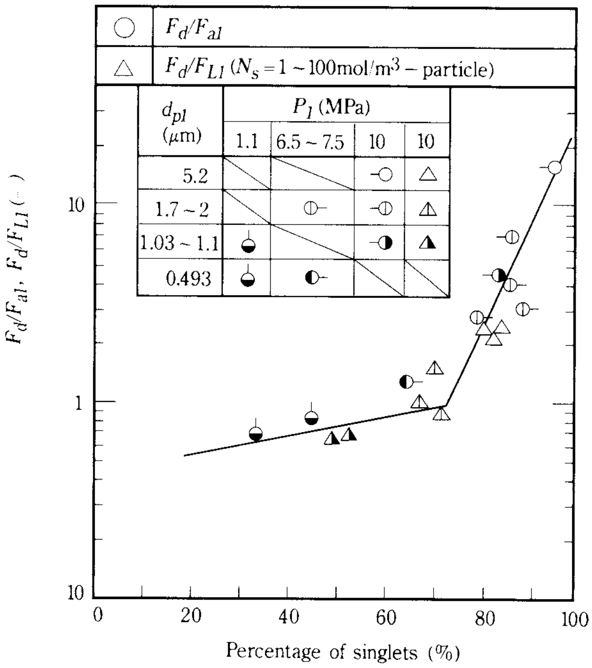

Fig 14 Ratio of dispersion force to adhesion force against percentage of singlets

4. Conclusion

The adhesion among submicron particles changes the behavior of aggregates or powder beds and is a cause of trouble in industrial particle processing. The adhesion force arising from a liquid bridge changes depending on the humidity of the surrounding in which the particles are placed. If trouble should occur in processing of particles, it is thought that some of the problems can be solved by considering the cause following the line of thought described here. Demands to handle fine particles as single particles are increasing in industry and the dispersion of aggregates has also become an important issue. It is expected that dispersion phenomena may be further clarified by conducting studies focusing on individual particles.

References

1) de Laplace, P.S.: "Supplement to book of Mecanique Celeste" (1806)
2) Young, T.: "Miscellaneous Works (Edited by G. Peacock)", vol. 1, p.418, J. Murray, London (1853)
3) Thomson, W.: Proc. Roy. Soc. (Edin.), 7, 63 (1876)
4) Kousaka, Y., Y. Endo and Y. Nishie: Kagaku Kogaku Ronbunshu, **18**, 942 (1992)
5) Endo, Y., Y. Kousaka and M. Ishii: Kagaku Kogaku Ronbunshu, **19**, 1128 (1993)
6) Carman, P.C.: J. Phys. Chem., **57**, 56 (1953)
7) Chikazawa, M. et al.: Funtai Kogaku Kenkyukaishi, **14**, 18 (1977)
8) Kruyer, S.: Trans. Faraday Soc., **54**, 1758 (1958)
9) Wade, W.H.: J. Phys. Chem., **68**, 1029 (1964)
10) Endo, Y., Y. Kousaka and Y. Nishie: Kagaku Kogaku Ronbunshu, **18**, 950 (1992)
11) Marson, B.J.: "The Physics of Clouds, 2nd ed.", p.24, Clarendon Press, Oxford (1971)
12) Endo, Y., Y. Kousaka and Y. Nishie: Kagaku Kogaku Ronbunshu, **19**, 411 (1993)
13) Ridgway, K. and K.J. Tarbuck: Brit. Chem. Eng., **12** 384 (1967)
14) Endo, Y., Y. Kousaka and Y. Nishie: Kagaku Kogaku Ronbunshu, **19**, 55 (1993)
15) Erle, M.A., D.C. Dyson and N.R. Morrow: AIChE J., **17**, 115 (1971)
16) Pietsh, W. and H. Rumpf: Chem. Ing. Tech., **39** 885 (1967)
17) Fisher, R.A.: J. Agric. Sci., **16**, 492 (1926)
18) McFarlane, J.S. and D. Tabor: Pro. Roy. Soc., A.202, 224 (1950)
19) Endo, Y. and Y. Kousaka: Kagaku Kogaku Ronbunshu, 19, 1136 (1993)
20) Rumpf, H.: Chem. Ing. Tech., **42**, 538 (1970)
21) Kousaka, Y., K. Okuyama, A. Shimizu and T. Yoshida: J. Chem. Eng. Japan, **12**, 152 (1979)
22) Kousaka, Y., Y. Endo, T. Horiuchi and T. Niida: Kagaku Kogaku Ronbunshu, **18**, 223 (1992)
23) Kousaka, Y., K. Okuyama and A.C. Payatakes: J. Colloid and interface Sci., **84**, 91 (1981)
24) Endo, Y. and Y. Kousaka: Kagaku Kogaku Ronbunshu, **18**, 760 (1992)
25) Endo, Y., Y. Kousaka and S. Fujii: Kagaku Kogaku Ronbunshu, 19, 698 (1993)

Author's short biography

Yasuo Kousaka

The author is Professor of Chemical Engineering Department at University of Osaka Prefecture since 1979. His major research interests are dynamic behavior of aerosol particles, sizing techniques of aerosol particles and powders, and dispersion of aggregate particles in air and water. He is currently editor in chief of Journal of the Society of Powder Technology, Japan, and vice president of Japan Association of Aerosol Seience and Technology.

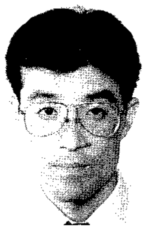

Yoshiyuki Endo

The author is Research Associate of Chemical Engineering Department at University of Osaka Prefecture since 1991. His research interests are almost same as those of Professor Kousaka.

Review

Crystallization and Crystallizing Processes to Produce Controlled-Properties Solid Particles†

C. Laguérie, B. Biscans and N. Gabas
*ENSIGC – Laboratoire de Génie Chimique (URA CNRS 192)**

Abstract

The need for preparing solid particles with required properties has led to the development of processes allowing control of these properties : high purity, size, size distribution, crystalline form, flowability, packability, or other specific effects. This paper deals with several ''new'' processes of preparation of solid particles of controlled properties. Most of these processes have been known for a long time but they have not been carried out extensively in production. The potential of such processes is shown.

1. Introduction

Over the past decade, the chemical industry has been faced with a quickening trend towards improvement of product quality in relation to the growing importance attached to fine chemicals, pharmaceuticals, special-effect chemicals and other high-value materials. The need for high-purity powders with controlled properties of size and size distribution, crystalline form, morphology, specific surface area, flowability, packability and specified effects for their use has led to the development of new processes for preparing chemicals in solid form. Most of these processes are based on fundamental principles of crystallization occurring naturally or combined with other operations such as solvent extraction, drying, and granulation. This contribution provides a non-exhaustive review of some of these processes which have already been known for a long time, but whose application to industrial purposes can be considered as rather new.

2. Some principles of crystallization from solutions

The crystallization or precipitation of powders involves the nucleation and growth of solid particles from a supersaturated solution.

Supersaturation can be induced in several ways. Systems in which the solubility of the solute increases with temperature can be brought to supersaturation by cooling the solution. For systems in which the solubility is not sensitive to temperature, supersaturation can be easily achieved by isothermal evaporation of the solvent. These two methods are often combined in the vacuum cooling crystallization process in which a hot concentrated solution is adiabatically flashed to a reduced pressure.

Supersaturation may also be induced by adding other miscible components to the solution in order to reduce the solubility of the solute. This method, extensively used to produce speciality chemicals, is usually called drowning out. In the case of a reaction product present, for example, as an anion in the solution, the addition of excess quantities of a countercation forces the product out of solution. This method is well known as salting out.

In many instances, a chemical reaction in the solution may produce an insoluble species which precipitates out as the reaction proceeds. This occurs for instance in the production of azopigments and disperse dyes from coupling reactions, and in a lot of inorganic chemical systems. The reactive crystallization is traditionally referred to as precipitation.

Drastic effects on crystallization kinetics and crystal morphology or purity may be related to the presence of impurities in the crystallizing systems. These impurities are often difficult to remove and several steps of recrystallization may be required to produce crystals with their desirable properties. In other cases, controlled trace quantities of selected species may be used specifically as additives to control the crystallization process.

In addition to nucleation and crystal growth, other phenomena may occur in industrial crystallizers. Attrition due to mechanical interactions between crystals and between crystals and moving mechanical

---

* 18, chemin de la Loge – 31078 Toulouse Cedex – France
† Received June 18th, 1994

parts results in the generation of small crystals a little larger than those created by nucleation, and makes parent crystals more rounded with free flowing properties. Dramatic damage to parent crystals as a result of high-energy contacts between crystals and moving parts of crystallizers can be induced through breakage with the formation of coarse fragments and a severe size reduction of damaged crystals.

With an opposite effect on the size distribution, agglomeration often takes place when two or more crystals are attracted by any kind of cohesion force and remain together sufficiently long that they grow into stable entities containing individual crystalline particles of irregular shape and usually poor flow properties.

2. Use of tailor-made additives to control crystallization processes

The morphology of a crystal results from the relative growth rates of its various faces, with the general rule that the slower the growth rate, the larger the face. The growth rate of each individual face is determined by intermolecular interaction between molecules in the crystal, as well as by external parameters such as solvent, temperature, supersaturation, impurities. Dramatic modification in crystal morphology may result from changes in any of these factors. In particular, small traces of surface-active impurities may induce morphological changes when adsorbed at specific surfaces of the growing crystal. These impurities can act either by reducing the specific surface energy or by blocking integration of a growing face or by limiting the supply of material to the crystal face. They can be ionic species, surfactants, chemical binding complexes or specific molecules subjected to electrostatic and van der Waals interactions, or tending to form hydrogen bonds with the substrate molecules at the surface[1-5]. Recently, owing to the increased power of computers and understanding of the solid state, potential energy calculations at the microscopic level and evaluation of molecular interaction in the growth layer faces have led to quantitative prediction of crystal morphology[6-9]. The effects on crystal habit caused by tailor-made additives whose molecular structures are very close to those of the substrate molecules comprising the crystal have been derived from these analyses. The additive is selectively adsorbed on the host crystal sites only on those faces where its modified part emerges from the crystal surface[7, 8]. On these faces, the additive is bound in a very similar way to a substrate molecule by virtue of interactions between its unmodified part and the neighboring substrate molecule at the surface layer. The regular deposition of oncoming crystal layers becomes thus disturbed, causing retardation of growth normal to these faces with the consequence of a relative increase in their surface area. From there, it is also possible to select inhibitors in order to modify the habit of organic crystals in a desired and controlled manner.

Figure 1 shows modifications of the habit of (E) – cinnamide crystals in the presence of additives obtained by substituting a bulkier functional group for a corresponding one of the substrate molecule.

A new form of engineering, namely morphological engineering, is now emerging and tailor-made additives are being designed, including surfactants[3, 7]. The important feature of this methodology is the specificity of tailor-made additives in technological applications. Besides changes in crystal morphology, additive design is starting to be used as an effective means of separating products from racemic solutions in relation to chiral products, and of controlling the production of a desirable polymorph even at the expense of the stable form[1, 8, 10, 11].

3. Hydrothermal synthesis of ultrafine crystalline powders

Fabrication of ceramic materials such as titanates, magnetic materials such as ferrites or of other component materials suitable for living bodies such as hydroxyapatites involves the sintering of powders whose required characteristics are usually high purity, high degree of crystallinity and ultrafine size with narrow size distribution. The hydrothermal process has been successful for preparing powders with the required specificities[12-16]. It allows liquid-phase reactions that do not occur below 100 °C to proceed appreciably. It consists in precipitating the product under a non-crystalline gel-like state in a first step at room temperature as the result of a reaction between two aqueous solutions, and then subjecting the suspension to the hydrothermal treatment in an autoclave at controlled heating rate and stirring speed, and maintaining it for several hours at a fixed temperature, generally between 100 and 300 °C. In the case of Ni-, Co- and Zn-ferrite synthesized by Kumazawa et al.[15], round ultrafine particles were formed whose size ranged from 6 to 16 nm dependent on hydrothermal conditions, and whose size

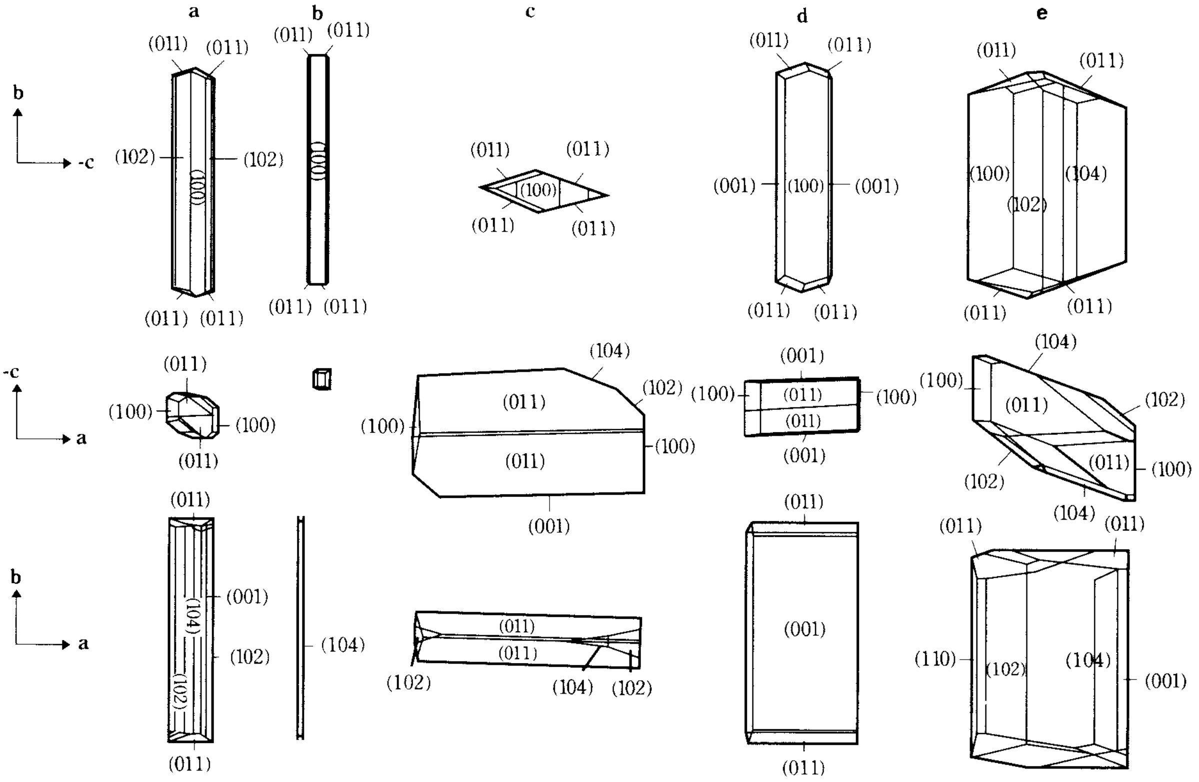

Fig. 1 Crystals of (E)-cinnamide grown in the absence (a) and presence of additives : N-methyl-(E)-cinnamide of p-chloro-(E)-cinnamide (b) ; (E)-cinnamide acid (c) ; αn β-chloro-(Z)-cinnamide (d) ; o-chloro-(E) cinnamide (e) (from reference 7).

distribution could be described by a log-normal function with a geometric standard deviation of about 1.2. The crystallinity degree increased with temperature.

4. Precipitation of microsized particles from supercritical fluid solutions

Hannay and Hogarth[17] observed the remarkable ability of supercritical fluids (SF) to dissolve solids as early as 1879. In recent years, there has been a growing interest in using SF as a solvent in a number of crystallization and precipitation processes[18-26] to ensure the manufacture of crystalline and amorphous powders with morphologically uniform particles and narrow size distribution. An important advantage of SF used as solvents is the high sensitivity of the solubility of solids with respect to temperature and pressure. Due to the high compressibility of SF, small changes in pressure result in large changes in density and solvent power. Addition of small amounts of a cosolvent to SF can also enhance solvent power by a very significant factor[23]. Moreover, as pressure perturbations propagate very quickly within SF, the medium is essentially uniform whereas in conventional crystallization, the suspension undergoes temperature gradients. The consequence is that nucleation generates particles more uniform in morphology and narrower in size distribution than those produced in conventional crystallizing systems[22].

4.1 Crystallization in the supercritical region

Tavana and Randolph (24) have reported experimental results of the crystallization of benzoïc acid in SF CO_2. The operation was run in a similar way as a conventional batch cooling crystallization. In conventional batch cooling crystallization, a saturated solution is cooled from an initial temperature at which the solute is highly soluble to a final lower operating temperature, with lower solubility, along an optimal cooling curve followed to maintain a reasonable level of supersaturation as crystallization proceeds. When the solute-laden solution is a SF, supersaturation can be induced by varying either temperature or pressure. It is more convenient to choose pressure as the main variable. Depressurisation curves can be fixed in order to promote formation of small -or large-sized particles as desired. The crystallization process remains in the supercritical region. The authors have shown that nucleation and growth mechanisms are the same as those involved in liquid solvents, but the process in SF offers the potential to change particle size distribution very easily without the limitations inherent in precipitation from liquid solution.

4.2 Use of supercritical fluid as an anti-solvent

Some processes involve SF for their anti-solvent effect on the product to be crystallized. They consist in preparing a solution of the solute with a classical liquid solvent. Mixing the solution with the non-solvent SF leads to the formation of two phases. The lighter one mainly contains the SF with a certain amount of the solvent without the solute. The heaviest one consists of the solvent, a large amount of the SF, and the solute whose solubility is considerably reduced so that it precipitates out. This process has been used successfuly to produce crystals of cyclotrimethylene trinitramine, RDX, commonly called plastic, by adding SF CO_2 to a solution of RDX in cyclohexanone. Other applications relate to pigments for paints, explosives, polymers, magnetic materials, semiconductors, supraconductors, and piezo-elastic materials26).

4.3 Rapid expansion of supercritical fluid solutions (RESS)

Several researchers have performed studies on the production of fine particles as the result of a rapid expansion of SF solutions. Battelle20, 21) has developed a process called the RESS process (**Figure 2**). It typically involves the dissolution of a solid in a solvent at increased temperature and pressure to enhance the solubility. The resulting solution is heated to supercritical conditions in a pre-expansion region. Then it is allowed to expand rapidly through a short nozzle into a low-temperature and low-pressure environment where the solvent power of the fluid is negligible. The time scale of the expansion ranges between 10^{-8} and 10^{-5} seconds. This provokes the rapid nucleation and growth of the particles, provided that sufficient solute density exists in the expansion jet (**Figure 2**).

Two situations can arise. Under proper pre-expansion conditions, the solvent passes from the SF state to the gaseous state and the product is collected essentially dry. When the pre-expansion temperature is not high enough, a two-phase gas-liquid region is traversed during the expansion producing droplets. This technology offers the potential to produce thin films, fibers, and fine powders with narrow size distributions in crystalline or amorphous form, dependent on the pre-expansion and post-expansion conditions22) as well as on the flow properties of the nozzle across which the expansion is allowed to occur21).

4.4 Production of aerogels by supercritical drying

Aerogels have been used as catalysts for more than fifty years. Their production involves synthesizing a sol-gel by using alkoxides. This begins by the formation of a sol which is a suspension of solid particles in a liquid, then of a gel which is a diphasic material with the solid encapsulating a liquid. The liquid can be removed from the gel by conventional drying, but drying with supercritical extraction (supercritical drying) gives better qualities to the product. Especially the surface area is twice as large and the pore volume is almost an order of magnitude higher. In addition, it remains amorphous after being

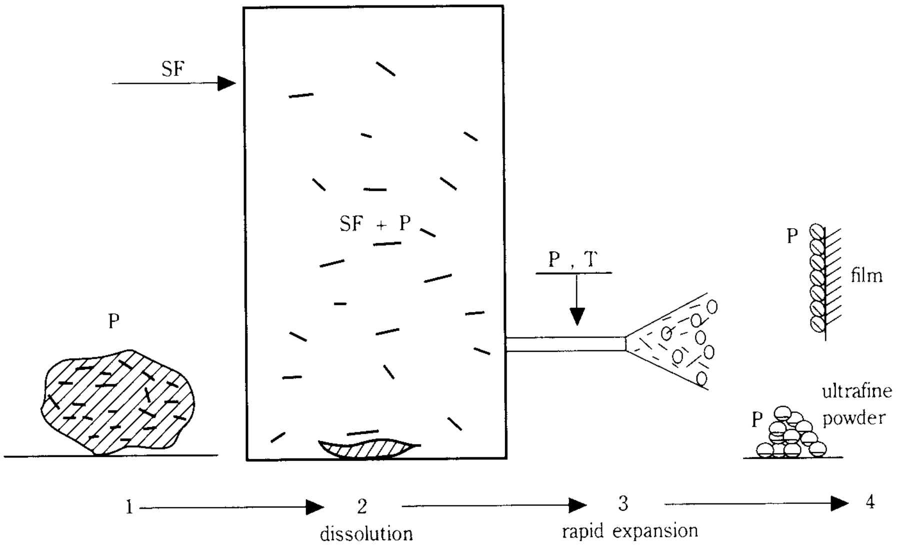

Fig. 2 Principle of RESS process (from reference 26)

heated up to 500 °C[27]. This process was developed by Teichner (19) in the 1960s. It could be carried out to produce other materials than aerogels (pharmaceuticals, optical fibers, catalysts, composite materials).

4.5 Other processes involving supercritical fluids to produce solid particles

Garabos et al (26) have reported several processes, all under study, involving supercritical fluids to produce solid particles. These processes will not be described in this paper. However, it can be noted that hydrothermal synthesis in a SF medium, which has been known for fifty years, is fairly analogous to the hydrothermal synthesis in a liquid medium presented in Section 3. This process allows the preparation of uniform-sized powders with very high chemical purity and very high crystallinity.

Recent studies have shown that reverse microemulsions can be formed in a continuous supercritical phase whose properties are the same as those generated in conventional liquid solvents at atmospheric pressure. The small droplets, whose diameter ranges between 3 and 20 nm, act as local microreactors and enhance interactions between the product in solution within the droplets and the continuous phase as a result of very high diffusivities in SF. This allows the generation of very fine particles with a very narrow size distribution.

SF has also been used as a reaction medium for a long time. The best example is polymerisation of ethylene at very high pressure (over 150 MPa) in supercritical ethylene. The polymer formed is dissolved in the SF monomer and is withdrawn continuously. It has been possible to produce many powders as the yield of reactions carried out in SF media, with the advantage of very easy recovery by expansion of the supercritical medium. Such processes allow one to operate at higher temperatures without any risks of damaging the reactants and products. Ti O_2 has already been obtained in the form of a very fine crystalline powder (less than 100 nm) from titane isopropoxide in supercritical ethanol at 360 °C

5 Spherical crystallization for the development of pharmaceutical preparation

Most dosage forms are solid: capsules, pellets, tablets. They are made from powders whose properties must be reproducible. Generally, crystallization and granulation are the two steps necessary to equip the initial powder with adequate properties (flowability, packability). Spherical crystallization can be seen as a new technique combining crystallization and agglomeration processes by which the crystals obtained are directly agglomerated into spherical form[28, 29]. Developed by Kawashima (22), this process proceeds according to two steps : the precipitation of the drug crystals and then their agglomeration thanks to the addition of a bridging liquid which wets the crystals preferentially. A very interesting method consists in using a three-solvent system : a solvent, a non-solvent and a third solvent that is miscible with the other two solvents. For instance, in the case of salicylic acid, water-chloroform-ethanol is a representative solvent combination. Crystallization occurs in the shaded region of the diagram shown in **Figure 3**. Liberation of small quantities of chloroform induces wetting of the salicylic acid crystals and provokes their agglomeration into spherical-form aggregates. These spherical aggregates can be directly compressed into tablets, whereas it is difficult to directly compress salicylic acid crystals due to their characteristic needle shape which is responsible for their poor flowability and packability (**Figure 3**).

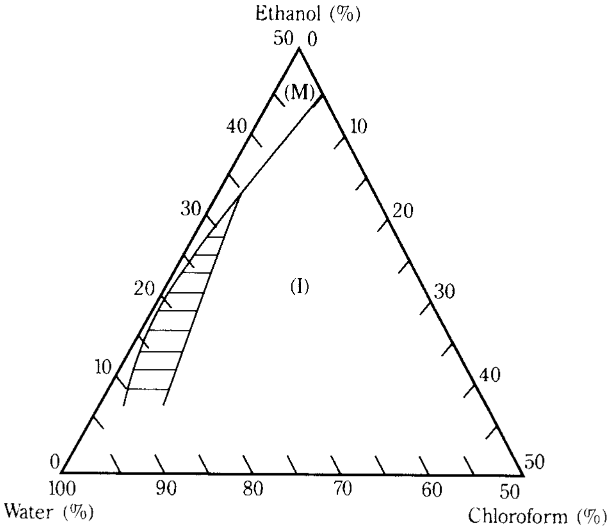

Fig. 3 Solubility diagram of chloroform in the ethanol-water mixture in relation to spherical crystallization of salicylic acid (from reference 28)

6. Preparation of solid particles of controlled properties in emulsions

6.1 Emulsion-solvent-diffusion method for preparing agglomerated crystals

With the same purpose as the spherical crystallization, Kawashima et al. (30) have developed a new emulsion-solvent-diffusion method (**Figure 4**) to agglomerate the crystals of poorly compressible pharmaceuticals during crystallization without using any binder. In this process, the drug X is dissolved in a solvent S at temperature T_1 in a storage tank. A non-solvent, NS, miscible with S and containing small quantities of an emulsifier, E, is kept agitated at temperature T_2 ($T_2 < T_1$) in the crystallizer. Then the X-S solution is fed at a constant flow rate from the storage tank to the crystallizer through a capillary tube. The crystallization system is thermally controlled at temperature T_2. An emulsion of small droplets of X-S solution is formed in the NS continuous phase due to the presence of the emulsifier E. The temperature of droplets is rapidly reduced. Simultaneously, the solvent S in the droplets diffuses to the outer continuous phase while the non-solvent NS enters the inner phase (droplets). These heat and mass transfers lead the droplets to their supersaturation limit from which nucleation occurs. Crystals grow within the droplets, and spherical drug crystal agglomerates are finally produced while retaining the initial shape of the emulsion droplets first formed[29]. The tensile and shear tests of the resultant agglomerated crystals prove their appreciable flowability and packability. They can be easily compressed into tablets without capping (**Figure 4**).

This technique has been extended recently to include direct encapsulation of a drug in biodegradable polymeric nanospheres serving as the carrier of the drug[31].

6.2 Chemical reactions in microemulsions to obtain ultrafine particles.

Ultrafine particles can be obtained as a result of chemical reactions in microemulsions acting as microreactors in order to control their growth[32, 33]. The method described by Lopez-Quintela and Rivas (33) consists in preparing two microemulsions formed by nanodroplets of water dispersed in oil, each containing an appropriate reactant. Once the right microemulsion systems are obtained, they are mixed (**Figure 5**). An interchange of the reactants A and B takes place during the collision of the nanodroplets in the microemulsions. This interchange is very fast and the reaction occurs rapidly, leading to nucleation and growth of the crystals produced inside the droplets which control the final size of the particles. Microemulsions should be chosen in such a way that the

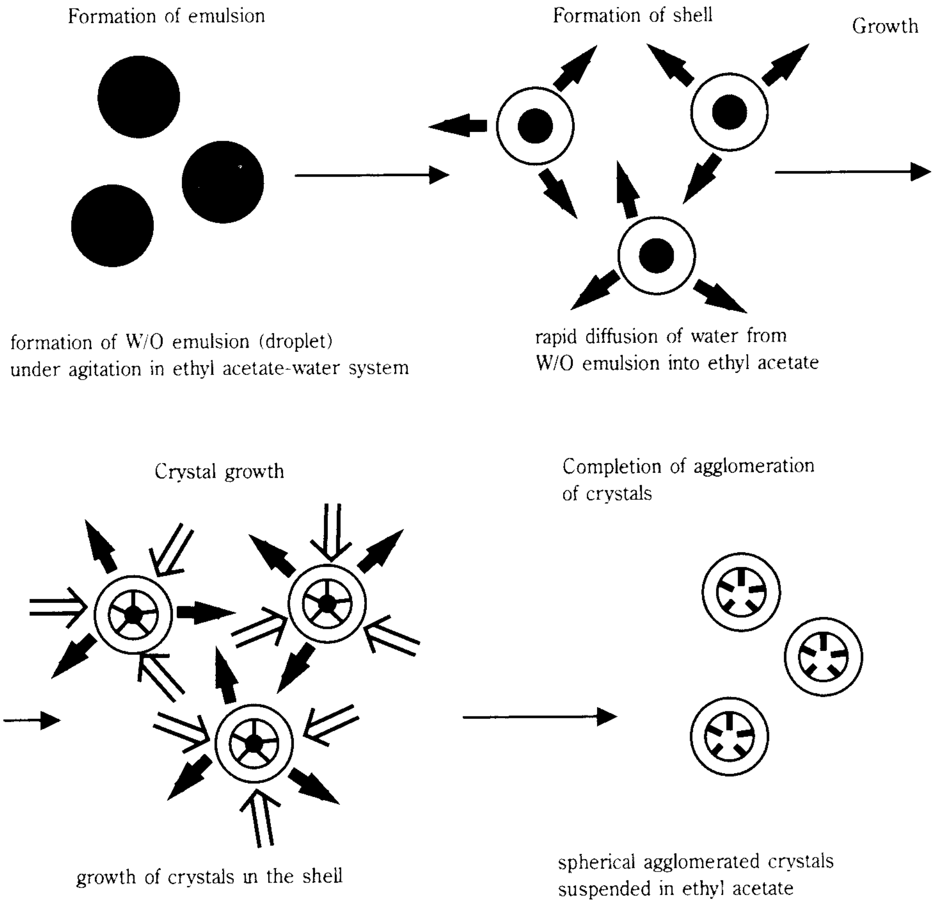

Fig. 4 Schematic process for emulsion-solvent diffusion method (from reference 30)

curvature radius is similar to the natural radius so that the surfactant film cannot be opened during collisions which would lead to an interchange of nuclei and would hinder the droplets in controlling the final size of the particles (**Figure 5**).

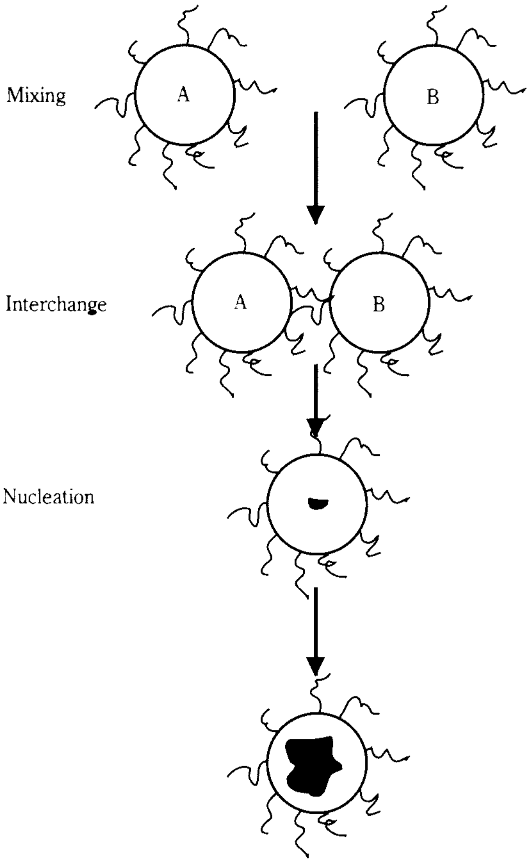

Fig. 5 Schematic process for the formation of ultrafine particles as the result of reactions in microemulsions

6.3 Precipitation in liquid membrane systems

A new technique to control the particle size in precipitation processes has been developed by Yang et al.[34] and Stewart et al.[35] using a liquid surfactant membrane emulsion (LSME). An LSME is actually a double emulsion in which an aqueous-in-oil type emulsion, stabilized by a surfactant, is dispersed in a second aqueous phase (oil/aqueous/oil LSMEs can also be formed). One of the reactants is transported from the outer aqueous phase via an oil phase containing a facilitating carrier to an internal aqueous phase of another reactant. A precipitation reaction takes place, and particles nucleate and grow at the internal aqueous/oil interface of the emulsion. The size distribution of the particles within the emulsion is found to be related to the emulsion drop size distribution. This technique was applied to produce copper oxalate crystals (34) with controlled size distribution. A further study (35) has shown that the morphology of the particles formed depends on the nature of the surfactant present in the organic phase.

6.4 Formation of ultrafine particles in reverse micelles

With the objective of preparing and stabilizing uniform ultrafine particles by preventing uncontrolled aggregation, processes involving crystallization in reverse micelles have been developed (36,37) and models have been proposed to explain them. Hirai et al.[36] have studied the formation mechanism of TiO_2 ultrafine particles in AOT/iso-octane reverse micelles by means of hydrolysis of titanium tetrabutoxide (TTB) by following the process via the UV-visible absorption spectra. They have observed that the increase of TTB concentration and water content facilitates particle formation, which is also controlled by the number of micelles. They have proposed a scheme which fits in well with the observed data.

Conclusion

The need for preparing solid particles with required properties – either to be used directly in the form they are obtained or, more generally, to be further processed to yield dispersions, tablets, pastes, powders, etc., as pharmaceuticals, dyestuffs, agrochemicals, polymers or basic materials of electronics components or advanced construction materials – has led to the development of processes allowing control of these properties. Most of these processes have been known for a long time but they have not been carried out extensively in production. They are based mainly on the fundamental principles of crystallization and precipitation, as was mentioned at the beginning of this contribution. A non-exhaustive presentation of some of these ''new'' processes has been made, including control of simple crystallization operations by tailor-made additives, hydrothermal synthesis of ultrafine crystalline powders, use of supercritical fluids as solvents, anti-solvents or reaction medium, rapid expansion of supercritical fluid solutions, supercritical drying, reverse microemulsion in a continuous supercritical phase, spherical crystallization, emulsion-solvent-diffusion method and chemical reaction in microemulsions, in liquid membrane systems and in reverse micelles.

References

1) Davey, R. J., Polywka, L. A. and Maginn, S. J.: The control of crystal morphology by additives : molecular recognition, kinetics, and technology, in Advances in Industrial Crystallization, Ed. J. Garside, R. J. Davey and A. G. Jones, Butterworth, Oxford (1991), 150-165
2) Dirksen, J. A. and Ring, T. A.: Fundamentals of crystallization: kinetic effects on particle size distributions and morphology, Chem. Eng. Sci., **46** (1991) 2389-2427
3) Canselier, J. P. and Chianese, A.: Surfactants in crystallization processes, in XXIII Jornadas del Comite Espanol de la Detergencia, **23** (1992) 261-280
4) Chen, D. B., Garside, J., Davey, R. J. and Maginn, S. J.: Meta-chloronitrobenzene: the description and prediction of polar morphologies, Proceedings of the 12th Symposium on Industrial Crystallization, Z. H. Rojkowski ed., Warsaw, Poland (1993)3-069
5) Myerson, A. S., Weisinger, Y. and Ginde, R.: Crystal shape, the role of solvents and impurities, Proceedings of the 12th Symposium on Industrial Crystallization, Z. H. Rojkowski ed., Warsaw, Poland (1993) 3-135/3-139
6) Berkovitch-Yellin, Z.: Toward and ab Initio derivation of crystal morphology, J. A. C. S., **107** (1985) 8239-8253
7) Berkovitch-Yellin, Z., van Mil, J., Addadi, L., Idelson, M., Lahav, M. and Leiserowitch, L.: Crystal morphology engineering by "tailor-made" inhibitors : a new probe to fine inter-molecular interactions, J.A.C.S., **107** (1985) 3111-3122
8) Lahav, M. and Leiserowitz, L.: "Tailor-made" auxiliaries for the control of nucleation, growth and dissolution of crystals, in Proceedings of the 11th Symposium on Industrial Crystallization, Garmisch-Partenkirchen, Ed. A. Mersmann, (1990) 609-613
9) Lin, C. H., Gabas, N., Canselier, J. P., Pèpe, G. and Laguérie: Surfactants effects on gamma-aminobutyric acid crystallization: nucleation and crystal habit, C., Proceedings of the 12th Symposium on Industrial Crystallization, Z. H. Rojkowski ed., Warsaw, Poland (1993) 3/51-56
10) Weissbuch, I., Zbaidia, D., Addadi, L., Leiserowitz, L. and Lahav, M.: Design of polymeric inhibitors for the control of crystal polymorphism. Induced enantiometric resolution of racemic histidine by crystallization at 25 °C, J.A.C.S., **109** (1987) 1869-1871
11) Staab, E., Addadi, L., Leiserowitz, L. and Lahav, M.: Control of polymorphisms by "tailor-made" polymer crystallization auxiliaries. Preferential precipitation of a metastable polar for second harmonic generation, Adv. Mater., **2** (1990) 40-43
12) Arends, J., Schuthof, J., van der Linden, W.H. and Bennema, P.: Preparation of pure hydroxyapatite single crystals by hydro-thermal recrystallization,J. Crystal Growth, **46** (1979), 213
13) Sada, E., Kumazawa, H. and Cho, H. M.: Synthesis of barium ferrite ultrafine particles by a hydrothermal method, Ind. Eng. Chem. Res., **30** (1991) 1319-1323
14) Sada, E., Kumazawa, H., and Murakami, Y.: Hydrothermal synthesis of crystalline hydroxyapatite ultrafine particles, Chem. Eng. Comm., **103** (1991) 57-64
15) Kumazawa, H., Oki, K., Cho, H. M. and Sada, E.: Hydrothermal synthesis of ultrafine ferrite particles, Chem. Eng. Comm., **115** (1992) 25-33
16) Thompson R. W.: Nucleation of molecular sieve zeolites in hydrothermal systems, Proceedings of the 12th Symposium on Industrial Crystallization, Z. H. Rojkowski ed., Warsaw, Poland (1993) 2-027/2-036
17) Hannay, J. B. and Hogarth, J.: Proc. Roy. Soc. London, **A 29** (1879) 324
18) Teichner, S. J.: Aerogels of inorganic oxides, in Proc. 1st Int. Symp. Aerogels, Ed. J. Fricke, p. 22, Springer Verlag, Berlin (1986), 22-30
19) Teichner, S. J.: Aerogels – Why they are in vogue, Chemtech, **21** (1991) 372-377
20) Petersen, R. C., Matson, D. W. and Smith, R. D.: Rapid precipitation of low vapor pressure solids from supercritical fluid solutions : the formation of thin films and pwders, J.A.C.S., **108** (1986) 2100-2102
21) Matson, D. W., Fulton, J. L., Petersen, R.C. and Smith, R. D.: Rapid expansion of SF solutions: solute formation of powders, thin films and fibers, Ind. Eng. Chem. Res., **26** (1987) 2298-2306
22) Mohamed, R. S., Debenedetti, P. G. and Prud' Homme, R. K.: Effects of process conditions on crystals obtained from supercritical mixtures, AIChE Journal, **35** (1989) 325-328
23) Tavana, A., Chang, J., Randolph, A. D. and Rodriguez, N.: Scanning of cosolvents for supercritical fluids solubilization of organics, AIChE Journal, **35** (1989) 645-648
24) Tavana, A. and Randolph, A. D.: Manipulating

Solids CSD in a supercritical fluid crystallizer: CO2-benzoic acid, AIChE Jl, **35** (1989) 1625-1630

25) Chang, C. J. and Randolph, A. D.: Precipitation of microsize organic particles from supercritical fluids, AIChE Journal, **35** (1989) 1876-1882

26) Garabos, Y., Le Neindre, B., Subra, P., Cansell, F. and Pommier, F.: Fluides supercritiques et gravité, fluides supercritiques et matériaux, Ann. Chim. Fr., **17** (1992) 55-90

27) Ko, E. I.: Aerogels as catalysts and catalyst supports, Chemtech **23** (1993) 31-36

28) Kawashima, Y.: Spherical crystallization as a novel particle design technique for the development of pharmaceutical preparations, Kona, **5** (1987) 69-75

29) Espitalier, F., Biscans, B., Laguérie, C., Authelin, J. R. and emulsion droplets. Intractions between usage properties and process, Proceedings of the 12th Symposium on Industrial Crystallization, Z. H. Rojkowski ed., Warsaw, Poland, (1993) 3-025/3-030

30) Kawashima, Y., Niwa, T., Takeuchi, H., Hino, T., Itoh, Y. and Furuyama, S. J.: Characterisation of polymorphs of tranilast anhydrate and tranilast monohydrate when crystallized by two solvent change spherical crystallization techniques, Pharm. Sci., **80** (1991) 472-478

31) Niwa, T., Takeuchi, T., Hino, N., Kunou, N. and Kawashima, Y.: Preparations of biodegradable nanospheres of water-soluble and insoluble drugs with D, L-lactide/glycolide copolymer by a novel spontaneous emulsification solvent diffusion method, and the drug release behavior, J. Controlled Release, **25** (1993) 89-98

32) Gobe, M., Konno, K., Kandori, K. and Itahara, A.: Preparation and characterization of monodisperse magnetite sols in W/O microemulsion, J. Colloid Interface Sci., **93** (1983) 293-295

33) Lopez-Quintela, M. A. and Rivas, J.: Chemical reactions in microemulsions : a powerful method to obtain ultrafine particles, J. Colloid Interface Sci., **158** (1993) 446-451

34) Yang, M., Davies, G. A. and Garside, J.: Precipitation of solids in a liquid membrane emulsion – the control of particle size, Powder Tech, **65** (1991), 235-242

35) Stewart, A. C., Chen, Q. H., Davies, G. A., Yang, M. and Garside: Morphology of precipitates formed in liquid membrane systems, J., Proceedings of the 12th Symposium on Industrial Crystallization, Z. H. Rojkowski ed., Warsaw, Poland (1993) 3-033/3-038

36) Hirai, T., Sato, H. and Komasawa, I.: Mechanism of formation of titanium dioxide ultrafine particles in reverse micelles by hydrolysis of titanium tetrabutoxide, Ind. Eng. Chem. Res., **32** (1993) 3014-3019

37) Osseo-Asare, K. and Arriagada, F. J.: Synthesis of nanosized particles in reverse emulsion, Ceram. Trans. **12** (1990) 3-16

Author's short biography

Claude Laguérie

Professor Claude LAGUERIE was born in 1947. He was graduated of the "Ecole Nationale Supérieure d'Ingénieurs de Génie Chimique de Toulouse" (ENSIGC) in 1969. He prepared a Ph.D. thesis on the oxidation of butanes to maleic anhydride in a catalytic fluidized bed reactor and got the Dr-Ing. degree in 1972. Then he prepared another Doctorate thesis on the growth rate of citric acid crystals in a fluidized bed reactor, to get the Dr-Sci. degree in 1976. Since 1976, he has developped and supervised many works in the fields of fluidization, chemical reactor engineering, crystallization, drying and solid processing. He has signed more than 100 papers published in international journals and he is now head of ENSIGC.

Béatrice Biscans

Dr Béatrice BISCANS was born in 1958. She is graduated from the Ecole Nationale Supérieure de Génie Chimique of Toulouse (1982). She obtained the Doctor degree of the Institut National Polytechnique de Toulouse in 1985 and she is entitled to be in charge of researchers.

Presently she is a researcher of CNRS (National Scientific Center of Research) in the Laboratory of Chemical Engineering of Toulouse (France) and she is in charge of several researches on crystallization.

Nadine Gabas

Dr Nadine GABAS was born in 1960. She is graduated from the Ecole Nationale Supérieure de Génie Chimique of Toulouse (1984). She prepared a doctorate thesis on the crystallization of D-xylose from aqueous solution of both D-xylose and D-manose and she obtained the Doctor degree of the Institut National Polytechnique de Toulouse in 1983.

Since 1989 she has developed several works in the domain of crystallization : thermodynamics of saturated solutions, effect of additives on crystal morphology, modelling of batch and continuous crystallizers, interpretation of the response of laser diffraction particle sizer to anisometric particles.

Review

Fundamentals of Electrostatic Precipitation at High Temperatures and High Pressures†

C. Riehle
*Bayer A.G. R&D Department ZF-TVG3**

Abstract

If exhaust gases are to be cleaned from particulate matter at high flow rates and, simultaneously, at low pressure drops, an electrostatic precipitator (ESP) is a suitable device. ESPs are widely used for removal of fly-ash in coal fired power plants commonly operating at moderate temperatures up to about 200°C and ambient pressure. Today, particle collection at high tempeartures and/or high pressures is of current interest because of new concepts for electrical power generation systems. However, the capabilities of electrical precipitators under these extreme conditions are only poorly investigated. Therefore, the paper works out the fundamentals of high-temperature and/or high-pressure electrostatic precipitation. It provides a basis for discussion and gives the interested reader several tools to permit estimating the potential for electrostatic precipitators under extreme conditions.

1. Introduction

Particle collection at high temperatures and/or high pressures is of current interest mostly because of new concepts for electrical power generation systems. These are, for example, coal combustion processes (pressurized fluidized beds) or coal gasification processes combined with a more or less conventional steam cycle. In order to achieve high energy efficiencies, the hot exhaust gas is fed directly into turbines which, to guarantee a long service life, can only operate with extremely low particle loadings. Because of this, high performance in dust collection is required which, under moderate conditions, is usually achieved by means of baghouses or electrostatic precipitators. As various investigations show, at high temperatures, rigid ceramic filters appear to be in widespread use, whereas the capabilities of electrical precipitators under these extreme conditions are only poorly investigated.

If exhaust gases are to be cleaned from particulate matter at high volume rates and simultanously at low pressure drops, an electrostatic precipitator (ESP) is a suitable device. ESPs are widely used for removal of fly-ash in coal-fired power plants commonly operating at moderate temperatures up to about 200 °C and ambient pressure. Electrical particle separation still works effectively at very small particle sizes.

Concerning their capability to operate at temperatures of about 1000°C, only a few experimental results have been published. Therefore, the goal of the following sections will be to outline the fundamentals of ESP design and operating conditions, especially emphasizing the effects of high temperature and/or high pressure.

2. Fundamentals

2.1 Effect of high temperature and/or high pressure

Changing gas temperature and/or changing gas pressure usually leads to a change in gas density. This can easily be seen when regarding the state equation of ideal gases (Eq. 1).

$$\frac{p}{\varrho} = R \cdot T \qquad (1)$$

For easy handling of different states, it is convenient to introduce the so-called relative gas density δ defined by equation 2. It relates the gas density of an interesting state 2 to the gas density of a known state 1. The relative gas density is obviously a function of the pressure ratio and the reciprocal temperature ratio.

$$\delta = \frac{\varrho_2}{\varrho_1} = \frac{p_2}{p_1} \cdot \frac{T_1}{T_2} \qquad (2)$$

Temperature and pressure are usually related to normal conditions, i.e.: $T_1 = T_0 = 273$ K and $p_1 = p_0 = 1$ bar. **Figure 1** illustrates the range of the

---

* D-51368 Leverkusen, Germany

† Received January 10th, 1994
Manuscript of a lecture on the "Post Experience Course: Gas cleaning at High Temperatures", University of Surrey, England, Sept. 22-24, 1993.

relative gas density for temperatures from 300 K to 1500 K and pressures from 1 bar to 30 bar represented by corresponding isolines.

A decreasing relative gas density corresponds with an increasing average distance between the gas molecules (which can be deduced from kinetic gas theory) or, in other words: when comparing two different gas states, the mean free path of the gas molecules behaves like the reciprocal of the relative gas density (Eq. 3). At normal conditions, $\lambda(p_0, T_0)$ is about 0.065 μm. Therefore, under normal conditions for particles smaller than 1 μm, the mean free path of the gas molecules has to be taken into account.

$$\lambda(p,T) = \frac{\lambda(p_0, T_0)}{\delta} \qquad (3)$$

Closely connected with the mean free path of the gas molecules is the mobility of the gas ions. The mobility of charge carriers is defined as the ratio of mean drift velocity v of the charge carriers to the electrical field strength E generating the drift, and a typical value for gas ions at normal conditions is given in equation 4. The mean drift velocity of the charge carriers is determined by the collision frequency with other (neutral) gas molecules; obviously the collision frequency decreases with increasing intermolecular distances, thus the mobility increases in the same way as the mean free path of gas molecules does (Eq. 5). The mobility of gas ions influences the current-voltage relationship, as will be discussed in the following sections.

$$b(T_0, p_0) = 2 \cdot 10^{-4}\ \frac{m^2}{Vs} \qquad (4)$$

$$b(p,T) = \frac{b(p_0, T_0)}{\delta} \qquad (5)$$

Finally, we have to consider how the viscosity of the gas flow is affected by high temperatures and/or high pressures. It can easily be demonstrated that viscosity is not influenced by pressure but only by temperature, since the p,T-dependence of gas density and mean free path compensate each other (Eq. 6). Thus the well-known $\sqrt{kT}$-dependence of the mean thermal velocity of a gas molecule with mass m remains (Eq. 7). Therefore, viscosity is not transferring in terms of relative gas density, but in terms of $\sqrt{T_2/T_1}$ (Eq. 8).

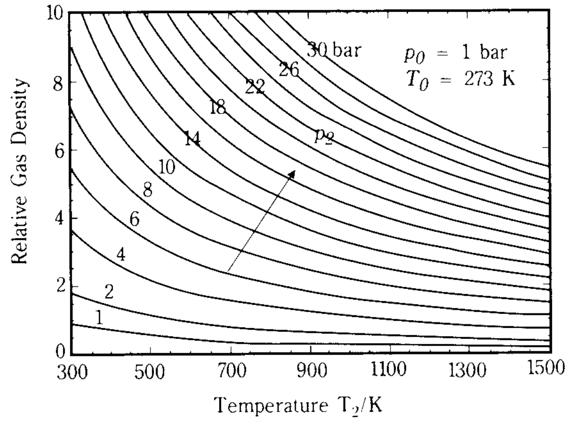

Fig. 1 Relative gas density as a function of temperature; isolines represent constant pressures, respectively.

$$\eta \sim \varrho \cdot \lambda \cdot <v> \qquad (6)$$

$$<v> \sim \sqrt{\frac{kT}{m}} \qquad (7)$$

$$\eta(T) = \sqrt{\frac{T}{T_0}} \cdot \eta(T_0) \qquad (8)$$

Viscosity of flow is decisive for the migration velocity of the particles which results as a balance between electrical force and drag force. The viscosity therefore determines separation efficiency, while relative gas density and mobility mainly govern the operating conditions.

Finally, some particle properties important for the ESP process are also a function of temperature: electrical resistivity (will be discussed in Section 2.7.1), particle-particle and particle-collector adhesive forces (are discussed elsewhere[20]), and the electrical permittivity ε_r of particulate material. The electrical permittivity ε_r is related to the electrical susceptibility $\mathcal{X}_e$ according to equation 9, which, in general, shows a temperature dependence as indicated in equation 10. The effect of equation 10 on the particle charge is neglected in all following calculations.

$$\varepsilon_r = 1 + \mathcal{X}_e \qquad (9)$$

$$\mathcal{X}_e = C_1 + \frac{C_2}{T} \qquad (10)$$

2.2 Minimum field strength for corona initiation

To generate charge carriers in a gas phase, a critical field strength has to be overcome. This can be done with the aid of a wire/plate or needle/plate geometry because the electrical field lines are focused onto the top of the needle or wire surface. When r_{SE} describes the radius of curvature or wire, respectively, then the corona initiation field strength E_0 at the wire surface can be calculated according to Peek's empirical relationship[1]. When using the relative gas density already introduced, equation 11 emerges:

$$E_0 = A\delta + B\sqrt{\delta / r_{SE}} \tag{11}$$

where the empirical constants for a negative corona (i.e. the wire is on negative potential) in air are:

$$A = 3{,}2 \cdot 10^6\ V/cm \qquad B = 9 \cdot 10^4 V/m^{1/2}$$

Figure 2 shows the corona initiation field strength E_0 as a function of wire radius and isolines for different relative gas densities. In general, an increase of wire radius leads to a decrease in electrical field strength; this trend weakens for radii >1 mm. Relative gas densities >1 need higher electrical field values to initiate corona in the same geometry. This seems reasonable because in a denser gas, the mean free path of molecules reduces and with it the time available for acceleration; compensated by higher electrical field values. Obviously, for relative gas densities <1, the opposite behaviour has to appear.

2.3 Tube-type ESP

Looking at high temperatures is often in line with high pressures (especially in electrical gas cleaning as demonstrated later); this is why wire-tube geometries might be favourable compared with wire-plate designs. In any case, i.e. without the intention of preferring either design, it will certainly suffice to discuss the effect of high pressure and high temperature for the tube-type ESP, which is in some ways easier to handle. Therefore the discussion of theoretical aspects will be deliberately restricted to the tube-type ESP, and its typical geometry is shown in **Figure 3**. The important geometric parameters are the wire radius r_{SE}, the radius of the collecting tube r_{NE}, and its length L_{NE}.

2.3.1 Corona onset voltage

According to White[2], the corona onset voltage can be estimated according to equation 12 and its dependence on relative gas density is plotted in **Figure 4**. For fixed geometries, an increasing relative gas densitiy generally needs higher voltage levels to initiate corona.

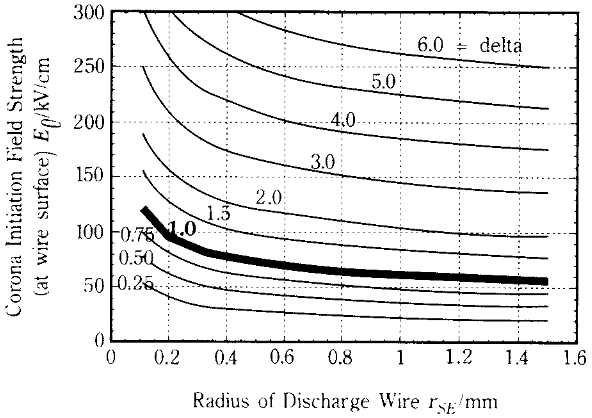

Fig. 2 Corona initiation field strength at wire surface as a function of wire radius; isolines represent const. relative gas densities.

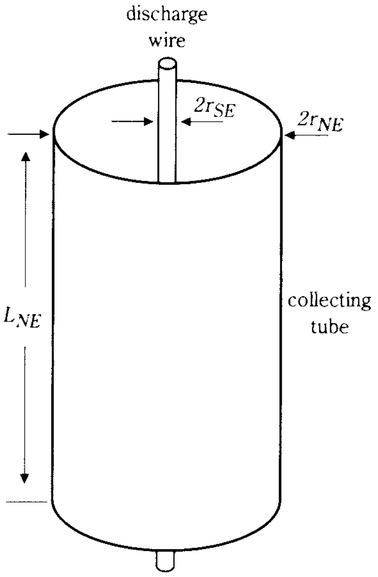

Fig. 3 Geometry of tube-type ESP.

$$U_0 = E_0(\delta) \cdot r_{SE} \cdot ln\, \frac{r_{NE}}{r_{SE}} \tag{12}$$

The thick line in **Figure 4** refers to a wire radius of 1.0 mm and a tube radius of 150 mm. As shown, a variation of the tube radius only has small effects on the voltage levels compared with changes of the discharge wire radius. Interesting to note is that the smaller the discharge wire, the weaker the dependence of onset voltage on gas density becomes.

2.3.2 Current-voltage relationship

Instead of "current", it is helpful to take current densities j_{NE}, i.e. the total current i is related to the total collecting area A_{NE} (Eq. 13). Sometimes, one can find a definition of an unconventional current density j_{SE} where the total current is related to the total length of discharge wire, which for a tube-type ESP, is approximately described by L_{NE} (Eq. 14). Considering this, the current density at the collecting surface can be estimated with equation 15[2].

$$j_{NE} = \frac{i}{A_{NE}} \qquad (13)$$

$$j_{SE} = \frac{i}{L_{SE}} \approx \frac{i}{L_{NE}} \qquad (14)$$

$$j_{NE}(\delta) = \frac{j_{SE}(\delta)}{2\pi \cdot r_{NE}} = \frac{4\,\varepsilon_0 \cdot b(\delta) \cdot U \cdot (U - U_0(\delta))}{(r_{NE})^3 \cdot \ln \frac{r_{NE}}{r_{SE}}} \qquad (15)$$

For a discussion of the relative gas density dependence, we have to keep in mind that the corona onset voltage U_0 and the mobility of gas ions b are also functions of δ (Eq. 11/12 and Eq. 4).

Figure 5 shows the calculated relationships for different relative gas densities for a tube-type design of r_{SE} = 1 mm and r_{NE} = 150 mm. The higher the relative gas density, the flatter the curve becomes, or in other words, at higher relative gas densities, a constant applied voltage can force less gas ions to pass the gas phase.

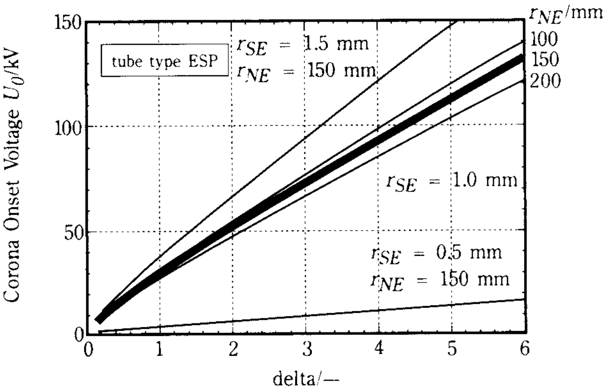

Fig. 4. Corona onset voltage as a function of relative gas density for different tube and wire radii.

2.3.3 Sparkover voltage

In reality, the current-voltage relationships will end suddenly at a critical current/voltage level (which is obviously not considered in **Figure 5**). Unfortunately, and as far as the author knows, no analytical formula is available for this electrical breakdown which allows an estimation of the so-called sparkover voltage U_{crit}.

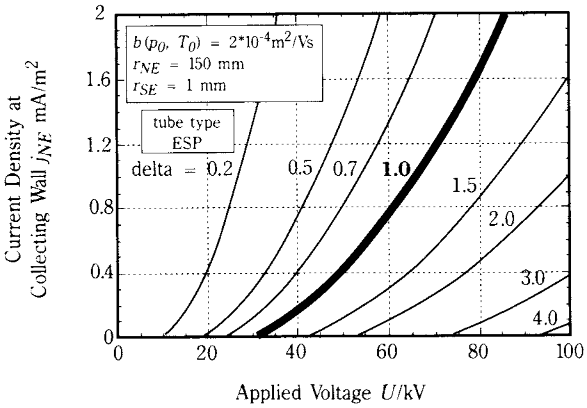

Fig. 5 Electrical current density at collecting wall as a function of applied voltage for different relative gas densities.

As experiments show, this sparkover voltage plays an important role for the operation of electrical precipitators, because stable operation is only possible if an essential difference between corona onset and sparkover (U_{crit}-U_0) exists. As the experimental results in **Figur 6** can show[3], the region of stable operation U_{crit}-U_0 in a tube-type ESP decreases continuously with increasing temperatures if the pressure is kept constant at 1 bar. However, if the pressure is also increased, then the region U_{crit}-U_0 widens up and extends to higher temperatrues. For example, at 1 bar and room temperature, U_{crit}-U_0 is about 25 kV in **Figure 6**; approximately the same voltage difference is observed at a pressure level of 21 bar at about 800°C. Stable operation of ESPs at high temperatures must therefore be accompanied by an appropriately high pressure level, i.e. high relative gas densities.

Furthermore, the high gas densities enable higher voltages to be applied, i.e. higher electrical fields can be sustained between the electrodes (**Fig. 6**) corresponding to considerable improvements in particle collection, as will be seen later on. Since no reasonable forecast of the sparkover voltage can be made, no reliable forecasts for achievable electrical field strengths are possible and experiments are necessary. For example, **Figure 7** shows j_{SE}/U-*curves* experimentally determined by Bush et al.[4] in a laboratory-scale tube-type ESP, allowing temperatures in the range 533-1366 K and pressures of between 3.4 and 35.5 bar (R_{NE} = 3.63 cm and R_{SE} = 0.8-1.6 mm). In the same way as other authors, they find no investigated general limitations for corona discharge at high pressures and high temperatures, and in most cases, negative corona is superior to positive corona. As is seen in **Figure 7**, relative gas densities of about $\delta \geq 6$ enable voltage levels of approx. 100 kV; bearing in mind the tube radius of approx. 3 cm, this corresponds to electric field strengths of the order of 30 kV/cm! Regarding standard operation conditions of about 3 kV/cm, this represents, obviously, an outstanding potential for successful particle collection at high temperatures and high pressures.

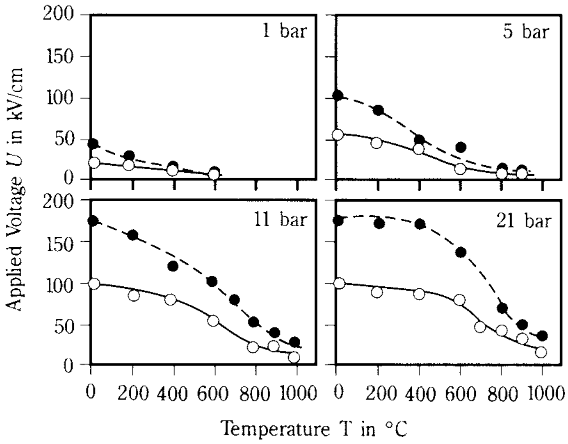

Fig. 6 Corona onset voltage (bright dots) together with sparkover voltage (dark dots) as a function of temperature for four different pressures. The measurements were done by Weber[3] in a tube-type ESP with R_{NE}/R_{SE} = 62.5.

2.4 Particle charging process

Usually, the charging process is divided into a field charging region for particles about >1 μm and a diffusion charging region for particles about <0.1 μm. Whereas field charging requires the presence of an electrical field and free movable charge carriers, the diffusion process needs the statistical movement caused by temeprature in addition to the charge carriers, but no electrical field at all. Obviously, in an ESP, both mechanisms are active simultaneously, i.e. particles <0.1 μm are also guided by an electrical field. It therefore seems reasonable to look for charging theories which allow continuous description of the charging process from small to larger particle sizes. The analytical equation of Cochet[5], which allows an easy discussion of basic principles[2,6,7], can be considered a reasonable alternative to published models based on numerical solutions.

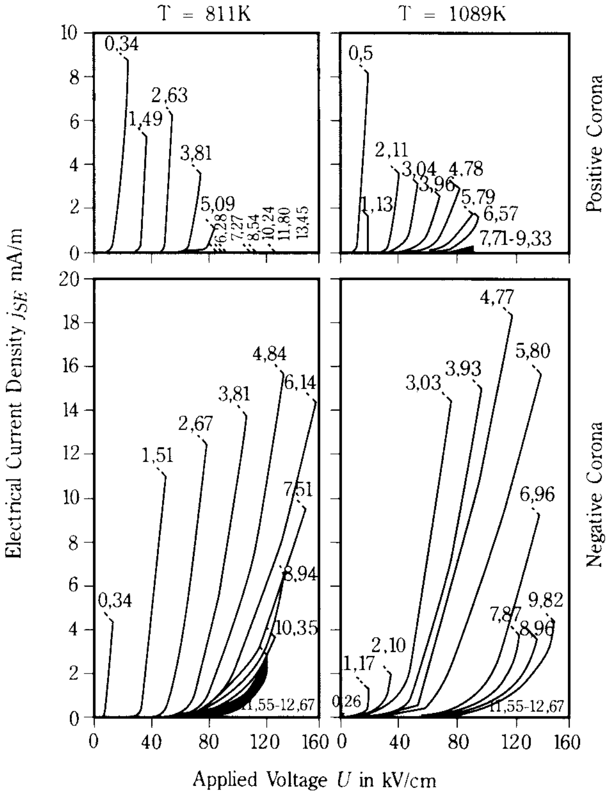

Fig. 7 Current voltage characteristics $j_{SE}(U)$ for dry air measured by Bush et al.[4].Diagrams on the left for T = 811 K, diagrams on the right for T = 1089 K. Top diagram represents positive corona, bottom diagrams hold for negative corona. The top end of the curves corresponds to electrical breakdown. The value of the relative gas density is written along each curve. The tube radius was R_{NE} = 3.63 cm and that of the discharge wire R_{SE} = 1.17 mm.

2.4.1 Saturation charge

The particle saturation charge according to Cochet is given by equation 16. For calculations, the electrical field strength E and the electrical permittivity of the particle material ε_r have to be specified.

$$Q_p^\infty = \left\{(1+2\lambda/d_p)^2 + \left(\frac{2}{1+2\lambda/d_p}\right)\cdot\left(\frac{\varepsilon_r-1}{\varepsilon_r+2}\right)\right\}\cdot \pi\varepsilon_0\, d_p^2 E \tag{16}$$

The results for E = 3 kV/cm and ε_r = 10 are shown in **Figure 8** as a function of the particle size for different relative gas densities. With decreasing particle size, the achievable particle charge generally also decreases because of decreasing surface area. This is why a straight line emerges for large particles in the log-log scale. Obviously at low relative gas densities, small-sized particles can bear much greater charges than at atmospheric conditions.

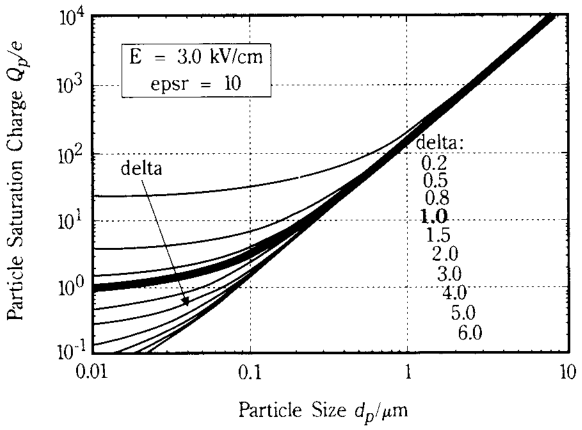

Fig. 8 Particle saturation charge according to Cochet[5] plotted over particle diameter. An electrical field strength of 3.0 kV/cm and a relative electrical permittivity of 10 is assumed for the calculations. Different lines correspond to different relative gas densities.

According to **Figure 1,** gas densities <1 correspond e.g. with atmospheric pressure and high temperature. But the charge carriers are also to be generated in a corona discharge which provides for stable operation at high pressure, as discussed before. Obviously, both effects do not fit together, thus we could suppose at this stage that ESPs will work less effectively in the fine particle region at high temperature and high pressure levels; on the other hand, the decrease in separation efficiency might be compensated by higher electrical field strengths.

2.4.2 Time dependence

The time dependence of the charging process is described by equation 17, using the time constant τ_Q for the charging process (Eq. 18)

$$Q_p\,(t) = Q_p^{\infty} \cdot \frac{t}{t+\tau_Q} \tag{17}$$

$$\tau_Q = \frac{4\,\varepsilon_0}{c_Q\, b} \tag{18}$$

To find the T/p-dependence of τ_Q, we first have to look for the T/p-dependence of the charge carrier concentration c_Q. Referring to Ohm's law, c_Q can easily be expressed in terms of current density, mobility and electrical field (Eq. 19). As already shown in equation 15, *j/b* will only be a weak function of the relative gas density; therefore the T/p-dependence of τ_Q will be approximately described by that of the mobility b, i.e. τ_Q is proportional to the relative gas density (Eq. 20). Using typical values, the constant in equation 20 is about 2 ms.

$$j = c_Q \cdot b \cdot E \tag{19}$$

$$\tau_Q\,(\delta) \approx \frac{4\varepsilon_0}{c_Q\, b\,(T_0,P_0)} \cdot \delta = const. \cdot \delta \tag{20}$$

2.5 Migration velocity

The forces acting on a particle in an ESP are the momentum force F_T (Eq. 21), the electrical force F_{el} (Eq. 22) and the drag force F_W (Eq. 23). For the drag force, the validity of Stokes' law is assumed.

$$\vec{F}_T = -m\vec{a} \tag{21}$$

$$\vec{F}_{el} = Q_p\,\vec{E} \tag{22}$$

$$\vec{F}_w = 3\pi\eta d_p \cdot /\vec{v} - \vec{w}/ \cdot \frac{1}{Cu} \tag{23}$$

Cu represents the drag force correction for particles in the size range of the mean free path of the gas molecules (λ) according to Cunningham (Eq. 24)[8,9]. The Cunningham correction is a function of the relative gas density, because of its dependence on λ.

$$Cu = 1 + 1{,}246 \cdot \frac{2\lambda}{d_p} + 0{,}42 \cdot \frac{2\lambda}{d_p} \cdot \exp\left(-0{,}87 \cdot \frac{d_p}{2\lambda}\right) \tag{24}$$

By using equation 3 for the dependence of λ on the relative gas density δ the dependence of *Cu* on δ as a function of the particle size d_p can easily be calculated; the results are plotted in **Figure 9.** For constant particle sizes, an increase in relative gas density leads to lower *Cu* values, i.e. the influence of δ on the Cunningham correction acts in the same direction as its influence on particle saturation charge.

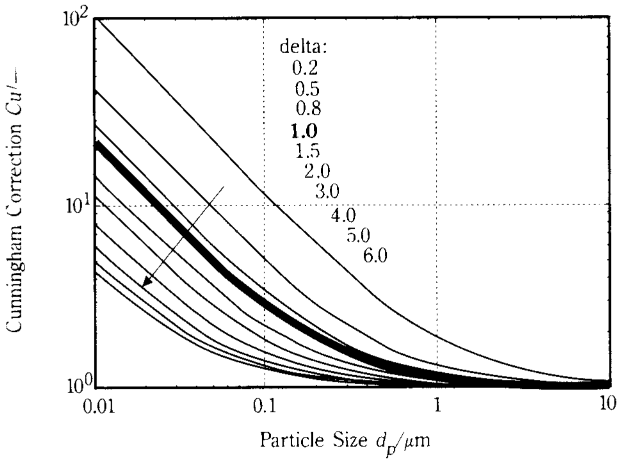

Fig. 9 Cunningham correction according to equation 24 as a function of particle size. Different lines correspond to different relative gas densities.

2.5.1 Steady state

Integrating the equation of particle motion (resulting from a balance of the forces mentioned above) and looking for the steady state solution leads to equation 25, the so-called theoretical migration velocity of an individual charged particle in an electrical field. For all calculations, an electrical field of E = 3 kV/cm and an electrical permittivity of ε_r = 10 have been applied.

$$w_{th}(\delta) = \frac{Q_p^{\infty}(\delta) \cdot E}{3\pi\eta(\delta) \cdot d_p} \quad (\cdot\ Cu(\delta)) \qquad (25)$$

Figure 10 illustrates what happens to the theoretical migration velocity as a function of the particle size under atmospheric pressure and raised temperatures corresponding to relative gas densities <1. The absolute value of the characteristic minimum in the migration velocity function is raised weakly and its location is shifted with decreasing relative gas velocity to larger particle sizes. For particles >1 μm, the influence of the dynamic viscosity η dominates the δ-dependence (compare **Figs. 8** and **9**), i.e. at higher temperatures or relative gas densities <1, respectively, the gas phase becomes more viscid and hence the particles migrate more slowly. For particles <1 μm, this behaviour turns around: here, the δ-dependences of particle charge and Cunningham correction dominate over the viscosity, i.e. at higher temperatures or relative gas densities <1, respectively, particles can penetrate the gas phase more easily, resulting in higher migration velocities.

Here again, this situation is different from the one in an ESP because for a corona discharge, the pressure level also has to be raised (see 2.3.3). Therefore, we consider the migration velocities of particles of fixed size as a function of the temperature, keeping the relative gas density constant. This was done in **Figure 11** for 10 μm particles, in **Figure 12** for 1.0 μm particles, and in **Figure 13** for 0.1 μm particles, respectively.

As seen in **Figure 11**, the migration velocity of a 10 μm particle decreases by about a factor of two when going from room temperature up to more than 1000°C with the relative gas density kept constant. In general, almost no δ-dependence can be observed for particles of around 10 μm and larger. This changes when looking at 1.0 μm particles (**Fig. 12**). Here, it can be seen that for constant temperatures, an increase in δ will weakly decrease the migration velocity, while doubling the relative gas density shows a higher effect than reducing it by half. This behaviour increases dramatically for 0.1 μm particles or smaller (**Fig. 13**).

Up to now, we did not consider the possibility or even the necessity of applying much higher electrical field strengths at high relative gas densities. An increase in the electrical field E ultimately leads to an enormous increase of the migration velocity because w_{th} depends quadratically on E (electric charge Eq. 16 and electrical force Eq. 22), as illustrated in **Figure 14** for a 1.0 μm particle at a relative gas density of δ = 4.0 for electrical field values of E = 3/6/9/12 kV/cm.

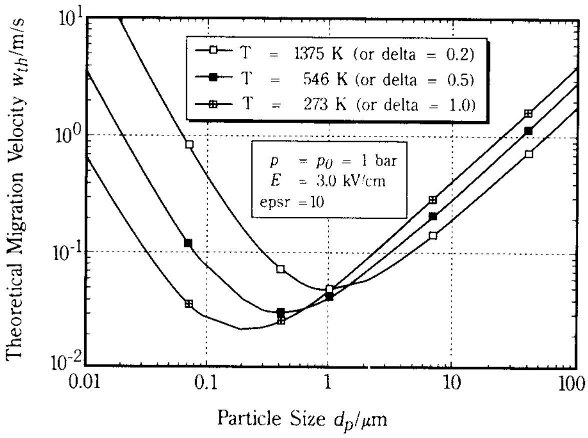

Fig. 10. Theoretical migration velocity calculated by equation 25 as a function of particle size for atmospheric pressure and three temperatures (or three relative gas densities, respectively). An electrical field strength of 3.0 kV/cm and a relative electrical permittivity of 10 is assumed for the calculations.

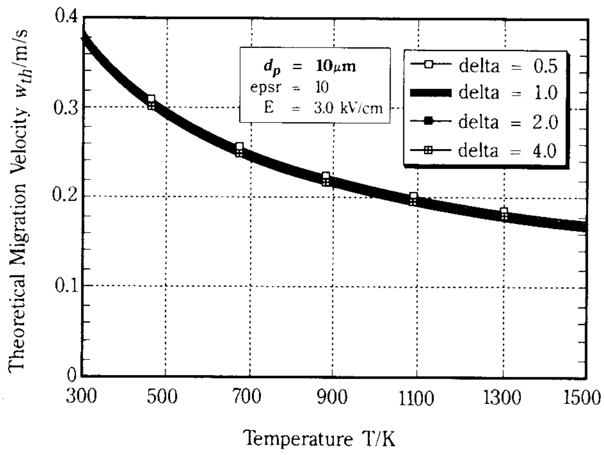

Fig. 11 Theoretical migration velocity of a 10 μm particle (E = 3.0 kV/cm; ε_r = 10) as a function of temperature; isolines correspond to const. relative gas densities.

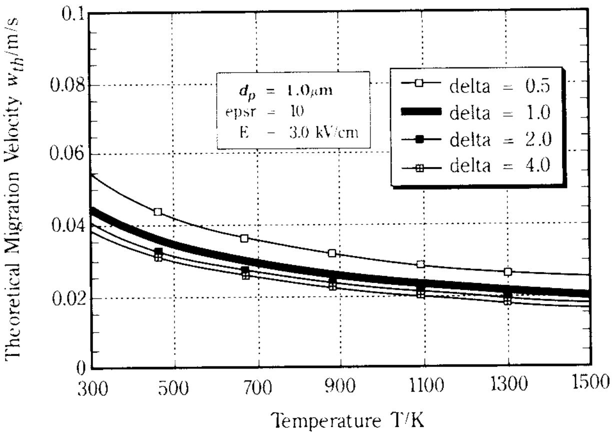

Fig. 12 Theoretical migration velocity of a 1.0 μm particle (E = 3.0 kV/cm; $\mathcal{E}_r$ = 10) as a function of temperature; isolines correspond to const. relative gas densities.

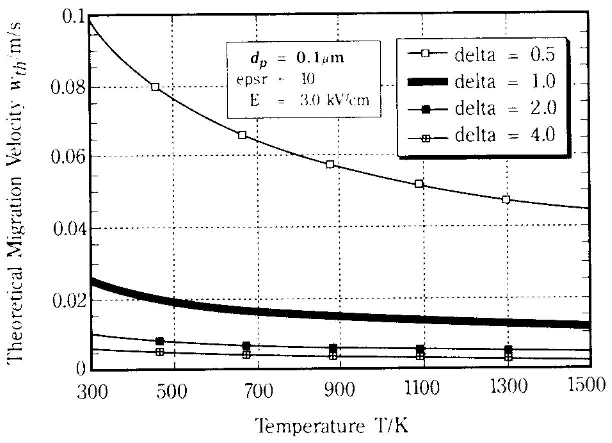

Fig. 13 Theoretical migration velocity of a 0.1 μm particle (E = 3.0 kV/cm; $\mathcal{E}_r$ = 10) as a function of temperature; isolines correspond to const. relative gas densities.

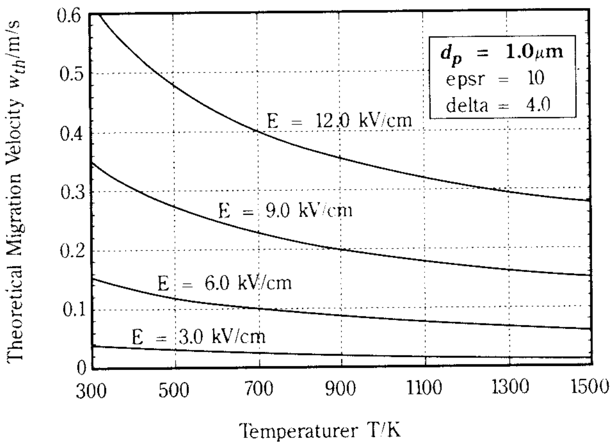

Fig. 14 Theoretical migration velocity of a 1.0 μm particle ($\mathcal{E}_r$ = 10) for a relative gas density of 4.0 as a function of temperature; different lines correspond to different electrical field strengths.

2.5.2 Time dependence

The time dependence of the particle velocity is described by equation 26, whereby the instationary particle movement is characterized by the relaxation time τ_p (Eq. 27).

$$w(t) = w_{th}\left\{1-\exp\left(-\frac{t}{\tau_p}\right)\right\} \qquad (26)$$

$$\tau_p(T) = \frac{m_p\,(\cdot\,Cu(\delta))}{3\pi\eta(T)\cdot d_p} = \frac{\varrho_p\cdot d_p^2}{18\,\eta(T)}\,(\cdot\,Cu(\delta)) \qquad (27)$$

In determining the T/p-dependence of τ_p, we neglect for simplicity the influence of the Cunningham correction, thus τ_p is solely a function of temperature. Remembering the viscosity dependence on temperature (Eq. 8) the relaxation time decreases with increasing temperature, i.e. particles reach their steady states faster. For solid spheres of $d_p > 1$ μm with a density of ϱ_p = 1000 kg/m³, the relaxation time can be calculated with equation 28.

$$\tau_p = 3{,}09\cdot 10^{-6}\,\frac{d_p^2}{\mu m^2}\ s \qquad (28)$$

2.6 Grade efficiency

A well-established model in ESP theory and practice is the one of Deutsch[10)]. In the original form, it allows prediction of the grade efficiency, i.e. efficiency as a function of particle size, on the basis of the main design and operation parameters. For tube-type ESPs, the Deutsch equation is given by:

$$T(d_p) = 1-\exp\left\{-w_{th}\,\frac{A_{NE}}{\dot{V}}\right\}$$

$$= 1-\exp\left\{-\frac{2\cdot w_{th}\,(d_p,\delta)\cdot L_{NE}}{v_0\cdot r_{NE}}\right\} \qquad (29)$$

In determining the T/p-dependence of $T(d_p)$, we first have to specify the tube design. We choose for further calculations r_{NE} = 150 mm and L_{NE} = 5.0 m with the operation conditions E = 3.0 kV/cm and v_0 = 1.0 m/s.

Figure 15 illustrates what happens to grade efficiency under atmospheric pressure and raised temperatures corresponding to relative gas densities <1. The efficiencies naturally show the same tendencies as those of the migration velocities in **Figure 10**; the absolute value of the typical minimum is strongly increased and the minimum's location is shifted as before to larger particle sizes for decreasing relative gas densities. As can be seen, reducing the relative gas densities leads to a dramatic improvement in efficiency when one neglects the high pressure levels needed for corona generation. **Figures 16** and **17** therefore show efficiency as a function of temperature with the relative gas density as a parameter for particles of fixed size, 0.1 μm and 1.0 μm, respectively.

As can be seen in **Figures 16** and **17**, particles will be collected less efficiently at high temperatures if the relative gas density is kept constant and assuming a constant electrical field strength. For the 0.1 μm particle and constant temperature, a dramatic breakdown in efficiency can be observed when increasing the relative gas density. For the 1.0 μm particle, the efficiency decrease for constant temperature is less, but compared with **Figure 16;** the decrease with rising temperature is more pronounced. A plot for 10 μm particles is not given because for the parameter settings investigated, the efficiency values always equals 1.0.

Finally, we have to take into account again the possibility and/or necessity of a higher electrical field strength at raised relative gas densities. **Figure 18** shows efficiency values of a 1.0 μm particle, calculated and plotted as a function of temperature as before, for a relative gas density of δ = 4.0 with the applied electrical field strength as the parameter. Obviously, particle collection is extremely sensitive to electrical field strength: e.g. at a temperature level of 1300K, doubling the electrical field strength from 3 to 6 kV/cm, which enlarges the migration velocity by a factor of 4 (compare **Fig. 14**), reduces penetration (1 – efficiency) by more than a factor of 25!

Experimental results for total mass efficiencies (integrating over all particle sizes occuring) have been published, e.g. by Feldman/Bush[11] and Rinard et al.[12]. As was to be expected, they found a strong influence of the electrical field on particle collection. Feldman and Bush refer to a wire-pipe ESP of Union Carbide Olefins Co. operating at temperatures of 870-1000 K, pressures of 3-8 bar and gas velocities of 0.2-1.2 m/s. It consists of 19 pipes of 15.2 cm in diamter, 1.8 m in length and discharge wires of 2.1/3.4 mm in diameter. Rinard et al. refer to a test facility located at the Denver Research Institute with one tube 30.5 cm in diameter and 2.1 m in length, operating at temperatures up to 1200 K, pressures up to 10 bar and with a flow rate of 0.078 m^3/s under these conditions.

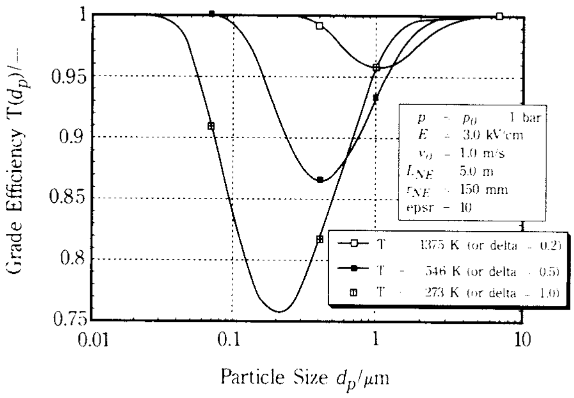

Fig. 15 Grade efficiencies at atmospheric pressure calculated according to Deutsch (Eq. 29) for three different temperatures; the ESP was designed to L_{NE} = 5.0 m, r_{NE} = 150 mm and operated with E = 3.0 kV/cm and v_0 = 1.0 m/s.

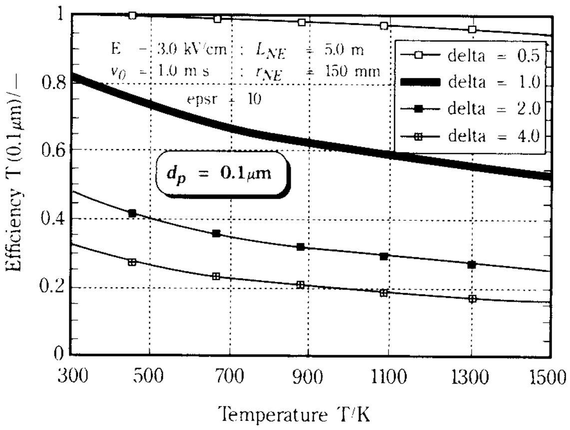

Fig. 16 Efficiencies according to Deutsch (Eq. 29) for a 0.1 μm particle as a function of temperature; different lines correspond to different relative gas densities. ESP design and operation conditions as before.

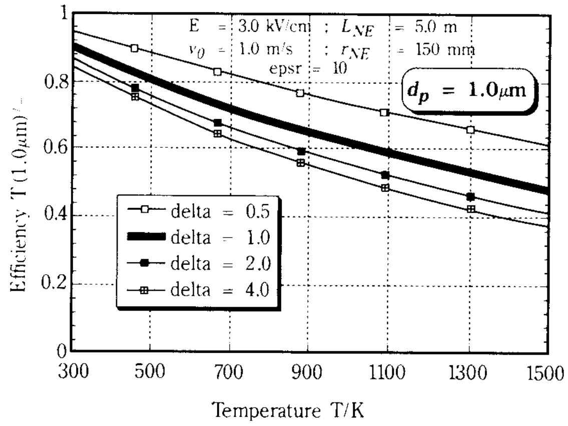

Fig. 17 Efficiencies according to Deutsch (Eq. 29) for a 1.0 μm particle as a function of temperature; different lines correspond to different relative gas densities. ESP design and operation conditions as before.

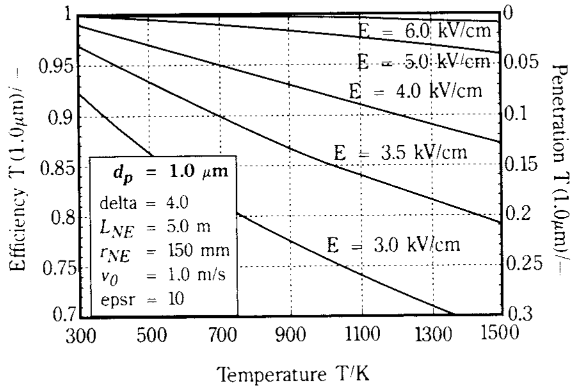

Fig. 18 Efficiency of 1.0 μm particle ($\mathcal{E}_r$ = 10) for a relative gas density of 4.0, as a function of temperature; different lines correspond to different electrical field strengths. ESP design and operation conditions as before.

2.7 Particle resistivity

The processes of particle deposition on the collecting electrode and detachment of the dust layer from the collecting electrode are the most important and critical stages of electrostatic precipitation. These processes are governed decisively by the electrical resistivity of the particles for the following reasons: The charge of the arriving particles is opposite to that at the collecting electrode. As soon as the particles contact the collector, they will more or less quickly discharge depending on their electrical resistivity or conductivity. If the particles discharge rapidly, upon capture they assume the same polarity as the collecting electrode and can therefore be reentrained into the gas stream. This behaviour is well known for particles with resistivities in the range of 10^4 Ωcm. At the other extreme, represented by electrical resistivities typically ≥ 10^{10} Ωcm, particles cannot lose their charges and cause a continuous charge build-up on the collecting electrode. This will reduce the voltage available for precipitation and the excess of charge within the dust layer can lead to such high electrical fields in the porous system that in extreme cases, a corona discharge is initiated, the so-called back-corona. Therefore both high and low electrical resistivities are detrimental to particle collection.

The electrical conductivity of particles consists of two contributing parts: the first one is the conductivity on the particle surface caused by the adsorption of gas molecules such as water or sulfuric acid; the second one is the conductivity caused by the volume of the material itself. Therefore, the temperature dependence of electrical resistivity can be divided into a surface-dominated and a volume-dominated part.

These tendencies are shown in **Figure 19.** At a constant temperature, a higher water content in the flue gas increases the surface conductivity, thereby reducing the electrical resistivity. An increase in temperature causes the desorption of water molecules, thereby increasing the surface resistivity. At the temperature where a maximum value in resistivity occurs, the volume conductivity of the particle material begins to predominate. A further increase in temperature reduces the electrical resistivity for most dusts in question. Even when the temperatures are raised up to levels of 1000°C, this behaviour does not change for fly ash, as experimental results of different researchers illustrate[12-14]. An example is given in **Figure 20.** Deviations are observed, e.g. for carbonaceous ash, as Shale et al. already found out in 1968[15].

Therefore, a first assumption might be that high-resisitivity ash – troublesome at common power plants at typical current densities of 0.1-0.2 mA/m^2 – is easily collected. But it must be remembered that at high temperature and high pressure levels, the current densities can reach orders of 5-10 mA/m^2. The combination of low ash resistivity at the operating temperatures, together with the high current densities, probably will not lead to back-corona since the high gas densities should suppress it. On the other hand , electrical re-entrainment of particles might also be caused by the low resistivity values.

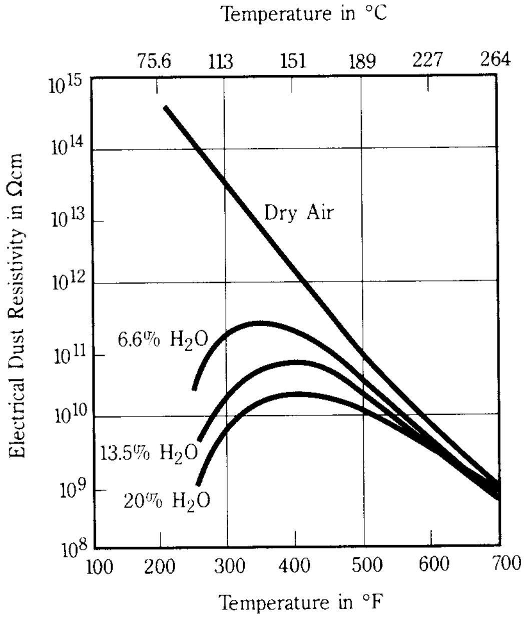

Fig. 19 Electrical resistivity of cement kiln dust as function of temperature (taken from (2)); curves demonstrate the effectiveness of moisture conditioning.

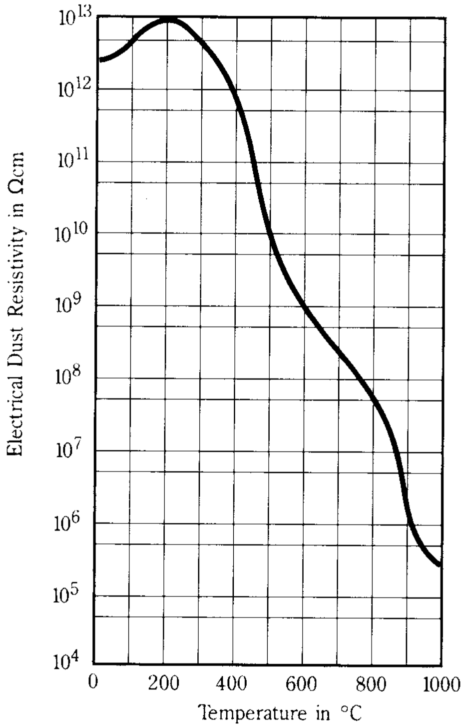

Fig. 20 Electrical resistivity trend of fly ash at high temperature levels measured by Arras/Mayer-Schwinning (13).

3. Problems

Apart from eventually reduced resistivity problems (discussed in section 2.7), all problems known from common ESP operations will certainly occur: re-entrainment caused by rapping, by-pass gas flow – so-called sneakage, and dust layers build-up on the discharge electrodes. Problems which are especially attributed to the high temperatures are for example:

- Mechanical stability of material

The hardness of the materials used at temperatures ≥ 1000°C has to be considered carefully. For long-term applications at elevated temperatures, the creeping behaviour of the material has to be taken into account. Furthermore, the flue gas at high temperature is much more aggressive, therefore corrosion will be a severe problem.

- Rapping

At temperatures above 700°C, the region of forgeability starts for some materials. This can become a problem if rapping is carried out by convential hammer systems. Cleaning by means of pulse jets analogous to those used in bag houses or by ultrasonic horns is also under discussion.

- Electrical insulation

Insulator arrangements commonly used on the roofs of ESP housings have temperatures of about 50°C less than the gas flow and they are stressed thermally, mechanically and electrically. Unfortunately, the electrical resistivity of most insulator materials drastically decreases at temperatures above approx. 200°C. An application of the so-called advanced ceramics as insulating material for extreme requirements might be promising and should be investigated.

- Discharge of hoppers

To bring the collected dust out of the hoppers means overcoming a pressure barrier of some ten bars. In order to guarantee secure dust handling, a carefully designed pressure sluice is absolutely necessary.

- Electrical power consumption

The electric power consumption, as a fraction of the total electric output from a PCFB electric generating plant, was observed to be between 1.5 – 2%[19]. In the case of inadequate efficiencies, the collecting area has to be increased, although this will lead to a probably unacceptable high power consumption. A solution might be to use power-conserving means on the transformer rectifier sets such as intermittent electrical energization.

4. Conclusions

This paper has tried to fundamentally work out the potential of electrostatic precipitation in gas cleaning at high temperatures and high pressures. Ultimately, this was done with special respect to grade efficiency under extreme conditions, resulting in promising trends. Furthermore, laboratory and pilot-plant results of various researchers[3,4,11-19] have demonstrated the feasibility of ESP operation at pressures up to 20 bars. In general, it is observed that negative corona is far more effective than positive corona. Stable coronas are generated and the current-voltage characteristics can be related to the relative gas density. Therefore, a successful ESP operation at high temperatures needs correspondingly high pressure levels. In this way, the gas can withstand the electrical breakdown much better than at standard conditions leading to much higher electrical field strengths. For the same reason, back-corona is not expected to cause severe problems. Therefore, such high electrical field strengths suggest rather small specific collecting areas for efficiencies ≥ 99%.

Tassicker concludes[19] that "the data available would be sufficient for the commercial-scale of an ESP for conditions of 5-15 bar and 400-700°C. The available data are less definite for a firm design at 850-900°C. More pilot-plant work is needed before a commercial-scale plant in this range could be confidently sized".

Symbols

a	acceleration
A_{NE}	collecting area
b	mobility of gas ions
c_Q	number concentration of gas ions
Cu	Cunningham correction
d_p	particle diameter
E	electrical field strength
E_0	corona initiation field strength
F	force
i	electrical current
j	electrical current density
j_{NE}	electrical current density at collecting wall
j_{SE}	electrical current density related to discharge wire length
L_{NE}	length of collecting tube
L_{SE}	length of discharge wire
m	mass of gas molecule
m_p	mass of particle
Q_p	particle charge
Q_p^∞	particle saturation charge
p	pressure
r_{NE}	radius of collecting tube
r_{SE}	radius of discharge wire
R	molmass related constant of gas
T	temperature
t	time
$T_{(d_p)}$	grade efficiency
U	applied voltage
U_0	corona onset voltage
U_{crit}	sparkover voltage
$<v>$	mean thermal velocity of gas molecules
v	fluid velocity
w	particle velocity
w_{th}	theoretical migration velocity of an individual particle
δ	relative gas density
ε_0	electrical permittivity of vacuum
ε_r	electrical permittivity of particle material
$\mathcal{X}_e$	electrical susceptibility of particle material
η	viscosity of fluid
λ	mean free path of gas molecules
ϱ	density of fluid
ϱ_p	density of particle material
τ_Q	time constant of particle charging process
τ_p	time constant of particle acceleration process

References

1) Peek F.W.: Dielectric phenomena in high voltage engineering; 3rd. ed. McGraw Hill, New York 1929
2) White H.J.: Industrial electrostatic precipitation; Addison Wesley, Pergamon Press 1963
3) Weber E.: Electrostatic precipitation under extreme conditions of temperature and pressure; Proc. of 2nd Int. Conf. Electrostatic Precipitation, Kyoto/Japan (1984) 85-95
4) Bush R.J., Feldman P.L., Robinson M.: High pressure, high temperature electrostatic precipitation; J Air Poll. Contr. Assoc. 29 (1979) 365-371
5) Cochet R.: Lois Charge des Fines Particules (Submicroniques) Etudes Théoretiques – Controles Récents Spectre de Particules; Coll. Int. la Physique des Forces Electrostatiques et Leurs Application, Centre National de la Recherche Scientifique 102 (1961) 331-338
6) Riehle C.: Bewegung und Abscheidung von Partikeln im Elektrofilter; Dissertation Universität Karlsruhe (TH) 1992
7) Robinson M.: Electrostatic Precipitation in E. Strauß (Edt.); Air Poll. Control, Part 1, John Wiley & Sons, New York 1971
8) Cunningham E.: Velocity of steady fall of spherical particles through fluid medium; Proc. Roy. Soc. 83A (1910) 357-365
9) Millikan R.: The general law of fall of a small spherical body through gas and its bearing upon the nature of molecular reflection from surfaces; Phys. Rev. 22 (1923) 1-23
10) W. Deutsch: Bewegung und Ladung der Elektrizitätsträger im Zylinderkondensator; Annalen d. Physik, 68 (1922) 335-344
11) Feldman P.L., Bush J.R.: Performance of electrostatic precipitators at high temperatures and high pressures; VDI-Berichte Nr. 363 (1980) 87-92
12) Rinard G., Rugg D.E., Yamamoto T.: High-temperature high-pressure electrostatic precipitator electrical characterization and collection efficiency; IEEE Trans. Ind. Appl. IA-23 (1987)

114-119

13) Arras K., Mayer-Schwinning G.: Fragen der Ausführung eines Elektrofilters für Hochdruck und Hochtemperatur; VDI-Berichte Nr. 363 (1980) 93-101
14) Tassicker O.J., Yung S.C.: Electric properties of PCFB Ash at elevated temperatures and pressures – effct on gas filtration; Symp. Gas Cleaning at High Temperatures and High Pressures, University of Surrey, Sept. 1986
15) Shale C.C., Holden J.H., Fasching G.E.: Electrical resistivity of fly-ash at temperatures to 1088 K; US Bureau of Mines, Report Investigation No. 7041.
16) Arras K., Mayer-Schwinning G., Weber E., Wiggers H.: HPHT-separation of fly ashes by means of electrostatic precptitators; Proc. of 4th Int. Conf. Electrostatic Precipitation, Beijing/China (1990) 237-249
17) Rinard D., Durham M., Armstrong J., Gyepes R.: The DRY HTHP ESP test facility; Proc. HTHP Particulate and Alkali Control in Combustion Process Streams, DOE/METC Contractors' Meeting, Morgantown/WV USA 1981
18) Kumar K.S., Feldman P.L.: Testing of electrostatic precipitator at New York University; Gas Stream Clean Up Papers from DOE/METC-sponsored Contractors' Review Meeting 1987/6082
19) Tassicker O.J.: High temperature-pressure electrostatic precipitator for electric power generation technologies: an overview of the status; IChemE Symp. Series No. 99 (1986) 331-339
20) Berbner St., Löffler F.: Influence of high temperatures on particle adhesion; Powder Technology 78 (1994) 273-280

Author's short biography

Claus Riehle

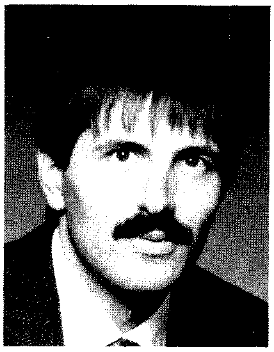

10/80-10/86:
study of physics at the University of Karlsruhe (TH) with emphasis on: low temperature physics, mathematical methods in physics, fluid mechanics. Receiving a diploma in Physics in Oct. '86.

11/86-8/92:
research assistant of Prof. Dr.-Ing. Friedrich Löffler at the Institute for Mechanical Process Engineering and Mechanics ("Institut für Mechanische Verfahrenstechnik und Mechanik") of the University of Karlsruhe; there dealing with air pollution control techniques, aerosol technologies, particle measuring techniques and multiphase flow problems. Receiving a doctoral degree in Feb. '92 with a thesis on electrostatic precipitation.

since 9/92:
with Bayer A.G. in Leverkusen/Germany, Department of Reasearch and Development/Applied Physics, working on particle technologies, gas/solid reactor systems and methods concerning measuring and modeling of multiphase flows.

Review

Particle Characterization – Can it be done? †

Thomas P. Meloy
*University of West Virginia**

Introduction

In the powder field, there exists a truism: *If one could measure particle shape, one could predict powder behavior.* Hausners early work on characterization was followed in the early sixties by intensive optimistic mathematical attacks attempting to find ways to quantify particle shape and then group particles into understandable shape categories. In the seventies the battle to conquer particle shape became a war in which the *holy grail* was a universal definition and quantification of particles shape.

This war and the quest for the *holy grail* were led mainly by theoreticians using powerful mathematical weaponry. Rapid advances were made, some of them spectacular, but the *holy grail* of particle shape was an elusive foe ever moving into more and more difficult terrain where the theoretical weaponry failed. In the mid nineties few meaningful theoretical attempts have been made to reach this elusive *holy grail* of particle shape. Most researchers are both discouraged and out of ideas. But was this long and often brilliant campaign to reach the elusive *holy grail* of particle shape in vain?

In *THE SHAPE OF POWDER-PARTICLE OUTLINES*, by Arthur E. Hawkins, Research Studies Press LTD. & John Wiley & Sons, £39.95, 150 pp, the author describes these research battles to define shape, the attacks by – Fourier, Harr and Walsh Functions; the attempt to use fractals – their successes and failures with the various mathematical weaponry, and the ground traversed during this long intense campaign. More important, the author reviews the sizable territory of knowledge gained in the quest for this *holy grail*, its meaning and uses for today's powder researcher and engineer.

To understand the importance of this book, one must understand the importance of powders to our civilization. In our galaxy, in our solar system and on our planet, particles are ubiquitous. Galaxies, stars and planets are formed from particles. Planetary surfaces are covered with particles. Our food is raised in a powder, soils. Food is usually in a powder form: rice, corn, wheat, peanuts, peas, and even milk is a powder. Most pharmaceutical, pills, are in a powder form. The pigment in the paint industry is another form of particles. Fibers in cloth, asbestos and paper are elongated particles. Large portions of our increasing pollution problems are caused by particles. Even daily diseases such as *hay fever* are caused by particles. Particles are ubiquitous.

That families of particles of the same material with the same history have similar shapes is clear to all. Large flat rounded stones on a pebble beach have the same general shape that all would recognize. Angular crushed bluestone ready to be used as the foundation for a road bed has a clear recognizable family of particle shape. A truckload of dried corn (maize) to be used as chicken feed has its own clear distinct recognizable general shape. The question is: how does one quantify these families of shapes? The problem is: *Like beauty, shape is in the eyes of the beholder.*

It is one thing to characterize particles, but it is another to characterize their shape. One can measure a particle's density, weight and surface characteristics. All one needs to do to complete a particle's characterization, is to measure its shape. After a quarter of a century of research into characterizing particle shape, this seemingly simple task that any child can master has not been mastered. The problem is that the human eye is the most sophisticated shape characterizing instrument in the universe.

While in a typical modern family, the biped and quadrupeds eat, sleep and play together, few mothers have difficulty distinguishing their children from the family turtles, snakes, dogs or cats. Each animal has its own distinct shape. Birds, beds, bats, benches and bees have their own shapes and each is readily recognized by its shape. Many objects in our lives have readily recognized shapes. While one recognizes shape, what is shape?

To define a particle's shape one must find a basis on which to define a particle's shape and then find a quantitative method of measuring those salient

---

* 413 Jefferson St. Morgantown, WV 26505, U.S.A.

† Received September 1st, 1994

shape characteristics. Thus far, no one can define a particle's shape and then measure that shape. Before making a transaction, coin vending machines recognize coins by their shape. What one needs is a particle vending machine. None exists now nor are they likely to exist in the future.

Coins have a round disk shape. There exists a world wide convention as to the shape of coins. Insects have shape. They have three body segments: a head, a thorax supporting six legs and an abdomen. If a bug does not have all these shape characteristics, then that *bug* is not an insect. Genetics determines an insect's shape. Each molecule of water has a characteristic shape, as does an SO_2 molecule. Molecular shapes are fixed by physical laws. Are there genetic conventions or physical laws that define particle shapes?

Different from small molecules like water, for large polymers, shape definitions become vague. These large molecules must still obey physical laws, but these laws governing shape become ambiguous in the larger molecular sizes. Physical laws govern particle shape. We have yet to find useable qualitative shape characteristics for defining a given particle's shape. For particles larger that one micron, no two particles in the knowable universe will have the same shape. Clearly finding a theoretical or experimental method for defining particle shape, has and will not be a simple task.

With the failure of the theoretical methods to define particle shape, what remains are the particle-instrument interaction characterization methods that yield one or two shape characteristics. Typical of these methods is screening wherein each particle repeatedly interacts with the sieve cloth. For sieved particles, physical laws play a less important role than stochastic process when it comes to determining particle shape. These simple methods are often rapid and yield enough information for powder process control. While there are good descriptive powder measurement books, regrettably, until now, there has been no meaningful description of the particle shape research, its trials, tribulations and future. Hawkins' book enables one to understand what were the research problems to be solved in the shape battle, and why they were not solved.

For those working in the particle shape field, so well does Hawkins book on particle-shape-outline describe the historical research work that it is required reading. This book traces the development of the separate methods of giving powders and individual particles a shape classification and then measuring this shape. In his book , Hawkins' blends a deep physical understanding of both the theoretical and experimental problem s in quantifying particle shape with the practical application of this knowledge to the shape characterization of powders or particle systems. This book will become a classic in the field. Written from a mature user's overview of the emerging shape analysis field, it reminds those of us who have spent a third of a century in the trenches, how little we know about the field of particle shape.

Hawkins is in the application of shape analysis to industrial problems. He understands both the theoretical research problems and the application of shape quantification. Wisely, he included a chapter on sampling, an often neglected area. Proper sampling techniques are essential to any type of particle characterization. Mixed powder left to stand will segregate as will powders transported for further processing. A dull subject often overlooked, proper sampling techniques, is important to proper powder experimental procedure.Sampling cannot be overlooked.

To many industries in many fields, powders are an important if not a major constituent in their products. This powder characterization field, important as it is, lacks a University Department home. In the powder field, publications are scattered across dozens of journals and international conference proceedings. In all but the most specialized of technical libraries, the latter are difficult to find. Investigators are usually unaware of what other powder researchers are doing, which shape problems are being investigated, or which problems have been solved. Fortunately, the author furnishes an extensive bibliography of roughly six hundred important papers. Whether one is in research, management, production or quality control, this extended bibiography alone is worth the price of the book.

Is this book worth buying? Definitely! While not a handbook, it is an important addition to any research library. It is a classical book and should be read, understood and on the shelf of everyone involved in the powder field.

Author's short biography

Thomas P. Meloy

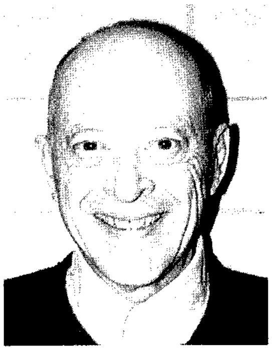

Dr. Thomas P. Meloy, Benedum Professor, graduated from Harvard and MIT. His field of specialization is in the modeling of powder systems, shape characterization, powder characterization, circuit analysis, and optimum separation circuits. Currently he is on several faculties at West Virginia University.

Analysis of Asbestos in Bulk Materials by X-Ray Diffraction: Influence of Grinding Methods on the Result †

Enea Occella*
Dept. ''Georisorse e Territorio'', Polytechnic School of Turin (Italy)

Abstract

The grinding method for sample preparation affects the results of X-ray diffraction analysis of minerals, mainly the soft and inelastic components of raw materials and synthetic matrices. This fact is determined by a ''disturbance'' of crystal order in the surface layer of particles and is more pronounced when a fine comminution is performed and when a high shearing stress is applied in grinding. This effect is remarkable on asbestos minerals.

Subsequent to some information on the development of the science of ''mechanochemistry'', this paper reports the results of several tests on single, binary and polygenic materials containing chrysotile and crocidolite under different grinding conditions (type of mill and grinding time). The aim of the research is to give suggestions about a sample preparation methodology for XRD quantitative determination of asbestos in bulk materials, suitable for obtaining more accurate results.

1. Introduction

According to the policy of the European Community in environment protection, it is currently necessary to know the rate of asbestos minerals in raw materials and synthetic matrices used for different applications and in the building industry. These materials are always polygenic and often very complex, as in the case of serpentinite rocks, cement-asbestos aggregates, insulating plates and waste materials containing chrysotile, amosite and crocidolite. The analytical problem has no easy solution and often requires different technical approaches because the grinding methods can alter the analytical response, which depends on the crystalline lattice of solids.

This is the case of X-ray diffraction (XRD) analysis, the results of which are connected to the mechanical, thermal and chemical stress the samples have been subjected to.

The present work deals with some historical backgrounds on the subject, in connection with the new field of the mechano-chemical sciences; it will also report on some tests on single, binary and polygenic materials with the aim of discussing the methods of grinding the samples for XRD quantitative determination of asbestos in coherent materials.

2. XRD analysis on very fine powders

X-ray analysis of dust and fine powders was used for a long time for the study of occupational diseases which are connected with the nature of airborne dusts (e.g. silicosis). For this type of analysis, the new surfaces arising from the fracture and the fine comminution of solids, as well as the layer immediately underneath represent an anomaly; their properties are accountable for the conditions that have caused the breakage.

These remarks have been considered for a long time in scientific literature with reference to several physical and chemical characteristics; Scherrer (1918) [1] mentioned the ''distorted crystal aggregates'' and defined the effects of both the decrease in the crystallite size and the lattice distortion on the XRD response. The degradation of crystalline perfection was described by Stokes (1944) [2] and Bacon (1952) [3], while later on, some mineralogical changes connected to the milling action were reported, e.g. transformation of calcite into aragonite [4].

Several hypotheses on the nature of the superficial layer of particles were suggested, mainly with regard to quartz. A ''disturbance'' in the crystalline lattice, not negligible in terms of mass for particles less than 0,5 μm in diameter, was supposed to be corresponding to a superficial ''amorphous'' or ''amorphyzed'', highy soluble layer (in borate or sodium hydroxyde dilute solutions), ''which blends smoothly into the less soluble core'' [5] [6].

---

* Mining Eng., Prof. of Solid Processing in the Dept; research worker at the Dept. ''Traumatologia, Ortopedia e Medicina del Lavoro'' of Turin University, via Zuretti 29, 10126 Torino, Italy, where this work was carried out.

† Received May 10th, 1994

This layer was estimated to be 20-30 nm thick (as resulting from specific surface determinations by permeability method, or by solubility tests), or 30-50 nm thick (from densimetric measurements, with reference to the volumic mass of quartz and amorphous silica).

In several tests [7] the well-known phenomenon of XRD line broadening was not evident, except for the region of back reflection where the diffractometric response (determined by photometric analysis on film) was lowered to 66% (pure quartz, ground under 2 μm) and to 58% (only classes of less than 1 μm). The reduction in peak intensity was observed to be much less when grinding was applied to foundry sands (quartz and minor quantities of soft accessories): in the narrow size range (0.5-1 μm), it was inferred that the high soluble surface layer is about 30 nm thick, based on the mass determination of amorphous silica removed from the grain surface by dilute hydrofluoric acid.

Some contrasting hypotheses were derived from the observation of an increased solubility also on the surface of vitreous silica; some authors [8] did not accept the theory of the amorphyzed layer on particles and suggested the hypothesis of a ''disorder'' in crystallite orientation. Some others [9] assumed that three different layers are present on the new particle surface: a mono-layer of hydrated silica, then a disturbed crystalline layer slowly soluble in dilute hydrofluoric acid and finally an ordered core. The disturbed layer produces the line broadening which is more evident on grain sizes of less than 2 micrometers.

It was subsequently proved that the nature and thickness of structural anomalies on the particle surface were due to grinding methods [10] by ascertaining that an increasing grinding time results in both a decrease of the number of observed spectra and in an increase of the background intensity. In contrast, when quartz was ground by hand milling in the presence of acetone, both a strong broadening of the X-ray reflection lines and a small decrease in their integrated intensity were observed. The particles did not lose their angular contour; this led one to believe that – when dry grinding was adopted – a region of the particle close to the surface momentarily melts and becomes amorphous on cooling.

A confirmation of the importance of the nature of solids (particularly as regards the deformability of weak minerals) on the XRD response was obtained by the author in 1963 [11]. In dry grinding 5 types of asbestos [12], a great reduction in height of the lines and even a disappearance of peaks was observed when a strong shearing stress was applied by protracting milling action by means of agate hand mortar and pestle for 30 minutes. In contrast, the use of a wet blade-blender or ultrasonic grinder prevented the re-agglomeration and sintering of solid microparticles and satisfactorily maintained the original diffractometric response. **Figure 1** [13] clearly represents the evolution of XRD response of a sample of crocidolite as run-of-mine (A), ground using a small hammer-mill (B), a wet blade-blender (C) and a dry agate mortar (D) for 15 min (1) and 30 min (2), respectively.

During the 2nd European Symposium of Comminution (Amsterdam, 1966), several effects of ''amorphyzation'' in relation to grinding time (with a vibration mill) were discussed [14] with reference to quartz, galena, rutile, magnetite, and cryolite. Quartz, in particular, revealed a reduction of the (101) peak from 3200 to 100 imp/s after 200 hours of comminution, the outcome differing according to the milling charge (corundum, iron) and the presence of additives. A ball mill with a porcelain pot [15] was also used to grind some zinc oxides (up to 384 hours!): the characteristics of grain-size, density, colour and specific surface of the products were determined and some phenomena of re-agglomeration identified and discussed, in relation to crystallite size and lattice distortion, as verified by the roentgenographic method.

3. Structural modifications in solids induced by mechanical action and ''Mechano-Chemistry''

The term ''mechano-chemistry'', coined by Ostwald [16], is currently employed to characterize the complex physical and chemical phenomena caused by the mechanical treatment of solids [17]. For a long time, however, these properties have been utilized in ore beneficiation, for flotation and selective flocculation, to control the inter-phase behaviour of solids, liquids and air.

Some meetings on mineral processing dealt with many problems of mechano-chemistry, for example, regarding the industrial grinding of quartz, hematite, boemite, hydrargillite, bauxite, titanomagnetite, anatase and kaolin [18]. In some cases, grinding time reached 280 hours; the importance of ore hardness and composition as regards XRD response was ascertained; e.g. when treating some bauxites, a milling duration of ''only'' 20 hours removed all diffraction traces.

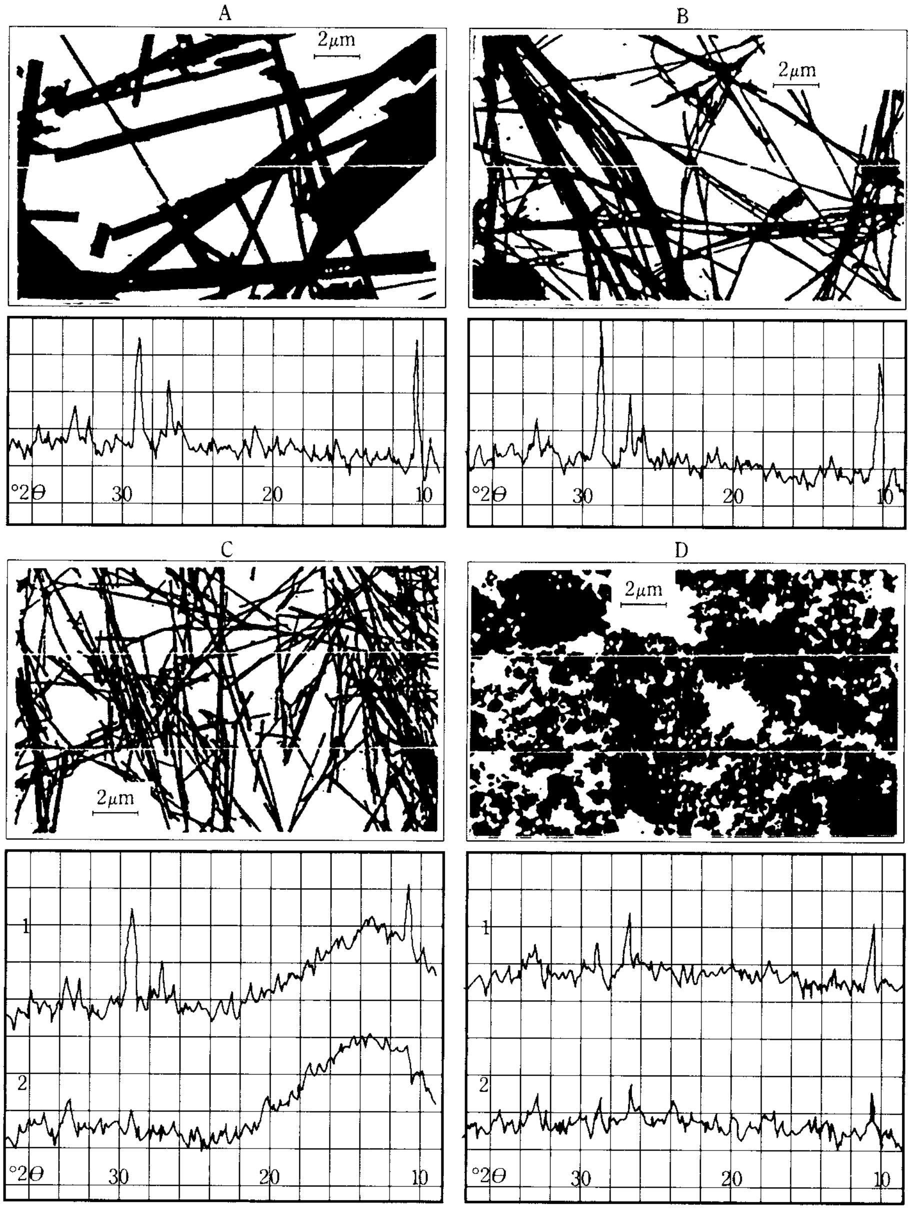

Fig. 1 XRD response of crocidolite: A (classified), B (ground by a hammer micronizer), C (treated by a wet blade blender), D (ground by an agate mortar). 1 and 2 denote a 15 and 30 min. grinding action, respectively.

Mineral engineers have more recently analysed the whole phenomenon of comminution from an energetic point of view, in terms of specific surface, energy activation and relaxation and on the basis of thermodynamic and crystallographic theories [19].

The differences between soft and hard compounds with respect to grinding behaviour, amorphization and chemical transformation following comminution were presented in the field of chemical and materials engineering as a new tool for the production of advanced materials [20].

Langer et Al. (1978) investigated the consequences of the mechanical action on fibres of chrysotile asbestos [21]. They first examined the structural modifications induced by stress and fracture on both Si-O and Mg-O interlayer bonding and brucite layer configuration. The decrease of "fibre crystallinity" produces some variations in the physico-chemical properties of finely ground products. Changes in XRD peak areas, IR and ESR spectra and SAED patterns were also analysed: unground and simply classified short fibres or fibres obtained by a "gentle" size reduction or cutting action have a much more relevant crystalline response than products of a "vigorous" ball-mill grinding, where impaction, compressive and shearing stresses are associated. Further implications of these changes may also involve biological responses such as hemolytic activity, organic free radical absorption and carcinogenic potency of short fibres.

Ultra-fine grinding is nowadays investigated as a cause of deep modifications in the surface layer of solid phase, which may determine changes in bonds, aptitude to selective ion adsorption and zeta and hemolytic potentials [22]. Some recent researches concern:

- the consequences of ultrasonic treatment on the properties and the physico-chemical behaviour of particle surfaces, similar to a mechanical action [23];
- interaction between solid and fluid phases after a mechano-chemical treatment of quartz and asbestos [24];
- surface active sites (atoms, ions, dangling bonds) and molecular modifications consequent to comminution [25];
- chemical functionalities, present on the extremities of mineral fibres, and their increase by mechanical rupture [26].

Some interesting examples of changes in the structure of solids and in the related reactivity consequent to fine comminution were given in a recent paper in this magazine [27]: ''mechanical activation'' may produce mechano-luminescence (e.g. tribo-luminescence), emission of radiations (fracto-emission), transformation of molecular composition (as in mullite, produced by high-energy grinding of kaolin).

4. Processing problems in asbestos sample preparation for XRD

The sensitivity, reproducibility and accuracy of the quantitative determination of mineral components can be strongly affected by variations in the diffractometric response of the crystalline structure caused by grinding (type and time). For this reason, it was formerly suggested [28] that when examining rocks and synthetic materials containing asbestos, analysis should be performed on unground samples. The problems arising from large-sized crystals and/or preferential fibre orientation in raw samples should, of course, be carefully considered.

A XRD method of high sensitivity and accuracy for chrysotile determination was developed by the I.S.S. (''Istituto Superiore di Sanitã.''), Rome [29]. Later on, a wet comminution system for bulk materials as well as an appropriate analysis were tested on asbestos-cement samples [30].

A method of producing asbestos-cement comparative standards was recently proposed by the Italian Institution for Standardization (UNI) [31]; this procedure carries some risk of error due to some processing uncertainties. It was therefore deemed useful to analyse some aspects of sample comminution.

4.1. XRD analysis for asbestos

ISS suggests the use of a silver filter as the support for 0.4 mg of powdered material, obtained from a slurry previously ground with a small vibrating mill in the presence of isopropyl alcohol, and then dried and sampled.

In contrast, the UNI proposal assumes the analysis of samples of about 1 g, consisting of powder contained in normal sample-holders; actually this type of support is easier to obtain and assures better accuracy of the final result, provided a uniform volumic mass concentration is realized in the powdered sample.

For this reason, we use the latter support for this analysis, which requires the preparation of several grams of raw material.

4.2. Preparation of reference standards

The case of cement-asbestos waste products, to which the UNI proposal is directed, cannot be oversimplified by assuming that these materials are made only of asbestos and a generic ''cement'' powder. In fact, besides calcite and quartz (present at various rates in commercial cement products), the old and altered cementos-asbestos plates and tubes contain some products of mortar hydration, hardening, transformation and alteration which are not well represented in the raw cement: the reference standards should represent the real possible composition of the samples to be analysed.

4.3. Classification and concentration of samples for analysis

The UNI proposal for preliminary classification of the dust released from bulk samples on a nylon screen is somewhat debatable due to a possible electro-static selective separation of some components from the original sample. The initial beneficiation of all materials by means of a dilute hydrochloric acid attack seems to be restricted to instances of real necessity, resulting from the preliminary microscopic analysis: even a weak acid dissolution could in fact damage the integrity of the finest chrysotile fibres. Nevertheless, it can be useful in that it eliminates great quantities of calcite, when present in the original samples.

4.4. Grinding of samples

In its experiments, ISS used a small special wet grinding apparatus (McCrone micronizing mill), which is useful for avoiding a damaging local temperature increase. The volume of the grinding cell, therefore, is rather small as compared to the mass of sample usually required by XRD analysis. On the other hand, in the UNI standard proposal only two parameters are specified, i.e. the use of a generic hand mortar and the maximum size of the particles (63 μm): such a grain size for test standards seems to be too large and must be confirmed by suitable tests.

For all the above reasons, an attempt to provide a preliminary answer, at least to some of the following questions, seemed useful:

1) what is the XRD response for some pure minerals, in relation to the milling action?
2) when milling is carried out on binary artificial mixtures, what are the results for the two different components?
3) what is the XRD response on the single components when grinding is applied to a cement-asbestos composite containing several types of asbestos, calcite, quartz, and accessories, in addition to the setting and transformation products of cement mortar?

5. The experimental work: materials and methods

The following minerals and materials (and some of their binary associations) were tested:

1. Quartz (hydrothermal crystalline, from Quincinetto, Torino),
2. Calcite (rose marble from Candoglia, Novara),
3. Chrysotile (industrial product "5 M" from Balangero, Torino),
4. Old asbestos-cement commercial product (a corrugated plate that roofed a shed for 20 years: it contains 2 types of asbestos, calcite, quartz and accessories).

When suitable, a preliminary comminution was carried out using a small hammer pestle to reach a grain size of less than 63 μm, then an intermediate grinding of 1 g of the sample was carried out using an agate mortar with 120 dangling movements, exerting an orthogonal force of about 20 N, and final grinding was executed on single 0.3 g samples using the same manual tool, with a rotating trajectory of the pestle, exerting a shearing stress under a normal force of about 20 N for 1, 2, 4, 7, 10 min (2 r.p.s.). In some cases, grinding was prolonged up to 20 min (binary mixtures) and 40 min (chrysotile).

A small toothed disc mill and a blade laboratory grinder were also utilized to grind a sample of an asbestos-cement composite; this device can reduce the sample particles to under 0.05-0.1 mm, dependent on the operation time.

Characterization of the ground products was obtained by means of optical microscopy (phase contrast and polarized light); the specific surface was calculated from the grain-size distribution from the Rosin-Rammler plot.

The XRD analysis was performed using a Philips PW 1800 apparatus with a Cu anode tube (40 kV generator voltage, 50 mA current, 10 mm irradiated length on sample, 0.02° step size, 1 s time per step, 5...65°, 2Θ angular prospecting). The sample (130 mg) was placed in a circular cell (14 mm in diameter, 0.4 mm thick), fixed by 2 drops (50 mg) of vaseline oil, 100 r.p.m. rotation speed.

The peaks were considered corresponding to the following characteristics: quartz ($d = 0.246$ and 0.343 nm), calcite (0.304 and 0.191 nm), chrysotile (0.736 and 0.366 nm), crocidolite (0.835 nm). The XRD response was determined by evaluating both the maximum height and integrated peak intensity.

As the aim of the experiments was mainly to verify the interference between hard and soft minerals as a consequence of the type and duration of grinding action, without any calibration for quantitative analysis, all results have a preliminary significance and must be considered only as an example of progressive selective degradation on the diffractometric response of mono-and polygenic materials.

6. Results

6.1. Monogenic powders

Several tests on quartz, calcite and chrysotile were performed to confirm and to complement the conclusions drawn from a number of old experiments [11].

Qualitative results for chrysotile confirm a progressive decrease of XRD response, which is more important for the line heights (final reduction after 10 min. grinding to 40% for $2\Theta = 12.2°$ and 34% for $2\Theta = 24.4°$) than for the integrated intensities (to 48% and 44%, respectively).

A lesser degree of reduction was observed on calcite, where final results (lines at $2\Theta = 25,5$ and 47,7°) were 65% and 68% of the original values and 80% and 70% in integrated intensities, respectively.

On quartz powders, there was a minor reduction limited to the final grinding phases (86% and 89%;

90% and 91% for lines and integrated intensities, with reference to peaks on 2θ = 20.9° and 26.7°, respectively).

For chrysotile, the reduction in the XRD response was minor during the first period of dry grinding, becoming higher after 5-10 min of mechanical action: the trend was asymptotic at values of 20-40% of the original state after 40 min grinding (where in the past all crocidolite response was found to be nearly cancelled in the same conditions).

This phenomenon also depends on the roughness of the grinding mill surfaces and is linked to a new aggregation state of particles smaller than 2-3 μm in size, which are compacted in aggregates that cannot easily be destructed, even by wet dispersion.

Chrysotile grinding in presence of H_2O_2 has also been observed to reduce the statistical dispersion of both the integrated intensities and background; further investigations are required on this subject.

6.2. Binary mineral associations

The response of some mixtures of chrysotile (10%) with quartz or calcite, when ground using a similar procedure, has been studied. As for single minerals, the height reduction of the peaks is greater for the weak components. However, for binary mixtures the height reduction of the peaks for weak components is lower than for single minerals. In fact, it seems that large crystals of rigid and hard minerals such as quartz could protect the weak ones, preventing their micronization and a corresponding strong reduction in their XRD response.

When grinding a mixture of 90% calcite and 10% chrysotile for 20 min, the chrysotile line at 2θ = 24.4° was unidentifiable, whereby the main peak (2θ = 12.2°) is just visible, together with a great line broadening (integrated intensity 45% of the primary one, for a simple homogenization of pure components).

6.3. Sample of cement-asbestos corrugated plate

The fibrous components of this tile-building material turned out to be amphibole and serpentine asbestos in nearly equal rates (abt. 30% in all).

The changes in XRD response for the main lines of crysotile (2θ = 12.2 and 24.4°), crocidolite (2θ = 10.65°), calcite (2θ = 25.5°) and quartz (2θ = 26.7°) were examined.

The evolution of peak heights and integrated intensities was similar to the previous examples (**Figs. 2** and **3**). Attention was also paid to the specific surface of the powders: the graph (**Fig. 2**) was plotted on the basis of the grain-size distribution, as determined by optical microscopy on calcite, quartz and cement crystals, disregarding asbestos fibres. The letters indicate the XRD response of the products obtained by the toothed disc (D), the manual pestle for intermediate grinding (P), and the blade grinder operating for 2 and 5 min., respectively (B1 and B2).

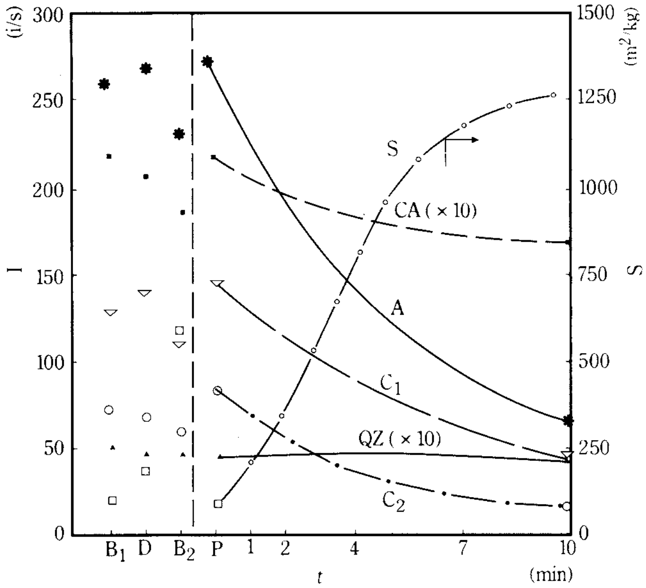

Fig. 2 Evolution of the XRD response (I: height of peaks) against milling time (t) for the main lines of chrysotile: C1 = (002), C2 = (004), amphibole asbestos chrocidolite (A), calcite (CA), quartz (QZ). S is the specific surface of powders; B1 and B2, D and P the treatment by a blade mill (2 and 5 min), a toothed disc grinder and an agate mortar (with a compression action only), respectively.

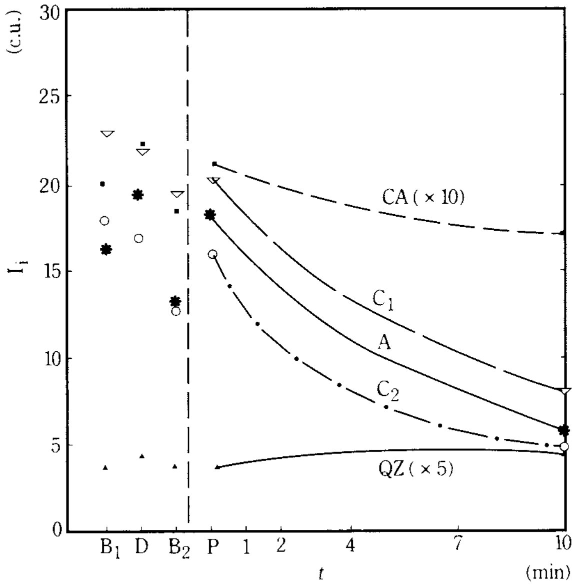

Fig. 3 Evolution of the XRD response (Ii: integrated intensities, in conventional units) against milling time (t) (Symbols as in **Fig. 2**).

With reference to the grinding product obtained using the hand pestle after 1 min of impact (P), the two main lines of chrysotile (and the corresponding integrated intensities) denote a concordant but not proportional reduction.

As in previous examples, the attenuation of XRD response for calcite was somewhat smaller than for asbestos and was very small for quartz. A maximum value for diffracted intensities was found for short grinding times (for instance, by exerting pressure and impact using a manual pestle for 1 min and by obtaining a grain-size distribution smaller than 0.04-0.05 mm, with a 30...50 m^2/kg specific surface).

In terms of specific surface, the XRD response of asbestos minerals is represented by some linear regressions (see **Fig. 4**, for the principal peaks of chrysotile, (002) and (004) reflex, and for the main line of crocidolite, and **Fig. 5** for the respective integrated intensities). These regressions are represented by the following relations:

$$I_1 = 112-0.048\ S;\quad I_{i1} = 21.8-0.0103\ S;$$
$$I_2 = 60-0.032\ S;\quad I_{i2} = 13.4-0.007\ S;$$
$$I_3 = 252-0.136\ S;\quad I_{i3} = 19.2-0.0104\ S$$

where I and I_i are the heights and integrated intensities (as counts per second and conventional units, respectively), 1, 2 and 3 are the two main lines of chrysotile and the first reflex of crocidolite, S the specific surface, as previously defined, in m^2/kg. The quoted relations I (S) are valid in the ranges S = 500...1,200 m^2/kg; the I_i (S) in the greater range 150...1,200 m^2/kg.

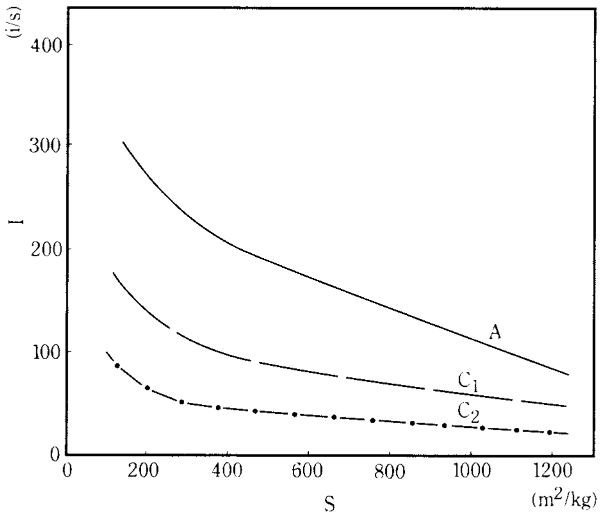

Fig. 4 Regression curves: diffracted intensities (I) against specific surface (S) for the main lines of amphibole and chrysotile asbestos, ground by a hand mortar and pestle (symbols as in **Fig. 2**).

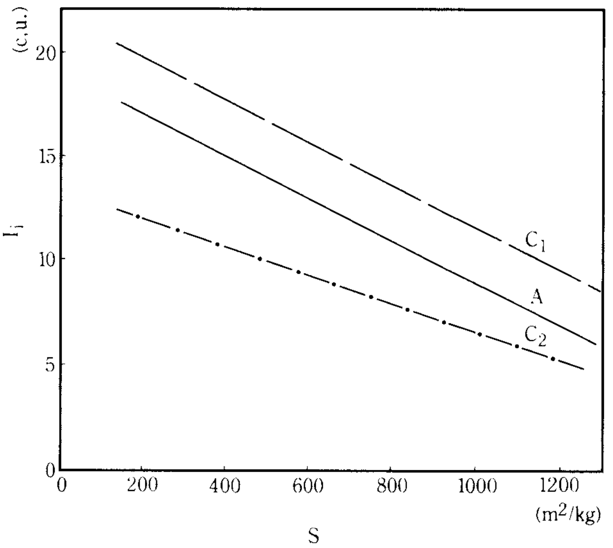

Fig. 5 Regression curves: integrated intensities (Ii) against specific surface (S) for the main lines of amphibole and chrysotile asbestos, ground by a hand mortar and pestle (symbols as in **Fig. 2**).

It is clear to see that crocidolite is more sensitive to grinding than chrysotile, so that its response decrease with comminution is greater; consequently, crocidolite was no longer detectable in a significant way after 10 min of milling action, even if its original percentage by mass was 10-15%. The results of dry comminution using suitable laboratory grinders are comparable with those obtained by a hand mortar and pestle, operating for 1-1.5 min.

7. Final remarks

Due to the great number of physical parameters involved, the results of this research cannot be generalized. They may be valid to assess the selective degradation of mineral and synthetic materials, according to the particular method of comminution.

The XRD response is strongly influenced by the "crystallite disorder", dependent on elastic and mechanical properties of the mixtures and aggregates, and reaches the maximum value for soft, ductile and inelastic components. However, it may vary under the same grinding conditions in accordance with the composition of the materials and particularly with the simultaneous presence of both hard and soft constituents.

Great attention should be paid to the method of getting samples for roentgenographic analysis and calibration standards, as the components may interfere with each other and may imply further complications.

7.1. Grain-size of samples for analysis

When operating with cement-asbestos materials, it is possible to obtain reproducible and accurate results with powders ground below 0.04-0.05 mm.

7.2. Grinding time

Milling duration should be related to the grindability and original sizes of materials, as well as to their crystalline texture; in general, the grinding time should be kept at the shortest level necessary to obtain the above reported sizes: 1-3 min are often enough, for both hand mortars and mechanical disc or blade grinders.

7.3 Grinding devices

Dry grinding by means of agate mortars is acceptable, provided that the shearing stress on samples and relied attrition effects are reduced to a minimum. If preliminary and intermediate screening are employed, overgrinding and its negative effects on the XRD response can be avoided; multi-stage grinding and screening are useful, provided that all sample particles are sufficiently reduced to pass the predetermined mesh size. The wet grinding method (in an alcoholic medium, as with the McCrone micronizer) should be confined to scientific research on very small samples, to be analysed after dispersion and filtration on suitable membranes.

7.4. Sample supports

When the holder is a simple disc cell, it is possible to reduce the sample mass to a small fraction of 1 gram [32], weakly fixed with vaseline oil when necessary. However, a constant volumic mass concentration in the powder layer should be ensured; this can easily be obtained with the normal pressed tablets.

Filters (cellulose or silver) can be confined to the mono-layer analysis for very small quantities of powder or dust.

7.5 Calibration standards

The more difficult step for XRD analysis on multiphase powders is to obtain a suitable standard. Calibration tests should be performed on the materials to be investigated. This is because the variability of diffraction angles reported for some international standards and by different authors is sometimes large: for instance, a variation interval of 0.65° 2Θ (for the main peak) and of 0.9° 2Θ (for the second) was quoted for kaolin, which can show some interference with asbestos minerals [33]. Similarly, the relative values of integrated intensities can be quite different for different types of the same asbestos (i.e. in the case of ortho- and clino-chrysotile and for some fibrous amphiboles).

Furthermore, a great flexibility in choosing the reference lines should be adopted by taking into account the possible interference of the associated components in commercial and natural materials; calibration curves should therefore be prepared on the basis of all identifiable and significant peaks.

7.6 Sensitivity and accuracy of analytical results

On the basis of the above remarks, it does not always seem plausible to achieve a detection limit as low as 1%, as stated by many scientists: a sensitivity of 2-4% was often found for polygenic substances. Finally, the accuracy of XRD quantitative asbestos determination can be acceptable when – according to the bulk material composition – the standard deviation of the experimental values is less than 20%. One should note that for more complex associations of asbestiferous materials, only a multiphase analytical method (always based on a careful microscopical analysis, with both polarized light and phase contrast technique) can reach good sensitivity and accuracy.

This analysis should be extended to all intermediate and final grinding products, to obtain complementary information on the nature of the components and the grain-size distribution.

8. Conclusions

1) The quantitative determination of asbestos minerals, and in general of soft and inelastic minerals, with the X-ray diffraction (XRD) analysis method is influenced quite strongly by the grinding of the sample. This fact is due to modifications of the crystalline structure in the surface layer of solids, which results in a reduction of the peak heights in the XRD response.
2) This reduction of the peak heights in the XRD response largely depends on the type of grinding method and on the grinding time, and reaches the maximum value for a grinding action based mainly upon shearing and attrition stresses.
3) As a consequence of the above, particular care must be taken in selecting and applying standard procedures for the preparation of the samples and of the calibration standards to be subjected to the XRD analysis.
4) For the preparation of XRD samples from asbes-

tos-cement composites, it is applicable to reduce the powder to under 0.04-0.05 mm using mechanical grinders or manual mortars; normal sample holders containing 0.1-1 g of sample can be used successfully.

5) Particular care must be exercised with respect to the calibration standards, which must accurately reproduce the quality and the size distribution of the material to be analysed.
6) In order to overcome several uncertainties of the analyses, some advantages are obtained by combining a preliminary microscopical examination (polarized light and/or phase contrast) with the usual XRD procedure. In this way, more information about both the composition and size distribution of the powders may be obtained.

Acknowledgements

The author is indebted to Prof. G. Ferrara (Mining Eng. Faculty, University of Trieste), Prof. L. Pettinati (Director of the Dept. of Traumatology, Orthopaedics and Occupational Medicine of the Turin University) and Prof. G. Scansetti (Director of the Industrial Hygiene Laboratory in the same University) for giving suggestions and encouraging the experimental work.

He is also grateful to Mr. P. Zuliani (chemist, techn. assistant in the quoted Laboratory), who carried out many XRD analyses with great care.

Nomenclature

d	Reticular distance	nm (10^{-9} m)
I	Diffracted intensity	i/s (impulses/s)
I_i	Integrated intensity	convent. units (dimensionless)
r.p.m.	Revolutions per minute	min^{-1}
r.p.s.	Revolutions per second	s^{-1}
S	Specific surface	m^2/kg
t	Grinding duration	min
2θ	Diffraction angle	degree °
ISS	Istituto Superiore di Sanitã (Italian Institution for Health)	
UNI	Unificazione Nazionale Italiana (Italian Institution for Standardization)	

References

1) SCHERRER P.: ''Bestimmung der Grösse und der inneren Struktur von Kolloidteilchen mittels Röntgenstrahlen''. Nachr. Ges. Wiss. Göttingen (1918) , 2; 96-100.
2) STOKES A.R., WILSON A.J.C.: ''The diffraction of X-rays by distorted crystal aggregates''. I. Proc. Phys. Soc. London (1994), 56; 174-181.
3) BACON G.E.: ''The reduction of crystalline perfection of graphite by grinding''. Acta Cryst. (1952), 5; 392.
4) BURNS J.H., BREDIG M.A.: ''Transformation of calcite to aragonite by grinding''. J. Chem. Phys. (1956), 25; 1281.
5) DEMPSTER P.B., RITCHIE P.D.: ''Surface of finely ground silica''. Nature (1952), 169; 538-539.
6) GORDON R.L., HARRIS G.W.: ''Effect of particle-size on the quantitative determination of quartz by X-ray Diffraction''. Nature (1955), 175; 1135.
7) NAGELSCHMIDT G., GORDON R.L., GRIFFIN O.G.: ''Surface of finely ground silica''. Nature (1952), 169; 539-540.
8) TALBOT J.H., KEMPIS E.B.: ''Finely ground quartz: evidence against a ''disturbed layer''. Nature (1960), 188; 927-929.
9) BERGMAN I., CARTWRIGHT J., BENTLEY R.A.: ''A mechanism for the dissolution of ground quartz powders in dilute hydrofluoric acid: an ''easily soluble core'' and its relation to the ''easily soluble layer''. Nature (1962), 196; 248-250
10) TALBOT J.H., KEMPIS E.B.: ''Effect of grinding on quartz particles''. Nature (1963), 197; 66-67.
11) OCCELLA E.: ''Variazioni della struttura cristallina conseguenti a sollecitazioni di rottura in alcuni minerali teneri''. Ric. Sci., Rendic. A (1963), 3,6; 897-906.
12) OCCELLA E.: MADDALON G.: ''X-ray diffraction characteristics of some types of asbestos in relation to different techniques of comminution''. Med Lavoro (1963), 54; 628-636.
13) OCCELLA E.: ''Influenza della comminuzione sulla struttura cristallina della crocidolite''. Boll. Ass. Min.Subalpina (1968), 5, 4; 740-742.
14) SZANTHO E.v., LINDNER K.H.: ''Untersuchung der Änderung physikalischer und chemischer Eigenschaften des Mahlgutes bei der Feinstzerkleinerung'' 2nd Eur. Symposium on Comminution (1966). DECHEMA Monographien (1967); 57; 455-474.
15) TAKAHASHI H., TSUTSUMI K.: ''Mechanochemical effects on zinc oxide powder crystals''. 2nd Eur. Symposium on Comminution, (1966). DECHEMA Monographien (1967), 57; 475-494.
16) OSTWALD W.: ''Handbuch der allg. Chemie'', Bd.1 (1919); Akad. Verlagsanstalt, Leipzig: 70-79.
17) PETERS K.: ''Mechanochemische Reaktionen'',

in: RUMPF H.: 1st Symposium on Comminution; Chemie/VDI-Verlag (1962); 78-98.
18) SZANTHO E.v.: "Physikalischer und Chemisches Verhalten fester Stoffe bei der Schwingmahlung". 8th Int. Min. Proc. Congr. (1968), A-4; 1-11.
19) LIN I.J. NADIV S.:; "Alteration of mineral properties during grinding through mechanical reactions". 16th Int. Min. Proc. Congr. (1988); 231-244.
20) SENNA M.: "Finest grinding and mechanical activation for advanced materials". 7th Europ. Symposium on Comminution (1990), preprints, 1; 21-36.
21) LANGER A.M., WOLFF M.S., ROHL A.N., SELIKOFF I.J.: "Variation of properties of chrysotile asbestos subjected to milling". J. Toxic. Env. Health (1978), 4; 173-188.
22) YOKOYAMA T. et AL.: "Ultra-fine grinding and consequent changes of powder characteristics". KONA (1983), 1; 53-64.
23) FUBINI B.: "The possible role of surface chemistry in the toxicity of inhaled fibers", in "Fiber Toxicology", Acad. Press. (1993), 229-257.
24) GIAMELLO E., FUBINI B., VOLANTE M., COSTA D.: "Surface oxygen radicals originating via Redox reactions during the mechanical activation of crystalline SiO_2 in hydrogen peroxide". Colloid and Surfaces (1990), 45; 155-165.
25) BOLIS V., FUBINI B., GIAMELLO E.: "Effect of form on the surface chemistry of finely divided solids". Mater. Chem. and Phys. (1991), 29; 154-164.
26) FUBINI B., BOLIS V., GIAMELLO E., VOLANTE H.: "Chemical functionalities at the broken fibre surface relatable to free radicals production", in "Mechanism in Fibre Carcinogenesis", Plenum Press (1991), 415-432.
27) STEINIKE U., HENNIG H.P.: "Mechanically induced reactivity of solids". KONA (1992) 10; 15-24.
28) MADDALON G., OCCELLA E.: "Analisi diffrattometrica diretta su materiali compositi flessibili". 11th Congr. Naz. AIDII; Quad. Fondaz. Clinica del Lavoro, I.R.C.C.S. (1992), 262-264.
29) PULEDDA S., MARCONI A.: "Quantitative X-ray diffraction analysis of asbestos by the silver membrane method: application to chrysotile". Am. Ind. Hyg. Assoc. J. (1990), 51; 107-114.
30) PULEDDA S., PAOLETTI L.: "Study on the effect of comminution on the diffractometric response of chrysotile contained in a bulk sample". Ann. Occup. Hyg. (1994), 38, 1; 59-65.
31) U.N.I.: "Determination of dust and free asbestos fibres content in asbestos-cement products". Proposal U 43.00.010.0 (1994), 1-5.
32) MADDALON G., OCCELLA E.: "Affinamento delle modalita di analisi diffrattometrica in rapporto alla superficie di preparato esposta ai Raggi X". Med. Lavoro (1989), 80, 1; 78-89.
33) VINCENTINI M. ET AL.: "Il problema del riconoscimento tra amianto crisotilo e caolino nell'uso della tecnica diffrattometrica a Raggi X: analisi di una casistica". Giorn. Ig. Ind. (1992), 17, 4; 91-104.

Author's short biography

Enea Occella

OCCELLA Enea, born in 1928 in Mondovi (Northern Italy), was mining engineer (1950), assistant professor in the Turin Polytechnic School (1950-1964), professor in charge of petrography, mineral processing and mineral prospecting (1953-1970).

Full professor of mineral processing (1965-1993) and solid processing (1993-94). Member of the Research Commission of European Community for Coal and Steel (C.E.C.A., Luxembourg: 1956-1989), Corresp. Member of the Academy of Sciences (Turin: since 1993), he has as his main professional and scientific interests: comminution, dust analysis and suppression in mines, rock mechanics, mine geothermics.

Tomographic Measurements of Granular Flows in Gases and in Liquids†

M. S. Nikitidis, M.E. Hosseini-Ashrafi, U. Tüzün
Department of Chemical and Process Engineering, University of Surrey, *
N. M. Spyrou
Department of Physics, University of Surrey, **

Abstract

Two distinct non-intrusive radiation methods known as scanning gamma ray tomography and single profile photon absorptiometry are presented in this paper as tools for the investigation of interstitial voidage distributions of granular flows in both gases and liquids. Single profile absorptiometry coupled with the consecutive radial transformation of the linear data obtained within seconds of flow time is used as a tomographic tool for dynamic voidage characterization in different flow regimes of air and liquid-based systems, as well as a complete tomographic projection procedure, which requires scan times of the order of minutes to achieve high spatial resolutions over a large cross-sectional area of the vessels. A novel tomographic technique currently under development known as dual photon tomography is proposed to facilitate simultaneous voidage mapping and particle tracking in 3-D granular flows.

1. Introduction

Various problems arise during the transport and handling of granular materials in the process industry. Particle segregation and attrition, lack of control in solids flow rates, build-up of adverse pore pressures are some of the major problems. It is a common belief that most of these problems are closely linked to the behaviour of the interstitial voidage within the process units. The need therefore emerged for reliable quality control methods, and a considerable amount of the research pursued during the last ten years in the particle technology area has been focused on the investigation and application of these methods. Based on various physical principles (nuclear emission, magnetic resonance, electrical impedance), these methods were already in use in other fields such as medicine, chemistry and biology with established success. The main consideration in choosing the appropriate method for characterizing the bulk voidage profiles in a granular system is the need for achieving the necessary spatial resolution, and in the case of dynamic events, the appropriate temporal resolution is also important.

Gamma ray tomography was one of the first non-invasive techniques used to investigate the two-phase flow behavior of single or multicomponent granular systems. The investigation of the voidage structure near the jet region of a fluidized bed and the effects of background fluidization and particle shape on the dissipation of the gas momentum in this region were first reported by MacCuaig et al. (1985)[12].

By using the same tomographic equipment, Seville et al. (1986)[16], investigated the jet and the bubbling region of a fluidized bed above a multi-orifice distributor and determined the transition height between them. All the results were in very good agreement with several previous theoretical predictions and other experimental methods. The tomographic scanner used for this work provided time-averaged profiles over a long period (6-7 hours) with a spatial resolution of 5mm.

A new tomographic facility now in use at Surrey opened new perspectives in the study of granular systems by meeting both the spatial and the temporal resolution requirements simultaneously. A preliminary work in gas-based granular systems is reported by Hosseini-Ashrafi and Tüzün (1993)[9], where consecutive scans at various heights of a hopper housing mono-sized and binary mixtures during start-stop experiments revealed a maximum value of voidage near the orifice propagating with time up the conical section of the hopper. The voidage values obtained from the gamma ray scan showed close agreement with published theoretical values, and their transformation in polar coordinates (both angular and annular)

---

* Guildford, Surrey GU2 5XH, U.K.
** Guildford, Surrey GU2 5XH,U.K.
† Received May 15th, 1994

proved the axial symmetry inside the hopper.

The axial symmetry inside the hopper enabled the development of a new technique (Hosseini-Ashrafi and Tüzün, 1993)[10], which offers considerably faster scans without sacrificing the spatial resolution. The new technique employs single photon absorptiometric profiles across the hopper within a few seconds, retaining a spatial resolution of 1mm necessary for quantifying the interstitial voidage, and consecutive transformation of the Cartesian data to polar coordinates resulting in a radial distribution of the density function. The main advantage of this technique is that tomographic information can be extracted from the single profile measurements in a shorter time period than if a complete scan were performed.

Work concerning the application of gamma ray tomography in spouted beds (a variant of a fluidized bed where gas enters the bed from a single orifice) is reported by Simons et al. (1993)[17]. The quantitative analysis of the raw data showed a higher central voidage region in the case of cohesive particles, as well as a ridge of high (adjacent to the jet) to low (near the vessel walls) voidage representing ''dead zones'' of fluidization.

As an alternative to scanning transmission tomography, Positron Emission Tomography has also been applied successfully in the investigation of flow characteristics in multiphase granular systems by monitoring the trajectories of single radio-labelled particles as they move in the system. A positron camera used to detect coincident photons coming out in opposite directions after a positron annihilation has been constructed by Hawkesworth et al. (1986)[18]. A spatial resolution of 6-8mm (full width at half maximum) is achieved in tracking a single particle of similar dimension, while the motion of the particle is monitored by taking a number of exposures over a short time period. Two statistical methods, one based on a conventional backprojection of the photon trajectories, the other based on the unprojected trajectories, have been developed to determine particle position.

The feasibility of the new technique for particle tracking was tested on a model fluidized bed by Bemrose et al. (1988)[2]. The method for particle tracking by using the photon trajectories has been improved in a recent work by Parker et al. (1993)[15]. The spatial resolution in Positron Emission Particle Tracking (PEPT) is referred to in terms of the uncertainty error in the estimation of the particle location (3-D standard deviation), and depends upon the number of events used for determination of the particular location. The temporal resolution meets very high standards as each exposure is logged-in within a time period at the order of milliseconds. The new algorithm rejects corrupted events due to scattering or invalid coincidences, and always keeps an optimum set of events for tracking the particle according to its velocity. The new method encourages the use of smaller tracers (2mm diameter) instead of the bigger ones used until now due to the limited resolution of the PET images. PEPT has also been applied recently to powder mixing studies, providing a way to calculate the particle density at each point as a function of the filling level and the shaft angle (Beynon et al., 1993)[3].

Non-ionizing methods such as electrical impedance and NMR are also in current use in the study of granular systems. Electrical imaging has found wide application in multiphase systems and especially in fluidized beds. Recent work in fluidized beds revealed useful information concerning global voidage distribution within the bed (Halow and Nicoletti (1992)[6], Halow et al. (1993)[7]. There are also some limitations in these electrical methods such as poor resolution, blurring due to averaged permitivity for each pixel, and non- linear effects due to the electrical interactions between particles which distort the proportionality of void fraction to measured permitivity.

Nuclear Magnetic Resonance imaging has been widely used in flow studies of multiphase systems in both the medical and industrial areas. Based on the excitation and relaxation of the magnetization of a medium, it provides images with high spatial resolution. The choice of solids to be used in an NMR study must be very strict since the NMR signal from dry solids has very short relaxation times, while the solids moisture content improves the detection accuracy significantly. Furthermore, the NMR technique is restricted in terms of hardware cost and implementation to the study of reasonably small objects thus being inappropriate for large-scale industrial applications. A recent work of NMR measurements from a rotating silo of packed particles has been reported revealing a shear and a rigid body motion region (Nakagawa et al. (1993)[13].

In addition to the work highlighted above, a novel tomographic facility is presently under development at Surrey which is dedicated to the investigation of 3-D granular systems. A single gamma-ray source providing a fan beam and facing an array of detectors will for the first time provide measurements of voidage profiles accurate to a spatial resolution of less than 1mm over scan times at least four times shorter (i.e. in seconds rather than minutes of flow) than those available with the existing parallel beam scanner configuration (Hosseini-Ashrafi and Tüzün (1993)[9]. Furthermore, a dual photon technique applied for the analysis of the raw data will enable the quantification and characterization of flow of particulate systems consisting of more than one solid phase. Various particles of a size comparable to the acquired spatial resolution will play the role of tracers following the flow of the system in order to facilitate the extraction of simultaneous velocity profiles and voidage patterns in 3-D flow vessels. The details of the experimental work in progress with different systems are described below. The bulk of the work to date at Surrey has been conducted using a multiple source parallel beam scanner whose details are given in sections 2 and 3, while the details of the most recent fan beam scanner project are presented in Section 4.

2. Investigation of air/solid systems using a parallel beam scanner

The CAT scanner used in these experiments employs a scanner head consisting of six 153Gd sources emitting gamma photons at energies of 44 keV and 100 keV, and six collimated CsI scintillation detectors arranged in a parallel geometry. 153Gd has a half life of 241 days and high specific activity which provides high photon fluxes with the minimum source size. Each scan is taken by translating the head laterally in small steps in order to sample the object properly, and then rotating by 1.5° to make another translation. The scan finishes after completing a rotation of 180°. The collimators used in these experiments had 1mm and 2mm aperture width, which actually governs to a large extent the final image resolution. The vertical resolution (length of the aperture) was 3 mm, allowing good precision in our measurements. The fastest total scan time achieved was 90 sec with the 2 mm collimator. A 2 m tall Perspex cylinder of 96mm inside diameter is mounted on a conical hopper section of 10° half-angle and a 10 mm diameter orifice. The hopper is allowed to move vertically with different velocities and in different steps. A schematic diagram of the experimental rig is shown in **Fig. 1**.

Polymethyl methacrylate spheres of size distribution 90-1000 μm were used to prepare mono-sized and binary beds in different proportions and size ratios. The experimental work involved consecutive scans at different heights of beds with flow history during a series of start-stop experiments to achieve better image reconstruction quality, and also of static beds with no flow history. **Fig. 2** compares images of a mono-sized and a binary mixture in a static condition. The boundaries of the particles cannot be distinguished since the spatial resolution of the scans is higher than the individual particle size, and the solid fraction content at every pixel cannot be calculated by direct observation methods.

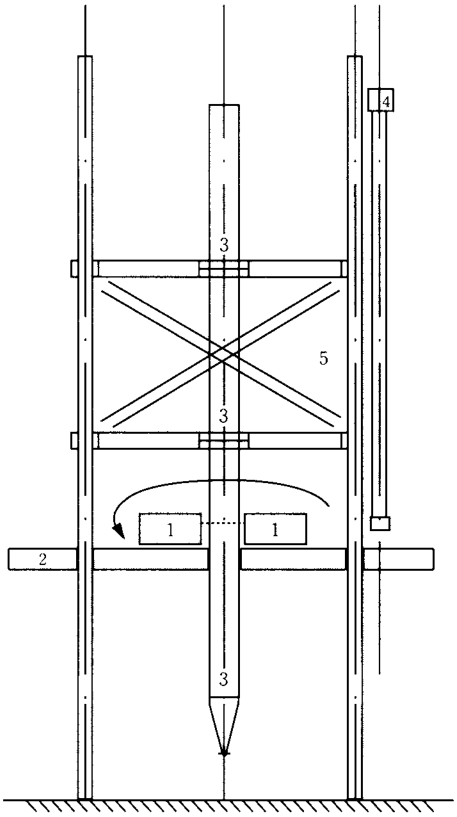

Fig. 1 Schematic diagram of the experimental apparatus for the air/solid systems: (1) Parallel beam scanner; (2) vibration-free table mount; (3) model hopper; (4) motorized vertical positioner; (5) model hopper support structure.

Therefore an analytical procedure has been developed according to the following equation

$$\eta(x,y) = \frac{\mu(x,y)-\mu_{air}}{\mu_{solid}-\mu_{air}} = 1-\mathcal{E}(x,y) \qquad (1)$$

where $\mu(x, y)$ represents the reconstructed linear attenuation coefficient value of the pixel with the unknown solids content, and μ_{air} and μ_{solid} are the reconstructed values for air and solid-filled pixels, respectively. These values are actually averaged over

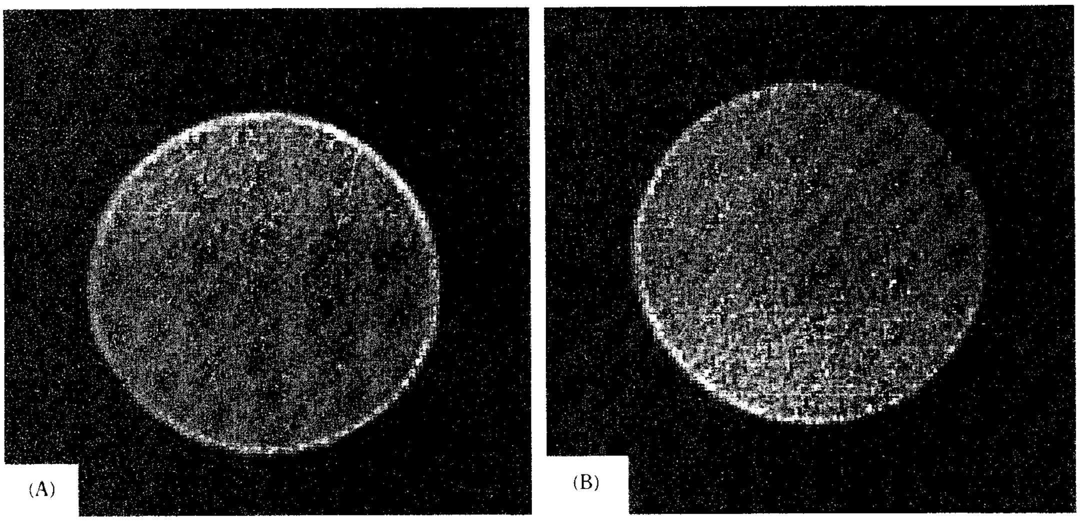

Fig. 2 Reconstructed images of the same horizontal plane across two different static beds:
(A) mono-sized bed of spherical particles, diameter 850-1000μm, no flow history, static imaging
(B) binary mixture bed of 850-1000μm and 90 – 125μm spherical particles, 30% by weight fines, no flow history, static imaging

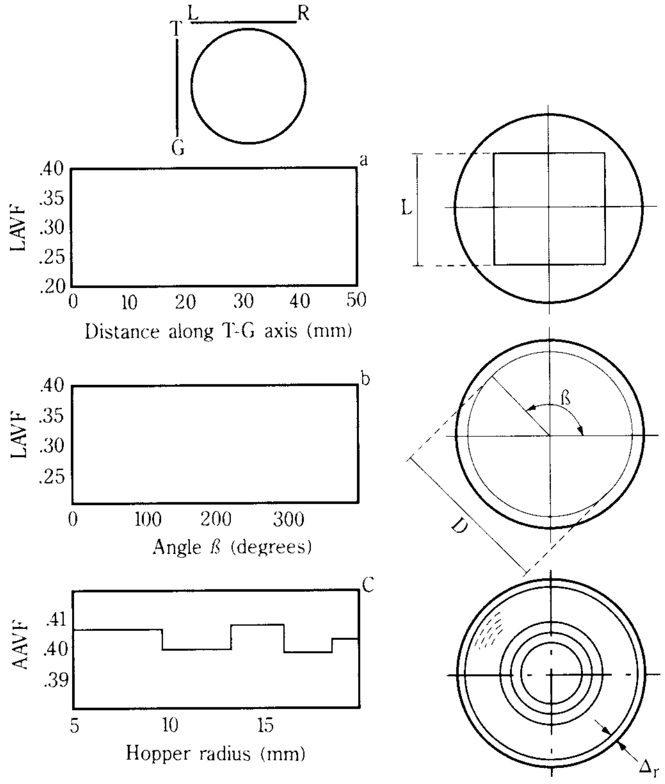

Fig. 3 Cross-sectional profiles of flowing voidage in axially symmetric flow: (a) line scan data for a binary bed of 75% b.w. of 850-1000μm and 25% b.w. of 125-212μm diameter spheres after 5s of discharge at height Z=230mm; (b) polar scan data for the binary mixture bed as in (a) but after 60s of discharge and at Z=400mm; (c) annular segment scan data for a mono-sized bed of 125-212μm diameter spheres after 7s of discharge and at Z=140mm (LAVF=line averaged void fraction and AAVF=annular averaged void fraction). Line scan data are averaged across L-R axis and plotted along T-G axis.

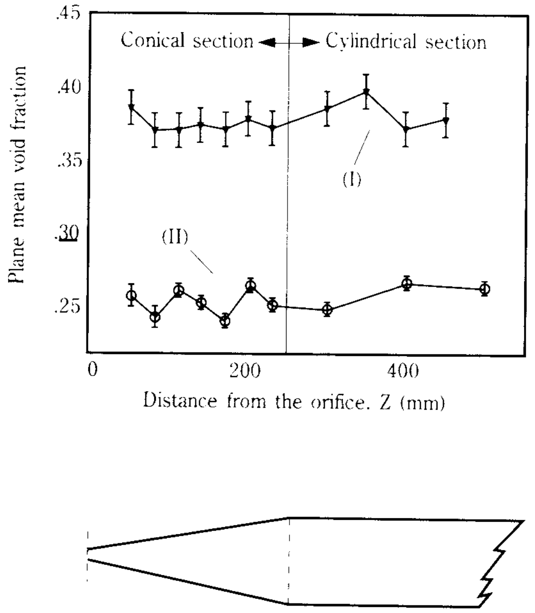

Fig. 4 Comparison of the static voidage profiles of: (i) mono-sized bed of 125-212μm diameter spheres, and (ii) binary bed of 75% b.w. of 850-1000μm and 25% b.w. of 125-212μm diameter spheres.

a sample of pixels of the image containing only air or solid. The above procedure was tested against phantoms of known solid content at every point with an accuracy of ±1.5%. The void fractions are calculated along each line (L-R) according to Eq.(1), and the mean values (PMVF) are plotted along line (T-R) as can be seen in **Fig. 3**. The possible axial symmetry of flow and the radial distribution of the density function is investigated by transferring the linear profiles of interstitial voidage to Cartesian and polar coordinates as can also be seen in **Fig. 3**. The Cartesian coordinate system keeps the pixel geometry of the image, whereas in the polar coordinate system, averaged values of voidage are calculated along a preselected radius and plotted against various angles *b*. Furthermore, interstitial voidage can be presented as averaged values within equal-area strips spanning radially away from the centre of the hopper. The averaging procedure within an annulus of thickness comparable with some tens of particle diameters causes a smoothing effect on the voidage fluctuations, as can be clearly seen in **Fig. 3** where voidage profiles on the other coordinate systems are presented as well.

Static profiles of mean voidage values with height for a mono-sized and a binary mixture is demonstrated in **Fig. 4**. There is no significant alteration of the mean void fraction with height in both the cylindrical and the conical section of the hopper, but there is a visible increase in going from the conical to the cylindrical section. A well-defined maximum propagating with time up the silo is demonstrated in **Fig. 5** where the flowing profiles with height of a mono-sized and a binary mixture are presented. A minimum value of voidage can be clearly detected within the cylindrical section close to the transition line.

Faster scan times of the order of 20 sec have been achieved by using a new quantitative technique employing single profile measurements across a bed of mono-sized and binary mixtures and a consecutive radial transformation of the linear data according to the equation

$$F(r) = -(1/\pi)\int_{r}^{R}\frac{F(x)dx}{(x^2-r^2)} \qquad (2)$$

where $F(r)$ is the radial density function and $F(x)$ is the line integral as can be seen in **Fig. 6**. The technique was tested successfully by using a specially constructed phantom presented in **Fig. 7**. A mono-sized bed consisting of polymethyl methacrylate powder in the 125-200 μm size range and a binary mixture of 80 % by weight of acrylic beads in the 0.85-1.0 μm size range with 20 % by weight of fines were scanned during discharge using the new absorptiometric method; the radially transformed data at different heights are presented in **Fig. 8**. The collimator aperture dimensions are 2 × 3 mm, providing a resolution of 2mm across the hopper and a precision of better than 1 %. The significant time variation of voidage in the case of the mono-sized bed of fine particles indicates the presence of air-impeded flow, whereas in the case of the binary mixture, the time variation of voidage is quite small and a dilated region in the centre of the hopper is evident. The spatial resolution of these scans is 2 mm, which is of the order of 2-10 particle diameters. Therefore, they will not allow the detection of the "empty annulus" at the orifice plane which is known to have a width of about 1-2 particle diameters (Arteaga and Tüzün (1990)[1]) The spatial variation of voidage with height is significant over a height of 50 mm above the orifice (5 or so orifice diameters) in the case of the binary mixture, whereas at greater heights the profiles are reasonably flat. A significantly dilated region in the case of the mono-sized mixture is predominant over a height of 50 mm from the orifice with a similar shape profile as in the binary case for greater heights.

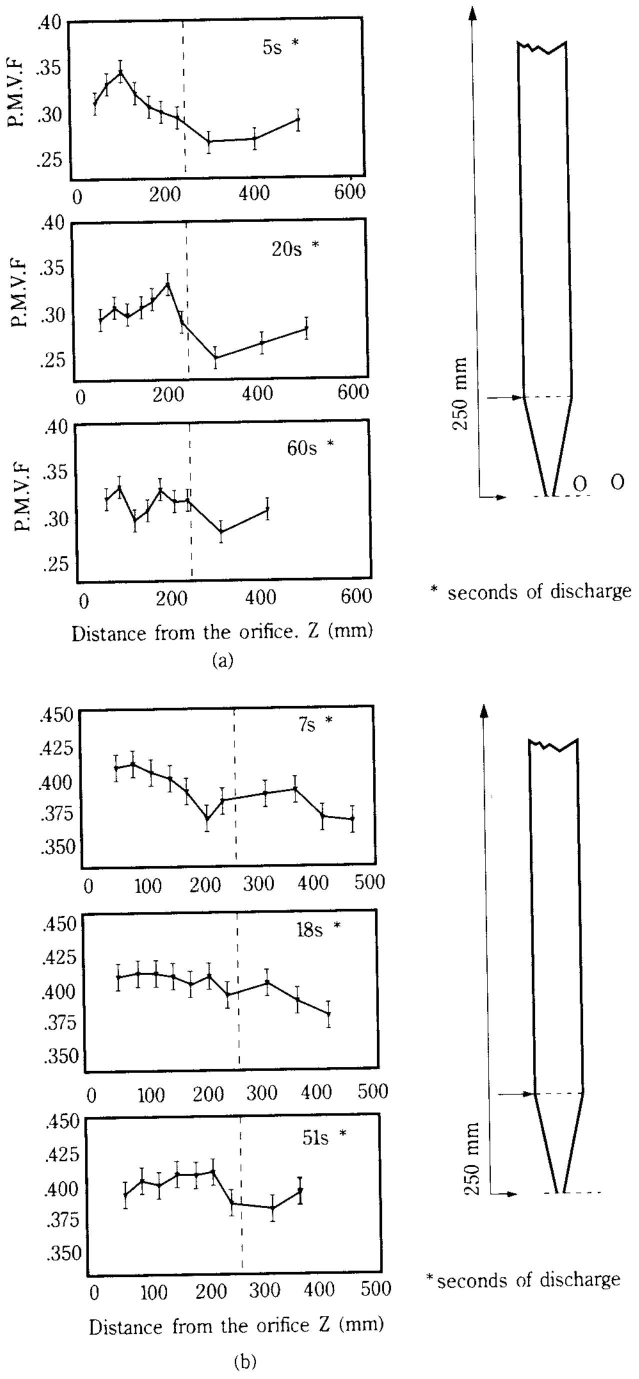

Fig. 5 (a) Vertical profiles of the plane mean voidage in the model silo during batch discharge of a binary mixture bed of 75% b.w. of 850-1000μm and 25% b.w. of 125-212μm diameter spheres (PMVF = plane mean void fraction); (b) Vertical profiles of the plane mean voidage in the model silo during batch discharge of a mono-sized bed of 125-212μm diameter spheres (PMVF = plane mean void fraction).

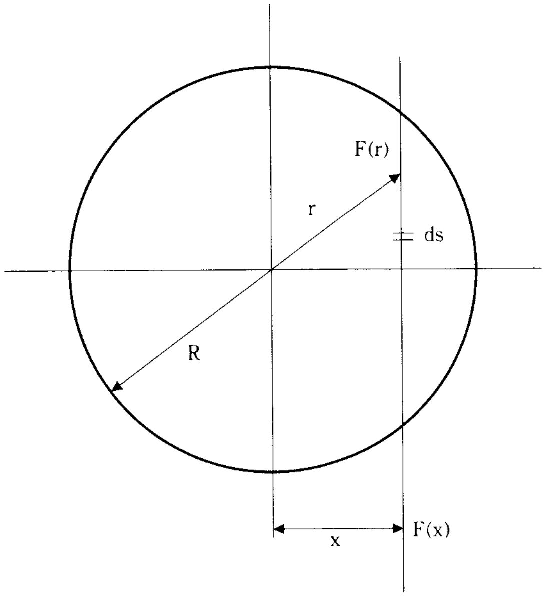

Fig. 6 Coordinate system used in the definition of the transformation coordinates.

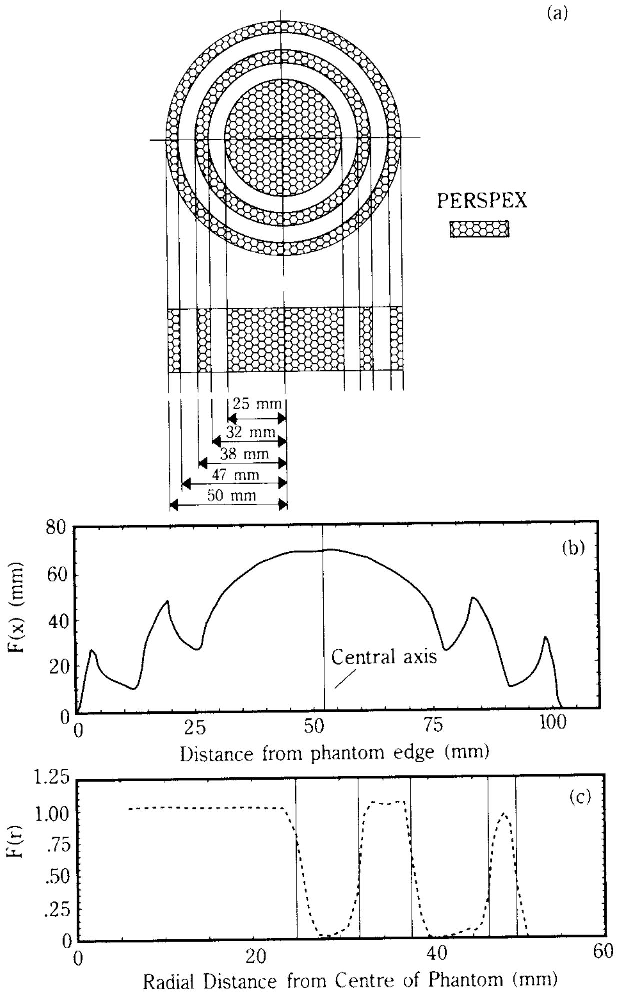

Fig. 7 (a) Schematic diagram of the axially symmetric Perspex phantom; (b) Experimental values of F(x) across the axially symmetric phantom of (a). (c) Calculated F(r) values for the axially symmetric phantom of (a)

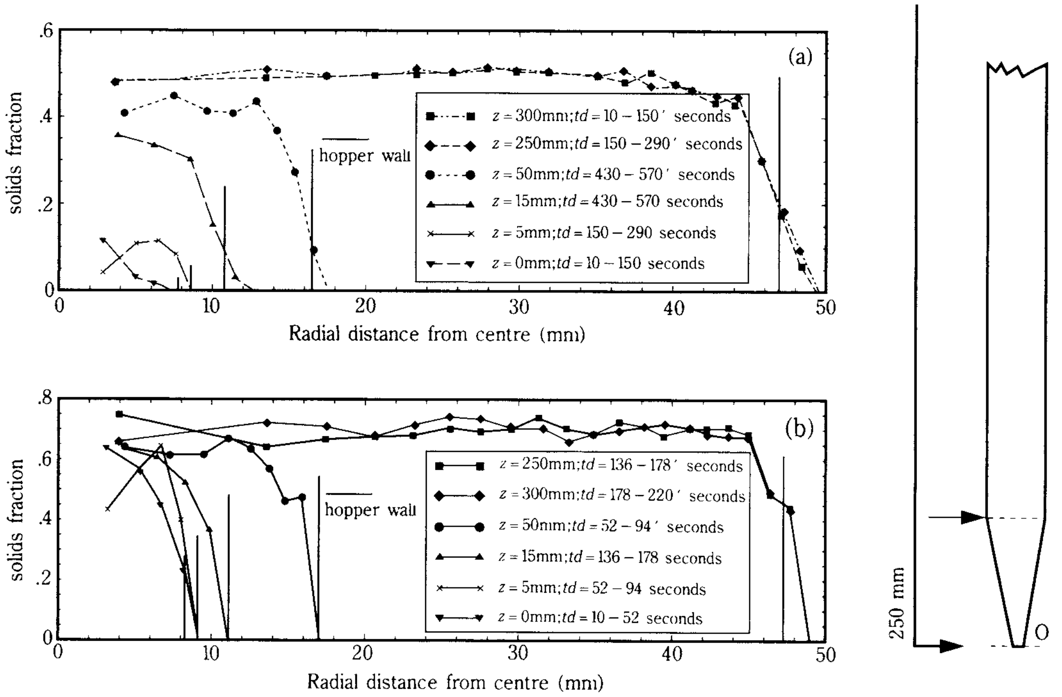

Fig. 8 Dynamic radial variation of the solids fraction across the hopper conical section at various heights from the orifice z of a mono bed of 179μm average diameter spherical particles; td: data acquisition time after flow initiation; Hd: top surface of material at td = 0. (b) Dynamic radial variation of the solids fraction across the hopper section at various heights from the orifice of a binary mixture bed of 80% b.w. of 915μm and 20% b.w. of 179μm average diameter spherical particles; Z = various; Hd = 1000mm, D_0 = 10mm.

3. Determination of radial voidage profiles in coarse granular solid/liquid mixtures

The encouraging results from the use of single profile photon absorptiometry in air-based systems provided us with the opportunity to investigate the interstitial voidage of the nearly buoyant, coarsely granular solid and liquid mixtures encountered often in food processing applications. Single profiles were taken across the hopper by scanning in 1mm steps over a time period of 5-10 sec. The experimental apparatus is shown in **Fig. 9**. A 2.17 m tall Perspex cylinder of 144 mm inside diameter is mounted on a conical hopper section of 30° half-angle and a 34 mm diameter orifice. The outlet of the conical section is connected to a stand pipe 34 mm in diameter used for retaining water control of the flow by preventing air from entering the system. The flow is controlled by a water column which is kept to a certain level by a main water supply connected at the top of the hopper. A small amount of potassium iodide (2 % by weight to avoid particle floating) is added to the water as a contrast agent to improve the precision in the measurements, since the attenuation coefficients of pure water and the nearly buoyant particles are very close to each other. A very small amount of a dye is added as well to monitor the penetration of the water column to the actual solid-liquid

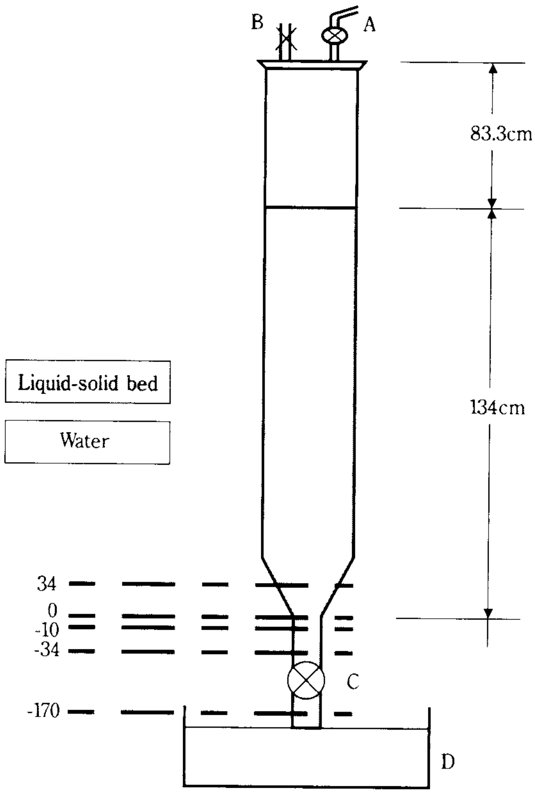

Fig. 9 Schematic diagram of the model hopper used in the solid/liquid absorptiometric measurements. (A) Main water supply (B) Ventilation (C) Stand pipe (D) Water tank. The inside diameter at the cylindrical section is 144mm and at the orifice and the stand pipe 34mm.

bed. Extruded plastic beads 3.76 mm in diameter are used to prepare a solid-liquid bed consisting of 60 % by weight solid and 40 % by weight water. The scanner is operated in the dynamic mode where the hopper travels vertically with different velocities and in various steps, and consecutive scans are taken at various heights. The scans were taken at heights of 34 mm above the orifice, at the orifice itself, and 10, 34, and 170 mm below the orifice as shown in **Fig. 9**. The solid fraction is calculated according to the equation

$$\eta = K\frac{F_s - F_c}{F_s - F_w} \qquad (3)$$

where Fs , Fc , Fware the measured raysums from the solution of water and potassium iodide only, the liquid-solid bed, and the hopper walls, respectively. The constant K is calculated from a calibration procedure applied to a packed bed prepared with a known solid fraction (0.71), and is found to have a value of about 5 for the particular plastic beads.

A whole tomographic image of the aforementioned solid-liquid mixture at the height of 170 mm below the orifice level is presented in **Fig. 10**. The boundaries of the individual particles can now be clearly distinguished since the particle size is larger than the collimator aperture, which in this case is 1 mm. The information obtained with the complete scan is actually three-dimensional, but the longer scan time necessary for a complete tomograph in contrast with the potential of the new single profile technique to provide fast information along any object diameter makes the latter more preferable. **Fig. 11** shows the line profiles obtained at the same height over two consecutive 2-minute scan periods under constant mass discharge rate condition. As seen in **Fig. 11**, the reproducibility of the scan data is accurate to within 1-2 %.

The linear profiles together with their radial transforms are presented in **Figs. 12-16**, and the spatial variation of solid fraction with height is presented in **Fig. 17**. These results give the best evidence for the symmetry of the profiles and the dilation of the bed during discharge. Another interesting feature is the smoothing effect that the radial transformation has on the linear profiles due to averaging within reasonably thick annular regions. It is also worth noting here that when the collimator aperture size is much smaller than the particle size being imaged, the fluctuation of the pixel-to-pixel value of the solids fraction becomes quite considerable. This is due to the large solid objects aligning themselves in front of a much narrower beam. To exclude this effect, it is necessary to choose a collimator aperture size larger than the particle size, which in this case requires at least a 5mm resolution.

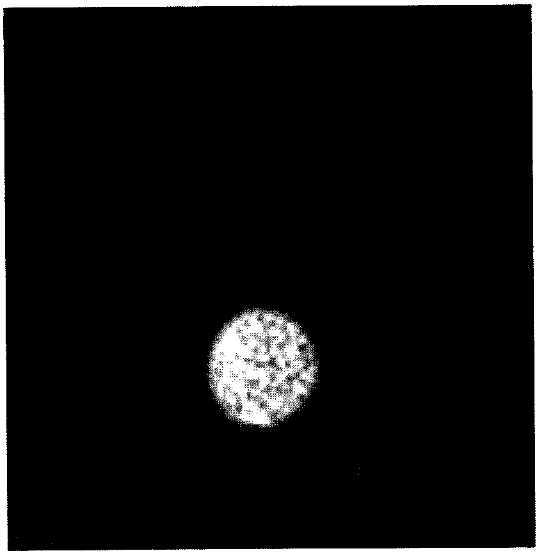

Fig. 10 Tomographic image of a solid/liquid static bed of 60% b.w. extruded plastic particles 3.76mm in diameter and 40% b.w. solution of water and potassium iodide at 170mm below the orifice.

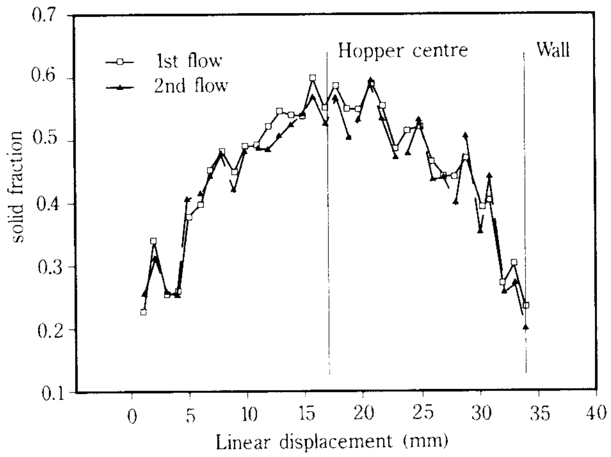

Fig. 11 Linear profiles at 34mm below the orifice of a bed of 60% b.w. extruded plastic particles 3.76mm in diameter and 40% b.w. solution of water and potassium iodide over two consecutive 2-minute periods under constant mass discharge rate condition.

As seen in **Fig. 17**, the variation of solid fraction with height appears to obey a similar pattern with both the linear and the radial data. However, it is

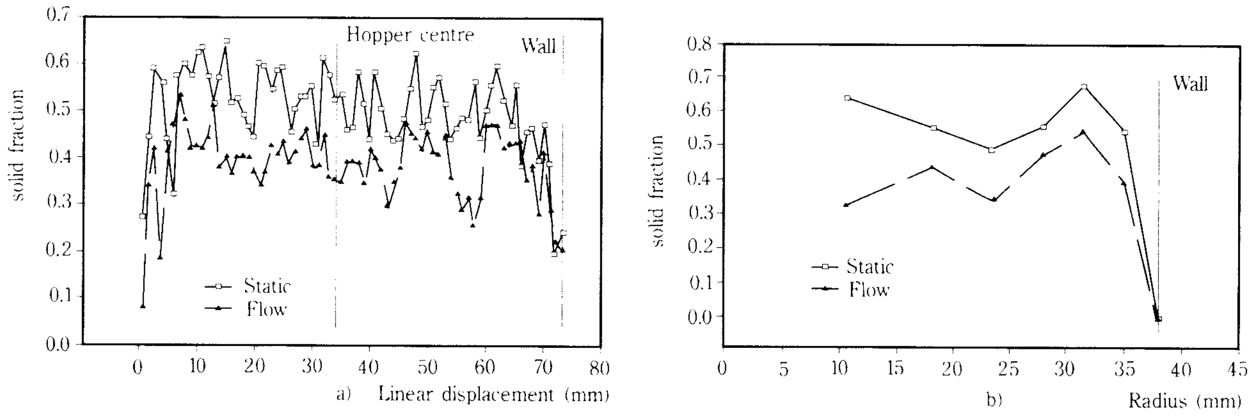

Fig. 12 (a) Linear profiles at 34mm above the orifice of a bed of 60% b.w. extruded plastic particles 3.76mm in diameter and 40% b.w. solution of water and potassium iodide in static condition and under constant mass discharge lasting 4.2 min. (b) Radially transformed profiles from (a).

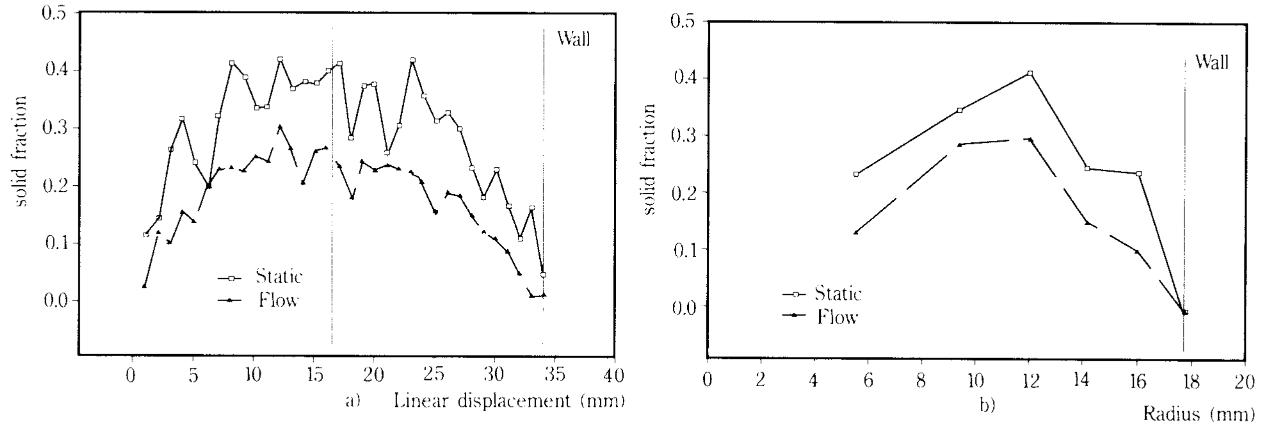

Fig. 13 (a) Linear profiles at the orifice of a bed of 60% b.w. extruded plastic particles 3.76mm in diameter and 40% b.w. solution of water and ptassium iodide in static condition and under constant mass discharge lasting 4.2 min. (b) Radially transformed profiles from (a).

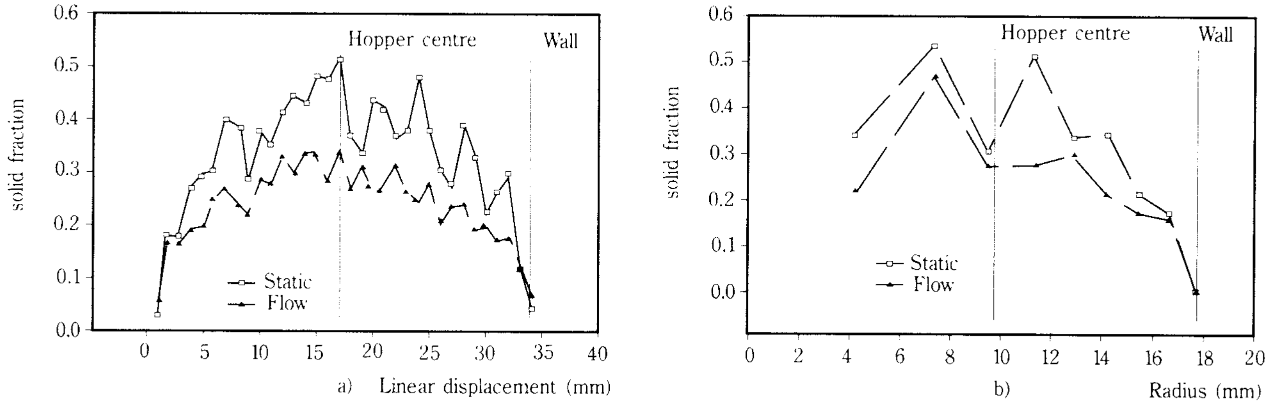

Fig. 14 (1) Linear profiles at 10mm below the orifice of a bed of b.w. extruded plastic particles 3.76mm in diameter and 40% b.w. solution of water and potassium iodide in static condition and under constant mass discharge lasting 2.1 min. (b) Radially transformed profiles from (a).

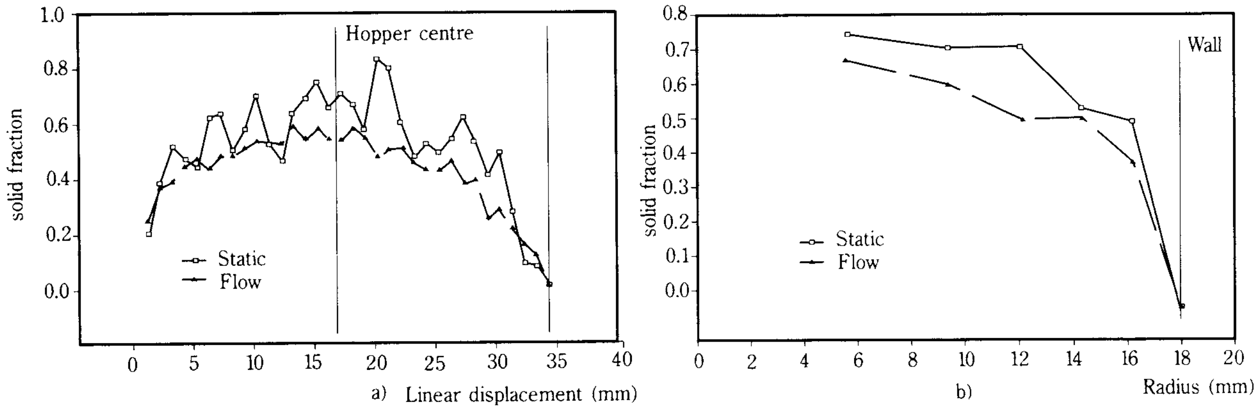

Fig. 15 (a) Linear profiles at 34mm below the orifice of a bed of 60% b.w. extruded plastic particles 3.76mm in diameter and 40% b.w. solution of water and potassium iodide in static condition and under constant mass discharge lasting 2.1 min. (b) Radially transformed profiles from (a).

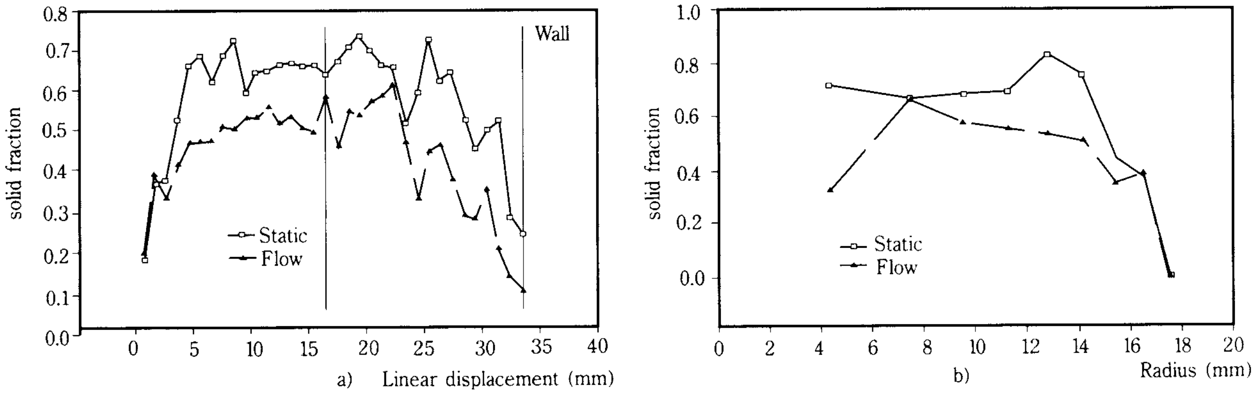

Fig. 16 (a) Linear profiles at 170mm below the orifice of a bed of 60% b.w. extruded plastic particles 3.76mm in diameter and 40% b.w. solution of water and potassium iodide in static condition and under constant mass discharge lasting 2.1 min. (b) Radially transformed profiles from (a).

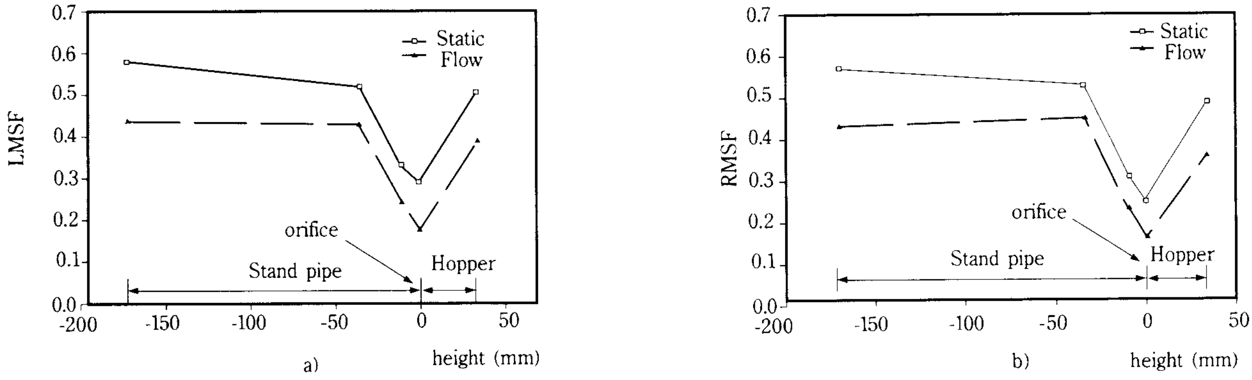

Fig. 17 (a) Vertical profiles of the linear mean solid fraction (LMSF) in static condition and under constatnt mass discharge of a bed of 60% b.w. extruded plastic particles 3.76mm in diameter and 40% b.w. solution of water and potassium iodide (b) Vertical profiles of the radial mean solid fraction (RMSF) in static condition and under constant mass discharge of a bed of 60% b.w. extruded plastic particles 3.76mm in diameter and 40% b.w. solution of water and potassium iodide.

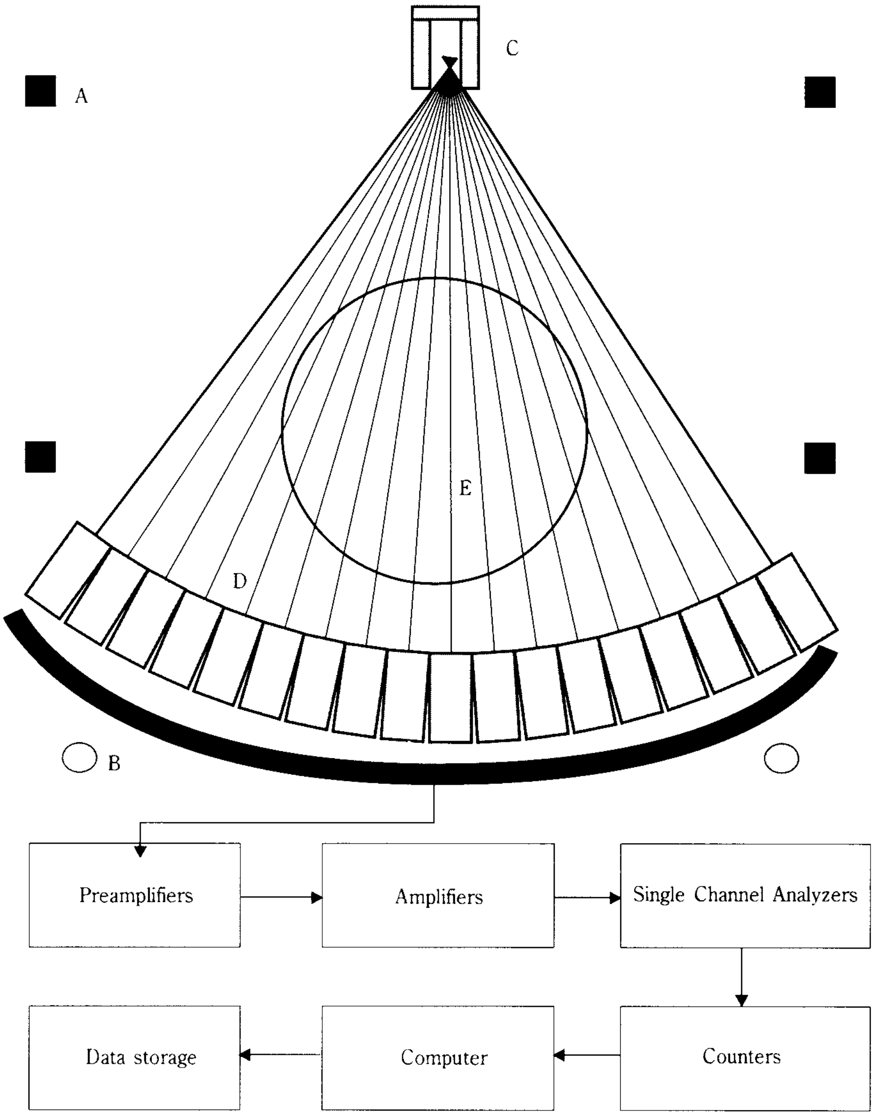

Fig. 18 Schematic diagram of the novel fan beam scanner. (A) Stepper motor for scanner head rotation (B) Stepper motor for detector array rotation only (C) Collimated source ^{153}Gd of 1.0 Ci (37GBq) activity (D) Collimated CsI scintillation detectors (E) Object.

worthwhile noting here that particles are moving faster than the surrounding liquid which results in noticeable voidage and porepressure gradient across the orifice. Further work is currently underway to quantify the sudden changes in voidage immediately above and below the orifice plane more accurately, in order to relate these voidage gradients to the measured pore-pressure gradients across the hopper orifice.

4. A novel fan beam scanner for simultaneous measurement of voidage and particle velocities

The new tomographic scanner is to be used as an inspection tool to simultaneously characterize the velocity field and voidage structure in 3-D granular flows with competitive spatial and temporal resolutions.

The new scanner presented in **Fig. 18** employs eighteen collimated CsI detectors arranged in a fan geometry facing a single source of 153Gd of 1Ci (37GBq) activity. The collimation consists of tungsten alloy blocks attached one to the other with a collimator aperture width of 2mm and 5mm in length, which permits good statistics and at the same time a spatial resolution that can be better than 1mm. The scanner moves over 180° completing 110 projections where each detector completes an eight-step move in every projection, thus infilling the empty space between the detectors according to the Nyquist criterion for sampling. Therefore, 110 projections with 144 raysums per projection contribute to the reconstruction of an array (144 × 144) of attenuation coefficient values. The convolution backprojection algorithm is used for the reconstruction after the fan beam data set has been transformed to the equivalent parallel one using a simple geometric transformation.

A range of object diameters (5-20 mm) can be fitted into the fan beam at various distances from the source, allowing scanning at various parts of an object such as the conical and the cylindrical section of a hopper. The spatial resolution of the new scanner can reach values of less than 1mm, whereby the timing resolution can be 4-5 times less than that of the parallel beam scanner used until now in granular flow experiments (i.e. best performance: less than 1min). The timing resolution can be improved by applying incomplete projection tomography where the scanning is focused either at a certain region of the vessel cross-section (Region of Interest Tomography) (Gentle and Spyrou (1990)[4] by incomplete linear sampling, or at a minimum number of symmetric positions around the object (Limited Angle of View Tomography) (Nalcioglou et al. (1983)[14] Specially developed algorithms will reconstruct the image by either interpolating or extrapolating the missing data. It is hoped that once this novel software is in place, it will be possible to obtain complete tomographic scans in a few seconds.

To track individual particles within the flow field, scanning is performed at two energy levels, allowing the concentrations of two different components together with the voidage distribution (third phase) to be determined simultaneously in a single experiment. Consecutive cross-sectional scans taken at different times along the vessel containing the tracer particles can be used to create a volume reconstruction of the system, which will in turn allow a three-dimensional determination of the velocity field as can be seen in **Fig. 19**.

In radiation tomography, the attenuation coefficient depends on the energy, the atomic number of a material with elemental constitution, and on the electron density at a particular position. Therefore, for a system with two components of different atomic numbers, the determination of their respective solid concentration is performed by using two photon beams with different energy peaks well separated from each other. If a third phase is present in the system, the determination of the solid concentration becomes difficult unless the third phase distribution is constant throughout the system. But this is not true for three-phase granular systems in the flow regime where the concentration varies randomly in any position. Therefore, a third equation expressing an a priori information about the object becomes necessary. Unlike the medical applications (Goodwin (1987)[5], the granular flow experiments are run under constant total volume conditions which provide the third necessary equation thus resulting in

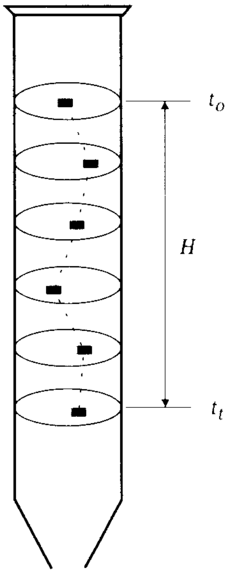

Fig. 19 Tracer monitoring and determination of 3-D velocity field; t_0 = time of initial particle position; t_t = time of final particle position; H = traveled distance

$$\begin{aligned}\mu^{low} &= c_A\mu_A^{low} + c_B\mu_B^{low} + c_C\mu_C^{low}\\ \mu^{high} &= c_A\mu_A^{high} + c_B\mu_B^{high} + c_C\mu_C^{high}\\ c_A + c_B + c_C &= 1\end{aligned} \tag{4}$$

where c_A, c_B, c_C are the volume fractions of each component having attenuation coefficients of μ_A, μ_B, μ_C, respectively, and μ_{low}, μ_{high} are the reconstructed mean attenuation coefficients for the two energies at a particular pixel where all three phases are present.

The selection of the materials to be used for the dual photon measurements of a two-phase solid mixture in air or liquid is based on the minimum detectable fraction (MDF) (Kouris et al. (1982)[11] of each solid component when it is embedded in a matrix consisting of the other solid component and the air or liquid. As shown in **Fig. 20**, for a water-based system, a difference of at least 10% of the attenuation coefficients between the two solid components is the

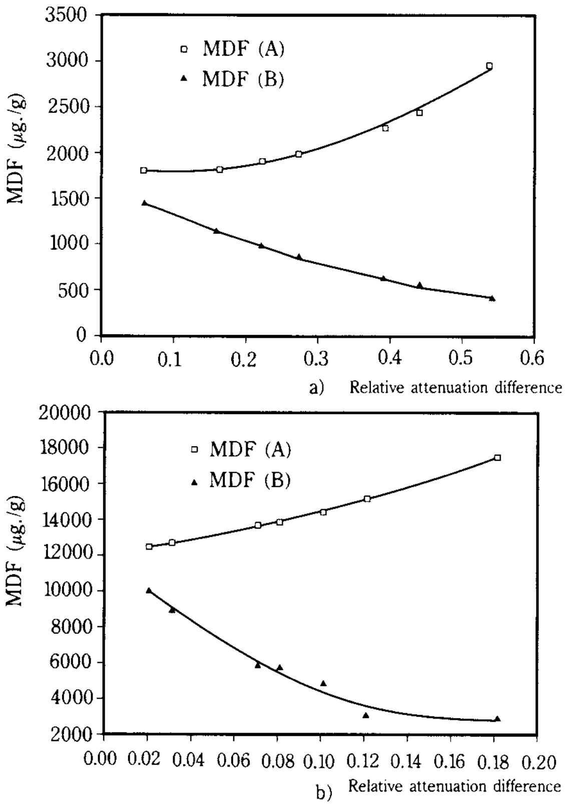

Fig. 20 Minimum detectable fraction of two solid species A and B embedded in water with respect to their attenuation coefficient relative difference. (a) At the energy level of 44keV (b) At the energy level of 100keV.

optimum threshold for the selection of the materials to be used in flow experiments, as in this region, the limits of detection for both components appear to have reasonable separation for attenuation changes of the order of 0.1 % (e.g. glass Pyrex with either silicon or polyvinyl chloride embedded in water will meet this criterion). It is expected that experiments will also be possible using agricultural and food materials as well as industrial ceramic and plastic powders.

5. Conclusions

A tomographic and an absorptiometric technique are demonstrated here as two powerful non-invasive tools to investigate the interstitial voidage in axially-symmetric particulate flows both in air and in liquids. The application of these methods to granular flow experiments, and especially to the solid-liquid systems, is believed to be the first of its kind in the particle technology field. Since both the spatial and the temporal resolutions reach a high level of compensation, providing highly reproducible dynamic data, very useful results related to the spatial and temporal variation of the interstitial voidage structure for flowing density powder are achieved. The particle tracking technique based on the dual photon transmission principle should soon allow us to couple these dynamic voidage maps with solids velocity fields, thus opening the way for new theoretical developments in the study of granular flows.

Nomenclature

c_A, c_B, c_C	Volume fractions of a three-phase mixture	
D_o	Orifice diameter	
F(r)	Radial density function	
$F(x)$	Line integral function	
F_s	Measured raysum from water-potassium iodide solution	
F_c	Measured raysum from solid-liquid bed	
F_w	Measured raysum from hopper walls	
K	Constant	
R	Object radius	[m]
z	Height above the outlet	[m]
Greek letters		
$\varepsilon(x,y)$	Void fraction	
$\eta(x,y)$	Solid fraction	
μ_{air}, μ_{solid}	Linear attenuation coefficients of a pixel filled with air or solid only	[m^{-1}]
$\mu(x,y)$	Mean linear attenuation coefficient of a mixture	[m^{-1}]
μ_{high}, μ_{low}	Linear attenuation coefficients at two different energy levels	[m^{-1}]
μ_A, μ_B, μ_C	Linear attenuation coefficients of three components of a mixture	[m^{-1}]

References

1) Arteaga P., Tüzün U.: Flow of binary mixtures of equal-density granules in hoppers – size segregation, flowing density and discharge rates Chem. Eng.Sci., 45, 205 (1990)

2) Bemrose C.R., Fowles P., Hawkesworth M.R., O'Dwyer M.A.: Application of positron emission tomography to particulate flow. Measurement in chemical engineering processes Nucl. Instr. Meth. Phys. Res., A273,874 (1988)

3) Beynon T.D., Hawkesworth M.R., McNeil P.A., Parker D.J., Bridgwater J, Broadbent C.J., Fowles P.: Positron-based studies of powder mixing Powders & Grains 93, Thornton (Ed.), Balkema, Rotterdam, 377 (1993)

4) Gentle D.J., Spyrou N.M.: Region of interest tomography in industrial applications Nucl. Instr. Meth. Phys. Res.,A299, 534 (1990)

5) Goodwin P.N.: Methodologies for the measurement of bone density and their precision and

accuracy Sem. Nucl. Med.,17(4), 293 (1987)

6) Halow J.S., Nicoletti P.: Observations of fluidized bed coalescence using capacitance imaging Powder Tech., 69, 255 (1992)

7) Halow J.S., Fasching G.E., Nicoletti P., Spenik J.L.: Observations of a fluidized bed using capacitance imaging Chem. Eng. Sci.,48,643 (1993)

8) Hawkesworth M.R., O'Dwyer M.A., Walketry J., Fowles P., Heritage J., Stewart P.A.E., Witcomb R.C., Bateman J.E., Connolly J.F., Stephenson R.: A positron camera for industrial application Meas. Sci. Tech.,4, 1394 (1993)

9) Hosseini-Ashrafi M.E., Tüzün U.: A tomographic study of voidage profiles in axially symmetric granular flows. Chem. Eng. Sci., 48,53 (1993)

10) Hosseini-Ashrafi M.E., Tüzün U.: Quantification of flowing bed porosity near the outlet of an axially symmetric hopper using signle photon absorptiometry Meas. Sci. Tech., 4, 1394 (1993)

11) Kouris K., Spyrou N.M., Jackson D.F.: Imaging with ionizing radiations Surrey University Press, UK (1982)

12) MacCuaig N., Seville J.P.K., Gilboy W.B., Clift R.: Application of gamma-ray tomography to gas fluidized beds Appl. Opt., 24, 4083 (1985)

13) Nakagawa M., Altobelli S.A., Caprihan A., Fukushima E.: Non-invasive measurements of granular flows by magnetic resonance imaging Powders & Grains 93, Thornton (Ed.), Balkema, Rotterdam, 383 (1993)

14) Nalcioglou O., Cho Z.H., Lou R.Y.: Limited Field of View Reconstruction in Computerised Tomography IEEE Trans. Nucl. Sci., 26, 546 (1983)

15) Parker D.J., Broadbent C.J., Fowles P., Hawkesworth M.R., McNeil P.: Positron emission particle tracking – a technique for studying flow within engineering equipment Nucl. Instr. Meth. Phys. Res., A326,592 (1993)

16) Seville J.P.K., Morgan J.E.P., Clift R.: Tomographic determination of the voidage structure of gas fluidized beds in the jet region Fluidization V., Ostergaard K., Sorensen A., (Eds), Engineering Foundation, New York, 87 (1986)

17) Simons S.J.R., Seville J.P.K. Clift R., Gilboy W.B., Hosseini-Ashrafi M.E.: Application of Gamma-ray Tomography to gas fluidized and spouted beds Tomographic Techniques for Process Design and Operation Beck M.S., Campogrande E., Morris M., Williams R.A., Waterfall R.C. (Eds) Computational Mechanics Publications, Southampton, 227 (1993)

Author's short biography

Mr. Michail S. Nikitidis

Mr. Michail S. Nikitidis received his first degree in Physics from the Aristotle University of Thessaloniki, Greece and joined the Department of Physics of the University of Surrey, UK. where he completed a Master's degree in Medical Physics. Currently, he is pursuing a Ph.D study working as a research assistant in the Department of Chemical and Process Engineering of the University of Surrey, developing novel tomographic techniques for the investigation of voidage structure and velocity field in multiphase granular systems.

Dr. Uğur Tüzün

Dr. Uğur Tüzün has a B. Sc. from leeds University and his Ph. D. from Cambridge University. He is an active member of the particle technology research community in UK with several current research contracts funded by EPSRC, BBSRC and the industry. His current work includes i) mathematical modeling of particle-particle and particle-fluid interactions in packed bed flows of polydisperse particle mixtures, ii) characterization of single particle and assembly frictional properties of granular materials and iii) discrete particle computer simulations of granular flows in 2-D and 3-D geometries. Dr. Tüzün has over 50 journal publications and chapters in books edited in UK, USA, Germany and Japan.

Senior Lecturer Department of Chemical and Process Engineering University of Surrey Guildford, Surrey GU2 5XH, U.K.
Tel: +44 0483 300800 ext 2188 Fax: +44 0483 259510

Dr. Nicholas M. Spyrou

Dr. Nicholas M. Spyrou obtained his first degree in Mechanical Engineering with Nuclear Engineering and joined Imperial College, University of London to do postgraduate work in reactor physics leading to a Master's degree. He was sebsequently employed there as a research assistant for doctoral research in neutron cross-section measurements. Since 1969 he has been at the University of Surrey using radiation physics in biomedical, environmental and industrial applications. His main fields of research are in imaging and in trace element analysis using nuclear probes, for which he was awarded an honorary doctor of medicine degree in 1987. He has been Chairman of Medical Physics since 1978 and is Reader in the Department of Physics. He has supervised successfully over 40 PhD students and is the author of more than 150 papers.

Reader Department of Physics University of Surrey Guildford, Surrey GU2 5XH, U.K.
Tel: +44 0483 259324 Fax: +44 0483 259501

Cyclone Separators for Fine Particles and Difficult Operating Conditions†

– Dedicated to Professor Gengi Jimbo on the occasion of his retirement –

M. Bohnet
Institute of Chemical Engineering
*Technical University of Braunschweig**

Abstract

The separation of fine particles from gases with particle sizes of about 1 μm is still a difficult problem, especially at high solids loadings of the gas stream and high gas temperatures. Practical experiences show that the separation efficiency really obtained with hot gas cleaning is generally less than calculated.

Based on new experiments and a better calculation procedure, it is also possible to use cyclone separators for these separation problems.

For a successful solution, it is necessary to increase the knowledge about the gas/solids flow and to pay attention to the boundary layer flow within the cyclone, but also to think about new multi-stage separation processes.

1. Introduction

The main design parameters of cyclones, namely pressure drop and separation efficiency, can be calculated with a number of models which have been developed on the basis of experimental data received under environmental conditions, i.e. at ambient pressures and temperatures. It has been shown by T. Lorenz [1] that based on these models, the separation efficiency of hot gas cyclones is always predicted as too good. One reason for this result is the dramatic change of the gas flow due to the increasing gas viscosity, which goes hand in hand with changes of the boundary layer flow.

Another approach to increase the separation efficiency is the use of a special multi-stage process. Similar to the separation of a solid/liquid suspension in a hydrocyclone, a certain amount of gas is removed along with the separated solids through the cyclone underflow. K. Iinoya et al. [2] used such a cyclone system as a classifier for small particles and showed that a shift to the separation of smaller particles is possible.

For gas cleaning, especially hot gas cleaning, two cases have to be considered:

- Gas cleaning at high solids loadings
  (fluidized bed combustion)
- Gas cleaning at low solids loadings
  (gas turbine process)

In the first case, it is necessary to also remove the very fine particles, whereas in the second case, the turbine manufacturers limit the acceptable solids loading to very low values, and the tolerated maximum particle size is also rather small.

2. Separation at high solids loadings

It is well known that the separated particle sizes, mostly characterized by the cut-size diameter d_p^* strongly depend on the tangential gas velocity u_i. Following W. Barth's proposal [3], the largest tangential gas velocity on the radius of the gas outlet pipe can be calculated for very small solids loadings as follows:

$$\frac{u_{io}}{w_i} = \frac{1}{\frac{F_e}{F_i}\,\frac{\alpha}{r_\alpha/r_i} + \lambda\,\frac{h}{r_i}} \tag{1}$$

h describes the equivalent friction height of the cyclone which is calculated from:

$$h = \frac{F}{2\pi(r_a \cdot r_i)^{1/2}} \tag{2}$$

F is the total cyclone surface, at which friction losses take place. (Cylinder and cone, cover plate and outer outlet duct surface.)

---

* Langer Kamp 7, D-38106 Braunschweig, Germany

† Received May 24th, 1994
This paper was presented orally by M. Bohnet in spring 1993 in Nagoya at the retirement celebration of Prof. Jimbo.

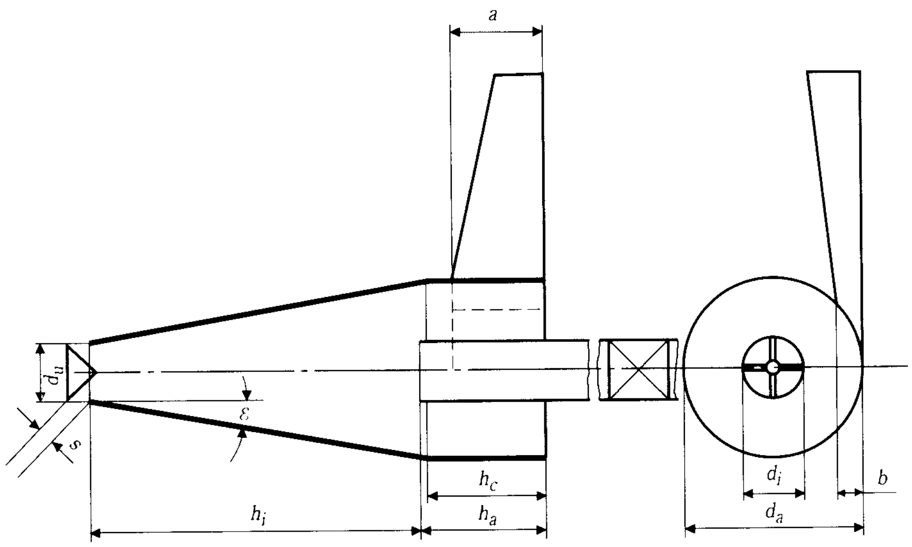

Fig. 1 Cyclone separator

With:

$$r_\alpha = r_a - \frac{b}{2} \tag{3}$$

and

$$\alpha = \left(1 - 0.54 - \frac{0.153}{F_e/F_i}\right)\left(\frac{b}{r_a}\right)^{1/3} \tag{4}$$

for a slit gas entrance [4], the tangential velocity can be calculated. The cyclone dimensions are given in **Fig. 1**.

E. Muschelknautz [5] has measured the decrease of the tangential velocity as a function of the solids loading. As can be seen from **Fig. 2**, the related tangential velocity u_i/u_{io} decreases remarkably and for a solids loading of about $\mu = 2$, the tangential velocity is only 50 % of the value obtained with a solids-free gas stream.

Calculating the cut-size diameter [6]

$$d_p^* = \left[\frac{18\eta\ w_{ri}\ r_i}{u_i^2\ (\varrho_p - \varrho)}\right]^{1/2} \tag{5}$$

with

$$w_{ri} = \frac{\dot{V}}{2\pi r_i h_i} \tag{6}$$

the influence of the real tangential velocity becomes obvious.

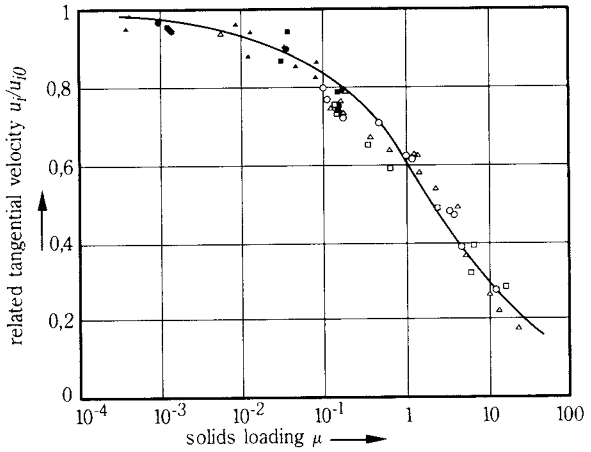

Fig. 2 Decrease of tangential velocity due to the solids loading

For higher solids loadings, it has to be considered that similar to pneumatic conveying, the gas stream entering the cyclone can only carry a certain amount of solids. The solid material exceeding this maximum solids loading is separated immediately in the entrance region, and this is important, almost without any fractionation of the solids. This means that also very fine particles are thrown directly to the cyclone wall within the bulk. The maximum solids loading depends on:

$$\mu_{max} \sim \left(\frac{u_i}{w_i}\right)^{3/2} \cdot \left(\frac{w_s^*}{w_{s50}}\right) \tag{7}$$

with w_s^* as the settling velocity of particles with the cut-size diameter d_p^* of the cyclone, and w_{s50}

as the settling velocity of particles corresponding to the 50 % value of the particle size distribution entering the cyclone.

Details on the calculation of the maximum solids loading have been published by E. Muschelknautz [7], M. Trefz [8] and W. Rentschler [9].

3. Multi-stage separation process

To increase the separation efficiency of cyclones, a technique used with hydrocyclones may be advantageous. First experiments in this field have been carried out by K. Iinoya et al. [2]. Their experimental set-up is shown in **Fig. 3**. Their intention was to increase the performance of a cyclone to be used as classifier. The solid particles leaving the cyclone through the underflow are separated from the gas by means of a filter. The dimensions of the cyclones used are given in **Fig. 4**. As can be seen from **Fig. 5**, the grade efficiency curve depends strongly on the amount of the blow-down gas stream. The amount is given as a percentage of the entrance flow rate. With increasing blow-down gas stream, the cut-size diameter is shifted to smaller particle sizes, and the grade efficiency curves become steeper.

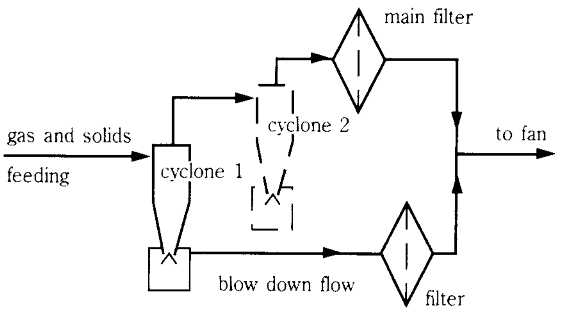

Fig. 3 Experimental set-up used by K. Iinoya et al. [2]

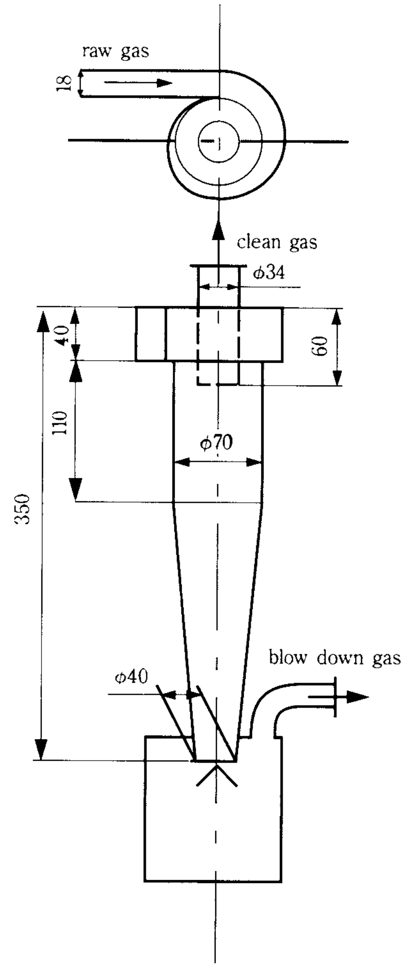

Fig. 4 Cyclone used as a classifier [2]

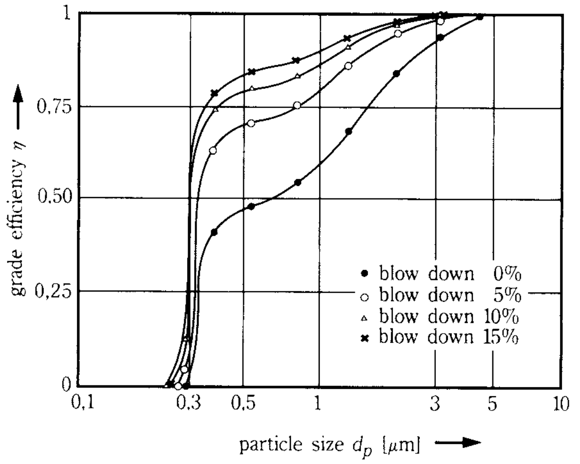

Fig. 5 Grade efficiency curves obtained for different blow-down gas streams [2]. Inlet gas velocity 25 m/s

To answer the question of whether a two-stage separation process with two cyclones is able to increase the total efficiency, an experimental set-up as shown in **Fig. 6** was used in Braunschweig. The solids-laden blow-down gas stream of the first cyclone enters a second cyclone. The measured and calculated grade efficiency curves of both cyclones are shown in **Figs. 7** and **8**. The raw gas particle size distribution used for the experiments is given in **Fig. 9**. **Table 1** shows a summary of the results, obtained with the data given in **Figs. 7**, **8** and **9**. Using only one cyclone, the total separation efficiency is 96.74%. Feeding the separated solids of the first cyclone with a blow-down gas stream of 10% of the entrance gas stream to the second cyclone leads to a separation efficiency of 99.81% for the second cyclone. Combining the two clean gas streams results in a total separation efficiency of the two-stage process of 98.12%. That means an increase of the total

Table 1 Comparison of a single and a two-stage seperation process

			single-stage	two-stage separation process		
			cyclone 1	cyclone 1	cyclone 2	cyclone 1 and 2
blow-down gas stream	$\dot{V}_{bd}/\dot{V}_e$	—	0	0,1	0	
entrance gas flow rate	$\dot{V}_e$	m^3/h	180	180	18	
entrance gas velocity	w_e	m/s	13,6	13,6	15,9	
raw gas solids content	$\dot{M}_{Re}$	kg/h	$18 \cdot 10^{-3}$	$18 \cdot 10^{-3}$	$17{,}66 \cdot 10^{-3}$	
raw gas solids loading	μ_e	—	$8{,}4 \cdot 10^{-5}$	$8{,}4 \cdot 10^{-5}$	$8{,}16 \cdot 10^{-4}$	
clean gas solids content	$\dot{M}_C$	kg/h	$5{,}86 \cdot 10^{-4}$	$3{,}04 \cdot 10^{-4}$	$3{,}29 \cdot 10^{-5}$	$3{,}37 \cdot 10^{-4}$
total separation efficiency	η	—	0,9674		0,9981	0,9812

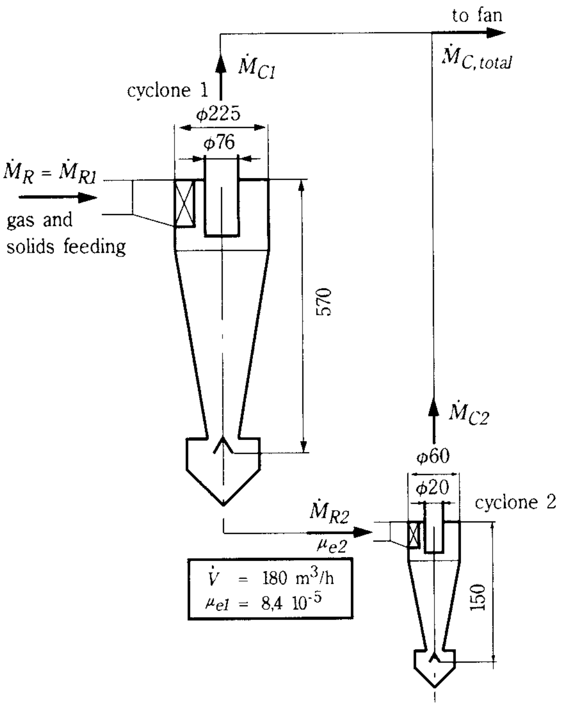

Fig. 6 Two-stage separation process

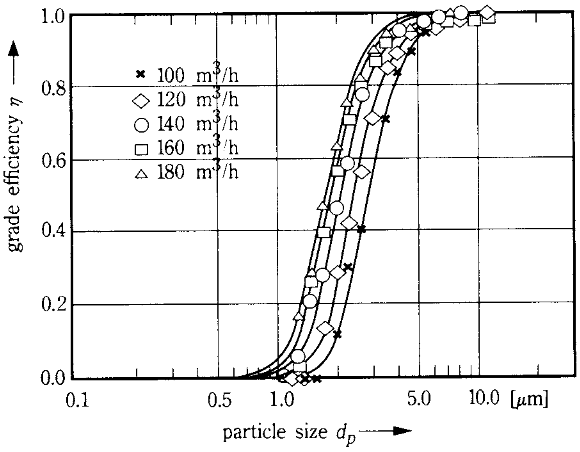

Fig. 7 Measured and calculated grade efficiency curves of cyclone 1 for different gas streams

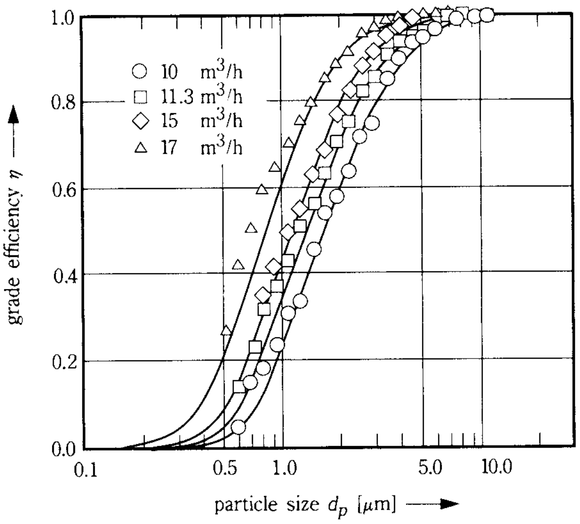

Fig. 8 Measured and calculated grade efficiency curves of cyclone 2 for different gas streams

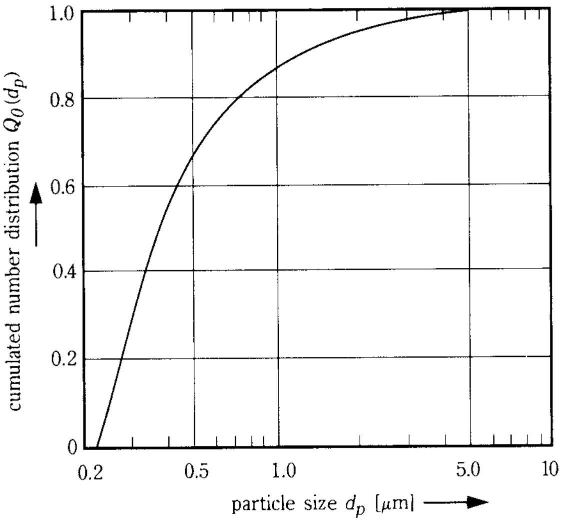

Fig. 9 Particle size distribution of the solids used in the experiments

separation efficiency of 1.38%. But more obvious is the fact that the solids content in the clean gas for the two-stage process is reduced to 57% compared with the single-stage process.

4. Hot gas cleaning

It is well known from experience that cyclone separators designed on the basis of data and models obtained under ambient conditions perform much worse than calculated. To receive more reliable data, the experimental set-up shown in **Fig. 10** was installed at the Institute of Chemical Engineering in Braunschweig. Measurements were carried out up to gas temperatures of 1173 K. The particle size distribution and the particle concentration in the inlet and outlet gas streams of the cyclone are measured with light scattering aerosol counters. The measured quantities are scanned and transmitted to a PC. The dimensions of the used cyclone are given in **Fig. 11**.

The pressure drop of the cyclone was measured as the difference between the static pressures in the inlet and the outlet duct behind a straightener for reducing the torque flow of the gas. The experimental data obtained in the temperature range between 293 and 973 K are given in **Fig. 12** as pressure drop coefficients, which are calculated from:.

$$\Delta_p = \xi_i \frac{\varrho}{2} w_i^2 \tag{8}$$

For the precalculation of the pressure drop coefficient, it is useful to separate it into two parts:

$$\xi_i = \xi_{ie} + \xi_{ii} \tag{9}$$

ξ_{ie} describes the pressure drop in the entrance region and the friction within the cyclone

ξ_{ii} describes the pressure drop in the outlet duct.

It is:

$$\xi_{ie} = \frac{r_i}{r_a}\left[\frac{1}{\left(1 - \frac{u_i}{w_i}\frac{h}{r_i}\lambda\right)^2} - 1\right]\left(\frac{u_i}{w_i}\right)^2 \tag{10}$$

$$\xi_{ii} = 0.8\left[3\left(\frac{u_i}{w_i}\right)^{4/3} + \left(\frac{u_i}{w_i}\right)^2 + 2\right] \tag{11}$$

The wall friction factor λ has been measured by T. Lorenz [1]:

$$\lambda = 0.0049 + \frac{0.87}{Re_z} \tag{12}$$

with

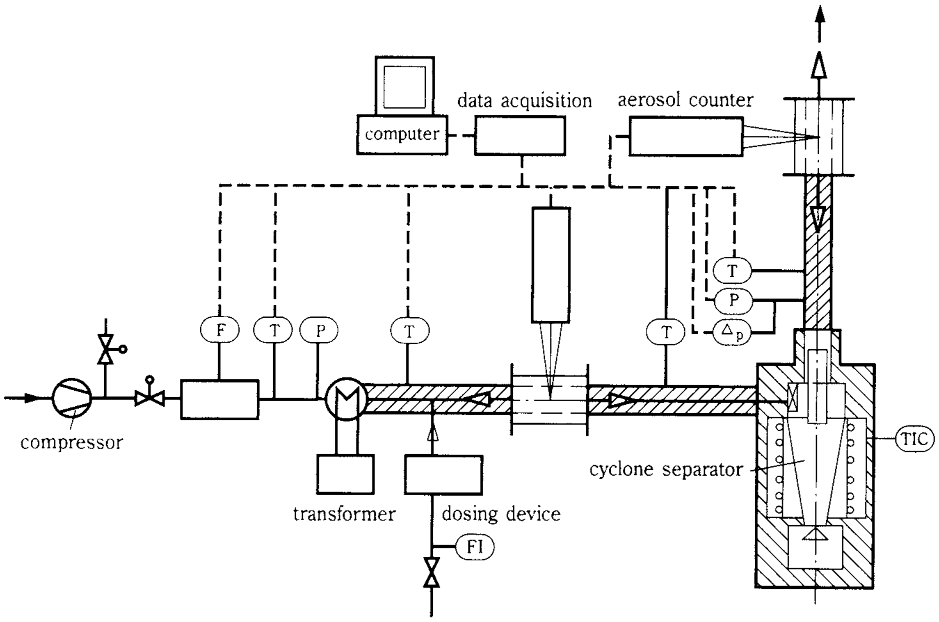

Fig. 10 Set-up for hot gas experiments

$$Re_z = \frac{w_i\, r_i\, \varrho}{\eta} \left[\frac{r_i/h}{r_a/r_i - 1} \right] \qquad (13)$$

The calculated pressure drop coefficient

$$\xi_i = \frac{\Delta p}{\frac{\varrho}{2}\, w_i^2} \qquad (14)$$

is plotted against Reynolds number

$$Re = \frac{w_i\, d_i\, \varrho}{\eta} \qquad (15)$$

in **Fig. 12** and shows a strong influence of the Reynolds number. The calculated curve and the measured data are in sufficient agreement.

Experimental results for the grade efficiency of the cyclone are given in **Fig. 13**. Using the proposal of H. Mothes et al. [10] for the calculation of the grade efficiency developed for ambient conditions, it can be seen that the calculated curves show a much better separation than actually obtained. With higher gas temperatures, the shape of the curves also changes: they become steeper. This is in agreement with theoretical considerations, but is not described correctly by the model of H. Mothes.

To improve the calculation procedure, the boundary layer flow at the cover plate and at the outer side of the outlet pipe, the reentrainment of already separated particles from the solids outlet region, and the influence of the turbulence all have to be considered. A very simplified illustration of the calculation is shown in **Fig. 14**. The cyclone is divided into 5 regions:

Region 1: Boundary layer flow at the cover plate and the outer side of the outlet pipe.
Region 2: Entrance
Region 3: Downstream flow
Region 4: Reentrainment
Region 5: Upstream flow

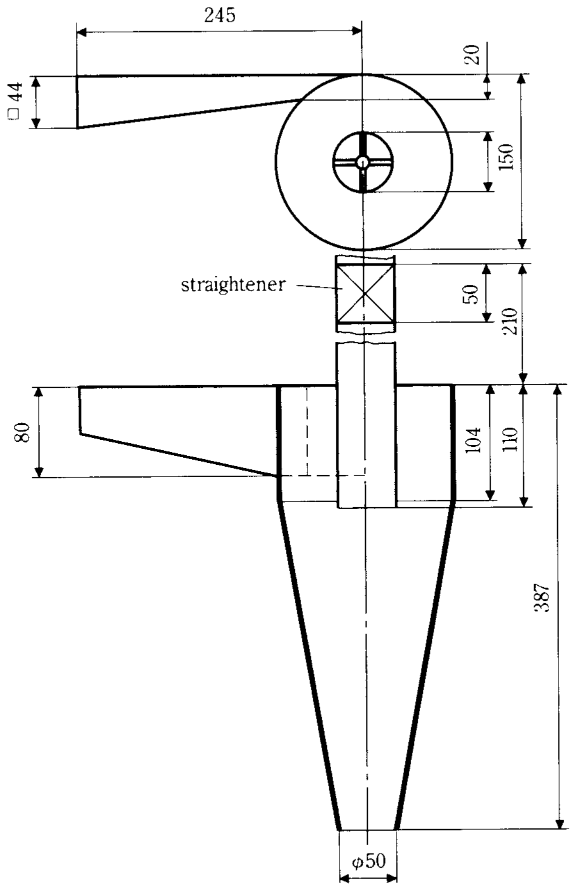

Fig. 11 Dimensions of the cyclone used for hot gas cleaning

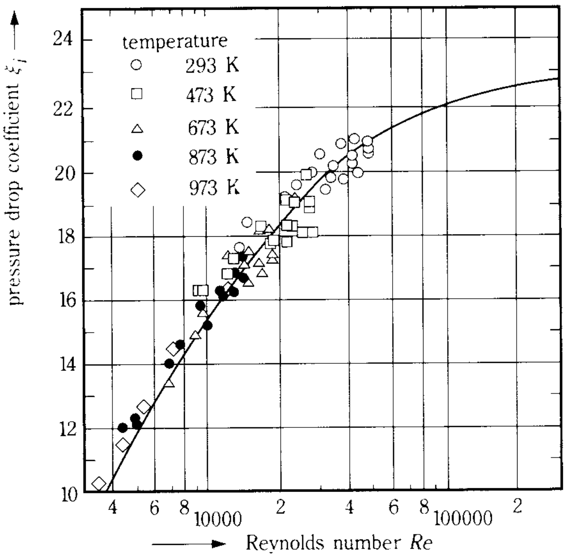

Fig. 12 Pressure drop coefficient dependent on Reynolds number

Depending on the axial coordinate z, the solids concentration changes due to the separation process. The mass balance of the solids is calculated in each area of the cyclone over the height of dz as illustrated for region 3. At the height z, a certain amount of particles with the same particle size enters the balance area. Some of the solids are thrown to the cyclone wall and are separated. Another part enters due to turbulence into region 5, but also particles from region 5 return to region 3. The difference between these particles leaves the balance area at $z + dz$. This calculation has to be repeated for all particle sizes and all cyclone heights. A particles

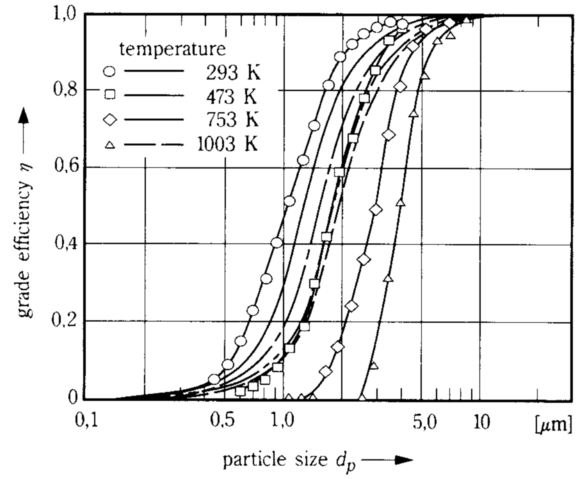

Fig. 13 Measured and calculated (Mothes) grade efficiency curves

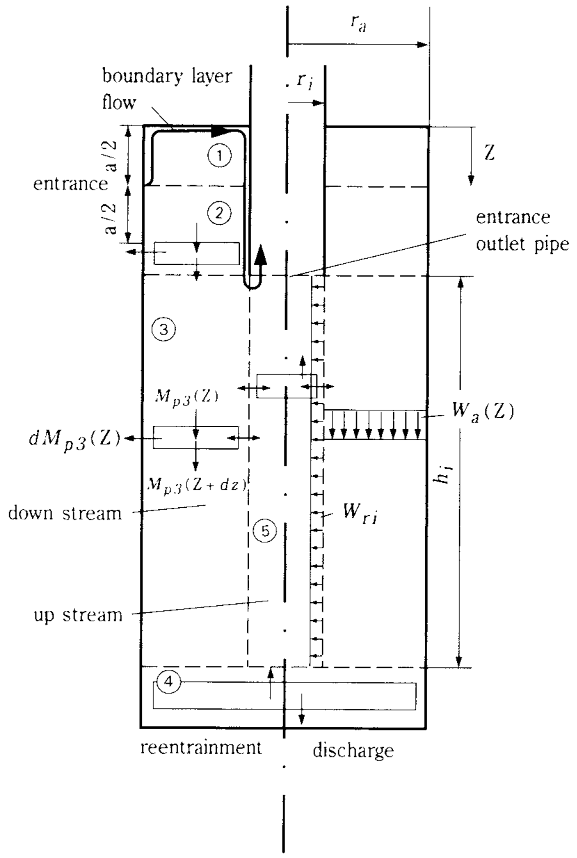

Fig. 14 Cyclone geometry for calculation of grade efficiency

which reach the entrance of the outlet pipe are not separated within the cyclone. Comparing the amount of solids of a certain particle size in the clean gas with the amount entering the cyclone gives one point of the grade efficiency curve.

The details of the calculation can be found in the Ph.-D.-thesis of T. Lorenz [11]. The new approach gives much better results. **Fig. 15** contains some of the results. The agreement between measured and calculated data is very good. For the two-stage separation process, a region 6 has to be incorporated into the model, in order to also capture the influence of the blow-down gas stream.

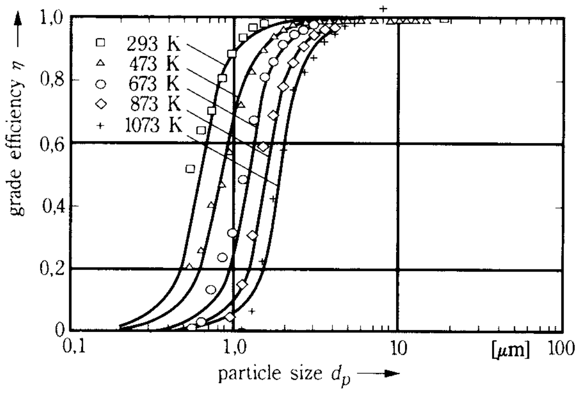

Fig. 15 Measured and calculated (Lorenz) grade efficiency curves

Nomenclature

a	[m]	entrance height
b	[m]	entrance width
d_p	[m]	particle diameter
d_p^*	[m]	cut-size diameter
d_{p50}	[m]	50% value of the particle size distribution
F	[m]	inner cyclone surface
$F_{e,i}$	[m^2]	inlet, outlet area $F_e = a\,b$, $F_i = \pi r_i^2$
h	[m]	cyclone friction height
h_i	[m]	cyclone height below the outlet pipe
Δ_p	[Pa]	pressure drop
r_i	[m]	outlet radius
r_a	[m]	cyclone radius
Re	[—]	Reynolds number
u_i	[m/s]	tangential velocity
w_i	[m/s]	axial outlet velocity
w_{ri}	[m/s]	radial velocity on outlet radius
w_s^*	[m/s]	settling velocity of particle with cut-size diameter
w_{s50}	[m/s]	settling velocity of particle with a diameter corresponding to the 50% value of the particle size distribution
$\dot{V}$	[m^3/s]	gas flow rate
λ	[—]	wall friction factor
η	[kg/m·s]	dynamic viscosity
η	[—]	grade efficiency

ϱ	[kg/m^3]	gas density
ϱ_p	[kg/m^3]	particle density
μ	[–]	solids loading
ξ	[–]	pressure drop coefficient

References

1) Lorenz, T.: Separation Efficiency and Pressure Drop of Cyclones at High Temperatures, Preprints 2. International Symposium on Gas Cleaning at High Temperatures, University of Surrey, Guildford, UK, 27.-29. September 1993.
2) Iinoya, K.; Fuyuki, T.; Yamada, Y.; Hisakuni, H.; Sue, E.: Dry Submicron Classification by a Small Blow Down Cyclone, Society Powder Technology Japan, 29, 1992, No. 5, pp. 351-355.
3) Barth, W.: Berechnung und Auslegung von Zyklonabscheidern, Brennst.-Wärme-Kraft 8, 1956, No. 4, pp. 1-9.
4) Spilger, R.; Brauer, H.: Computerberechnung von Zyklonen, VDI-Berichte 294, VDI-Verlag 1978, pp. 77-84.
5) Muschelknautz, E.: Untersuchungen an Zyklonen, Chemie-Ingenieur-Technik 39, 1967, No. 9/10, pp. 531-538.
6) Bohnet, M.: Cyclone Separation of Gas/Solids Mixtures, Ger. Chem. Eng. 6, 1983, No. 4, pp. 211-220.
7) Muschelknautz, E.: Auslegung von Zyklonabscheidern in der technischen Praxis, Staub-Reinh. Luft 30, 1970, No. 5, pp. 187-195.
8) Trefz, M.: Die verschiedenen Abscheidevorgänge im höher und hoch beladenen Gaszyklon unter besonderer Berücksichtigung der Sekundärströmung, VDI-Fortschrittsberichte, Reihe 3, No. 295, Düsseldorf, 1992.
9) Rentschler, W.: Abscheidung und Druckverlust des Gaszyklons in Abhängigkeit von der Staubbeladung, VDI-Fortschrittberichte, Reihe 3, No. 242, Düsseldorf, 1991.
10) Mothes, H.; Löffler, F.: Zur Berechnung der Partikelabscheidung in Zyklonen, Chem. Eng. Process. 18, 1984, pp. 323-331.
11) Lorenz, T.: Heißgasentstaubung mit Zyklonen, Dissertation, TU Braunschweig, 1994.

Author's short biography

Matthias Bohnet

Dr.-Ing. Matthias Bohnet: 1954/59 Academic education Technical University of Karlsruhe, 1964 Ph.-D. Thesis at Professor Walter Barth's Institute at Karlsruhe. 1964/73 BASF AG, Ludwigshafen and BASF Corporation, New York. 1973 full professor and director of the Institute of Chemical Engineering, Technical University of Braunschweig.

Pneumatic Conveying Characteristics of Fine and Granular Bulk Solids†

R. Pan, B. Mi and P.W. Wypych
Department of Mechanical Engineering
*University of Wollongong**

Abstract

Fine and granular products possess significantly different pneumatic conveying characteristics. Fine products usually have smooth conveying characteristic curves from dilute- to dense-phase. Between dilute- and dense-phase there is a pressure minimum curve. However, when granular products are conveyed between dilute- and dense-phase, significant fluctuations in pressure and vibration can occur along the pipeline. To obtain reliable operating conditions for the designed pneumatic conveying system, three semi-empirical correlations are developed in this paper for the calculation of the pressure minimum curve for fine powders and the boundaries between dilute-phase, unstable-zone and dense-phase flow for granular products in terms of particle properties and conveying conditions. Finally, a new procedure is presented for the prediction of total pipeline air pressure drop and the economic design of pneumatic conveying systems with the aim of reducing power consumption and particle damage.

1. Introduction

Over the past two decades, pneumatic conveying systems have been employed successfully to transport both fine and granular bulk solids. However, these two types of material display dramatically different pneumatic conveying characteristics.

Fine powders that fluidise readily and also have good air retentive properties (e.g. flyash, pulverised coal) usually can be transported smoothly and reliably from dilute- to dense-phase1). Between dilute- and dense-phase there is a pressure minimum curve. However, when granular products (e.g. plastic pellets, wheat) are conveyed between dilute- and dense-phase, significant fluctuations in pressure and vibration can occur along the pipeline2). This region is referred to as the unstable zone. These differences in conveying performance can affect significantly the operation of the pneumatic conveying system and should be given adequate consideration during the design stage.

Therefore, to ensure dilute- or dense-phase (depending on the application), it is very important to determine:

- the pressure minimum curve (PMC) for fine powders,
- the boundaries between dilute-phase, unstable zone and dense-phase for granular products.

In this paper, three semi-empirical correlations are presented to calculate the pressure minimum curve for fine powders and the boundaries between dilute-phase, unstable-zone and dense-phase flow for granular products in terms of particle properties and conveying conditions. Also, a new procedure is presented for the prediction of total pipeline air pressure drop and the economic design of pneumatic conveying systems with the aim of reducing power consumption and particle damage. Numerous experiments on a range of fine and granular bulk solids and in different configurations of pipeline have been conducted by the authors. Good accuracy and reliability have been achieved for all the test materials and configurations of pipeline considered in this paper.

2. Flow Pattern

A typical set of pneumatic conveying characteristics for fine products is shown in **Fig. 1**.

When the air mass flow rate is decreased from high to low and along a line at constant product mass flow rate, the pressure drop also decreases and reaches a minimum value. This region usually is referred to as dilute-phase conveying. As the air mass flow rate is decreased further, the pressure drop increases usually at a higher rate than in dilute-phase. This region generally is called dense-phase. Therefore, from

---

* Wollongong NSW, 2522 Australia

† Received May 30th, 1994

Fig. 1, between dilute- and dense-phase there is a pressure minimum curve which is one of the main parameters that should be determined during the design stage.

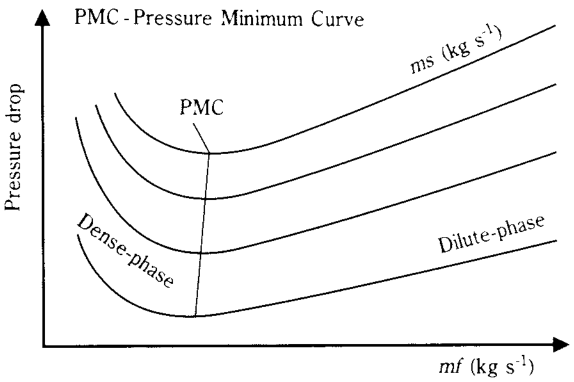

Fig. 1 General form of pneumatic conveying characteristics for fine products

Fig. 2 shows a typical set of pneumatic conveying characteristics for free-flowing granular bulk solids (e.g. wheat, plastic pellets, rice).

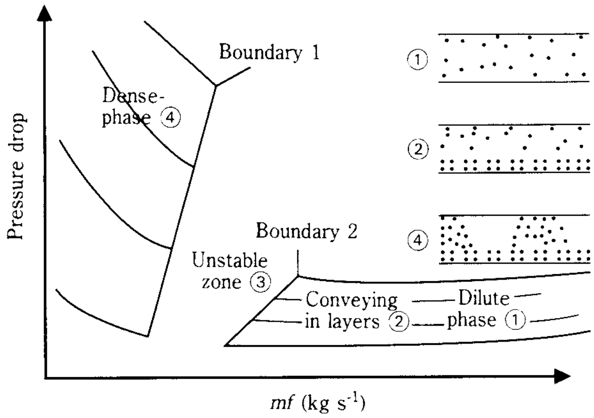

Fig. 2 General form of pneumatic conveying characteristics for granular products

In dilute-phase, the particles are distributed evenly over the entire cross section of the pipe (see point 1 in **Fig. 2**). When conveying takes place along a line at constant product mass flow rate in the direction of decreasing air mass flow rate, this line reaches a point of minimum pressure. At this stage, a "layer" of particles is being conveyed along the bottom of the pipe (see point 2 in **Fig. 2**). With such information, it is possible to operate at minimum air flows for dilute-phase by selecting operating conditions say, slightly to the right of pressure minimum.

As the air mass flow rate is decreased further, the particles accumulate on the bottom of the pipeline and form long plugs. These long plugs are "forced" through the pipeline and produce high fluctuations in pressure and vibration. This region is referred to as the unstable zone (see point 3 in **Fig. 2**).

If the air mass flow rate is reduced even further, it is found that the particles are conveyed gently and in the form of slugs (see point 4 in **Fig. 2**). Along the horizontal pipeline, the slugs pick up the particles from the stationary layer in front of it and deposit the same quantity of particles behind it. Note that there is no inter-particle motion within the slug itself.

Therefore, from **Fig. 2** there are two boundaries separating the dilute-phase, unstable-zone and dense-phase regimes.

3. Test Program

The products and pipelines employed in the test program are listed in **Tables 1** and **2**.

Coal 1, Coal 2, Coal 3, Coal 4 and Flyash all were fine powders and the others were granular materials.

The compressed air was supplied at a maximum pressure head of ≈ 800 kPag from any combination of three screw compressors. The air mass flow rates were measured by annubar for Pipelines II, VI and VII and by an orifice plate for the other pipelines. The product mass flow rates were obtained from the load cells on which the receiving hoppers were mounted.

The steady-state conveying characteristics for several pipelines and products are shown in **Figs. 3** to **10** which clearly demonstrate that fine and granular products display significantly different pneumatic conveying characteristics. Also the experimental data points are superimposed on the figures.

Table 1 Test products

Product	ϱ_s (kg m^{-3})	ϱ_b (kg m^{-3})	d_p (μm)	ϕ (°)	ϕ_w (°)	Test Pipeline(s)
Coal 1	1390	563	30	—	—	I, II
Coal 2	1390	541	18	—	—	I, II
Coal 3	1360	568	29	—	—	I, II
Coal 4	1600	538	41	—	—	III, IV, V
Flyash	2197	634	16	—	—	VI, VII, VIII, IX, X
BPP$^{\alpha}$	834	458	3760	43.8	12.1	VI, X, XI
WPP^{ß}	865	494	3120	44.7	15.2	XI
Duralina	1494	688	350	34.5	17.0	XI
Wheat	1416	778	3500	43.7	16.0	XI

$^{\alpha}$BPP = Black Plastic Pellets.
^{ß}WPP = White Plastic Pellets.

Table 2 Test pipelines

Pipeline	D (mm)	L (m)	N_b	N_h	N_v	R (mm)	Feeder
I	25.4	63	9	8	2	254	BT[θ]
II	52.5	48	4	4	1	254	BT
III	105	110	5	5	1	1000	BT
IV	52.5	104	12	11	2	1000 & 254	SFB[ω]
V	52.5	117	12	11	2	1000	SFB
VI	52.5	102	9	9	1	254	BT
VII	52.5	135	9	9	1	254	BT
VIII	69	172	5	5	1	1000	BT
IX	69	553	17	17	1	1000	BT
X	80.5	137	9	9	1	254	BT
XI	105	96	10	10	1	1000	RV[τ]

[θ] BT = Blow Tank.
[ω] SFB = Screw-Feeding Blow Tank.
[τ] RV = Rotary Valve.

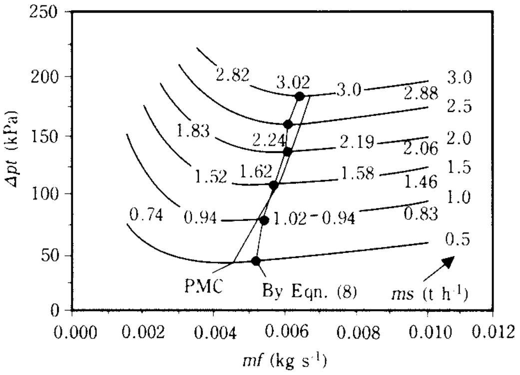

Fig. 3 Steady-state conveying characteristics of Coal 1 and Pipeline I

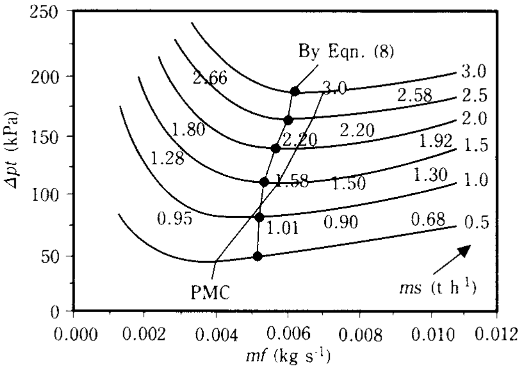

Fig. 4 Steady-state conveying characteristics of Coal 2 and Pipeline I

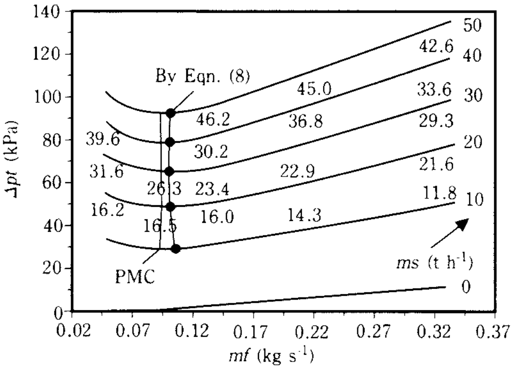

Fig. 5 Steady-state conveying characteristics of Coal 4 and Pipeline III

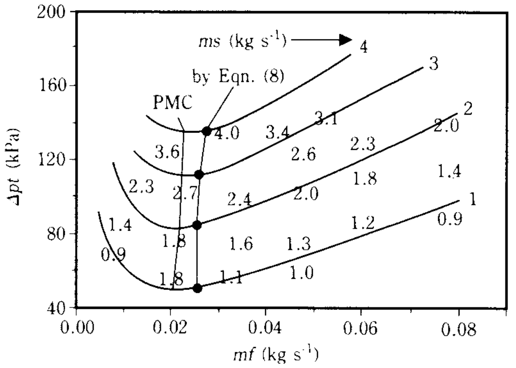

Fig. 6 Steady-state conveying characteristics of Flyash and Pipeline VI

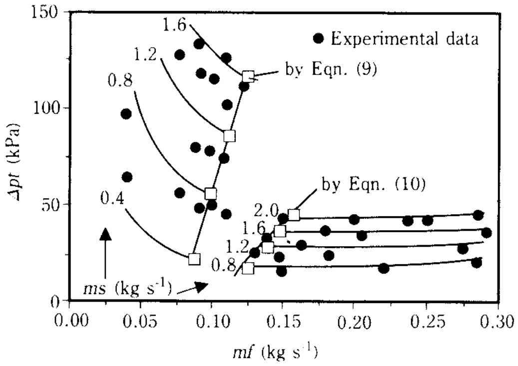

Fig. 7 Steady-state conveying characteristics of Black Plastic Pellets and Pipeline XI

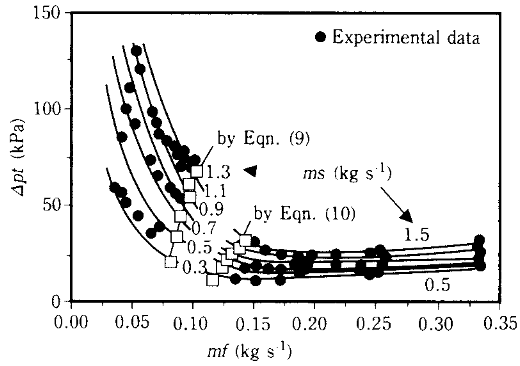

Fig. 8 Steady-state conveying characteristics of White Plastic Pellets and Pipeline XI

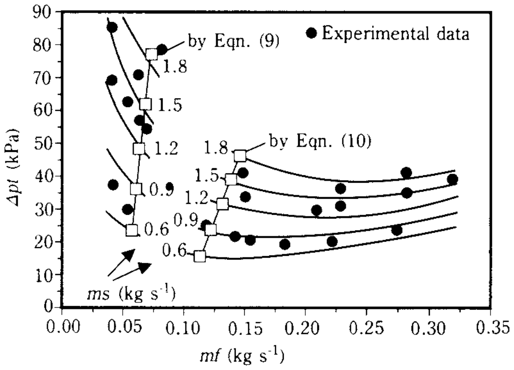

Fig. 9 Steady-state conveying characteristics of Duralina and Pipeline XI

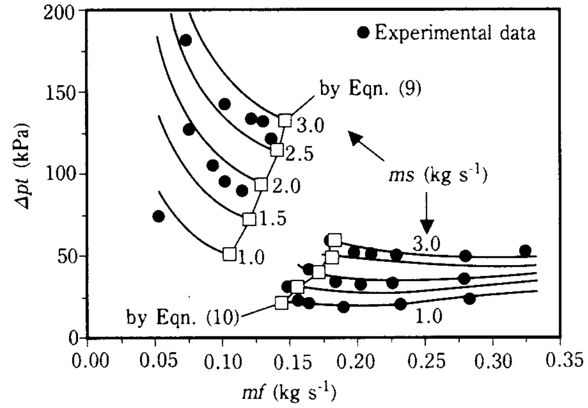

Fig. 10 Steady-state conveying characteristics of Wheat and Pipeline XI

4. Prediction of PMC and Boundaries

4.1 Dimensional Analyses

To describe the pressure minimum curve (PMC) for fine powders and the boundaries between dilute-phase, the unstable-zone and dense-phase flow for granular products, the Froude number at the pick-up point is employed in this paper and defined as:

$$Fr_i = \frac{V_{fi}}{\sqrt{g\,D}}$$

For a given pipeline material and conveying air, the Froude number, Fr_i can be considered as a function of particle properties and conveying conditions, such as bulk density ϱ_b, median particle diameter d_p, pipe diameter D, product mass flow rate m_s, air mass flow rate m_f and air density at the pick-up point ϱ_{fi}. By using dimensional analysis[3], an expression of the form given in Equation (1) is considered initially.

$$Fr_i = k\,m_s^a\,m_f^b\,\varrho_{fi}^c\varrho_b^d d_p^e D^f \qquad (1)$$

Equation (1) normally would involve the evaluation of seven unknowns, but these may be reduced with the aid of dimensional analysis.

The dimensional equation corresponding to Equation (1) is:

$$[L^0M^0T^0] =$$

$$[MT^{-1}]^a[MT^{-1}]^b[ML^{-3}]^c[ML^{-3}]^d[L]^e[L]^f \qquad (2)$$

Equation (2) may be resolved into three component auxiliary equations:

$$L:\ 0 = -3c - 3d + e + f \qquad (3)$$

$$M: 0 = a + b + c + d \qquad (4)$$

$$T: 0 = -a - b \qquad (5)$$

There are now six unknowns and three equations; hence three of the unknowns may be expressed in terms of the remaining three unknowns. Numerous combinations are possible. One possible combination is to express b, d, and f in terms of a, c and e. From Equations (3), (4) and (5),

$$b = -a$$

$$d = -c$$

$$f = -e$$

Substituting these values into Equation (1) results in:

$$Fr_i = k\,m_s^a\,m_f^{-a}\,\varrho_{fi}^c\varrho_b^{-c}d_p^e D^{-e}$$

$$= km^{*a}\left(\frac{\varrho_{fi}}{\varrho_b}\right)^c\left(\frac{d_p}{D}\right)^e \qquad (6)$$

From **Tables 1** and **2**, the particle diameter of the fine powders can be neglected compared with the pipe diameter. Also, based on the authors' experiences, for a given pipeline the particle diameter of fine powders which have similar properties has little influence on the system performance in dilute-phase conveying. However, the pipe diameter still has a great effect on system performance (*i.e.* Fr_i). Therefore, Equation (6) is simplified for fine powders as:

$$Fr_i = km^{*a}\left(\frac{\varrho_{fi}}{\varrho_b}\right)^c D^e \qquad (7)$$

Exponents k, a, c and e in Equations (6) and (7) are determined empirically.

4.2 Determination of Exponents

To predict accurately the pressure minimum curve for fine powders and the boundaries between dilute-phase, the unstable zone and dense-phase flow for granular products, the exponents k, a, c and e are determined initially by using the experimental data of pressure minima and the boundaries for different pipe diameters and products (e.g. Pipeline I and Coal 1, Pipeline VIII and Flyash for fine powders and Pipeline III and Black Plastic Pellets, Pipeline I and Duralina for granular products). The determined values of the exponent are listed in **Table 3**.

Table 3 Values of exponent

Exponent	PMC (see **Fig. 1**)	Boundary 1 (see **Fig. 2**)	Boundary 2 (see **Fig. 2**)
k	3.504	3.151	2.959
a	-0.230	-0.018	0.097
c	-0.152	-0.254	-0.219
e	-0.302	0.213	0.069

Hence, Equations (6) and (7) are rewritten as:

$$Fr_i = 3.504\ m^{*\,-0.230} \left(\frac{\varrho_{fi}}{\varrho_b}\right)^{-0.152} D^{-0.302} \quad \text{for PMC} \tag{8}$$

$$Fr_i = 3.151\ m^{*\,-0.018} \left(\frac{\varrho_{fi}}{\varrho_b}\right)^{-0.254} \left(\frac{d_p}{D}\right)^{-0.213} \quad \text{for Boundary 1} \tag{9}$$

$$Fr_i = 2.959\ m^{*\,0.097} \left(\frac{\varrho_{fi}}{\varrho_b}\right)^{-0.219} \left(\frac{d_p}{D}\right)^{-0.069} \quad \text{for Boundary 2} \tag{10}$$

The pressure minimum curves and boundaries for each pipeline and product then are predicted by using Equations (8), (9) and (10), respectively. Some of the predictions are shown in **Figs. 3** to **10**, which clearly demonstrate that Equations (8), (9) and (10) have good accuracy and reliability for all the test materials and pipeline configurations considered in this paper.

5. Prediction of Pressure Drop and Economic Operating Point (EOP)

To determine accurately the pressure minimum curve by Equation (8) for fine powders and the boundaries between dilute-phase, the unstable-zone and dense-phase by Equations (9) and (10) for granular products, it is required to predict accurately the total pipeline air pressure drop. Since the properties of the conveyed material have great influences on system performance, to date no general correlations have been developed that can predict accurately the total pipeline air pressure drop for conveying fine products from dilute- to dense-phase and granular products in dilute-phase[1]. Fortunately, an accurate test-design procedure has been developed recently[4] where the experimental data from a test rig can be scaled up accurately to actual installations for a given product. Therefore, the following section presents the results from recent investigations into predicting theoretically the pressure loss in the horizontal dense-phase transport of granular products.

5.1 Pressure Drop in Dense-Phase

The following correlation has been developed to predict the pressure gradient for a horizontal particle slug[5, 6]:

$$\frac{\Delta p}{l_s} = \frac{4\ \mu_w \lambda}{D} \sigma_f + 2\ \varrho_b\, g\, \mu_w \tag{11}$$

λ is the stress transmission coefficient (i.e. ratio of radial stress to axial stress). Note that the radial stress caused by gravity in a horizontal pipe is excluded. Based on the measured results of wall pressure and a theoretical analysis, the following equations have been developed[7] to determine the value of the stress transmission coefficient in a slug.

$$\lambda = \frac{\sigma_{rw}}{\sigma_x} = \frac{1 - \sin\phi_s \cos\,(\omega - \phi_w)}{1 + \sin\phi_s \cos\,(\omega - \phi_w)}$$

$$\sin\omega = \frac{\sin\phi_w}{\sin\phi_s}$$

$$\phi_s = \frac{4}{3}\ \phi_w\ \gamma_b^{\ 0.33}$$

σ_f is the stress on the front face of the slug and can be estimated by the following equation.

$$\sigma_f = \alpha \varrho_b\, V_s^{\,2}$$

α is ratio of cross sectional area of stationary layer to pipe and calculated by:

$$\alpha = \frac{A_{st}}{A} = \frac{1}{1 + V_s/(0.542\,\sqrt{gD})}$$

V_s is the slug velocity and the relationship between the slug velocity and the superficial air velocity has been presented[8], that is:

$$V_s = 105\ \frac{\epsilon\, d_p}{D} \left[\frac{\tan\phi_w}{\tan\phi}\right]^{0.33} (V_f - V_{fmin})$$

where V_{fmin} is the minimum superficial air velocity for horizontal flow,

$$V_{fmin} = \frac{\varrho_s\, g\, \tan\phi_w\, \epsilon^3 d_p^{\,2}}{180\,(1-\epsilon)\eta}$$

Therefore, the pressure gradient in a single slug can be calculated easily from Equation (11) and the other relevant expressions. Also, the pressure drop over the entire slug can be obtained if the length of the slug is known.

A dense-phase slug-flow pneumatic conveying system usually contains several slugs along the pipeline. It has been found that the sum of the pressure drop caused by each slug is equal to that caused by a single slug having a total length equal to all the small slugs[7]. This is contrary to the exponential relationship described by Doig[10]. The reason is that the slugs in a low-velocity conveying system are in an aerated state and do not behave like a "mechanical pushing" system[11]. The pressure gradient along this "single" slug still can be calculated by using Equation (11), as long as the mean conditions (based on average air density) are used[9].

Since the air mass flow rate and the slug velocity in dense-phase are very low, the pressure drop caused by conveying air and the effect of bends on the pressure drop can be neglected (i.e. the pipeline can be approximated as a straight section of pipe with the same actual length).

The total length of slugs in the pipeline can be calculated by the following correlation:

$$L_s = \frac{m_s L}{A\,(1-\alpha)\,\rho_b\,V_s}$$

The total pressure drop is:

$$\Delta p_{th} = \left(1 + 1.084\,\lambda\,Fr_s^{0.5} + 0.542\,Fr_s^{-0.5}\right)\frac{2\,g\,\mu_w\,m_s\,L}{A\,V_s} \qquad (12)$$

where $Fr_s = \dfrac{V_s^2}{g\,D}$

Using Equation (12) and the other relevant expressions, curves of constant m_s (i.e. steady-state conveying characteristics) are predicted for black plastic pellets, white plastic pellets and wheat in Pipeline XI.

Figs. 11 to **13** present the pneumatic conveying characteristics for the experiments conducted on pipeline XI. Note that the pressure drops on these figures represent the values of total pressure drop for a 78 m horizontal section of pipeline. Experimental results are superimposed onto each figure for comparison. **Figs. 11** to **13** clearly show that the new model presented in this paper has good accuracy and reliability.

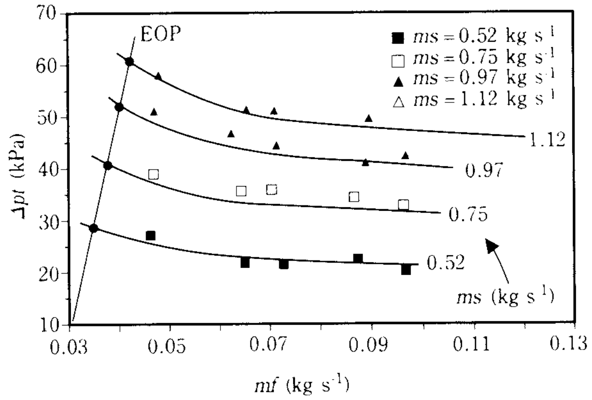

Fig. 11 Predicted steady-state conveying characteristics of Black Plastic Pellets and horizontal section in Pipeline XI

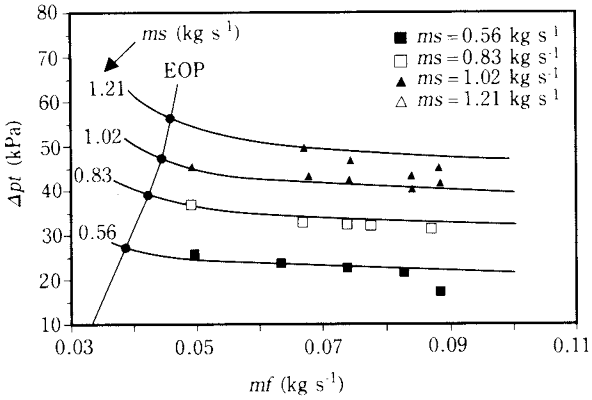

Fig. 12 Predicted steady-state conveying characteristics of White Plastic Pellets and horizontal section in Pipeline XI

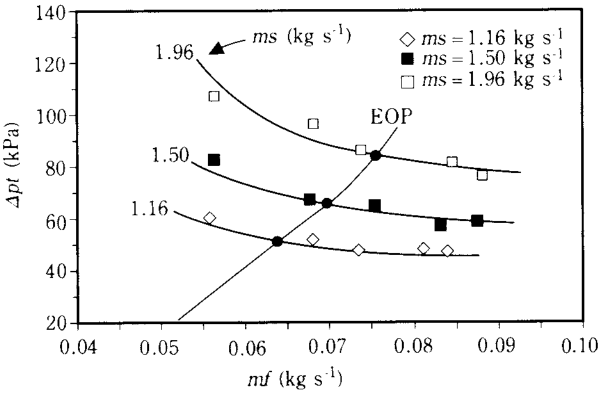

Fig. 13 Predicted steady-state conveying characteristics of Wheat and horizontal section in Pipeline XI

5.2 Economical Operating Point for Slug-Flow

The dense-phase slug-flow pneumatic conveying characteristic curves shown in **Figs. 11** to **13** demonstrate that, for a given m_s, Δp_{th} decreases with increasing m_f. Also, it can be seen that the pressure gradient increases quite sharply at low values of m_f. Theoretically, it is possible to operate at any point along the m_s curve. However, from an energy point of view, this may not be feasible.

That is, it is desirable to operate the slug-flow system at minimal energy. The following equation can be used to estimate the nominal power of the conveying system.

$$P_n = \Delta p_{th} A V_f$$

Replacing Δp_{th} with Equation (12), then

$$P_n = (1 + 1.084 \lambda F_{rs}^{0.5} + 0.542 F_{rs}^{-0.5}) \frac{2 g \mu_w m_s L}{V_s} V_f \qquad (13)$$

To minimise power consumption, Equation (13) is differentiated with respect to V_f and let equal to zero. That is,

$$k_o^2 V_f^3 - 3 k_o^2 V_{fmin} V_f^2 + (3 k_o^2 V_{fmin}^2 - \frac{\sqrt{g D}}{1.084 \lambda} k_o V_{fmin} - \frac{g D}{2 \lambda}) V_f - (k_o^2 V_{fmin}^3 - \frac{\sqrt{g D}}{1.084 \lambda} k_o V_{fmin}^2 + \frac{g D}{2 \lambda} V_{fmin}) = 0 \qquad (14)$$

where $k_o = 105 \frac{\epsilon d_p}{D} [\frac{\tan\phi_w}{\tan\phi}]^{0.33}$

Three roots of solution can be obtained from Equation (14). Actual calculations have found that two of them are complex and obviously unrepresentative of a real system. The real root is the mean superficial air velocity which minimises energy consumption. From Equation (14), it can be seen that this "economical" superficial air velocity is representative of a given conveyed material and pipe diameter. However, the corresponding "economical" value of m_f still is dependent on the mass flow rate of solids and pipe length (i.e. due to the air flow being compressible). As an example, the superficial air velocities at the economical operating point are calculated as 2.76, 3.07 and 4.74 ms^{-1} for white plastic pellets, black plastic pellets and wheat according to Equation (14). Also, using computer iteration, the corresponding calculated values of "economical" mass flow rate of air for different conveying rates lie on the economical operating point (EOP) lines shown in **Figs. 11** to **13**.

6. Conclusions

Fine and granular products have significantly different pneumatic conveying characteristics. Fine products usually can be transported smoothly and reliably from dilute- to dense-phase. However, when granular products are conveyed between dilute- and dense-phase, significant fluctuations in pressure and vibration can occur along the pipeline.

When designing a pneumatic conveying system,it is very important to consider the differences in conveying performance of fine and granular products.

The correlations presented for the determination of the pressure minimum curve for fine powders and the boundaries between dilute-phase, the unstable zone and dense-phase for granular products and for the prediction of total pressure drop along horizontal sections of pipe have been demonstrated to provide good accuracy and reliability for the test materials and configurations of pipeline considered in this paper.

After the correlations for the prediction of total pressure drop are obtained, it is easy to obtain the economic operating points in terms of minimum energy consumption and low particle degradation.

List of Symbols & Abbreviations

$a,\ldots,f$	Exponents in Equation (1)
A	Pipe cross sectional area, m^2
A_{st}	Cross sectional area of stationary layer, m^2
D	Pipe diameter, m
d_p	Median particle diameter, m
Fr_i	Froude number at pick-up point
Fr_s	Froude number of slug
g	Acceleration due to gravity, m s^{-2}
k	Coefficient in Equation (1)
k_o	Coefficient in Equation (14)
L	Total effective pipeline length, m
L_s	Total length of slugs, m
l_s	Single slug length, m
m_f	Air mass flow rate, kg s^{-1}
m_s	Product mass flow rate, kg s^{-1}
m^*	Product to air mass flow rate ratio, $m^* = m_s m_f^{-1}$
N_b	Number of 90° bends
N_h	Number of horizontal straight sections
N_v	Number of vertical lift sections
P_n	Nominal power, W
R	Centreline radius of 90° bends, m
V_{fi}	Superficial air velocity at pick-up point, m s^{-1}
V_{fmin}	Minimum superficial air velocity for initiating motion of slug, m s^{-1}
V_s	Slug velocity, m s^{-1}
α	Ratio of cross sectional area of stationary layer to pipe

Δp	Pressure drop across a single slug, Pa
Δp_t	Total pipeline air pressure drop, Pa
Δp_{th}	Total pressure drop for horizontal pipeline, Pa
ϕ	Internal friction angle, ^{o}
ϕ_w	Wall frictional angle on bright mild steel, ^{o}
ϕ_s	Static internal friction angle, ^{o}
γ_b	Bulk solid specific density
η	Dynamic viscosity of air, Nsm^{-2}
λ	Stress transmission coefficient
μ_w	Wall friction coefficient, $\mu w = \tan\phi_w$
ϵ	Bulk voidage, $\epsilon = 1 - \varrho_b \, \varrho_s^{-1}$
ϱ_b	Loose-poured bulk density, kg m^{-3}
ϱ_{fi}	Air density at pick-up point, kg m^{-3}
ϱ_s	Particle density, kg m^{-3}
σ_f	Stress on front face of slug, Pa
σ_{rw}	Radial stress of slug at wall, Pa
σ_x	Axial stress of slug, Pa

7. References

1) Pan, R., "Improving Scale-Up Procedures for the Design of Pneumatic Conveying Systems", PhD Thesis, University of Wollongong, Australia, 1992.
2) Pan, R., Mi, B. and Wypych, P.W., "Design of Pneumatic Conveying Systems for Granular Bulk Solids", Int. Conf. on Advanced Technology and Equipment of Materials Handling, Shanghai, P.R.China, October, 1994.
3) Murphy, G., "Similitude in Engineering", The Ronald Press Company, New York, 1950.
4) Pan, R. and Wypych, P.W., "Scale-up Procedures for Pneumatic Conveying Design", Powder Handling and Processing, Vol. 4, No. 2, 1992, pp 167-172.
5) Konrad, K. and Harrison, D., "Prediction of the Pressure Drop for Horizontal Dense Phase Pneumatic Conveying of Particles", Pneumotransport 5, Int. Conf. on the Pneumatic Transport of Solids in Pipes, London, UK, April, 1980.
6) Legel, D., and Schwedes, J., "Investigation of Pneumatic Conveying of Plugs of Cohesionless Bulk Solids in Horizontal Pipes", Bulk Solids Handling, Vol. 4, No. 2, 1984, pp 399-405.
7) Mi, B. and Wypych, P. W., "Investigations into Wall Pressure in Horizontal Slug-Flow Pneumatic Conveying", Internal Research Report 93-05-BM-1, May, 1993, Department of Mechanical Engineering, University of Wollongong.
8) Mi, B. and Wypych, P. W., "Particle Slug Velocities in Horizontal Slug-Flow Pneumatic Conveying", Powder Handling & Processing, Vol. 5, No. 3, 1993, pp 227-233.
9) Pan, R. and Wypych, P.W., "Pressure Drop due to Solid-Air Flow in Horizontal and Vertical Pipes", 4th Int. Conf. on Bulk Materials Storage, Handling and Transportation, Wollongong, Australia, July, 1992.
10) Doig, I.D., "Dense-Phase Pneumatic Conveying", Chapter 6 in Pneumatic Conveying of Solids,
Leung, L.S. (Editor), Department of Chemical Engineering, University of Queensland, Australia, June, 1977.
11) Wypych, P.W., "Introduction to Pneumatic Conveying", Chapter 1 in Design and Operation of Pneumatic Conveying Systems, Short Course Notes, ITC Bulk Materials Handling, University of Wollongong, Australia, July, 1989.

Author's short biography

Dr. Renhu PAN, BE, ME, PhD

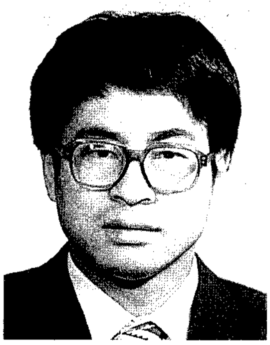

Dr. Pan is a Fellow with the Department of Mechanical Engineering at the University of Wollongong, Australia. Dr. Pan has been involved with the pneumatic conveying of bulk solids since 1988 and his main interest is in the field of researching and developing new technologies for pneumatic conveying system design.

Mr. Bo MI, BE, ME

Mr. Mi received his BE and ME degrees in Mechanical Engineering from the University of Science and Technology Beijing, P.R. China. At present Mr. Mi is working for his PhD degree at the Department of Mechanical Engineering at the University of Wollongong. His main interest is in the areas of researching and developing new technologies for low-velocity pneumatic conveying of bulk solids.

Dr. Peter Wypych, BE, PhD, CPEng, MIEAust

Dr. Wypych is a Senior Lecturer with the Department of Mechanical Engineering at the University of Wollongong and has been involved with pneumatic transportation of bulk solids since 1981.

Dr. Wypych also is a consultant of ITC Bulk Materials Handling and has been responsible for over 150 consulting projects assisting industry in the areas of design, trouble-shooting, system upgrading, feasibility studies, and new technology.

As a result of this effort, Dr. Wypych has been responsible for setting up one of the largest and most advanced Bulk Solids Handling Laboratories in the World.

Mechanically Induced Reactivity of $ZnFe_2O_4$[†]

Sepelák, V.
Institute of Geotechnics of the Slovak Academy of Sciences,*
Jancke, K., Richter-Mendau, J., Steinike, U., Uecker, D.-Chr.,
*Institute of Applied Chemistry e.V.,**,*
Rogachev, A. Yu.
*Institute of Solid State Chemistry of RAS****

Abstract

$ZnFe_2O_4$ plays an important role as an adsorbent in the process of hot gas desulfurization. The influence of mechanical activation on the capacity S of $ZnFe_2O_4$ and on the following oxidation (regeneration) is investigated. The particle size is changed by mechanical activation in a characteristic way, and an inverse spinel structure is formed. With the mechanically induced degree of inversion the decomposition temperature of $ZnFe_2O_4$ is strongly diminished. The formation of the inverse spinel structure as well as the breakage of particle size lead to an essential increase of reactivity in the reaction with H_2S. The following oxidation of the sulfurized zinc ferrite is also influenced by the primarily performed mechanical activation.

For the investigations, $ZnFe_2O_4$ which had been treated in a planetary mill was used. The sulfurization was carried out with compressed powders. The characterization was performed mainly by X-ray diffraction (XRD), scanning electron microscopy (SEM), measurement of particle size and chemical analysis.

1. Introduction

The development of hot gas desulfurization technologies has focused on solid metal-oxide adsorbents that can remove sulfur species from the coal gas and that can be reused for further sulfur removal after regeneration with air. Zinc ferrite is presently the leading adsorbent candidate[1,2,3,4,5]. It has a high sulfur removal capability and is easily regenerated[6,7,8].

Reduction, sulfurization and regeneration kinetics of zinc ferrite as a function of the operating conditions, temperature, pressure, gas composition (concentration), adsorbent radius and flow rates were studied in a number of papers[9,10,11]. However, the influence of the internal structure of the adsorbent on the desulfurization process has not yet been studied.

According to the literature[12,13,14,15], the structure and properties of zinc ferrite can be significantly modified by the action of mechanical stress. The structure of non-treated zinc ferrite is characterized by the space group Fd3m (normal spinel structure) in which Zn^{2+} and Fe^{3+} cations occupy tetra- and octahedral sites within the lattice of cubic close-packed oxygens. Tetrahedral sublattice A is formed only by Zn^{2+} cations with no magnetic moment, and all octahedral B-sites are occupied by Fe^{3+} cations. For this reason the A-B exchange interaction does not exist, and non-treated zinc ferrite is paramagnetic above the temperature of 9 K[16].

In the process of mechanical treatment, the redistribution of Zn^{2+} cations into octahedral interstices and of the Fe^{3+} cations into tetrahedral interstices of the closely packed anionic sublattice takes place, i.e. the degree of inversion changes[17,18,19]. This effect is caused by a shift of the close-packed anion layers. The redistribution of the cations gives rise to exchange interaction between tetahedral and octahedral sublattices and leads to magnetic ordering at 77 K in mechanically treated $ZnFe_2O_4$. The mechanical treatment of zinc ferrite brings about an increase in the Néel temperature and the formation of spin arrangement in the structure.

The action of mechanical energy on solids changes their structure and properties. The resulting structural defects lead to a storage of energy in the solid which may raise its chemical reactivity. Investigations on the mechanically induced reactivity of solids have been carried out with the specific aim of influencing

---

* Kosice, Slovakia
** Rudower Chaussee 5, 12484 Berlin, Germany
*** Novosibirsk, Russia
[†] Received January 18th, 1994

chemical reactions in order to obtain high yields, high reaction velocities or selective reactions[20,21,22,23,24]. Two papers have appeared which have documented the positive influence of mechanical treatment on the reactivity of zinc ferrite in the process of its leaching[25,26]. Mechanical activation of zinc ferrite by grinding enables an increase in the rate of leaching and recovery of zinc into a leach solution.

Based on the knowledge of mechanically induced changes in the structure, physical properties and chemical reactivity of zinc ferrite in the process of its leaching, the influence of the mechanical activation on the reactivity of zinc ferrite in a high-temperature desulfurization process will be discussed in this paper.

2. Experimental

Zinc ferrite, $ZnFe_2O_4$ (JCPDS 22-1012) prepared by the conventional ceramic method, was investigated in the as-received (non-treated) as well as in the mechanically activated state.

The mechanical activation was carried out in a planetary mill EU 2 × 150 (made by the Institute of Solid State Chemistry, Novosibirsk, Russia) at 750 rpm. The weight of ground samples was 2g. The grinding was performed in a ceramic-covered drum. $ZnFe_2O_4$ was ground for 5, 12 and 24 min. The grinding bodies consisted of α-Al_2O_3 ceramics.

XRD analysis was carried out using a URD 6 powder diffractometer (Freiberger Präzisionsmechanik GmbH, Germany) with CuKα radiation. Data interpretation was carried out using the database of the Joint Committee on Powder Diffraction Standards (JCPDS). The qualitative and semi-quantitative determination was carried out with the program APX 63-PADS by Wassermann based on Fiala[27,28].

The particle size distribution of zinc ferrite powders was measured by the method of laser radiation scattering on a Fritsch particle sizer Analysette 22 (Fritsch, Idar-Oberstein, Germany). The mean particle diameter and specific surface area were calculated from granulometric data.

The scanning electron micrographs of the starting sample of zinc ferrite, as well as of the samples after mechanical activation and after sulfurization, were taken on a scanning electron microscope (SEM) BS-300 (TESLA, Czech Republic) equipped with an Energy Dispersive X-Ray Spectrometer EDR 184.

The Mössbauer spectra were taken on a constant acceleration spectrometer (JAGRS-4, Russia) working with a moving absorber and static source. As a source of γ-rays, ^{57}Co in Pa matrix was used.

The sulfurization was carried out in a special reactor[29]. Gases from compressed cylinders were mixed to simulate a coal gas during sulfurization tests. Gas composition is shown in **Table 1.**

Table 1: Operating conditions

gas composition	49.75 vol-% CO, 49.75 vol-%H_2, 0.5 vol-%H_2S
flow rate	280 l/h
working temperature	550 °C
pressure	1 bar
reaction time	45 min.

The regeneration was carried out by means of O_2 contained in the air. The regeneration took 2 × 6 h at 550 °C and 2 × 6 h at 650 °C or in a GUINIER-LENNÈ camera (at 170 °C to 600 °C, heat rate 1.2 K/min).

3. Results and Discussion

Due to the increase of structure defectiveness with prolongation of mechanical treatment, the well-known phenomenon of intensity decrease and diffraction lines broadening is observed on diffraction patterns of ground samples (see **Fig. 1**).

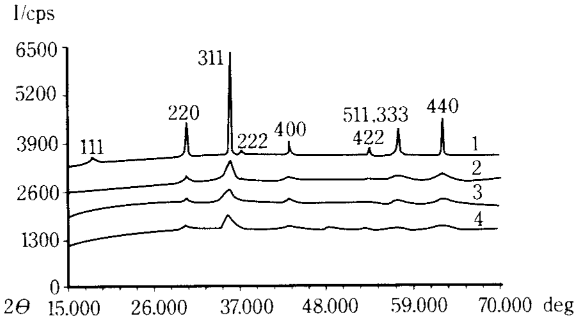

Fig. 1 Diffraction patterns of non-activated zinc ferrite (1) and of zine ferrite mechanically activated for 5 min. (2), 12 min.(3), 24 min. (4)

A significant decrease of particle size (**Fig. 2**, breaking of agglomerates) and the formation of a typical bimodal distribution of particle size are found (**Fig 3**).

The mean particle diameter of the as-received samples was 13.44 μm and the specific surface area 1.55 $m^2/c.c.$ As a result of 24 min. grinding, the mean particle diameter decreased to 1.97 μm and the specific surface area increased to 6.45 $m^2/c.c.$

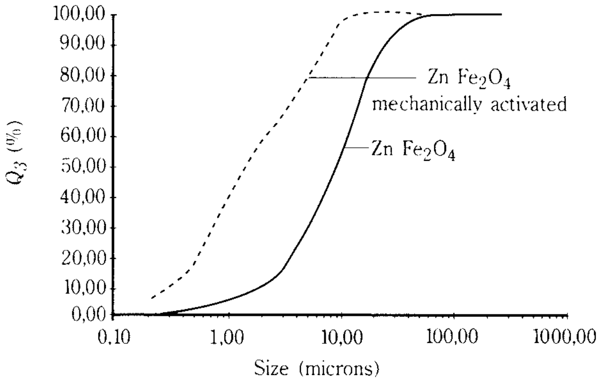

Fig. 2 Particle size distribution of non-activated and of mechanically activated $ZnFe_2O_4$ 24 min. (total cumulative curve)

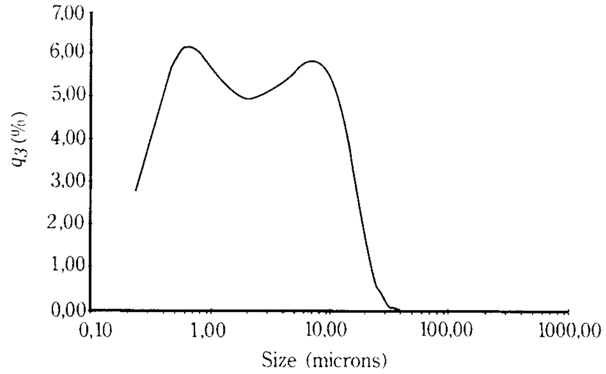

Fig. 3 Particle size distribution of (24 min.) activated $ZnFe_2O_4$ (distribution curve)

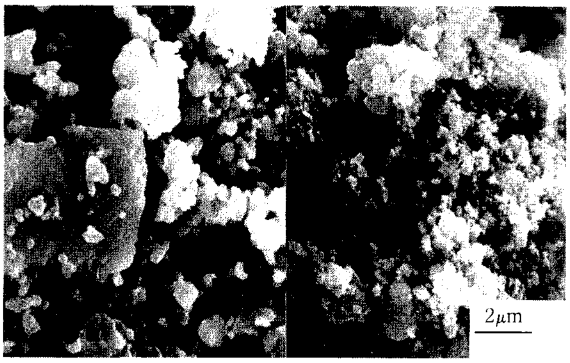

(A) (B)

Fig. 4 Scanning electron micrograph of non-activated zinc ferrite (A) and of zinc ferrite mechanically activated for 24 min. (B)

The SEM pictures of the as-received and the mechanically treated samples are compared in figures 4A and 4B. Both samples are relatively finely dispersed and therefore show a strong tendency to aggregation caused by adhesion forces. However, the particles sizes in agglomerates of the as-received and the ground sample are quite different.

The degree of inversion determined by the integral analysis of X-ray diffraction intensities[30, 18] of samples ground for 5, 12 and 24 minutes was 0.67, 0.83 and 0.94, respectively.

Transition from the paramagnetic to a magnetically ordered state, due to cations redistribution taking place in the structure during mechanical treatment of zinc ferrite, was detected by Mössbauer spectroscopy (see **Fig. 5**). From the Mössbauer spectra parameters the values of the inversion degree of investigated samples were determined, and these values were found to be equal to those determined by XRD analysis.

Based on the results given above, the sample ground for 12 and 24 minutes and characterized by the inversion degree $\delta > 0.8$ was chosen for sulfurization and regeneration tests.

The mechanical treatment leads to a decrease of zinc content in $ZnFe_2O_4$ (**Table 2**). The necessary breakage is caused by the mechanical treatment. Moreover, the decomposition temperature of $ZnFe_2O_4$ is decreased by its mechanically induced inversion.

Table 2 Zn content in $ZnFe_2O_4$ as a function of grinding

sample	Zn mass content / %
$ZnFe_2O_4$ (theoretical value)	27.12
$ZnFe_2O_4$ (starting material)	27.1
$ZnFe_2O_4$ (activated for 24 h)	25.0

The overall reaction describing the adsorption of H_2S from coal gas by $ZnFe_2O_4$ is given by

$$ZnFe_2O_4 + 3H_2S + H_2 \rightarrow ZnS + 2FeS + 4H_2O \qquad (1)$$

Thermodynamic studies[30, 31] have shown that the preferred path for H_2S adsorption, reaction 1, is

$$\begin{aligned} 3ZnFe_2O_4 + H_2 &\rightarrow 3ZnO + 2Fe_3O_4 + H_2O \\ Fe_3O_4 + 3H_2S + H_2 &\rightarrow 3FeS + 4H_2O \\ ZnO + H_2S &\rightarrow ZnS + H_2O \qquad (2) \end{aligned}$$

Other paths involve the formation of intermediate products such as Fe and FeO. In the presence of highly reducing gases (i.e., coal gases containing a large fraction of H_2 or a high CO/CO_2 ratio), Fe_3O_4 is reduced to FeO or Fe, leading to the formation of iron carbide Fe_3C, as follows[33]:

$$\begin{aligned} 3FeO + CO &\rightarrow Fe_3C + 2O_2 \\ 3Fe + CO &\rightarrow Fe_3C + 1/2\ O_2 \qquad (3) \end{aligned}$$

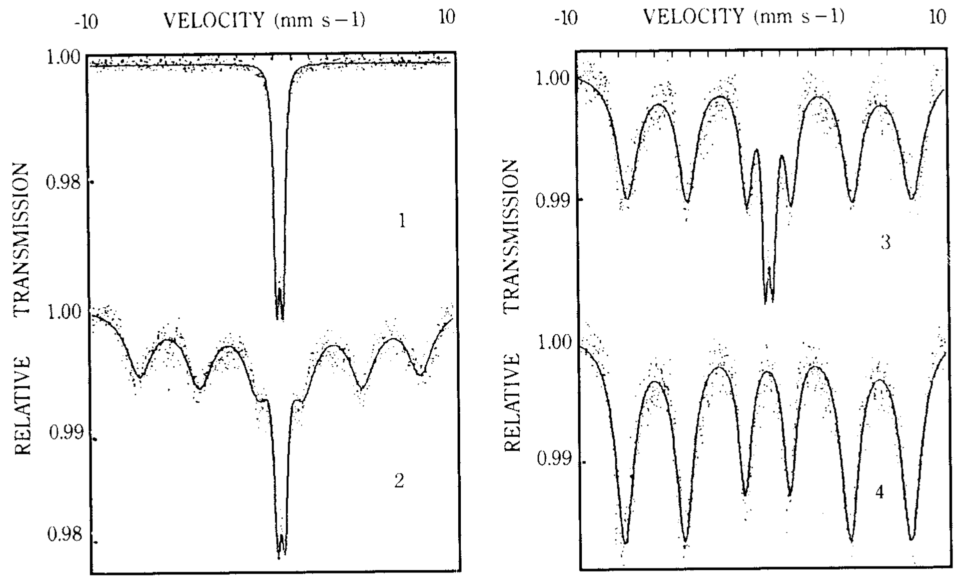

Fig.5 Mössbauer spectrum of non-activated zinc ferrite (1) and of zinc ferrite mechanically activated for 5 min. (2), 12 min. (3), 24 min. (4)

Under the conditions of our experiments, both paths were involved. It follows from the XRD phase analysis of sulfurization products that the as-received sample of zinc ferrite reacts with components of gas mixture forming ZnS (sphalerite, JCPDS 5-566), FeS (iron sulfide, 23-1123) and Fe_3C (cohenite, 35-772). The non-reacted part is represented by ZnO (zincite, 36-1451) and C (carbon, 26-1077) (see **Fig. 6**).

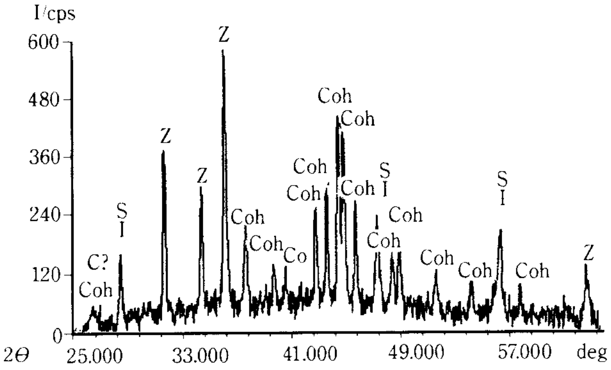

Fig. 6 Diffraction pattern of non-activated zinc ferrite after sulfurization
C = Carbon I = Iron sulfide S = Sphalerite Coh = Cohenite
Z = Zincite

Mechanical treatment (12 min., 24 min.) results in a more than two-fold increase in the capacity S (formation of S^{2-}) of zinc ferrite sulfurization, see **Fig. 7**.

This positive effect is represented by an increased content of sphalerite and FeS, by the presence of wurtzite (36-1450), as well as by the decrease of the non-reacted zincite content. Carbon was not detected in the reaction products. In addition to cohenite, the proportion of which remained more or less the same, FeC (3-411) was also found in products of sulfurization of the ground sample (see **Fig. 8**).

Using XRD to prove the presence of FeS and ZnS is problematic, but the existence of very small quantities of FeS in both samples was proved by EDX measurements. The samples of zinc ferrite after sulfurization were subjected to morphological investigation by scanning electron microscopy. Typical morphology of zinc ferrite after sulfurization is shown on the scanning electron micrographs (see **Fig. 9**).

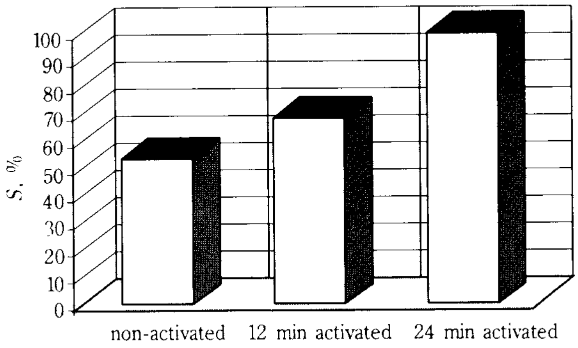

Fig. 7 Influence of mechanical activation on the capacity S of zinc ferrite (related to ZnS formation)

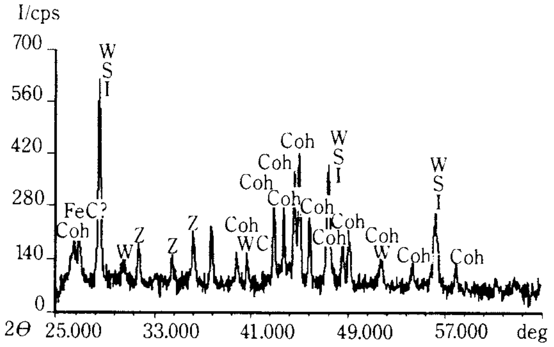

Fig. 8 Diffraction pattern of mechanically activated (24 min.) zinc ferrite after sulfurization
Coh = Cohenite I = Iron sulfide S = Sphalerite
W = Wurtzite Z = Zincite

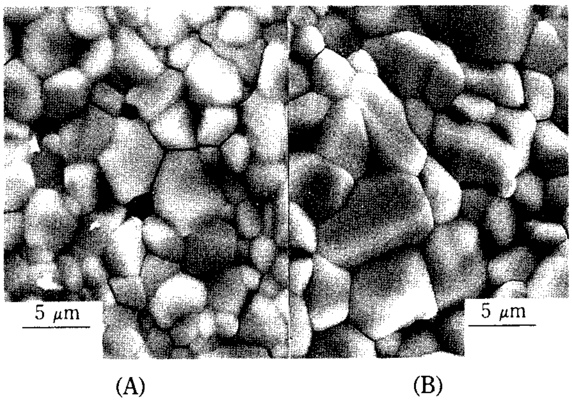

(A) (B)

Fig. 9 Scanning electron micrograph of zinc ferrite after sulfurization. (A) – non-activated, (B) – mechanically activated for 24 min.

The increase of the conversion degree of zinc ferrite is a result of the generally known positive effect of mechanical activation on the rate of chemical processes [22,23,24]. The increased number of phases in sulfurization products of mechanically treated zinc ferrite leads to the assumption that the rate of chemical reactions is changed simultaneously with the change of reaction mechanism. To verify this assumption, a more detailed study of this process is necessary, varying the reaction conditions and scope of mechanically induced structural changes of the adsorbent.

In regeneration, the sulfided metal adsorbent reacts exothermally with oxygen and converts back to the oxides [3,10]. Sulfur and carbon are then oxidized to SO_2 and CO_2. Regeneration kinetics are a strong function of temperature, pressure, and oxygen concentration [9,10]. Regeneration of products obtained by sulfurization of both the as-received and mechanically treated samples took place under the same reaction conditions. It is evident from the comparison of diffraction patterns (see **Fig. 10**) that mechanical activation also has a positive effect on the regeneration process. This is manifested, for the ground sample, by a higher content of zinc ferrite and, for the as-received sample, by a higher content of simple oxides (ZnO, Fe_2O_3 [33-664]). Because the same conditions of regeneration were chosen for both samples, the observed differences may be attributed to differences in the composition of desulfurization stage products.

The regeneration of the activated sample is already complete after 6 h at 550 °C. A part of haematite remains, which does not react. This could be attributed to the diminishing of zinc caused by the process of mechanical treatment, whereby ZnO and Fe_2O_3 are not present in their stoichiometric ratio. The regeneration of the non-activated sample, on the other hand, is finished after a temperature treatment at 550 °C or 650 °C for 24 h in air. During this time, $ZnFe_2O_4$ from ZnO and Fe_2O_3 is formed. After-

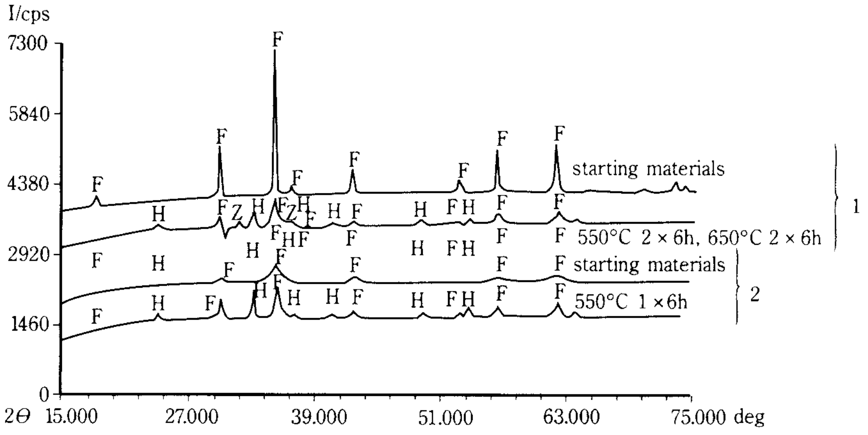

Fig. 10 Dependence of the regeneration on the primary mechanical activation
F = Franklinite H = Haematite Z = Zincite
1 : non-activated $ZnFe_2O_4$, regeneration finished after 2 × 6 h at 550 °C, 2 × 6 h at 650 °C
2 : 24 min. activated $ZnFe_2O_4$, regeneration is finished after 1 × 6 h at 550 °C

wards, no ZnO can be detected, however, a traceable part of haematite remains. A further diminishing of zinc in this case cannot be detected chemically. The following result was obtained from the in-situ regeneration: The formation of $ZnFe_2O_4$ starts at about 430 °C, resp. 390 °C (mechanical activated sample). The mechanical activation decreases the temprature of formation of $ZnFe_2O_4$. Altogether, it is stated that the activated sample can be regenerated in an essentially shorter time.

CONCLUSIONS

The mechanical activation of $ZnFe_2O_4$ leads to a decrease of grain size and to an inversion of spinel structure. The mechanically induced degree of inversion strongly decreases the decomposition temperature of $ZnFe_2O_4$ as well as the breakage of grain size, and leads to an increase of reactivity of $ZnFe_2O_4$ in the reaction with H_2S. The following oxidation of the sulfurized zinc ferrite is still influenced by the primarily performed mechanical activation.

ACKNOWLEDGEMENT

The measurements were carried out in the "Center of Heterogeneous Catalysis" (new address: Institute of Applied Chemistry e.V.) in Berlin, Germany. The authors would like to thank the "Deutscher Akademischer Austauschdienst" (DAAD) for financially supporting one of the authors (Vladimír Sepelák) during his stay at the "Center of Heterogeneous Catalysis" in Berlin, and the ERP-Fonds, Project 2646, for their financial support towards the purchase of equipment. Our sincere thanks are also due to Mrs. Chr. Staedler for chemical investigations and particle size measurements, Mr. B. Rosahl for his help on the reactor, and all co-workers in the group for their support.

REFERENCES

1) GANGWAL, S.K., STOGNER, J.M., HARKINS, S.M., BOSSART, S.J.: "Testing of Novel Sorbents for H_2S Removal from Coal Gas" Environmental Progress, 8 (1989), 26
2) HEDERER, H.: "Trockenentschwefelung für Kombikraftwerke mit Kohlevergasung" Chem.-Ing.-Tech., 61 (1989), 948
3) AYALA, R.E., MARSH, D. W.: "Characterization and Long-Range Reactivity of Zinc Ferrite in High-Temperature Desulfurization Processes" Ind. Eng. Chem. Res., 30 (1991), 55
4) FLYTZANI-STEPHANOPOULOS, M., et al.: "Novel Sorbents for High Temperature Regenerative H_2S Removal", DOE/MC/20417-1898 (DE86004261), Morgantown, (1984)
5) GRINDLEY, T., STEINFELD, G.: "Testing of Zinc Ferrite H_2S Absorbent in a Coal Gasifier Sidestream", Proc. Fourth Ann. Mtg. on Contaminant Control in Hot Coal-Derived Gas Streams, DOE/METC/85-3, Morgantown, (1984), 314
6) BISSET, T.B., STICKLAND, L.D.: "Analysis of a Fixed-Bed Gasifier IGCC Configuration" Ind. Eng. Chem. Res., 30 (1991), 170
7) GANGWAL, S.K., HARKINS, S.M., BOSSART, S.J.: "Bench-Scale Testing of High-Temperature Desulfurization Sorbents" Environmental Progress, 8 (1989), 265
8) GRINDLEY, T., STEINFELD, G.: "Development and Testing of Regenerable Hot-Coal-Gas Desulfurization Sorbents", Proc. Sec. Ann. Mtg. on Contaminant Control in Hot Coal-Derived Gas Streams, DOE/METC/82-47, Morgantown, (1982), 332
9) WOODS, M.C., GANGWAL, S.K., HARRISON, D.P., JOTHIMURUGESAN, K.: "Kinetics of the Reactions of a Zinc Ferrite Sorbent in High-Temperature Coal Gas Desulfurization", Ind. Eng. Chem. Res., 30 (1991), 100
10) AYALA, R.E., KIM, B.M.: "Modeling and Analysis of Moving-Bed Hot-Gas Desulfurization Processes", Environmental Progress, 8 (1989), 19
11) GRINDLEY, T.: "The Effect of Temperature and Pressure on the Regeneration of Zinc Ferrite Desulfurization Sorbent", Proc. Sixth Ann. Mtg. on Contaminant Control in Hot Coal-Derived Gas Streams, DOE/METC/86-6042, Morgantown, (1986), 190
12) PAVLJUKHIN, Yu.T., MEDIKOV, Ya.Ya., BOLDYREV, V.V.: "Magnetic and Chemical Properties of Mechanically Activated Zinc and Nickel Ferrites Mat. Res. Bull., 18 (1983), 1317
13) PAVLJUKHIN, Yu.T., MEDIKOV, Ya.Ya., BOLDYREV, V.V.: "On the Consequences of Mechanical Activation of Zinc and Nickel Ferrites" J. Solid State Chem., 53 (1984), 155
14) PAVLJUKHIN, Yu.T.: "Mechanical Activation of Solids with Close-Packed Structures" Izv. Sib. Otd. Akad. Nauk SSSR, Ser. Chim. Nauk, 4 (1987), 45 (in Russian)
15) ERMAKOV, A.E., YURCZIKOV, E.E., ELSUKOV, E.P., BARINOV, V.A., CZUKALKIN, Yu.T.: "Transition "Order-Disorder" in the Process of Mechanical Grinding of Zinc Ferrite", Solid State Physics, 24 (1982), 1947 (in Russian)

16) KRUPICKA; S.: Physics of Ferrites and Relative Oxides, Acedamia, Prague 1969
17) PAVLJUKHIN, Yu.T., RYKOV, A.I., BOLDYREV, V.V., MEDIKOV, Ya.Ya.: ''Structural Transformations in Oxides with Close-Packed Sublattice during Mechanical Activation'' Proceedings of the Second Japan-Soviet Symposium on Mechanochemistry, Tokio, (1988), 119
18) RYKOV, A.I., PAVLJUKHIN, Yu.T., MEDIKOV, Ya.Ya.: ''Mechanical Disordering in Ferrites with Spinel and Perovskite Structure'' Proc. Indian. Natn. Sci. Acad., 55 (1989), 721
19) SEPELÁK, V., TKACOVA, K., RYKOV, A.I.: ''Rietveld Analysis of Mechanically Activated Powdered Zinc Ferrite'' Cryst. Res. Technol., 28 (1993), 53
20) HEINICKE, G., HENNIG, H.-P., LINKE, E., STEINIKE, U., THIESSEN, K.P.: ''Tribochemistry'', Akademie-Verlag, Berlin 1984
21) STEINIKE, U., HENNIG, H.-P.: ''Mechanically Induced Reactivity of Solids'' KONA, 10 (1992), 15
22) TKACOVA, K.: Mechanical Activation of Minerals, Elsevier, Amsterdam 1989
23) BOLDYREV, V.V., BULENS, M., DELMON, B.: The Control of the Reactivity of Solids, Elsevier, Amsterdam 1979
24) AVVAKUMOV, E.G.: Mechanical Methods of Activation of Chemical Processes, Nauka, Novosibirsk 1986 (in Russian)
25) PAVLJUKHIN, Yu.T., MEDIKOV, Ya.Ya., AVVAKUMOV, E.G., BOLDYREV, V.V.: ''Mössbauer Investigation of the Defect Formation in Oxide Systems after Mechanical Activation'' Izv. Sib. Otd. Akad. Nauk SSSR, Ser. Chim. Nauk, 9 (1981), 11 (in Russian)
26) LI XIMING, CHEN JIAYONG, KAMMEL, R., PAWLEK, F.: ''Effect of Mechanical Activation by Fine Grinding on the Leaching Behaviour of Zinc Ferrite'' Proceedings of the Ist. International Conference on Mechanochemistry, (Ed. Tkacova et al.) Cambridge Interscience Publishing, Cambridge, (1993)
27) FIALA, J.: ''Algebraic Conception of the Powder-Diffraction Identification System'' Appl. Phys., 5 (1972), 1874
28) FIALA, J.: ''Optimization of Powder-Diffraction Identification J. Appl. Cryst., 9 (1976), 429
29) WUTZLER, R., STEINIKE, U., LORENZ, P., ROSAHL, B.: ''Keramikfilter für die Heißgasentschwefelung'' Brennstoff-Wärme-Kraft (VDI-Verlag) 45(1993) 477
30) SEPELÁK, V., TKACOVA K., BUCHAL, A.: ''Thermal Relaxation of Mechanically Induced Defects in Ferrites'' International Journal of Mechanochemistry and Mechanical Alloying, (1993) accepted.
31) KRISHNAN, G.N., TONG, G.T., LAMOREAUX, R.H., BRITAIN, R.D., WOOD, B.J.: ''A Study of Sulfate Formation During Regeneration of Zinc Ferrite Sorbents'' Proc. Fifth Ann. Concractors Mtg. on Contaminant Control in Hot Coal-Derived Gas Streams, DOE/METC/85-6025, Morgantown, (1985), 6
32) GRINDLEY, T., KIM, S.S., GORSKI, E.E., STEINFELD, G.: ''Aspects of the Design of a Process Development Unit for High-Temperature Coal Gas Desulfurization'' Proc. Fifth Ann. Concractors Mtg. on Contaminant Control in Hot Coal-Derived Gas Streams, DOE/METC/85-6025, Morgantown, (1985), 33
33) LAMOREAUX, R.M., BRITAIN, R.D., ZEIGER, J., LEACH, S.C.: ''Determination of Solid Phase Boundaries in Coal Gas Desulfurization by Zinc Ferrite'' Technical Report DOE/MC/21096-2192, U.S. Department of Energy/METC, Morgantown, (1986)

Author's short biography

Dr. Vladimír Sepelák

Vladimír Sepelák studied physics at the Safarik University, Kosice. He obtained his doctorate (RNDr.) 1986 in the field of solid state physics. Since 1986 he is working in the Institute of Geotechnics of Slov. Academy of Sciences, Kosice. He is postgraduate student in the Institute of Solid State Chemistry of the Russían Academy of Sciences, Novosibirsk.
As a specialist in X-ray diffraction analysis he has published about 30 papers mainly devoted to a study of structural metastability in solids, especially ferrites.

Prof. Dr. habil. Ursula Steinike

Ursula Steinike studied mineralogy, special direction crystallography at Humboldt University, Berlin. She obtained her doctorate (1961) and the postdoctoral lectury qualification (1969) in the field of crystal growth.
Since 1976 she is professor for crystallography and X-ray diffraction.
More than 25 years she is working on the field of X-ray powder diffraction in connection with the development of special substances like catalysts and sorbents. Mechanically activated substances played an important role.
She has about 100 publications and is editor of the German Crystallography-News.
She is the head of the group for structure analysis and surface science in the Institute of Applied Chemistry, Berlin-Adlershof.

Doris-Christiane Uecker

Doris-Christiane Uecker is working at the Institute of Applied Chemistry Adlershof in Berlin in the function materials group. After studying crystallography at the Humboldt University of Berlin she went to the Institute of Physical Chemistry of the Academy of Sciences in Berlin. Since that time she dealt with X-ray investigations of solid state reactions of inorganic materials. At the Institute of Applied Chemistry she connects this fields with problems of the desulfurization of hot coal gases.

Hydrodynamic Modeling of Swirling Flow and Particle Classification in Large-Scale Hydrocyclones†

Raj K. Rajamani and Balaji Devulapalli
*Comminution Center, University of Utah**

1. Introduction

The fluid flow in a hydrocyclone is extremely challenging from the modeling point of view, because the flow field is a vortex flow with flow reversal. Furthermore, there exists a great need to predict the particle size classification efficiency in this device. The mining and chemical industries use hydrocyclones in large numbers wherever there is need to separate fines from coarse particles. Due to the complexity of the flow, early researchers took the empirical approach of relating key operating variables with classification efficiency. Although the empirical models were very successful in size classification predictions, they could not be used universally since such models are confined to the bounds of data from which they were developed and their applicability diminished even further when models developed at a given site were used in other situations. Consequently, models based on the physics of fluid flow began appearing in the literature, from those incorporating very simple ideas at first to very detailed models requiring numerical solutions in recent years. In this manuscript we present such a model which uses all the known principles of fluid flow as much as possible, leaving only the turbulence closure to empiricism, as this phenomenon is still unsolved in the larger context of fluid mechanics.

The complete fluid-flow based model lends itself as a computer-aided design software for hydrocyclone, not merely confined to the traditional cylinder plus cone design but to explore newer geometries as well. In fact the traditional design suffers from a few inherent flaws. The numerical modeling approach is well suited to examining with ease the classification performance of conceptual designs. For this reason the model must be perfected to the point where it can predict traditional industrial hydrocyclones for different slurry properties and device designs.

1. Background Literature

Fortunately, the physics of fluid flow in hydrocyclones has been the subject of investigation in the last decade as reviewed by Chakraborti and Miller (1992), and so the key ideas in modeling have been forthcoming steadily. Leaving aside the early investigations of measuring fluid-flow with mechanical aids and dyes, and also early works which had some semblance to the Navier-Stokes momentum balance equations, we come to the work of Bloor and Ingham (1987), who gave an analytical solution to the Navier-Stokes equations, albeit for overly simplifying assumptions. In the region near the central axis, the vortex conservation was applied, with inviscid and rotational flow assumptions, which yields axial and radial components. In the region along the wall the boundary-layer approach was used to derive velocities. Despite Bloor and Ingham's efforts in predicting velocity data measured by Kelsall (1952), a data set often referred to in numerous publications, the lack of an adequate turbulence description led others to revise the analytical solutions as necessary. The first successful work in predicting the fluid flow in hydrocyclones is that of Pericleous and Rhodes (1986), who used the PHOENICS computer code for the solution of the partial differential equations. Using the simple Prandtl mixing length model and the axisymmetry assumptions, the authors reported the velocity predictions in a 200-mm hydrocyclone. Later, Hsieh and Rajamani (1991) numerically solved the turbulent momentum equations to obtain the velocities and compared them with the Laser Doppler Velocimetry measurements in a 75-mm hydrocyclone. The success of this comprehensive work may be attributed to the Prandtl mixing-length model assumed in this work, to be described later in this manuscript. This work showed that, by a simple balance of forces on a particle present in the flow field, the trajectory of the particle can be traced inside the hydrocyclone, from which the entire size-classification efficiency is computed. In a sequel, Monredon, Hsieh and

---

* 306 WBB, Salt Lake City, UT 84112, U.S.A
† Received Sep. 1, 1994

Rajamani (1992) showed that the same model is evidently applicable even if the vortex finder and spigot dimensions were changed drastically besides the operating conditions. All of these modeling works have been confined to hydrocyclones processing slurries in the 5 to 10 % solids range, and so Rajamani and Ludovic (1992) took a further step in the direction of higher percent solids, reporting that volume concentration of a particle in a computational cell is proportional to the residence time of that particle within that cell. This idea extended the numerical model to an iterative scheme, with which the spatial concentration distributions were predicted. Notable among the numerical modeling works is that of Davidson (1994), who modeled the multiphase flow by treating the fluids and solids as interpenetrating continua, from the constitutive relations for solid-liquid mixtures developed by Roco (1990). The treatment of solid particles as an interpenetrating continuum of liquid is a pioneering approach that has been proved successful in slurry flow in pipes. Davidson's use of these concepts in hydrocyclone modeling awaits further experimental confirmation. Nevertheless, it brings about the importance of Bagnold and turbulent diffusive forces exerted by the dense suspension of particles near the walls.

The modeling of turbulence is much needed because it disperses the classified particles. In the larger context of modeling thus far, turbulence has been dealt with a linear algebraic stress model, and as far as particle phase is concerned a diffusion-type model is used. Dyakowski and Williams (1992) have carried out a detailed analysis of turbulence in small diameter hydrocyclones. In the fluid mechanics literature it is very common to describe the turbulent quantities by the k-ε model, but Dyakowski and Williams (1992) pointed out that the equality of normal Reynolds stresses presumed in the k-ε model is questionable in small diameter hydrocyclones due to the extreme curvature of streamlines as well as the presence of high swirl. The authors proposed a revised k-ε model, incorporating both partial differential and algebraic equations for Reynolds stresses.

Indeed such cumbersome numerical solution of mean flow and turbulence is largely unnecessary for modeling size-classification in hydrocyclones. Barrientos and Concha (1992) used the analytical solutions of Bloor and Ingham (1987) with a set of data from an operating hydrocyclone to determine a few unknown constants. While the model has been confirmed in 150-mm diameter hydrocyclones, this work too must await more experimental confirmation in larger diameter hydrocyclones. Hwang et al. (1993) too used Bloor and Ingham's inviscid flow analytical solutions to verify velocities measured in a 60-mm hydrocyclone. There is some merit in these analytical solutions, but their applicability seems to be device specific, in other words limited to the data set from which the constants were estimated.

There is second major issue in modeling vortex flow in a hydrocyclone. It is the size and the stability of the air core. The air core occupies space along the central axis, and hence it inherently regulates flow out of the spigot and vortex finder. In the extreme, at very high inlet flow rates the air core can completely occupy the spigot opening, causing all the flow to reverse toward the vortex finder, resulting in substantial degradation in size-classification efficiency. Until recently, this issue has been set aside because solving the Navier-Stokes equations itself posed a challenge. Hsieh and Rajamani (1991) and Davidson (1994) specify the diameter of the air core in their numerical calculations. Pericleous and Rhodes (1986) intentionally keep numerous air bubbles along with the particles in the numerical solution. The air bubbles naturally migrate to the central axis forming the air core, and hence its dimension falls out of the numerical calculation. However, the stability of such a numerical procedure is questionable, according to Davidson (1994). Barrientos et al. (1993) computed the air core diameter by balancing the viscous forces and surface tension force at the air/water interface. This is a plausible explanation but needs more experimental validation. An alternative is to solve the complete Navier-Stokes equations for air core diameter as done by Steffens et al. (1993). These authors computed the air core sizes by simplifying the hydrocyclone geometry to a flat cylinder with a radial inlet and one central outlet. Until data on hydrocyclones operating with high concentration of solids appear, Steffens solution can be regarded as valid for water flows only. Even though the stability and the nature of the air core surface is of minimal importance in modeling, yet further understanding depends on detailed studies. In this direction Williams et al. (1994) have used Electrical Impedance Tomography (EIT) to map the oscillating air core as well as its dimensions. In summary, the physics of air core is at its infancy but is expected to develop very rapidly. A rigorous method of computing the air core diameter while computing velocities is shown in this manuscript.

This paper describes the development of the fluid-flow model and provides model verification with experimental data collected in a 250-mm hydrocyclone. The experimental data includes both velocity measurements with a Laser Doppler Velocimetry and particle size classification measurements in a sump-pump recirculation system.

2. Transport Equations

The flow field is essentially symmetric except in the region of the inlet. Symmetric flow field is established about halfway in the cylindrical part. Hence axisymmetry (Pericleous and Rhodes, 1986; Davidson, 1994; Dyakowski and Williams, 1992) is a useful assumption that reduces the fluid-flow problem to two dimensions. In the computational model the fluid is assumed to enter through a full 360° ring inlet instead of the single tangential inlet tube. The governing equations are written in vorticity stream-function form to avoid the pressure balance during computations. For two-dimensional incompressible turbulent flow with constant properties, the dimensionless transport equations are as follows:

Vorticity :

$$\frac{\vartheta \eta}{\partial t} = \frac{}{r^3}\frac{\partial \Omega^2}{\partial z} - \frac{\partial u\eta}{\partial r} - \frac{\partial w\eta}{\partial z} + \frac{1}{Re}\left[\frac{\partial^2 \eta}{\partial r^2} + \frac{1}{r}\frac{\partial \eta}{\partial r} - \frac{\eta}{r^2} + \frac{\partial^2 \eta}{\partial z^2}\right] \tag{1}$$

Stream function :

$$\frac{\partial^2 \Psi}{\partial r^2} - \frac{1}{r}\frac{\partial \Psi}{\partial r} + \frac{\partial^2 \Psi}{\partial z^2} = -r\eta \tag{2}$$

Angular spin velocity :

$$\frac{\partial \Omega}{\partial t} = -\frac{\partial u\Omega}{\partial r} - \frac{u\Omega}{r} - \frac{\partial w\Omega}{\partial z} + \frac{1}{Re}\left[\frac{\partial^2 \Omega}{\partial r^2} - \frac{1}{r}\frac{\partial \Omega}{\partial r} + \frac{\partial^2 \Omega}{\partial z^2}\right] \tag{3}$$

and

$$\frac{1}{r}\frac{\partial \Psi}{\partial r} = w, \quad -\frac{1}{r}\frac{\partial \Psi}{\partial z} = u, \quad \frac{\Omega}{r} = v. \tag{4}$$

Here Re is the Reynolds number defined as $R_c U_o / \nu$. The normalization constant used here is the advective time scale R_c / U_o, where R_c is the hydrocyclone radius and U_o is the mean inlet velocity.

3. Turbulent Transport

The k-ε model is often found in recent literature, as it models the generation and dissipation of turbulent kinetic energy by means of partial differential equations akin to that of Navier-Stokes equations. However, this model in its standard form is not applicable in hydrocyclones, since the high swirling flows impose anisotropic turbulence. Therefore, the revised k-ε model of Dyakowski and Williams (1992) with an algebraic Reynolds stress model as proposed by Boysan et al. (1982) seems like the most appropriate in this direction. However, the use of the k- ε model entails solving three more partial differential equations which require at least five empirical constants. To avoid this extra numerical effort, one tries the simpler Prandtl mixing length model first. It relates the turbulent transport terms to the gradient of the mean flow quantities. For two-dimensional boundary-layer flows, particularly those developing over rigid boundaries, the mixing-length offers both accuracy and numerical simplicity. The mixing length model used in the present model uses the following expression for turbulent viscosity:

$$\mu_t = \varrho_m \lambda^2 \left[\left| \frac{\partial v}{\partial r} - \frac{v}{r} \right| + \left| \frac{\partial w}{\partial r} \right| \right] \tag{5}$$

Equation 5 uses a single unknown parameter, the mixing length λ, which is the characteristic length scale of turbulence and whose dependence over the flow field must be prescribed only with empirical information. In this work we consider that the mixing length varies both radially and axially and that separate expressions should be prescribed for swirling and non)swirling components as follows (Hsieh and Rajamani, 1991):

$$\lambda_n = 0.010\, R_c \left(\frac{\mu_m}{\mu_o}\right)^{1/5} \left(\frac{R_z}{R_c}\right)^{1/4} \left(\frac{R}{R_c}\right)^{1/2} \tag{6}$$

$$\lambda_\Omega = 0.015\, R_c \left(\frac{\mu_m}{\mu_o}\right)^{1/5} \left(\frac{R_z}{R_c}\right)^{1/4} \left(\frac{R}{R_c}\right)^{1/2} \tag{7}$$

where R_Z is the radius of the hydrocyclone at the horizontal level of the numerical mesh, μ_m is the viscosity of the slurry, and μ_o is the viscosity of water. Indeed the above model holds good in experimental studies of a 75-mm hydrocyclone and its design variations (Monredon et al., 1992). The same model is being used to describe the turbulent quantities in a 250-mm hydrocyclone, and its adequacy and validity is beyond the scope of this study.

4. Numerical Solution

The physical dimensions of the actual hydrocyclone are explicitly specified in the numerical solution, and the entire domain is divided into a rectangular grid system. A 180 × 98 grid system covering a half view of the hydrocyclone, as seen in **Figure 2**, was sufficient for the solution. Such a grid system results in a grid spacing of 1.25 mm in the radial direction and 4 mm in the axial direction.

The fluid dynamic equations are a set of coupled parabolic and elliptic differential equations. Equations 1 and 3 are parabolic and pose an initial value problem, while equation 2 is elliptic and poses a boundary value problem. The parabolic equations are solved with the Hopscotch method, and the elliptic equation is solved by the Successive Over-Relaxation method (Hsieh, 1988).

5. Experimental Work

There are two kinds of experiments in this modeling study: Particle size classification experiments and liquid phase velocity measurements. In the size classification experiments, a KREBS D10B (250-mm diameter) hydrocyclone was installed in a sump-pump recirculation system. **Table I** and **II** shows the dimensions of the hydrocyclone and the operating conditions along with two sets of vortex finders and spigots used in this study. Experiments were done at various flow rates and solids concentrations Boththe overflow and underflow streams were sampled, and the size distributions as well as percent solids and respective flow rates were measured The size-classification efficiencies were determined from the test results by calculating the fraction of the feed reporting to the underflow for each size interval Duplicate tests exhibit a scatter of ±5% error in the experimental results.

The velocity measurements were done with a TSI Laser Doppler Velocimetry (LDV) system. A schematic drawing of the LDV)pump)sump hydrocyclone rig is shown in **Figure 1**. A 100-mW argon-ion laser (ILT model 5500A) generated a coherent light source. The laser beam passed through a beam splitter (TSI model 9115), which splits the laser beam into two parallel, equal intensity beams. Beam spacing was fixed by the prism design. One of the split beams passes through a Bragg cell which shifts the frequency by 40 MHz. The flow direction is detected by downmixing the required frequency to 40 MHz with the help of the frequency shifter (TSI model 9186A). The frequency shifter also helps in the measurement of low-velocity flow, removes the pedestal frequency and reduces the fringe bias. The intersecting beam measurement volume is a 1.997mm × 0.1997mm ellipsoid. Back-scattering alignment was chosen because of the presence of the air core at the center of the hydrocyclone. The output signals from the photomultiplier are sent to the signal processor (TSI IFA 550) which filters the signal, digitizes and transmits the Doppler frequency to the computer. The computer software displays the velocity spectrum measured at that point. The entire LDV system is mounted on a three-dimensional traverse system which allowed the probe volume to be positioned with ±0.5 mm resolution.

Table I. Dimensions of the Experimental Hydrocyclone

Diameter of the hydrocyclone	250 mm
Diameter of the inlet	75 mm
Length of the vortex finder	160 mm
Length of the cylindrical section	412.5 mm
Diameter of the vortex finder	
Series I	100 mm
Series II	62.5 mm
Diameter of the apex	
Series I	50 mm
Series II	43.75 mm
Included cone angle	12°

Table II. Experimental Operating Conditions

	Series I	Series II
Pressure Drop (KPa)	21	28
Feed Flow Rate (Kg/min)	550	557
Overflow Rate (Kg/min)	476	425
Underflow Rate (Kg/min)	74	132

6. Experimental Results

A few qualitative observations can be made with LDV measurements. The tangential velocity profiles in four different planes along the axis are shown in **Figure 2**. These profiles always exhibit a forced vortex near the air core and a free vortex thereafter. The slopes of the forced vortex region are nearly the same throughout the axis, suggesting the inviscid nature of the flow in the central region. In all the four planes shown, the tangential velocity reaches a maximum of about 8 m/s, which corresponds to

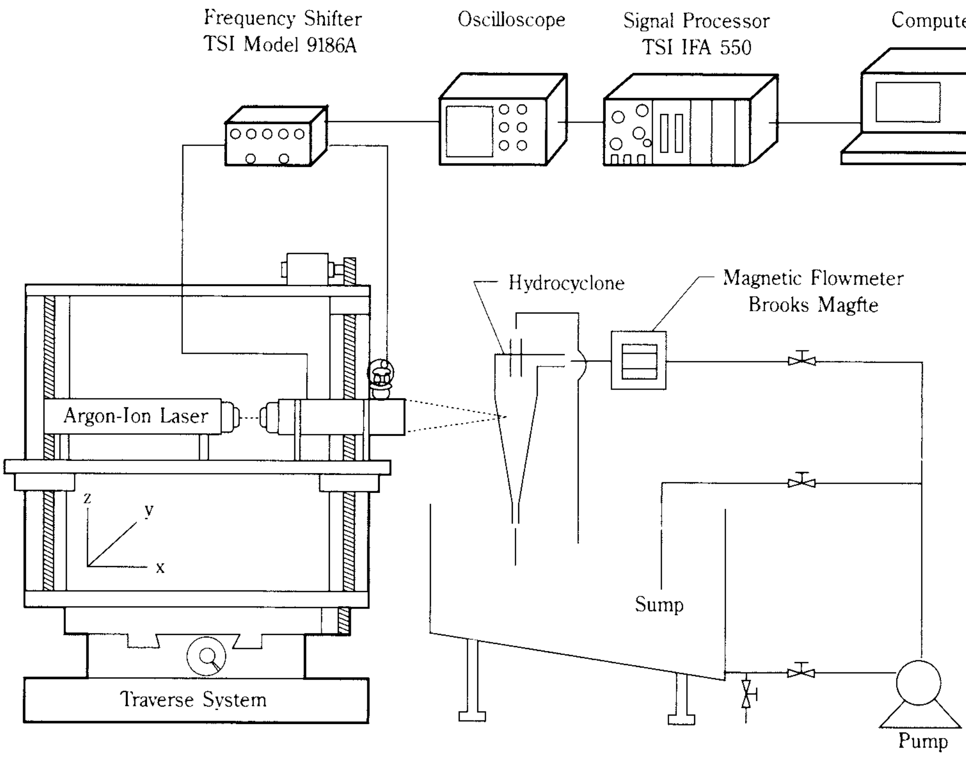

Fig. 1. Schematic of the Hydrocyclone and the LDV System

a centrifugal force of 210 g. Hence the centrifugal force overwhelms the gravitational force, even more in smaller diameter hydrocyclones. The gradient of the forced vortex in the conical section is nearly the same as that in the cylindrical section. Since the cone narrows downwards the increase in tangential velocity is compensated by frictional dissipation of momentum, hence the constant gradient.

The measured axial velocities for Series I and II are shown in **Figure 3**. Not shown here is the asymmetry observed near the inlet as well as the apex region, but everywhere else symmetry prevails. In fact multiple flow reversals were observed in the horizontal planes over the vortex finder in a 75-mm hydrocyclone (Hsieh and Rajamani, 1991). The vortex flow spirals downward along the cone walls, and since the cone narrows, part of the flow in the central column spirals upwards. As two flows interact, multiple flow reversals occur. The axial velocities decrease rapidly toward the air core, presumably to zero at the air/water interface. But the LDV is unable to measure the velocities in the vicinity of the air core surface since the air core vibrates continuously.

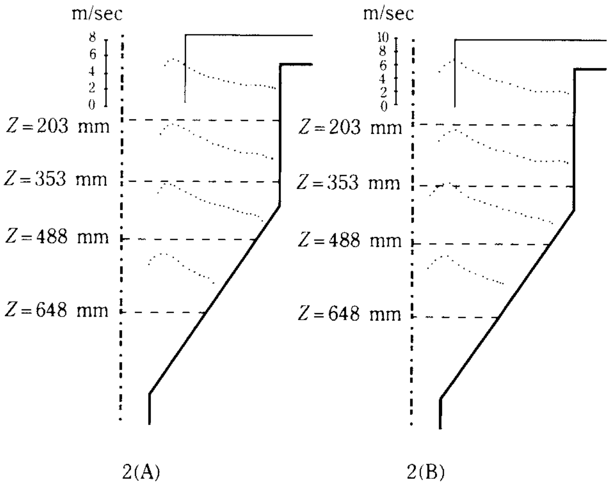

Fig. 2 LDV Measurements of the Tangential Velocity Profiles. 2(A) for Series I; 2(B) for Series II.

The generation and dissipation of turbulence is interesting from the point of view of fluid dynamics in the hydrocyclone. However, not much can be gained without restoring to complex turbulence models. The measured turbulent fluctuating components of both tangential and axial velocities at 203 mm and

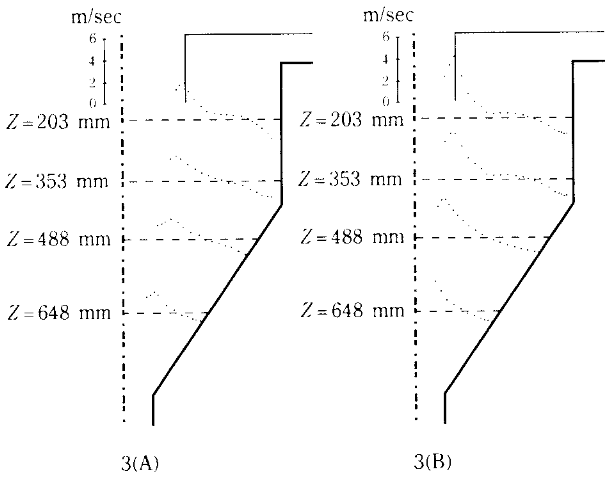

Fig. 3 LDV Measurements of the Axial Velocity Profiles. 3(A) for Series I; 3(B) for Series II.

488 mm from the top are shown in **Figure 4**. The fluctuating components are relatively constant in the main body except when approaching the wall or the air core. It is very obvious that the vibrating air core is the cause for high fluctuating components in that region, but near the wall the signal to noise ratio of the LDV signals itself may have contributed to the rapid rise in fluctuations. What is important to this modeling study is the effect due to the presence of solid particles on turbulent fluctuations. Since LDV measurements are currently confined to transparent liquids only, this point could not be investigated any further. One would expect the fluctuating components to diminish in magnitude as the streams gets weighed up by solid particles.

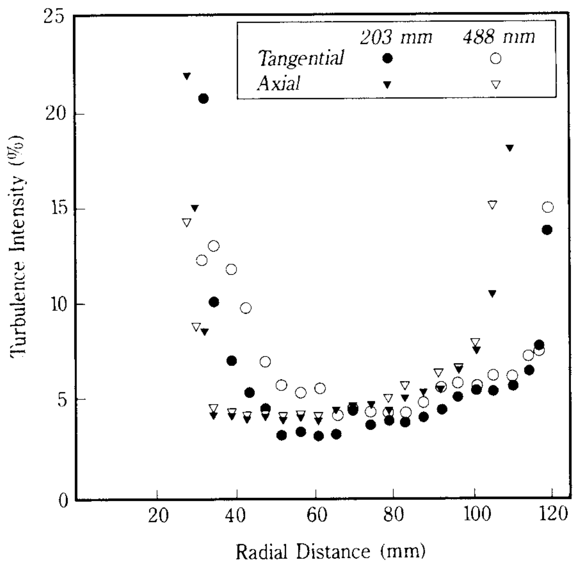

Fig. 4. Measured Turbulence Intensity Averaged over Mean Velocity for Series I.

Finally, the radial velocity could not be measured at all reliably with the LDV, since its magnitude is of the order of 10 cm/sec. Hence this component was computed by applying the continuity condition.

7. Predicted Velocity Profiles

The purpose of predicting velocity profiles is to verify the assumed form of the Prandtl mixing-length model and check the relevancy of the boundary conditions. The ability to predict the flow field leads to accurately predicting solid particle trajectories. The LDV data and predicted tangential velocities are shown in **Figure 5**. It is seen there is good quantitative agreement both in the forced- and free-vortex regions. The gradients and the peak velocities are also accurately predicted at each horizontal level.

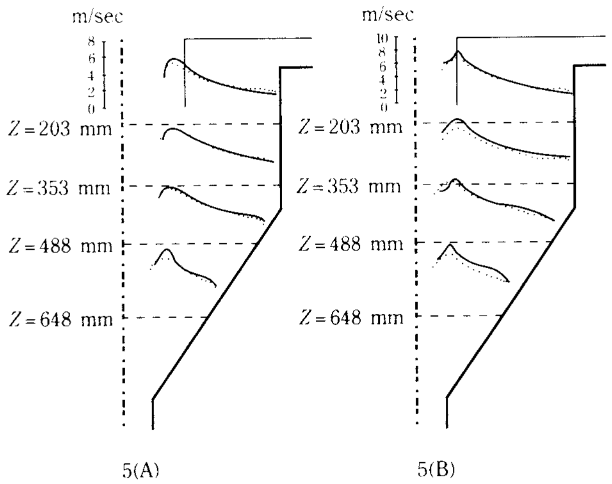

Fig. 5. Measured and Predicted Tangential Velocities. 5(A) for Series I; 5(B) for Series II.

Figure 6 shows the LDV data and predictions of axial velocities. It is evident that the model is able to track the upward flow in the center and downward flow along the wall. There is a slight discrepancy in the conical part: There is a small lateral shift in the loci of zero axial velocity, and the predicted maximum axial velocity is shifted toward the air core more than the LDV data would indicate. The flow patterns near the air core, where the axial velocities rapidly tend to zero, are also well predicted.

The excellent velocity predictions thus achieved are singularly attributed to the form of the empirical

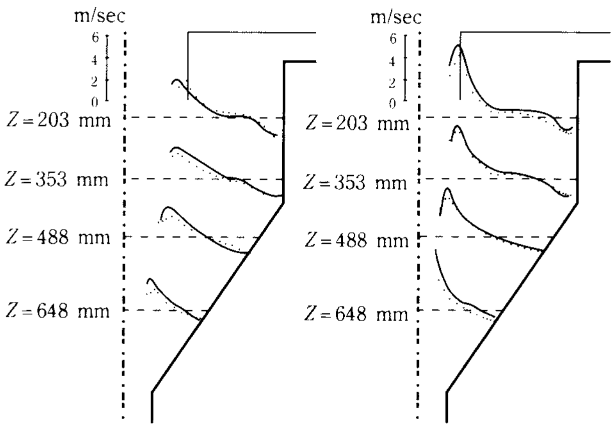

6(A) 6(B)

Fig. 6. Measured and Predicted Axial Velocities. 6(A) for Series I; 6(B) for Series II.

mixing length model. This model was arrived at after examining many others in the work done on a 75-mm hydrocyclone (Hsieh, 1988). Indeed the same formulation is used here in the 250-mm hydrocyclone, which confirms that the basic structure of turbulence generation and dissipation remains same in both smaller and larger hydrocyclones. It is reasonable to presume this is true also in much larger hydrocyclones of 625-mm diameter. Predicting velocities is the key to the hydrocyclone modeling, and it hinges squarely on the turbulent closure as is true in many other fluid dynamic applications.

8. Air Core Diameter

The diameter of the air core measured in Series I and II were about 70 mm just below the vortex finder and 60 mm at the apex. The entire envelope of the air core was specified in the numerical calculations to solve for the velocities. In the design and evaluation of industrial hydrocyclones operating with the slurries, the size of the air core is unknown and must be computed. Instead of taking highly simplified methods proposed by Barrientos et al. (1993) or Steffens et al. (1993), we use the Navier-Stokes equation combined with the turbulence closure model itself to determine air core diameter. The Navier-Stokes equation itself is a balance for viscous and body forces; hence the solution must satisfy zero pressure condition at the air core when the inlet pressure is specified. The only quantity that is missing in such an approach is the pressure jump across the air/liquid interface. In addition, the hydrocyclone entrains the central column of air through the apex and discharging through the vortex finder. Therefore there is a small but nonzero pressure gradient in the air column which is neglected here.

Once the velocity set has been solved for at all nodal points, the gradient of the pressure in the two directions can be easily determined by substituting the computed velocities in the Navier-Stokes equations. To make matters even easier the SIMPLER algorithm (Patankar, 1980) is used to calculate the pressure. The consistency of the pressure calculations can be verified by measuring pressure along the wall in addition to the inlet pressure. **Figure 7** shows the measured and predicted pressures. The agreement is consistent with the excellent velocity predictions reported in **Figures 5** and **6**. Curiously the pressure drops to zero at the air core boundary. Hence this pressure prediction can be used in the reverse manner to determine the envelope of the air core. First the calculations are begun with as small an air core as the grid spacing would permit. Then fixing the measured inlet pressure, the entire pressure profile is mapped over the whole domain. If the pressure at the presumed air core surface is greater than zero, the core must be widened in the next iteration and vice versa. The results of such calculations would be reported in the future.

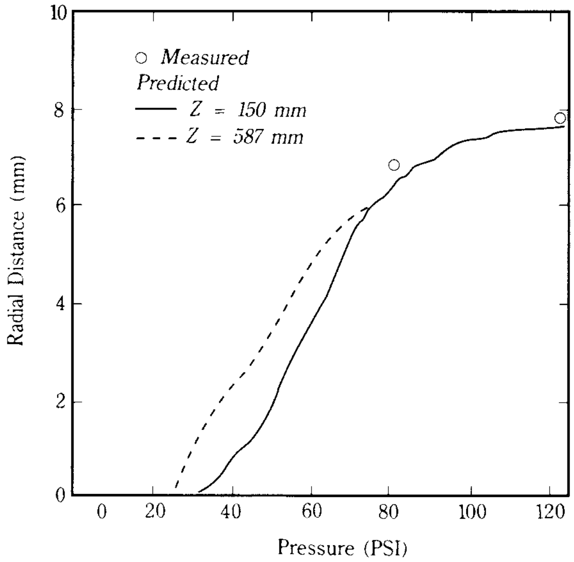

Fig. 7. Radial Pressure Distribution inside the Hydrocyclone for Series II.

9. Particle Size Classification Experiments

The ultimate aim of the modeling work is to predict the size classification performance of the hydrocyclone. The efficiency of the hydrocyclone is measured by the "size classification curve," which is a plot of particle size versus the fraction of the amount of the feed (in each particle size interval) reporting to the underflow.

Now, having solved the fluid dynamic equations for the water phase only, what is needed is a method of how particles migrate in the centrifugal field and exit via the apex or the vortex finder. Once particles are introduced in the fluid phase, the properties of the fluid phase change and there is some question about the validity of the computed velocity field. There are two ways to remedy this problem: The first one is to assume that the fluid is ''dilute,'' especially when the concentration of solids in the feed is less than 15 weight percent, in which case the fluid-flow problem and particle classification problem can each be solved independently of the other. To a large extent this approach works because, even if the feed concentration is high, particles quickly migrate to the wall, and so the central body of fluid surrounding the vortex finder and below it becomes very dilute. Therefore particle separation occurs in this dilute regime. In fact industrial hydrocyclones processing 40-55% by weight of solids discharge a thick slurry of 65-70% by wt. in the underflow and a mere 20% by wt. in the overflow. Since the overflow is made up of fluid migrating from all along the air core, it can be concluded that the central column is ''dilute'' within the hydrocyclone. Anyhow, the second and more rigorous method is to start with the water phase only, solve for particle concentrations, and iterate between the Navier-Stokes solution and the particle concentration calculations. A logical way of calculating the concentration is to determine the residence time of particles in a control volume and proportion the feed concentration to the nodal point with respect to its residence time among all the particles in the inlet (Rajamani and Milin, 1992).

Under the assumption of dilute inlet slurry the path of the particles from the inlet to one of the outlets is easily determined by computing the particle slip velocities. The balance between the centrifugal force and the radial drag force yields the radial slip velocity:

$$U_S = \left[\frac{4}{3}\left(\frac{\varrho_p-\varrho_m}{\varrho_l}\right)\frac{V^2}{R}\,\frac{d_p}{C_D}\right]^{1/2} \tag{8}$$

Similarly the balance between gravity and the axial drag force yields the axial slip velocity:

$$W_S = \left[\frac{4}{3}\left(\frac{\varrho_p-\varrho_m}{\varrho_l}\right)g\,\frac{d_p}{C_D}\right]^{1/2} \tag{9}$$

Since the axisymmetry assumption was used, the particle is considered to move along with the fluid in the azimuthal direction. With equations 8 and 9 the slip velocities at every grid point are calculated, and hence the trajectory of the particle phase is precisely calculated. Calculating the fraction of particles (in the feed) reporting to the underflow and repeating the above procedure for all sizes in the feed stream yields the classification curve.

The experimental and predicted classification curves for a feed solid concentration of 10% by wt. are shown in **Figures 8** and **9**. There is generally a good agreement, especially in the vicinity of the size at which 50% reports to underflow. The overall flow split to the underflow is also predicted well. However, there is a slight discrepancy in the fine particle range, which is due to the computed drag force in the fine particle size range being higher than what might have been the actual drag force. It is believed that the use of Reynolds number versus drag coefficient commonly found in the literature may be in error because these correlations are determined under

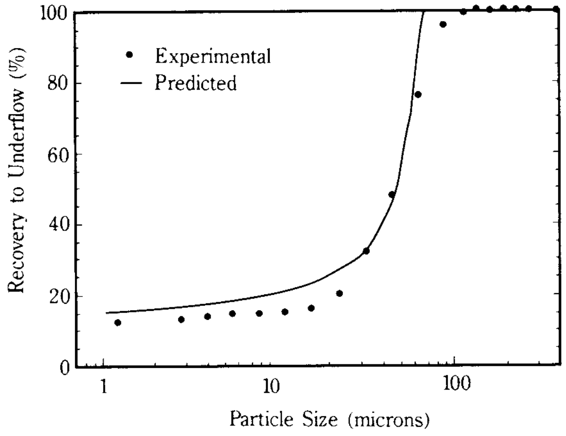

Fig. 8. Measured and Predicted Classification Curves for 10% Limestone by wt for Series I.

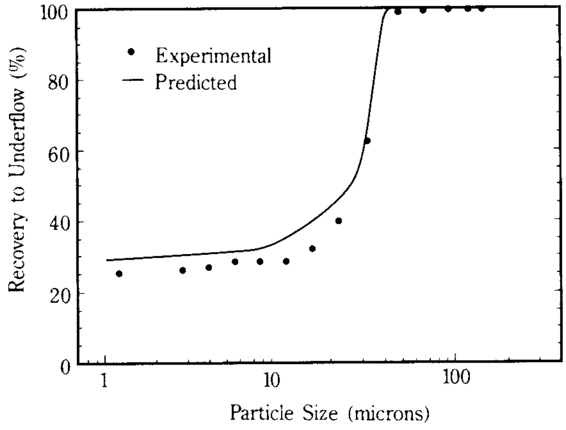

Fig. 9. Measured and Predicted Classification Curves for 10% Limestone by wt for Series II.

unit gravitational field, while the centrifugal field inside the hydrocyclone is of the order of a hundred times gravity. Also, turbulent diffusion which is not accounted for in this modeling work may contribute to fine particle migration. In the coarse size range too there is a slight discrepancy: This is due to the axisymmetry assumption in which the model does not account for the coarse particles passing via the boundary layer on the outer wall of the vortex finder, especially on the surface 180° from the inlet flow direction. Nevertheless, the predictions are more than satisfactory for industrial purposes.

10. Concluding Remarks

The fluid-flow model fully takes into account the design of the hydrocyclone as well as the slurry properties. The design of the hydrocyclone, such as the cone angle, vortex-finder diameter etc., are specified, and the initial/boundary conditions of the numerical procedure are assigned, which in turn influences the computed vortex flow. The concentration of solid particles influences the the slurry viscosity which in turn affects computed flows. This influence is more so in the iterative particle concentration model. If a correlation of particle size and particle concentration versus slurry viscosity is available, then the numerical model reported here accounts for the effect of particle size distribution also. Turbulent diffusion of particles in slurries is still an emerging field, and as correlations become available, they could be incorporated into the model. The only empiricism involved is in the formulation of the turbulence model. A fully mechanistic explanation of turbulence, such as direct simulation approach, is not anticipated in the immediate future. Being so, the model which holds well in the 75-mm and 250-mm hydrocyclones may in fact correctly describe even larger hydrocyclones.

Acknowledgments

This research has been supported by the Department of the Interior's Mineral Institute program administered by the U.S. Bureau of Mines throughthe Generic Mineral Technology Center for Comminution under grant numbers G1115149 and G1125249.

Nomenclature

C_D	drag coefficient
d_p	particle diameter, cm
R	radial distance from the axis of symmetry in cylindrical coordinates, cm
R_c	radius of the hydrocyclone, cm
R_e	Reynolds number of the hydrocyclone defined as $R_c U_O / \upsilon$
R_z	radius of the hydrocyclone at the horizontal level in consideration, cm
r	dimensionless radial distance from the axis of symmetry in cylindrical coordinates
t	dimensionless time
U_o	mean inlet velocity, cm/s
u	dimensionless radial velocity of the fluid
U_s	particle radial slip velocity, cm/s
V	tangential velocity of the fluid, cm/s
v	dimensionless tangential velocity of the fluid
W	axial velocity of the fluid, cm/s
w	dimensionless axial velocity of the fluid
W_s	particle axial slip velocity, cm/s
z	dimensionless axial distance from the roof of the hydrocyclone in cylindrical coordinates
λ	Prandtl mixing length, cm
ϱ_l	density of the fluid, g/cm^3
ϱ_m	density of the slurry, g/cm^3
ϱ_p	density of the particle, g/cm^3
μ_o	viscosity of water, g/cm-s
μ_m	viscosity of the slurry, g/cm-s
μ_t	turbulent viscosity, g/cm-s
υ	kinematic viscosity, cm^2/s
η	dimensionless vorticity
Ψ	dimensionless stream function
Ω	dimensionless angular spin velocity

References

1) Bloor, M. I. G., and Ingham, D. B., 1987, "The Flow in Industrial Cyclones," Journal of Fluid Mechanics, Vol. **178**, p. 507.
2) Barrientos, A., and Concha, F., 1992, "Phenomenological Model of Classification in Conventional Hydrocyclones," Comminution – Theory and Practice, SME 1992, Editor S. Komar Kawatara, p.287.
3) Barrientos, A., Sampaio, R., and Concha, F., 1993, "Effect of the Air Core on the Performance of a Hydrocyclone," Proc. XVIII Int. Mineral Processing Congress, Sydney, Australia, p. 267.
4) Chakraborti, N., and Miller, J. D., 1992, "Fluid Flow in Hydrocyclone: A Critical Review," Mineral Processing and Extractive Metallurgy Review, Vol. 11, p. 211.

5) Davidson, M. R., 1994, "A Numerical Model of Liquid-Solid Flow in a Hydrocyclone with High Solids Fraction," ASME Fluids Engineering Conference, FED-VOL. 185, p. 29.
6) Dyakowski, T., and Williams, R. A., 1994, "Validation of Particle Concentration Distribution within a Hydrocyclone by using a Tomographic System," First International Particle Technology Forum, Vol. 1, p. 24.
7) Dyakowski, T., and Williams, R. A., 1992, "Modelling Turbulent Flow within a Small-Diameter Hydrocyclone," Chem. Eng. Sci., Vol. 47, p. 1.
8) Hsieh, K. T., 1988, "Phenomenological Model of the Hydrocyclone," Ph.D. thesis, University of Utah, Salt Lake City, UT 84112.
9) Hsieh, K. T., and Rajamani, R. K., 1991, "Mathematical Model of the Hydrocyclone Based on Physics of Fluid Flow," AIChE Journal, Vol. 37, p. 735.
10) Hwang, C. C., Shen, H. Q., Zhu, G., and Khonsari, M. M., 1993, "On the Main Flow Pattern in Hydrocyclones," Journal of Fluids Engineering, Vol. 115, p. 21.
11) Kelsall, D. F., 1952, "A Study of the Motion of Solid Particle in a Hydraulic Cylcone," Trans. Instn. Chem. Eng, Vol. 58, p. 33.
12) Patankar, S., 1980, "Numerical Heat Transfer and Fluid Flow," Hemisphere Publ. Cor.
13) Monredon, T. C., Hsieh, K. T., and Rajamani, R. K., 1992, "Fluid Flow Model of the Hydrocyclone: An Investigation of Device Dimensions," Int. J. Min. Proc, Vol. 35, p. 65.
14) Pericleous, K. A., and Rhodes, N., 1986, "The Hydrocyclone Classifier – A Numerical Approach," Int. J. Min. Proc, Vol. 17, p. 23.
15) Rajamani, R. K., and Milin, L., 1992, "Fluid-Flow Model of the Hydrocyclone for Concentrated Slurry Classification," 4th International Conference on Hydrocyclones, Southampton, England, p. 95.
16) Roco, M. C., 1990, "Turbulent Flow of Incompressible Mixtures," Encyclopedia of Fluid Mechanics, Gulf Publ.Co., Vol. 10, p. 748.
17) Steffens, P. R., Whiten, W. J., Appleby, S., and Hitchins, J., 1993, "Prediction of Air Core Diameters for Hydrocyclones," Int. J. Mineral Processing, Vol.39, p. 61.

Author's short biography

Raj K. Rajamani

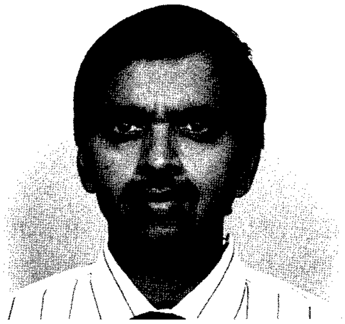

Prof. Raj K. Rajamani has been at the University of Utah, USA since 1979. His research interest lies in particle comminution, powder processing, and vortex flow in particle classifiers. He holds B.S. and M.S. degrees in Chemical Engineering and a Ph. D. in Metallurgical Engineering.

Balaji Devulapalli

Balaji Devulapalli is a graduate student in Metallurgical Engineering at University of Utah, U.S.A. Before joining University of Utah, he worked as a process engineer for a year at Sundaram Fasteners Ltd, India. His areas of research include particle separation methods, particle characterization using light scattering techniques, numerical simulation of two-phase flows and flow measurement techniques using laser doppler anemometry. He is currently a member of SME, TMS and ASME.

Measuring the Fractal Dimensions of Fume Aerosols in situ Using Light Scattering†

I. Colbeck
*Institute of Aerosol Science, University of Essex,**

1. Introduction

Many workers have found it convenient to work with what is defined as the boundary fractal of the agglomerate, obtained from the two dimensional projection of the structure. Others have studied the internal structure of agglomerates and obtained the mass or density fractal dimension. The boundary fractal dimension is generally less than the density fractal dimension as information is lost in the two dimensional image of a three dimensional object. In many studies rather drastic sample preparation techniques have been employed, starting with collection on a filter, and then perhaps resuspension in a liquid. The important structural information in delicate aggregates may not survive such preparations undistorted. Such sample preparation artifacts may be eliminated with in situ measurements. Numerous methods have been reported in the literature for colloidal particles (e.g. Raper and Amal, 1993) and aerosols which are then suspended in solution (Martin et al, 1986, Hurd et al., 1987); fewer have appeared for aerosols, in situ and we will only consider the latter.

2. Scattering methods

In situ optical techniques are highly desirable because of their ability to provide remote sensing in hostile environments. The amount of information regarding details of the structure of the particle clusters obtainable through optical techniques is significantly lacking compared with the straight forward concept of collection and visual examination by electron microscope. Both theoretical (Mountain and Mulholland, 1988) and experimental (Zhang et al., 1988, Gangopadhyay et al., 1991; Bonczyk and Hall, 1992) research has shown how it is possible to use light scattering to measure the mean size and fractal dimension. In systems without distinct surfaces scattering occurs from the bulk of the object and the fractal dimension relates mass, M, to radius of gyration, R_g, by MR_g^D. Objects obeying this relationship are mass fractals such as those formed by diffusion limited aggregation.

The principle of a scattering experiment is shown in **figure 1**. In a scattering experiment, a beam of light is directed onto a sample and the scattered intensity is measured as a function of scattering angle θ, to the incident direction. If the scattering object is a fractal of fractal dimension D then the intensity as a function of angle is given by $S(q) \sim q^{-D}$ *where* $S(q)$ is the scattered intensity (often called the structure factor) and q is the scattered wave vector, a wavelength λ, $q = 4\pi \lambda^{-1} \sin\theta/2$. This result is obtained under the approximation that multiple scattering with the aggregate is small, which is a good approximation for soot when the monomer size is small. This relation holds for $qR_g > 1$, but $S(q)$ is constant for $qR_g < 1$, and this crossover can be used to determine Rg, the radius of gyration. Since length scales in typical colloids or aerosols range from 10 nm for the monomer size to hundreds of nanometers for the cluster size, scattering of light is often used.

It is now possible by comparison of the well established scattering-extinction measurement of the mean size to cluster radius of gyration to yield the fractal dimension, the mean radius of its monomers and the mean number of monomers per cluster (Sorensen et al., 1992). This method is of use when qR_g is small and structure-factor measurements are inaccurate.

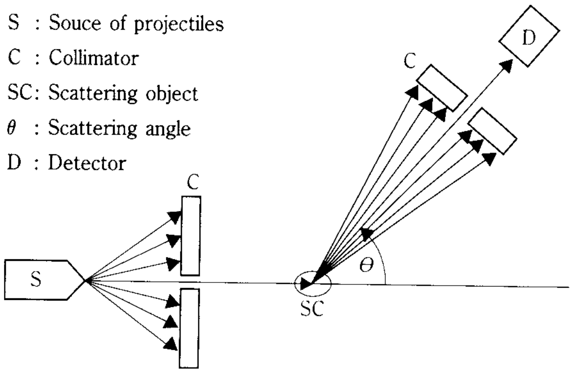

Fig. 1 The principle of a scattering experiment

---

* Colchester, C04 3SQ, UK.

† Received Sep. 20th 1994

3. Aerodynamic/mobility methods

Schmidt-Ott (1988) reported on a method which involves comparing the aerodynamic radii of the agglomerated particle before and after tempering. Tempering causes the agglomerate to collapse into close-packed clusters of $D = 3$. This technique is only valid for $D > 2$ in the free molecular regime. Kutz and Schmidt-Ott (1990) have described a method based on a comparison of the mobility equivalent radius, determined by differential mobility analysis, with the ratio of mass and drag, measured by a low pressure impactor. For silver agglomerates produced by heating silver up to 1000°C they found a fractal dimension of 2.06.

For one cluster falling with velocity v_1 and colliding with another moving with velocity v_2 the velocity of the resultant particle, v_3 is given by $v_1^\gamma + v_2^\gamma = v_3^\gamma$ where $\gamma = D/(D-1)$ (Zhangfa et al., 1994). Hence if measurements of v_1, v_2 and v_3 are made the fractal dimension may be obtained. To observe the process of kinematic coagulation and to measure the settling velocities a CCD camera with output to a video-recorder was used (**Figure 2**). The process of kinematic coagulation could then be traced and photographed from the recorded images. The fractal dimension for carbonaceous particles ranged from 1.61 to 2.38 with an average value of 1.97. For magnesium oxide the fractal dimension ranged from 1.10 to 1.41 with an average value of 1.19.

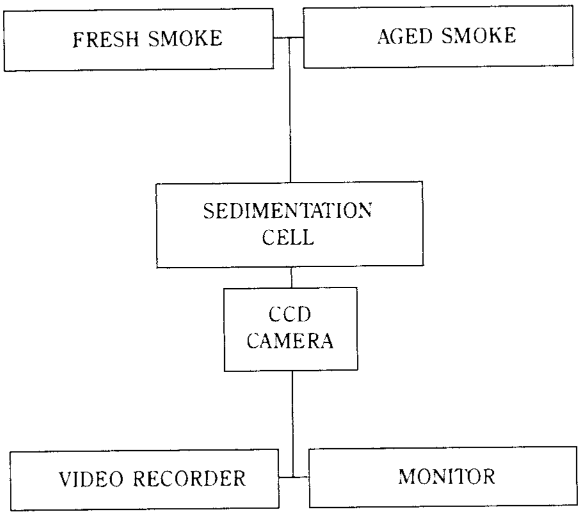

Fig.2 Schematic diagram of experimental apparatus for kinematic coagulation

4. Other techniques

By combining Inductively Coupled Plasma Optical Emission Spectrometry (ICP-0ES) with an epiphaniometer and Differential Mobility Analyzer it is possible to determine, simultaneously, the mass, surface area and diameter of agglomerated aerosols (Weber, 1992). From these measurements the fractal dimension and the monomer size may be determined. The results indicate that silver agglomerates, produced by spark discharge, are multifractal. In the free molecular regime the fractal dimension was 3, while in the transition regime a value of 1.9 was obtained.

The fractal dimension has also been determined from measurements of the terminal velocity, V_{TS}, of a cluster and the electric field strength, E, required to balance the gravitational force (Colbeck et al., 1989). This technique utilises the classical Millikan cell. A plot of log V_{TS} against log E enables D to be computed from the gradient. This method assumes that the clusters are spherically symmetric and they possess the same number of charges. These problems have been overcome by using a similar technique in conjunction with a photoemission method which enables the fractal dimension for single agglomerates in three dimensions to be determined (Nyeki and Colbeck, 1994). In this method a modified Millikan cell is used to obtain in situ measurements of D for single agglomerates in the transition/continuum regime (Colbeck et al., 1992). The method relies on the measurement of the aerodynamic diameter, based on a sedimentation technique, and the absolute mass of the agglomerate using a photoemission method. Hence the volume equivalent diameter (d_v) and the measured aerodynamic diameter (d_a) allow the dynamic shape factor and the mobility equivalent diameter (d_m) to be calculated. The latter diameter is equivalent to the hydrodynamic diameter. The relationship between d_a and the radius of gyration has been investigated both theoretically and experimentally and may then be used to derive the fractal dimension. The only parameters required for these determinations are an accurate estimation of the sedimentation velocity and various balance voltages in the cell (**figure 3**).

Measurements were reported for both soot agglomerates, up to $d_a = 3$ μm, and PVT spheres. The results for 10 soot and 4 PVT particles appear in **Tables 1** and **2** respectively. The particle mass was calculated using a linear least-squares fit to the photoemission data and gave regression coefficients greater than 98% in all cases. From this calculation

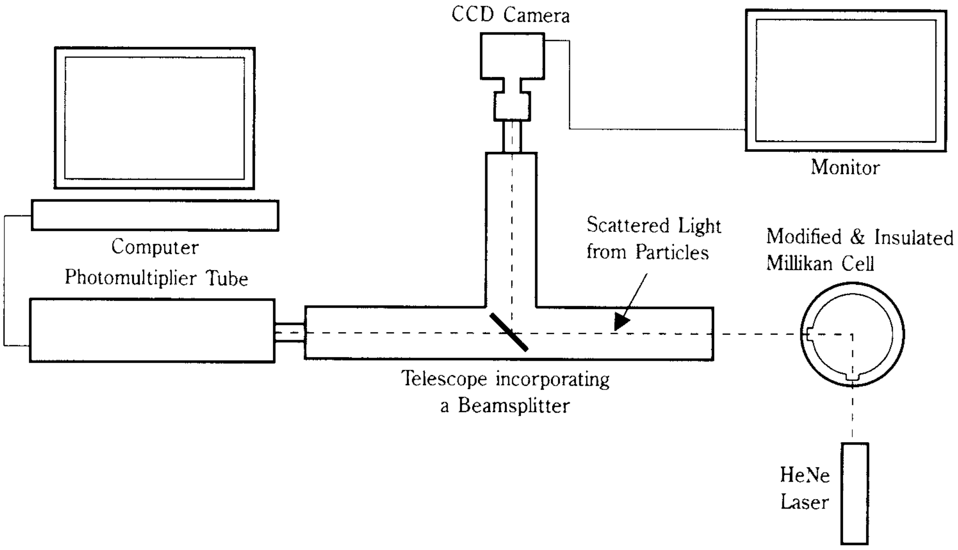

Fig.3 Schematic of the Modified Millikan Cell to determine the Fractal Dimension of Carbonaceous Agglomerates

Table 1 Data obtained via the Millikan cell method.

Number	Initial Number of charge	mass (pg)	d_v (μm)	V_{TS} (cm/s)	V_{TE} (cm/s)	d_a (μm)	d_m (μm)	Fractal dimension
1	23	3.32	1.47	0.0035	0.0057	1.00	5.64	2.11
2	15	3.48	1.49	0.0023	0.0028	0.80	8.83	1.93
3	40	3.55	1.50	0.0029	0.0036	0.90	7.20	2.02
4	12	1.13	1.03	0.0010	0.0015	0.51	6.36	1.83
5	30	3.94	1.56	0.0022	0.0045	0.77	10.65	1.89
6	27	3.25	1.46	0.0032	0.0047	0.94	6.08	2.07
7	39	2.19	1.28	0.0031	0.0054	0.93	4.24	2.16
8	39	11.30	2.21	0.0032	0.0074	0.95	20.68	1.85
9	50	12.53	2.29	0.0048	0.0065	1.19	15.07	1.98
10	10	4.14	1.58	0.0030	0.0031	0.91	8.23	1.99

Table 2 Data for PVT spheres.

mass (pg)	Number of charges	d_a (μm)	D
4.67	14	2.06	2.99 ± 0.03
4.63	28	2.07	2.99 ± 0.03
4.71	23	2.03	2.96 ± 0.03
4.95	39	2.07	2.96 ± 0.03

the initial charge on the particle was found. In the final column of **Table 1** the fractal dimension has been calculated with a primary spherule diameter of 50 nm, measured from SEM images. Most values lie around $D = 1.9$ for diffusion limited cluster-cluster (DLCC) growth but as they occur in the upper part of the range linear trajectories are implied (Meakin 1984). Such linear impacts may also occur due to differential coagulation, in which agglomerates collide with each other under gravitational sedimentation.

A number of agglomerates appeared with $D > 2$ for which it was conjectured that restructuring effects were responsible (Nyeki and Colbeck, 1994: Nyeki and Colbeck, 1993). To illustrate the case two soot particles ($D = 2.11$ and 2.16) were deliberately restructured by reversing the electric field polarity several times and observing the changing morphology on the monitor. In this manner an open structure could be transformed into essentially a spherical structure with ease. It is therefore possible that this mechanism was responsible for the other high observed values of D. Various models have been reported which simulate restructuring and readjusting effects present in real aggregation experiments. A simple model investigated by Jullien and Meakin (1989) allowed restructuring immediately after two agglomerates came into contact. For DLCC aggregation D increased from ~1.8 to ~2.1 and reached ~2.2 after the last stage of restructuring. It was found that as restructuring occurred it became increasingly difficult for D to increase. Thus in a similar manner reaction limited cluster-cluster (RLCC) aggregation only reached D ~2.25 as the initial value was relatively higher at D ~2.0. Although electrical restructuring mechanisms were not considered it is seen that simple restructuring mechanisms lead to increases in D. Important areas for the implications of agglomerate re-structuring, identified by Jullien and Meakin (1989) were rheology, and air and water pollution. Using the method presented here D may be measured for a variety of materials and the effects of restructuring on agglomerates may also be observed.

As a verification of the technique and equations utilised PVT particles were used as calibration standards. Fractal dimensions vary from 2.96 – 2.99 and show excellent agreement to the theoretical value of 3, hence verifying the method.

5. Conclusions

The characterisation of particle shape has been an active research area and source of contention for over fifty years. The application of fractal geometry to aerosol science lies in the necessity to parameterise complex aerosol shapes, such as those produced by combustion processes. Various in situ techniques have been presented allowing the fractal dimension of both a single agglomerate and an ensemble to be calculated. These methods are summarized in **Table 3**.

The instrument developed to study single particles has many applications. The ability to measure and monitor D for single particles allows their micro-chemical/physical properties to be investigated. Diagnostic information on formation dynamics of aerosol agglomerates is embedded in the fractal structure. This is an area which will require further investigation.

Table 3 Summary of *in situ* techniques used to measure the fractal dimension of aerosols

Author	Method	Material	Fractal Dimension
Schmidt-Ott (1988)	mobility	silver	2.18
Hurd and Flower (1988)	light scattering	silica	1.49 ± 0.15
Zhang *et al.* (1988)	light scattering	soot from premixed CH_4/O_2 flame	1.62 ± 0.06
Colbeck *et al.* (1989)	Millikan cell	soot from C_4/H_{10} flame	1.9
Kutz and Schmidt-Ott (1990)	aerodynamic	silver	2.06
Gangopadhyay *et al.*. (1991)	light scattering	soot from premixed CH_4/O_2 flame	1.6 ± 0.15
Bonczyk and Hall (1992)	light scattering	soot from C_4/H_{10} flame	1.49
Sorensen *et.al.* (1992)	light scattering	soot from premixed CH_4/O_4 flame	1.73
Weber (1992)	ICP-OES	silver	3.0 free molecular regime 1.9 transition regime
Nyeki and Colbeck (1994)	Millikan cell	soot from C_4H_{10} flame	1.87 – 2.19
Zhangfa *et.al.* (1994)	aerodynamic	soot from C_4H_{10} flame magnesium oxide	1.97 ± 0.07 1.19 ± 0.02

References

1) Bonczyk P.A. and Hall R.J. (1992) Measurement of the fractal dimension of soot using uv laser radiation.Langmuir, **8**, 1666-1670.
2) Colbeck I., Eleftheriadis K. and Simons S. (1989) The dynamics and structure of smoke aerosols. J. Aerosol Sci., **20**, 875-878.
3) Colbeck I., Nyeki S. and Zhangfa Wu (1992) In situ measurement of the fractal dimension of aerosols.J. Aerosol Sci., **23**, S365-S368.
4) Colbeck I. and Nyeki S. (1993) On the measurement of the fractal dimension of individual restructured agglomerates. Aerosols: Their Generation, Behaviour and Application, The Aerosol Society, 123-127.
5) Gangopadhyay S., Elminyawi I. and Sorensen C.M. (1991) Optical structure factor measurements of soot particles in a premixed flame. Appl. Opt., **30**, 4859-4864.

6) Hurd A.J., Schaefer D.W. and Martin J.E. (1987) Surface and mass fractals in vapor-phase aggregates. Phys. Review A., **35**, 2361-2364.
7) Jullien R. and Meakin P. (1989) Simpel models for the re-structuring of 3D ballistic aggregates, J. Colloid Inter. Sci., **127**, 265-272.
8) Kutz S. and Schmidt-Ott A. (1990) Use of a low-pressure impactor for fractal analysis of submicron particles.J. Aerosol Sci., **21**, S47-S50.
9) Martin J.E., Schaefer D.W. and Hurd A.J. (1986) Fractal geometry of vapor-phase aggregates. Phys. Review A, **33**, 3540-3543.
10) Meakin P. (1984) Effects of cluster trajectories on cluster-cluster aggregation: A comparison of linear and Brownian trajectories in two and three-dimensional simulations. Phys. Review A., **29**, 997-999.
11) Mountain R.D. and Mulholland D.W. (1988) Light scattering from simulated smoke agglomerates. angmuir, **4**, 1321-1326.
12) Nyeki S. and Colbeck I. (1994) The measurement of the fractal dimension of individual in-situ soot agglomerates using a Millikan cell technique. J. Aerosol Sci., **25**, 75-90.
13) Nyeki S. and Colbeck I. (1993) Electric field induced restructuring of single, in-situ, carbonaceous aerosols. J. Aerosol Sci., **24**, S547-S548.
14) Raper J.A. and Amal R. (1993) Measurement of aggregate fractal dimensions using static light scattering. Part. Part. Syst. Charact., **10**, 239-245.
15) Schmidt-Ott A. (1988) In situ measurement of the fractal dimensionality of ultrafine aerosol particles. Appl. Phy. Lett., **52**, 954-956.
16) Sorensen C.M., Cai J. and Lu N. (1992) Light scattering measurements of monomer size, monomers per aggregate, and fractal dimension for soot aggregates in flames. Appl. Opt., **31**, 6547-6557.
17) Weber A.P. (1992) Characterization of the geometrical properties of agglomerated aerosol particles. Ph.D. Thesis, Paul Scherrer Institut, Villigen, Switzerland.
18) Zhang H.X., Sorensen C.M., Ratmer E.R., Olivier B.J. and Merklin J.F. (1988) In situ optical structure factor measurements of an aggregating soot aerosol.Langmuir, **4**, 867-871.
19) Zhangfa Wu, Colbeck I. and Simons S. (1994) Kinematic coagulation, aerosol agglomerates and the fractal dimension. Aerosols: Their Generation, Behaviour and Application, The Aerosol Society, 24-28.

Author's short biography

Dr. Ian Colbeck

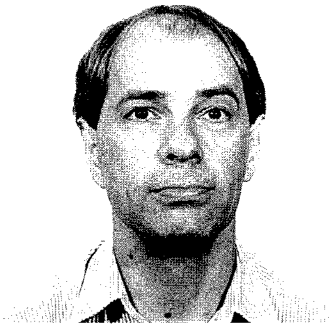

Dr. Ian Colbeck studied physics at Queen Mary College, University of London before obtaining an MSc in Atmospheric Physics at Oxford University and a PhD at Lancaster University in Environmental Physics. Initially appointed to teach a MSc course in Aerosol science and Technology he is currently a Senior Lecturer in the Department of Chemistry and biological Chemistry and Director of the Institute For Environmental Research, University of Essex. His fields of interest include photochemical oxidants, atmospheric modelling, the physico-chemical properties of aerosols, filtration, characterization of particle shape and vapor-phase synthesis and processing of nanoparticle materials.

Hierarchically Ordered Particle Mixtures by Thermally-Triggered Granulation†

Paul R Mort and Richard E. Riman*
*Department of Ceramics, Rutgers, The State University of New Jersey***

Abstract

A method was developed to granulate ceramic particles using metallo-organic soap as a binder. A high shear mechanical mixer (i.e., mechanofusion) was used to coat the soap over the ceramic particle surfaces. Agglomeration of the coated particles was triggered by increasing the mixing temperature to the softening point of the soap and transforming the soap from a crystalline to an amorphous phase. The crystalline soap acted as a solid lubricant and the amorphous phase was a cohesive binder. Granule growth was correlated to the thermo-mechanical properties of the soap, which depended on temperature, applied pressure and compaction history. The resultant spherical granules were densely packed assemblages of coated particles (i.e., multicore microcapsules). Sequential cladding of layers onto pre-formed core granules resulted in microstructures with hierarchical compositional ordering.

1. Introduction

Mechanofusion is a high energy powder mixing process used to mechanically bond coatings to core particles. Typically, at least one of the components in the powder mixture must be subject to plastic deformation, and mechanical bonding occurs either by embedding a hard coating particle into a softer core or by shearing a soft coating material over the surface of a harder core. Mechanofusion has been used to form single core coated particles (i.e., single-core microcapsules) using substantially spherical core particles.[1-3] The authors previously expanded on this approach to include granulation by coalescence of coated particles (i.e., multicore microcapsules).[4] The current work further expands this to include compositional ordering on a granular scale by layering additional components onto a granular structure. Single-core, multicore and hierarchical structures are illustrated as a function of their forming mechanisms (**Fig. 1**).[5, 6]

In the current work, mechanofusion is used to mix relatively soft powders (i.e., metallo-organic soaps) with harder core particles (i.e., ceramic oxides). During initial mixing, the soap coats the ceramic particle surfaces and acts as a dry lubricant. This improves the flowability of the fine powders and reduces adhesion of fine powders to the mixer. As the mixing temperature increases to a critical softening point, the soap becomes cohesive and is transformed into a binder. The transition of the soap from a lubricant to a binder is critical to the granulation process.

A noteworthy feature of the current process is dry-state mixing of solid phase precursor materials (i.e., no solvent removal is required). In addition, the process may be used with irregularly shaped precursor particles with little restriction on particle size distribution or the particle size ratio of core and coating components. The process results in dense spherical granules with high tap density and narrow size distribution. The sequential addition of precursors results in agglomerate structures that are compositionally ordered on both particle and granular scales.

2. Experimental

The process was run in a laboratory-scale batch mixer (Mechanofusion Model AM-15F, Micron Powder Systems, Summit, NJ, USA). The powder was loaded batch-wise into the mixing chamber (**Fig. 2**). Approximately 100 – 200 g of powder was processed per batch. During processing, the internal fixed piece and scraper assemblies remain stationary while the chamber rotates. For the experiments described in this work, the spacing of the fixed piece

---

* Current address: Procter & Gamble Company, 4550 Este Ave., Cincinnati, OH 45232, U.S.A

**Box 909, Piscataway, NJ 08855, U.S.A.

† Received Sep. 30th 1994

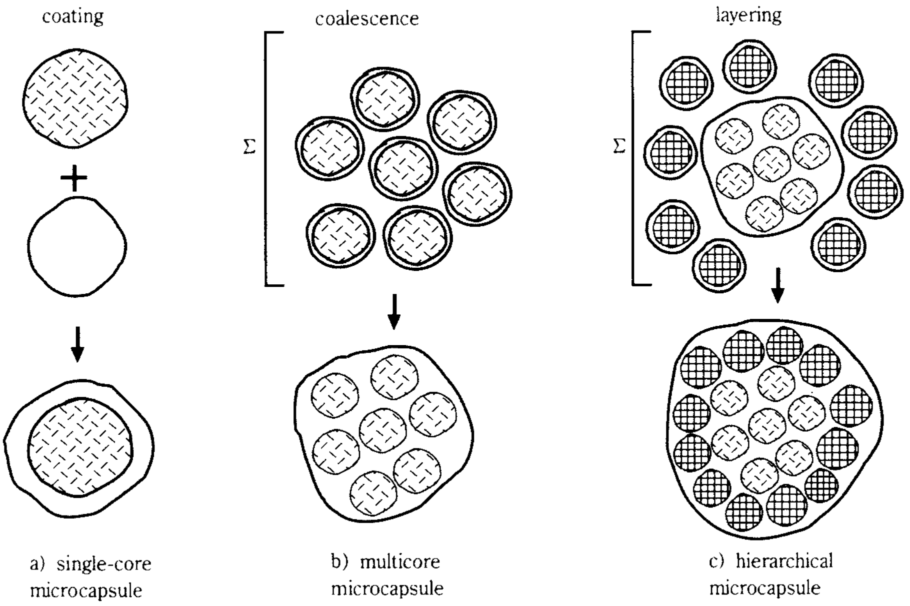

a) single-core microcapsule

b) multicore microcapsule

c) hierarchical microcapsule

Fig. 1. Microcapsule morphology and formation mechanism: a) single core microcapsule; b) multicore microcapsule formed by coalescence; c) multicore microcapsule with a core-cladding structure formed by layering (i.e., hierarchical ordering).

relative to the chamber wall was held constant at ~1.2 mm, and the scraper edge was adjusted as close to the chamber wall as possible without making physical contact. A convective heater was used to heat the air surrounding the mixing chamber; the heated air temperature was monitored by an external thermocouple. The temperature inside the mixing chamber was monitored by an internal thermocouple, which was located inside the fixed piece. The end of the internal thermocouple and the outside surface of the fixed piece was separated by ~2 mm of stainless steel. A calibration experiment showed only a slight lag in the temperature of the internal thermocouple (<5°C) for heating rates used in the process.

The compositions used in this work were based on the molar ratios required to form compounds in the system lead-zinc-magnesium-niobate, $Pb_3(Mg_{1-x}Zn_xNb_2)O_9$, where $0 \leq x \leq 0.5$. Precursors included lead oxide (PbO, Fisher Scientific, Fairlawn, NJ, USA), magnesium oxide (MgO, Fisher Scientific), zinc oxide (ZnO, Fisher Scientific), niobium pentoxide (Nb_2O_5, Alfa Products, Johnson Matthey, Danvers, MA, USA), magnesium stearate ($Mg(C_{17}H_{35}COO)_2$, Witco Corp., New York, NY, USA) and zinc stearate ($Zn(C_{17}H_{35}COO)_2$, Witco Corp.). The mean particle sizes of the ceramic particles were finer than 10 μm; the stearate particles were finer than 100 μm. The melting points of stearate soaps, $Mg(C_{17}H_{35}COO)_2$ and $Zn(C_{17}H_{35}COO)_2$, were ~145°C and ~125°C, respectively.

Processing of powder mixtures in the mixer was done according to 1-step and 2-step procedures. Process variables included external heating, rotation speed of the mixer and processing time. In the 1-step method the full powder mixture was processed in a single batch operation, resulting in the coalescence of fine coated particles to form granules (**Fig 1b**). The 2-step method used the results of the first step as seed granules, to which a second mixture of fine

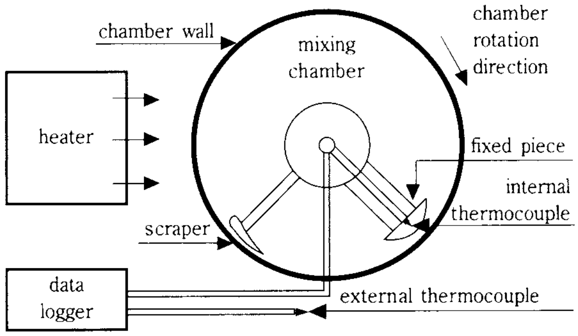

Fig. 2 Schematic of mixing apparatus, Mechanofusion AM-15.

powders was added and processed to form an agglomerate layer onto the seed granules (**Fig 1c**).

Process conditions were documented using a 2-step mixing process (**Fig. 3**) with a net composition of $Pb_3(Mg_{0.9}Zn_{0.1}Nb_2)O_9$. The first step in the process used a mixture of 3 PbO + $0.375Nb_2O_5$ + 0.375 Mg $(C_{17}H_{35}COO)_2$ with no granule seeds; the volume fractions of components were 26% PbO, 7% Nb_2O_5 and 67% $Mg(C_{17}H_{35}COO)_2$. The external heater was required to heat the mixture to ~85°C; above this point, frictional forces were sufficient to continue up the temperature ramp (**Fig. 3, flags c-e**). Granulation of the mixture occurred at ~120 to 130°C (**Fig. 3**, coalescence), which is ~20°C below the melting point of the $Mg(C_{17}H_{35}COO)_2$ binder. These granules were the seeds for the second process step, to which a mixture of 0.625 Nb_2O_5 + 0.525MgO + 0.1 $Zn(C_{17}H_{35}COO)_2$ was added. The volume fractions of the added powders were 35% Nb_2O_5, 7% MgO and 58% $Zn(C_{17}H_{35}COO)_2$. The cladding of the added powders onto the seed granules occurred at a substantially lower temperature (**Fig. 3**, layering), ~35°C below the melting point of the $Zn(C_{17}H_{35}COO)_2$ binder. It was not necessary to use the external heater in the second step.

The rate of frictional heating was observed to increase during the initial formation of granules in the first step (**Fig 3**, coalescence). Thus, it was very easy to develop a situation that would lead to a rapid increase in temperature and fusion of stearate soap. This type of runaway situation resulted in larger granule sizes and irregular granule shapes. In extreme cases, the fusion of the full batch of material into large (i.e., centimeter scale) pieces could result. To avoid runaway situations, it was important to turn off the external heater well enough in advance of granulation (**Fig. 3, flag c**) to allow for a reversal in the thermal gradient across the mixing chamber wall. In addition, it was important to gradually reduce the rotation speed near the onset of granulation (**Fig. 3, flag d**) to prevent the generation of excess frictional heat during granulation.

The sequence of granulation was investigated by extracting samples intermittently during the process, prior to and after the onset of granulation. To measure to progression of agglomerate size growth, the extracted powder samples were dispersed in isopropanol and sized using laser light diffraction (Microtrac FRA, Leeds and Northrup, Willow Grove, PA, USA). Particle and granule morphology was observed using light microscopy. Structural transformation of the soap binder was examined by X-ray diffraction (XRD, Siemens AG, Karlsruhe, FRG), using Cu *Kα* radiation at 40 keV 30 mA. Powder tap density of the samples was also measured.

The sequence of particle coating was investigated by extracting samples prior to the granulation onset. The extent of particle surface coating was measured using X-ray photoelectron spectroscopy (XPS, Model XSAM-800, Kratos, Ramsay, NJ, USA) with Mg *Kα* radiation at 15 keV and 15 mA. XPS is sensitive only to elements found on the near-surface layer (i.e., <10 nm) of the sample. As such, it can be used to measure the obscuration of a core particle element (e.g., Pb) by the soap coating, which produces a measurable signal for carbon. The atomic concentration of lead (C_{Pb}) with respect to

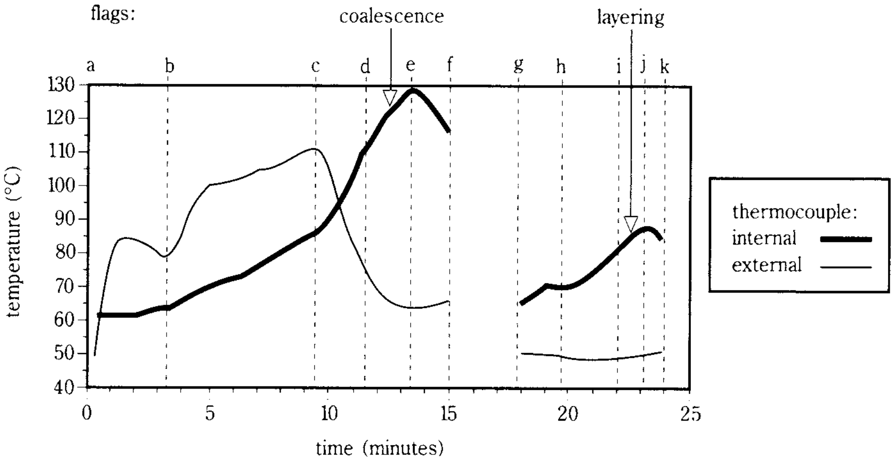

Fig. 3 Process schedule: a) load powder for first step, mix at 800 rpm, heater on low; b) 1200 rpm, heater on medium; c) heater off; d) gradually reduce rotation speed; e) 500 rpm; f) stop, end of first step; g) add powder for second step, mix at 800 rpm; h) 900 rpm; i) gradually reduce rotation speed; j) 500 rpm; k) stop, end of second step.

carbon and oxygen was calculated according to eq. 1, where I_i is integrated signal intensity and S_i is a known scaling factor for each element. The peaks used for evaluation were Pb 4*f*, C 1s and O 1s.

$$C_{Pb} = \frac{I_{Pb}}{I_{Pb} + I_O(S_{Pb}/S_O) + I_C(S_{Pb}/S_C)} \qquad (1)$$

A coating efficiency parameter (E_{coat}) was developed in order to normalize for ubiquitous surface carbon and the number fraction of lead atoms in the bulk mixture (eq. 2).

$$E_{coat} = 1 - \frac{N_{Pb}}{N_{Pb,0}} * \frac{C_{Pb,0}}{C_{Pb}} \qquad (2)$$

Coating efficiency was calculated by comparing the lead concentration at the surface of the as-received PbO powder $C_{Pb,0}$ to the lead concentration detected at the surface of the coated particles (C_{Pb}). This was done in order to account for carbon that is routinely present on the surface of commercial powders (i.e., surface carbon due to washing and/or adsorbed CO_2). The coating efficiency was also normalized to the calculated number fraction of lead atoms in the bulk mixture (N_{Pb}) relative to the number fraction in the pure PbO powder $N_{Pb,0}$. Normalization to the bulk number fraction of lead atoms in each mixture was done to account for the change in the bulk ratio of carbon, oxygen and lead atoms for each level of soap addition. A coating efficiency of 100% indicates a uniform coating thick enough to completely attenuate the Pb 4*f* photoelectrons (i.e., coating thickness >10 nm).

The thermo-mechanical properties of the stearate soap binders were evaluated using thermo-mechanical analysis (TMA-7, Perkin-Elmer, Plainfield, NJ, USA). Samples for TMA experiments were made by pressing the soap powders into pellets (diameter = 9.5 mm; thickness ≈ 2.5 mm). Pre-compaction of the $Mg(C_{17}H_{35}COO)_2$ soap powder was investigated by making a series of pellet samples pressed to 6, 23, 90 and 340 MPa. The sample pellets were individually loaded into the TMA and a penetration probe was centered on the flat pellet surface. Samples were heated at a constant rate of 6°C/min using a probe tip force of 100 mN (0.13 MPa). The penetration rate was calculated as the time derivative of tip position. A penetration rate of -0.2 μm/s was selected as the criterion for the onset of softening (i.e., initial softening point). A penetration rate of -2.0 μm/s was the criterion for the point of rapid deformation (i.e., viscous flow).

The compositional distribution of components within the granule structure was examined by scanning electron microscopy with energy dispersive x-ray spectroscopy (SEM/EDS, Model 1400, AMRAY, Inc., Bedford, MA, USA). Cross sections were prepared by mounting the granules in a low-viscosity epoxy and polishing on a wet cloth with an alumina polishing compound. The polished samples were carbon coated and examined using an accelerating voltage of 20 keV. EDS mapping was done using Pb *Mα*, Nb *Lα*, and Mg *Kα* transition energies.

3. Results and Discussion

Particle coating occurred during the initial stages of mixing, well in advance of agglomerate growth. Fine ceramic oxide particles were coated by stearate soap as a result of high shear mixing without a substantial increase in mixing temperature. This is shown by the increase in coating efficiency with time (**Table 1**). Thus, the surfaces of the ceramic oxide particles were already modified by a stearate soap coating prior to the onset of granulation. Tap density also increased steadily during the initial stages of mixing (**Fig. 4**) indicating that powder flow and packing was improved by the stearate soap coating.

The coalescence of fine powders to form granules occurred abruptly upon reaching an agglomeration onset temperature (**Fig. 4**). Particle size analysis showed very little change in the particle size distribution of powders mixed below the agglomeration onset temperature. The non-granulated powders exhibited similar size distributions to the volume sum of the precursor particles (i.e., <100 μm). The sample processed above the agglomeration onset temperature had a narrow size distribution with a mean size of ~200 μm and only a small remnant of the initial fine powder distribution. Granules formed by this process were very uniform in size and spherical in shape (**Fig. 5**). Typically, sieving resulted

Table 1. Coating efficiency (E_{coat}) as a function of the amount of zinc stearate coating phase and processing conditions for a PbO + $Zn(C_{17}H_{35}COO)_2$ mixture. Samples were extracted before the onset of granulation

amount of coating phase (vol%)	E_{coat}	
	350 rpm, 5 min.	1200 rpm, 20 min.
28.6%	50.1%	95.3%
44.4%	65.3%	96.5%

cumulative revolutions	T (°C)	tap density^t
0	20	21%
2,000	25	25%
7,000	30	29%
20,000	35	40%
50,000	35	49%
60,000	100 *	49%
65,000	130	60%

* external heater used

^{t}2.88 g/cm^3 = 100%

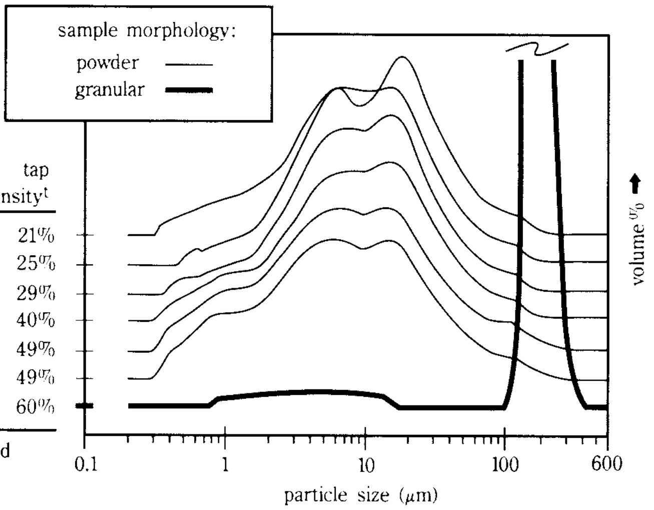

Fig. 4 Particle size distributions and tap density of samples taken from a 1-step process with magnesium stearate binder, as a function of cumulative mixing revolutions and internal mixing temperature

in >80 product wt% in the cut between 125 and 250 μm.

The granulation onset was accompanied by a transition in the phase structure of the stearate soap binder. XRD results show peaks for crystalline magnesium stearate at points prior to granulation while the pattern for the granulated sample is amorphous (**Fig. 6**). Thus, the combination of heat and high shear mixing energy acted to transform the stearate soap binder from a crystalline to an amorphous state. It should be noted that there was no evidence of bulk melting during this transition. It is hypothesized that substantial softening of the binder was localized to the high shear region of the mixer between the chamber wall and the fixed piece (**Fig. 2**), where high frictional interactions were sufficient to transform the crystalline soap to a more cohesive amorphous phase.

The softening properties of the stearate soap correlated empirically to granulation behavior. Coalescence was empirically correlated to the rapid deformation temperature of the stearate binder (i.e., penetration rate ≈ −2.0 μm/s). In contrast, layering of additional fines onto pre-formed seed granules occurred at a substantially lower temperature, correlating to the initial softening point of the second step binder (i.e., penetration rate ≈ −0.2 μm/s).

Process stability appeared to be related to the thermo-mechanical properties of the binder. In terms of process stability, coalescence was much more sensitive to small process variations (i.e., temperature, time, speed) than layering. If process conditions were

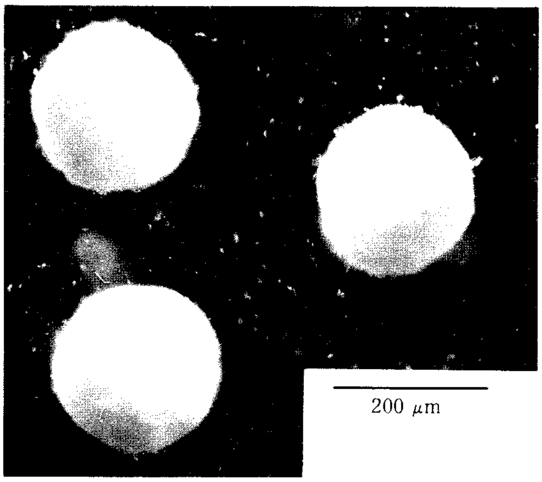

Fig. 5 Darkfield optical micrograph (125x) of granules produced by 2-step process

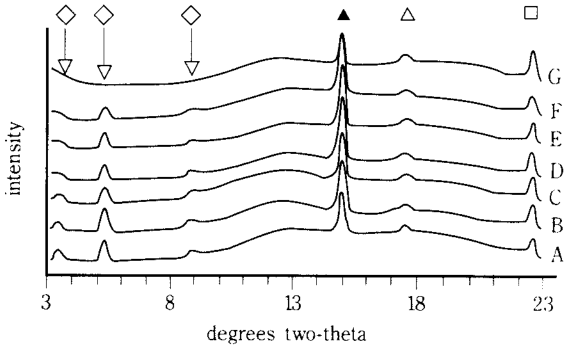

Fig. 6 X-ray diffraction scans for samples shown in **Fig. 4**:A) initial precursor mix; B) 2,000 revolutions (rev); C) 7,000 rev; D) 20,000 rev; E) 50,000 rev; F) 60,000 rev with external heater, T_{max} ≈ 100°C; G) ~65,000 rev, T_{max} ≈ 130°C. Key to crystalline phases: □) Nb_2O_5; ◇) $Mg(C_{17}H_{35}COO)_2$; ▲) PbO, massicot; △) PbO, litharge.

not carefully controlled during coalescence, the binder became too soft, causing over agglomeration and/or make-up in the mixer. During granule formation and growth, the binder was substantially compressed by the high shear and compressive forces in the mixer. Increased compression resulted in a reduction in the temperature of rapid deformation (**Fig. 7**), further softening the binder phase and promoting more agglomeration. On the other hand, increased compression had the opposite effect on the initial softening point; therefore, the layering mechanism was not as susceptible to overgrowth.

The internal microstructure of the granules consisted of densely packed ceramic particles in a matrix of the metallo-organic soap (**Fig. 8**). The particles were well dispersed in the matrix and there was no evidence of internal porosity. The microstructure represents an ordered mixture of core particles coated by a matrix component. For the 2-step process, an additional level of compositional ordering was evident on a granular scale. The central granular core was comprised of components processed in the first step (i.e., predominantly PbO, (**Fig. 9a**)). A sharply defined layer, rich in components added in the second step (niobium and magnesium), appeared at the outer surface of the granular core

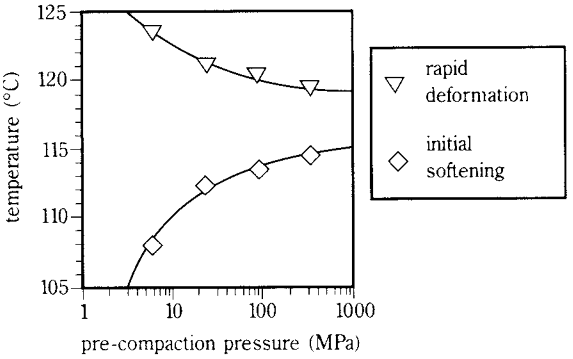

Fig. 7 Thermo-mechanical properties of magnesium stearate as a function of sample compaction pressure. Initial softening point (penetration rate ≈ -0.2 μm/s) correlated to layering; rapid deformation (penetration rate ≈ -2.0 μm/s) correlated to coalescence

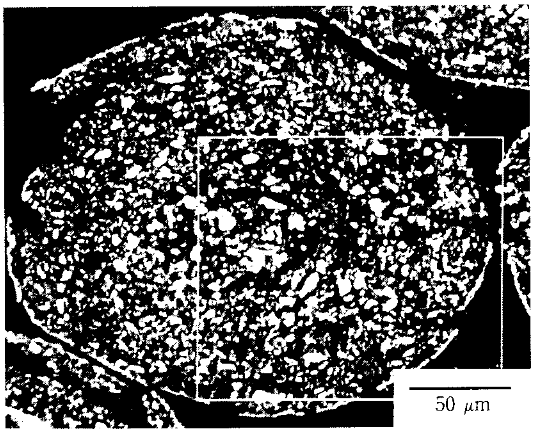

Fig. 8 Cross sectional SEM micrograph (450x) of granule produced in 2-step process. Box shows area of detail for **Fig. 9**

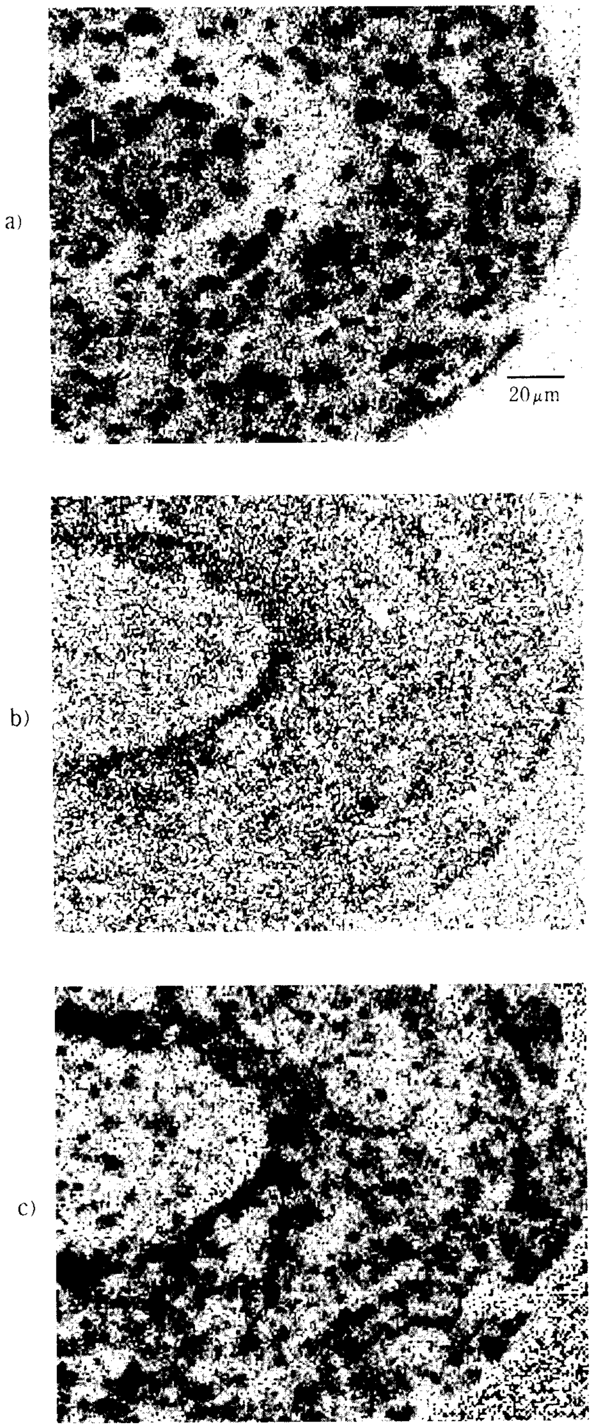

Fig. 9 Element map of detail area shown in **Fig. 8**: **a)** Pb, **b)** Mg, **c)** Nb. Darker areas correspond to higher elemental concentrations

(**Figs. 9b-c**). Beyond this layer, however, there was a distribution of elements from both seed and cladding compositions. Thus, it appeared that significant attrition of seed granules occurred in the second processing step, and the attrited material was incorporated into the outer cladding layer.

4. Conclusion

A dry-mixing technique was developed to form granules with a multicore microcapsule morphology. Additional agglomerate cladding layers could be added to granular cores to form hierarchical structures with compositional ordering on both particle and granular scales. The technique used a thermally activated binder that formed a matrix around primary particles. For the initial coalescence of fine particles, the agglomeration onset temperature corresponded to the rapid deformation (i.e., viscous flow) of the binder phase. For subsequent layering, the agglomeration onset occurred at a lower temperature, corresponding to the initial softening point of the binder.

Acknowledgments

Funding for this work was provided by the Center for Ceramic Research and the New Jersey State Commission on Science and Technology. In addition, the authors wish to acknowledge Mr. J. Oliver and Dr. W.-L. Chiang for their assistance with electron microscopy and energy-dispersive spectroscopy, Dr. D. Hensley for his assistance with X-ray photoelectron spectroscopy and Mr. R. Sabia for his assistance with mechanofusion experiments.

References

1) T. Yokoyama, K. Urayama, M. Naito, M. Kato and T. Yokoyama, "The Angmill Mechanofusion System and its Applications," *Kona*, **5**, 59-68 (1987).
2) M. Alonso, M. Satoh and K. Miyanami, "Mechanism of Combined Coating-Mechanofusion Processing of Powders," *Powder Technol.*, **59**, 45-52 (1989).
3) K. Tanno, "Current Status of the Mechanofusion Process for Producing Composite Particles," *Kona*, **8**, 74-82 (1990).
4) P. Mort and R. E. Riman, "Reactive Multicomponent Powder Mixtures Prepared by Microencapsulation: $Pb(Mg_{1/3}Nb_{2/3})O_3$ Synthesis," *J. Am. Ceram. Soc.*, **75** 1581-86 (1992).
5) A. Kondo and J. W. Van Valkenburg; Microcapsule Processing and Technology. Marcel Dekker, New York, 1979.
6) K. V. S. Sastry and D. W. Fuerstenau, "Mechanism of Agglomerate Growth in Green Pelletisation," *Powder Technol.*, **7** 97-105 (1973).

Author's short biography

Paul R. Mort

Paul Mort is employed with the Process Systems Technology group of Procter & Gamble Company, where he is currently working on agglomeration processes for dry laundry detergents. His Ph.D. thesis (Rutgers University, Ceramic Science and Engineering, 1993), ''The Effect of Ordered Mixing on the Synthesis of Multicomponent Ceramics'', included computer modeling and experimental work on powder mixing, granulation, powder compaction and solid-state reactivity. Several publications and numerous presentations have been based on this work. Previous to his graduate studies, Paul worked in two separate careers as a computer programming consultant and an urban planner. His undergraduate work (M.I.T., 1978) included Urban Studies and Materials Science and Engineering. Long term career goals are aimed at leveraging process efficiency and waste reduction towards improved productivity and environmental quality. Paul is a member of the American Ceramic Society, the American Institute of Chemical Engineers and the Particle Technology Forum.

Richard E. Riman

Richard E. Riman graduated M.I.T. in February 1987 with a Ph.D. degree in Ceramic Science. Following his graduate degree, he joined the Ceramics Facility at Rutgers, The State University of New Jersey. He is currently a tenured associate professor teaching at both the undergraduate and graduate levels. He is also a visiting professor at the Technical University of Denmark. Professor Riman has been recognized as an ONR Young Investigator. He is a member of Kermos, Tau Beta Pi and Sigma Xi honor societies and professional societies that include the American Ceramic Society, Materials Research Society and American Chemical Society. His research interests focus on the synthesis, and characterization of ceramic powders for advanced and traditioanl ceramics. Synthesis technologies of interest include microencapsulation, hydrothermal synthesis, sol-gel synthesis, and fluorothermal nitridation. He has authored over 60 publications and delivered over 100 papers.

Formation of Composite Latex Particles by Deposition of Amphoteric Particles†

Ko Higashitani
*Department of Chem. Eng., Kyoto University**
Takuya Yamamura, Yumiko Isshiki,
Akiko Kage and Akihiko Kondo
*Department of Applied Chemistry, Kyushu Inst. of Tech.,***

Abstract

Composite particles are formed using negative and amphoteric monodispersed latices as the core and shell respectively, and the experimental conditions to obtain maximum coverage of the surface of core particles with amphoteric particles and the mechanism of the deposition process are investigated. As results, (1) the experimental conditions for forming the composite particles are clarified; (2) the maximum coverage of the core surface with amphoteric particles is found not to be greater than 0.3; and (3) the coverage is mainly determined by the strength of the repulsive force between deposited particles. The relation between the coverage and the zeta potential of composite particles is also clarified.

1. Introduction

The production of functional materials from fine particles is being actively pursued. Especially in the fields of medicine and cosmetics, much research is being carried out on methods to give further functions to materials by covering core particle surfaces with materials possessing other characteristics and forming core-shell type composite materials with a different surface quality[1,6,7,10,11].

As one method to form core-shell type composite particles, mixing of two kinds of particles of opposite charge in a liquid phase and hetero-coagulating the two are possibly considered but quantitative studies on this method are hardly available. In this study, negative and amphoteric monodispersed latex particles were used as the core particle and particles depositing on the core particle surface respectively, and by mixing both in a suitable liquid phase, it was attempted to form a composite particle of depositing particles on the core particle surface. A search for various conditions to obtain the maximum coverage of depositing particles and a study of the mechanism which controls the depositing process were carried out.

The deposition process of amphoteric particles onto the charged surface in this study is similar to the deposition process of proteins, which are amphoteric, on solids[8,9], and also the deposition process of electrolyte polymer coagulants on surfaces of suspended particles in the coagulation process[2,3]. It is believed that the results of the present experiment will be also highly useful as information to understand these phenomena.

1. Experiment

1.1 Specimen

As the core particle, 3 types of spherical polystyrene latex (PSL) particles, superior in monodispersity, were used. Particles with a diameter of $D_c = 1.27$ μm were prepared by aqueous polymerization[4] while particles of $D_c = 3.19$ μm and 11.9 μm were the standard particles made by the Dow Chemical Company. PSL particles have sulfuric acid residues on their hydrophobic surface and are negatively charged. **Figure 1** shows the dependency of ζ-potential of these particles on the pH of the medium. All 3 particles have about the same negative ζ-potential at $3 \leq \mathrm{pH} \leq 12$ and their absolute values tend to increase with an increase in pH. As the depositing particles, amphoteric latex particles with a diameter $D_a = 0.39$ μm synthesized by aqueous polymerization from styrene and methacrylic acid 2 dimethylethelene were used. This particle has sulphuric acid

---

* Yoshida Honmachi, Sakyo-ku Kyoto 606, Japan

** Suisen-cho, Kitakyushu 804, Japan

† This report was originally printed in *Kagaku Kougaku Ronbunshu*, **18**, 637 (1992) in Japanese, before being translated into English with the permission of the editorial committee of the Soc. Chemical Engineers, Japan.

residues and diethylamino groups on the surface and so, as shown in **Fig. 1**, ζ-potential changes from positive to negative in sign with an increase in pH with an isoelectric point near pH 7. Hydrochloric acid and sodium hydroxide were used to adjust the pH, and sodium chloride was used as the electrolyte.

1.2 Experiments

For the depositing experiment, 20 ml each of suspensions of given concentrations for core particles and depositing particles were prepared with the same pH and electrolyte concentration. After mixing them in a tank with turbine blades, a part of the suspension was sampled and diluted in an aqueous solution identical to the medium. This operation was performed to prevent particles in the medium from depositing on core particles during the drying process through which specimens for observation on a microscope was prepared. The dilution factor was decided after confirming that further dilution disallowed changes in the number of depositing particles per core particle. A part of the solution was placed on the electron microscope stage. After drying at about 30°C, it was dried further for one day in a vacuum desiccator, and then gold vapor was deposited. Using this specimen, the composite particles was observed from a zero and 60° angles with the use of a scanning electron microscope. Example photos are shown in **Fig. 2**.

The coverage θ of deposited particles on the core particle surface is defined as the value obtained by dividing the total cross sectional area of the deposited particles by the core particle surface area. Consequently, the maximum coverage on this two dimensional surface is 0.91. The value of θ was determined by two methods. In the case of D_c = 1.27, 3.19 μm, the number of deposited particles per core particle is small and therefore the number of deposited particles was calculated from the total observable particles as follows: For particles which are completely within the diameter of the core particles, it is considered that the same number of particles exist on the back side and therefore these were counted as two, while particles which protruded beyond the contour of the core particle were counted as one. In the case of D_c = 11.9 μm, calculations were made from the number of particles deposited on a certain area near the center. Furthermore, since it is possible that deposited particles move along the surface of the core particle during the drying process, the SEM photos taken from straight above and from an angle of 60° were compared and only data in which the coverage of the two agreed within the error of a few percents were used. The average value of the two coverages was adopted as the coverage.

The ζ-potential of core particles, deposited particles and the composite particles were measured using a microscopic electrophoresis equipment (Rand Brothers Mark II).

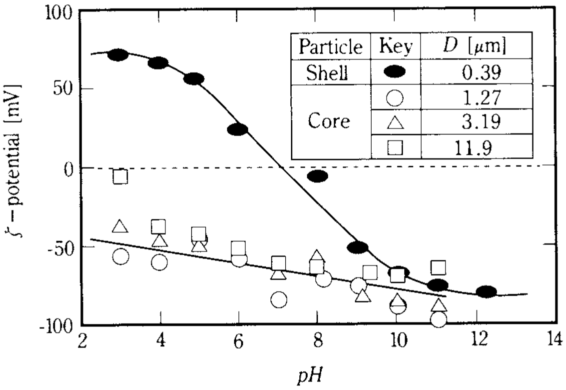

Fig. 1 Dependence of ζ-potential of employed particles on pH

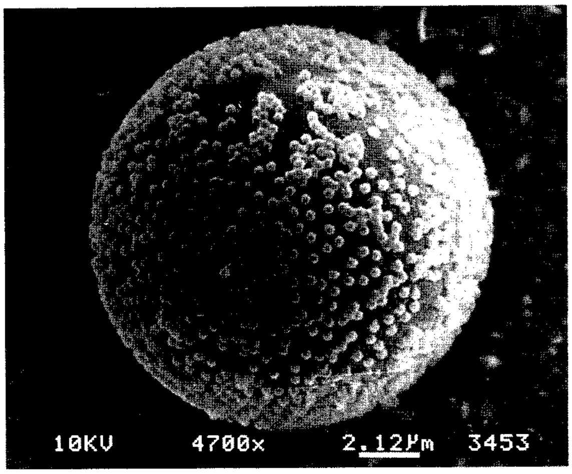

Observation angle 0°

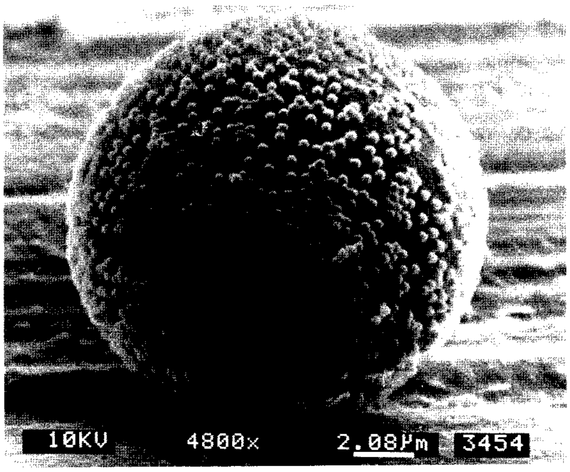

Observation angle 60°

Fig. 2 Typical SEM photographs of composite latex particles (D_a = 0.39 μm, D_c = 11.9 μm, θ_m = 0.2, n_c = 1×10^6 cm^{-3}, R_i = 5×10^3, pH = 5, N_R = 120 rpm, t_m = 150 minutes)

2. Results and discussions

2.1 Effect of agitation time and speed

As seen in **Fig. 1**, the charge of the deposited particle is positive at pH 5 while the charge of the core particle is negative. When the two are mixed, the deposition of the amphoteric particles on the surface of the core particle occurs to form core-shell type composite particles as shown in **Fig. 2**. The following experimental conditions were employed, unless stated otherwise; pH = 5, KCl concentration C_e = 0 mol/l, number concentration of core particle $n_c = 1 \times 10^6$ cm^{-3}, D_c = 11.9 μm, and rotational speed of the agitator N_R = 120 rpm.

Figure 3 shows the dependence of θ on the agitation time (t_m) when the ratio of the number concentration of depositing particles against that of core particles, R_d, are 5×10^2, 5×10^3, and 5×10^4. With the increase of R_d, the initial coating rate increases and this is considered to be caused by an increase in flux of the depositing particles to the core particle surface. Here, the constant value of θ after sufficient agitation is defined as the maximum coverage θ_m. The value of θ_m for $R_d = 5 \times 10^3$, 5×10^4, is small at about 0.2 and moreover it is seen that they roughly coincide. This implies that θ_m is not determined by the flux of depositing particles but each deposited particles have the electrostatic interparticle repulsive force which disallows further approach of deposited particles [5]. Also the reason for the value of θ being small in $R_d = 5 \times 10^2$, is believed to be because the flux of the depositing particles is extremely small and does not reach the maximum coverage within the time of this experiment. In further experiments, unless stated otherwise, the particle concentration ratio is taken to be $R_d = 5 \times 10^3$.

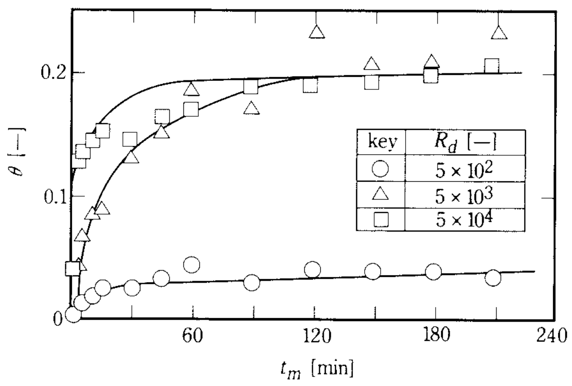

Fig. 3 Variation of coverage for various concentrations of dosed depositing particles

Figure 4 shows the variation of θ for various agitation speeds N_R. The variations of θ roughly show the same tendency regardless of N_R. This indicates that the flux of depositing particles to the core particle surface does not change much within the scope of changes of the agitation speed in the present experiment. In either case, a constant value is reached in about 90 minutes and therefore the value at t_m = 150 minutes is used as θ_m hereafter.

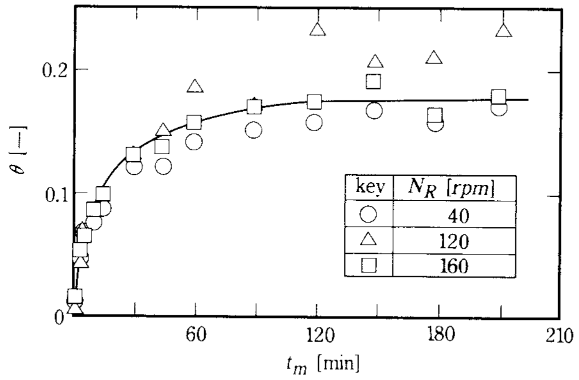

Fig. 4 Variation of coverage for various mixing intensities

To find out whether the constant value of θ in **Fig. 4** is due to the equilibrium between adsorption and desorption of particles, 1 cm^3 of the suspension was taken after agitating for 150 minutes under the experiment conditions of **Fig. 4**, diluted by 40 times in the same medium, agitated again at the same agitation intensity, and then the particles desorbed from the core particle was counted. The results are shown in **Fig. 5**. Here, since the diluting factor is sufficiently large, the re-deposition of desorbed particles will be neglected. The positive value of the desorption ratio α indicates the particle desorption by agitation. At any agitation speed, and any agitation time t_d, the value of α is approximately 0. Hence it is considered that the effect of desorption is small enough to be neglected.

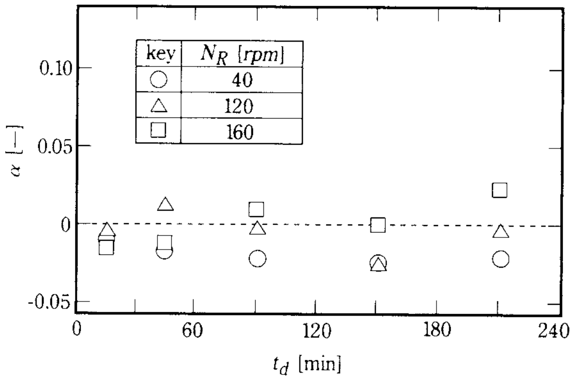

Fig. 5 Desorption fraction of deposited particles by dilution

2.2 Effect of concentration of depositing particles

Figure 6 shows the variation in the maximum particle number R_m deposited on one core particle and the residual particle number R_r in the medium per core particle for the values of R_d between 50 and 1×10^5. At $R_d \geq 5 \times 10^3$, the value of R_m becomes constant to be approximately 1×10^3. This corresponds to $\theta_m \fallingdotseq 0.2$. It is clear that R_m does not increase even if R_d increases. This is probably because, as mentioned above, the repulsive force between the deposited particles resists dense loading of deposited particles. At $R_d \leq 5 \times 10^3$, the value of R_r is constantly several times to 10 times more than that of R_m and even though depositing particles and surfaces to be deposited are available, R_m decreases with a decrease in R_d. It is thought that with the decrease in R_d, the time required to reach the maximum deposition becomes longer and the agitating time in the present experiment is not sufficient.

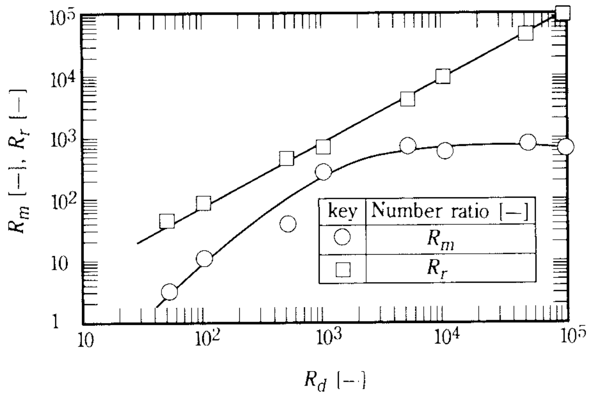

Fig. 6 Relations between normalized concentrations of maximum deposited particles (R_d), residual particles in the medium (R_r) and dosed depositing particles (R_d)

Figure 7 shows the relation between θ and ζ-potential of composite particles. It is clear that with a very low coverage of $\theta \fallingdotseq 0.10$, namely about 1/2 of the maximum coverage, ζ-potential becomes roughly zero. A similar relation between the coverage and ζ-potential was observed in the case where electrolyte polymers are adsorbed on suspended particles[2,3]. At $\theta \geq 0.16$, even though the deposited particles are dotted on the core particle surface in an insular form, it is interesting to note that the apparent ζ-potential of composite particles roughly coincides with the ζ-potential of the deposited particles.

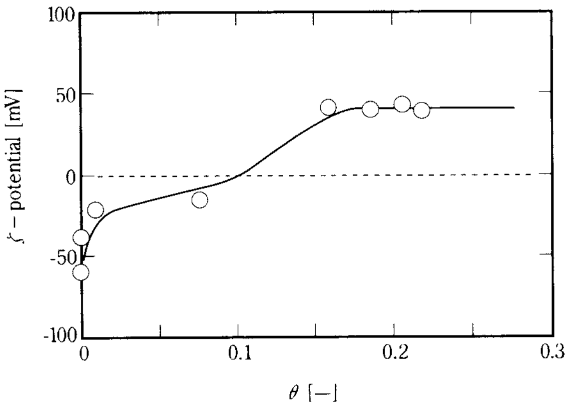

Fig. 7 Dependence of apparent ζ-potential of composite particle on coverage

2.3 Effect of pH and electrolyte concentration

Figure 8 shows the dependence of θ_m on pH. As shown in **Fig. 1**, the isoelectric point of the deposited particles is at about pH 7. Therefore, up to the isoelectric point, the ζ-potential of the deposited particles becomes smaller with an increase of pH and electrostatic attraction between the core particle and deposit particles also becomes smaller. But θ_m increases as shown in **Fig 8**. This will be because, as shown schematically in **Fig. 9**, the adhesion force between deposited particles and the core particle is weak around the isoelectric point, but the repulsive force between deposited particles is also weak. Therefore dense loading is possible. A similar tendency was reported in the adhesion of proteins on the surface of solids[8,9]. Around pH = 7, aggregation between depositing particles occurs and at pH ≥ 10, the ζ-potential of the depositing particles become negative and so any deposition hardly occurs.

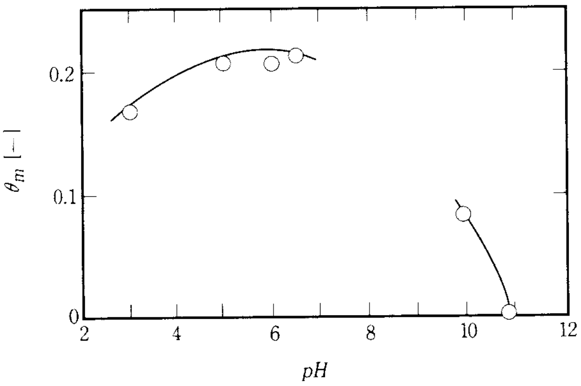

Fig. 8 Dependence of the maximum coverage on pH

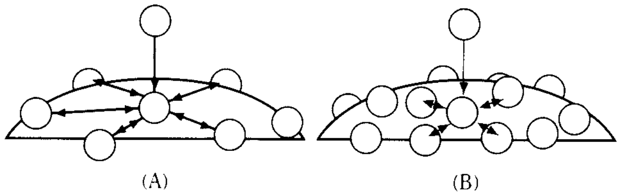

	(A)	(B)
Attractive force between core and deposited particles	large	small
Repulsive force between deposited particles	large	small
pH	≒ 3	≒ 6
θ_m	low	high

Fig. 9 Schematic drawing of interactions between depositing, deposited and core particles

It was confirmed in **Fig. 5** that deposited particles do not desorb in the same medium. **Figure 10** shows the dependence of the desorption fraction α of deposited particles on the agitation time (t_d), after depositing particles are adsorbed at pH 5 and then diluted 40 times at pH 11 and agitated. The deposited particles desorb immediately after dilution and thereafter, by agitation, α becomes about 0.9. It is clear that desorption occurs readily.

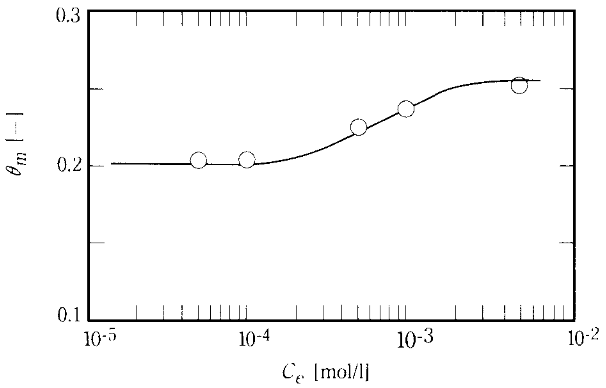

Fig. 10 Desorption fraction of deposited particles with the change of pH from 5 to 11

Figure 11 shows the changes of θ_m against the concentration C_e of dosed KCl. Where C_e is low, the effect of C_e on θ_m is not observed but at $C_e \geq 1 \times 10^{-4}$ mol/l, θ_m increases with the increase of C_e. This increase of θ_m also, same as the increase of θ_m near the isoelectric point, is presumed to be caused by the compression of the electrical double layer and the weakening of the electrostatic repulsive force between deposited particles.

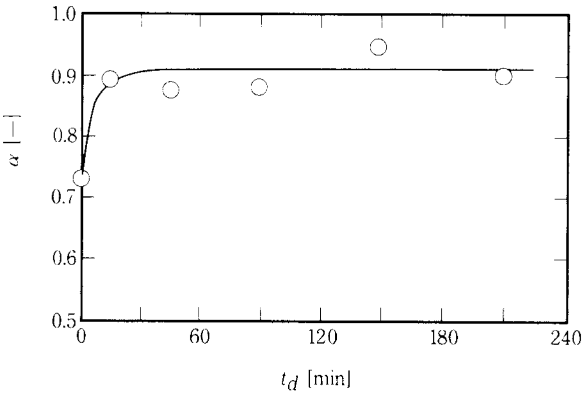

Fig. 11 Dependence of the maximum coverage on KCl concentration

2.4 Effect of particle diameter ratio

Figure 12 shows the comparison of the dependence of θ_m on R_d between 3 types of core particles. θ_m increases with the increase of R_d, and θ_m becomes constant at $R_d = 1 \times 10^4$ irrespective of the particles. Therefore, to obtain the maximum coverage within the agitating time of the present experiment, the number of depositing particles must be at least 10^4 times greater than the number of core particles. It is also observed that the value of θ_m becomes larger as the core particle diameter becomes smaller. This θ_m-value is the value obtained by dividing the total cross sectional area of the deposited particles by the core particle surface area. As shown in **Fig. 9**, the density of deposited particles depends upon the repulsive force between deposited particles, that is, it is controlled by the distance between centers of the deposited particles. When the core particle diameter is reduced and the curvature of the particle surface becomes greater, apparent θ_m-value is calculated to be greater than as it is. If we presume that particles deposited on a spherical surface with a radius of $(D_a/2 + D_c/2)$, then θ_m for particles of D_c = 1.27 μm, 3.19 μm becomes 0.31, and 0.23 respectively. This θ_m-values are close to the θ_m-value for particles of D_c = 11.9 μm. Consequently, the increase in the apparent θ_m-value with the decrease of core particle diameter is presumed to be mainly because the curvature of the particles was not taken into account. The above results indicate that when a core shell-type composite particle is formed by this method, the coverage of deposited particles is low and will not exceed the maximum of 0.3.

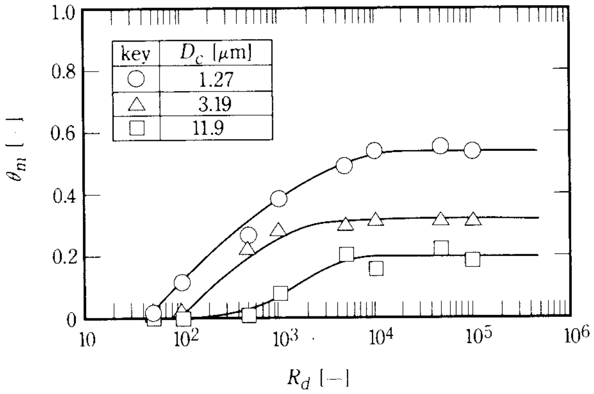

Fig. 12 Dependence of the maximum coverage on concentration of dosed depositing particles for core particles of three different sizes

Conclusion

By mixing an excessive amount of amphoteric particles with negatively charged core particles in a liquid phase, core-shell type composite particles were formed and the followings were clarified.

1) Achieving a coverage over 0.3 of depositing particles on core particle surface is difficult. To achieve maximum coverage, the presence of electrostatic attraction between core particles and depositing particles is necessary but the intensity of the adhesive force hardly relates to the coverage. The coverage is determined by the intensity of electrostatic repulsive force between the deposited particles. Moreover, the maximum coverage does not depend upon the ratio of particle diameter between two particles nor by agitation in the container if the number concentration ratio of depositing particles against core particles is 10^4 or more.
2) The depositing particles hardly desorb from the core particle during the depositing process but by changing the pH of the medium to the zone in which both particles are repulsive each other, deposited particles are easily desorbed.
3) The apparent ζ-potential of core-shell particles becomes approximately 0 when the θ-value becomes roughly 0.10 which is the half of the maximum coverage. When the coverage becomes greater than 0.16, the apparent ζ-potential of the composite particles becomes roughly the same as the ζ-potential of the depositing particles.

Nomenclature

C_e = electrolyte concentration [g-mol·ℓ$^{-1}$]
D = particle diameter [μm]
D_a = diameter of amphoteric depositing particle [μm]
D_c = diameter of core particle [μm]
N_R = rotation speed of impeller [min^{-1}]
n_c = number concentration of core particle [cm^{-3}]
R_d = number concentration normalized by n_c of dosed depositing particles [–]
R_m = number concentration normalized by n_c of maximum deposited particles [–]
R_r = number concentration normalized by n_c of residual depositing particles in the medium [–]
t_d = agitating time for desorption [min]
t_m = mixing time [min]
α = desorption fraction [–]
θ = coverage [–]
θ_m = maximum coverage [–]

References

1) Furusawa, K. and C. Anzai: *Colloid and Polymer Sci.*, **265**, 882 (1987)
2) Higashitani, K., G. Hosokawa, H. Aimoto and Y. Matsuno: *Kagaku Kogaku Ronbunshu*, **9**, 543 (1983)
3) Higashitani, K. and T. Kubota: *Powder Technology*, **51**, 61 (1987)
4) Higashitani, K. and Y. Matsuno: *J. Chem. Eng. Japan*, **12** 460 (1979)
5) Hunter, R.: "Foundations of Colloid Science", p. 395, Oxford Science Pub., New York (1987)
6) Kawase, S.: "Biryushi Sekkei Kogaku", p.114, *Funtai to Kogyosha*, Tokyo (1988)
7) Kitahara, F. and K. Furusawa: "Saishin Colloid Kagaku", p.30, Kodansha, Tokyo (1990)
8) Kondo, A. and K. Higashitani: *J. Colloid Interface Sci.*, **150**, 344 (1992)
9) Kondo, A., S. Oku and K. Higashitani: *J. Colloid Interface Sci.*, **143**, 214 (1991)
10) Naito, M.: "Funtai", p.282, Nihon Kikaku Kyokai Tokyo (1991)
11) Tanno, K.: *Kona*, ***8***, *74 (1990)*

Study of the Shape Separation of Fine Particles Using Fluid Fields
– Dynamic Properties of Irregular Shaped Particles in Wet Cyclones† –

Shigehisa Endoh, Hitoshi Ohya, Kaoru Masuda, Shigeyuki Suzuki, and Hiroyuki Iwata
*Natinal Inst. for Resources and Environ (NIRE)**
Chihiro Ikeda
*Hosei Univ., ***

Abstract

In order to apply hydrodynamic fields to the shape separation of fine particles, the dependencies of dynamic properties of particles in a cyclone on the particle shape were discussed. Glass beads, glass powders, silica sands and mica particles in a 10 – 100 μm size range were classified into five fractions by wet cyclones. The equivalent diameters of classified particles were measured by a free settling method, and the geometric parameters were obtained from SEM microphotos. The Stokes diameters in free settling were in agreement with the mean values which were estimated for an ellipsoid and a thin disc to settle in random orientation. On the other hand, Stokes diameters in the cyclones were smaller than those in free settling. The discrepancy between these diameters was large especially for flaky mica particles, suggesting that a cyclone can be used to separate flaky particles from bulky ones.

1. Introduction

The uniformizing of size and shape of particles is an extremely important issue in enhancing the functions of particulate materials. Control over particle shape at the initial formation stage is desirable but with the exception of spherical particles and a few particulate materials, uniformizing of shape is difficult and moreover production costs for monodispersed regular shaped particles such as latex are extremely high, making such processes unsuitable for general powder production processes. Therefore, a shape adjusting technique after particle formation becomes indispensable in the production process and especially the development and establishment of a shape separation technique is desired.

Studies of the shape separation have centered around techniques which use the shape dependency characteristics of rolling and sliding of particles(1). These techniques mainly separate particles of 500 μm or more with relatively weak adhesion properties. Recently, with increasingly finer particles, separation techniques using electrostatic force or fluid drag can be considered to cope with such fine size areas(2,3). For example, the possibility of shape separation by rotary flow has been suggested(4) and the use of shape dependency (especially aspect ratio)(5) of particle rotation or orientation is promising. However, shape separation methods targeting fine particles remain at present yet to be established. Therefore, in the present study, experimental studies of the possibility of shape separation using rotary flow is attempted for basic studies to develop a shape separation method using a fluid field.

2. Experiment apparatus and method

As specimens, glass beads (Toshiba Balloty, EGB 301, abbreviated as GB), silica sand (SS), glass powder (GP) and mica particles (Nippon Mica, A100; MC) filtered to a certain grain size range were used. **Figs. 1** to **4** show the respective size distributions by dotted lines, measured by the photo extinction method using gravitational sedimentation (Shimadzu, SA CP-2). To make the conditions similar to those for classification in making measurements, particles were dispersed without any dispersing agent and only stirring in tap water by a magnetic stirrer was performed.

---

* 16-3 Onogawa, Tsukuba-shi Ibaraki 305, Japan
** 3-7-2 Kajino-cho, Koganei-shi, Tokyo 184, Japan
† This report was originally printed in *J. Soc. Powder Technology, Japan.* **29**, 838 (1992) in Japanese, before being translated into English with the permission of the editorial committee of the Soc. Powder Technology, Japan.

In the classification experiment, a 5 stage type wet cyclone (Cyclosizer by Warman Co,) was used. Its outline is shown in **Fig. 5**. First, a certain quantity (30 grams) of the specimen was charged in a container. Next, while tap water was being poured at a flow rate exceeding that of the classification operation condition, the specimen was gradually poured into the entire cyclones and preparatory classification was done for 5 minutes. Thereafter, the flow rate was set to a specified value and classification was done for 90 minutes. After classification, particles in each collector container were recovered and their particle size distribution was measured by the photo extinction sedimentation method. Also their shape was observed by a SEM. For the sake of convenience, numbers 1 to 5 were affixed from upstream to downstream of the cyclones to distinguish between the respective recovered samples.

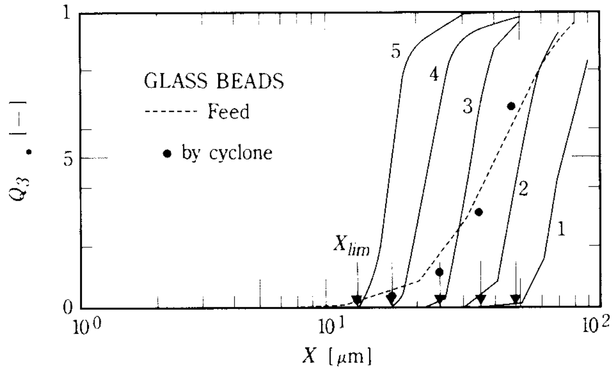

Fig. 1 Size distributions of feed particles and classified ones by the wet cyclones; Glass beads

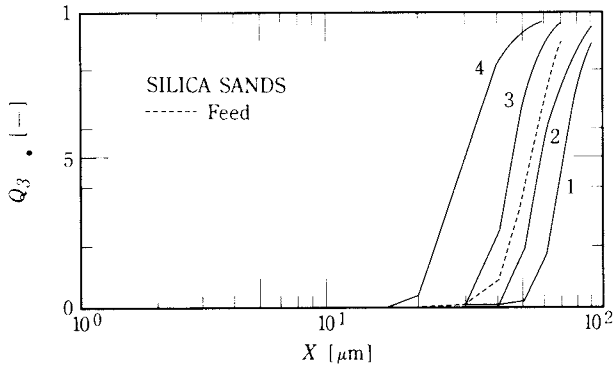

Fig. 3 Size distributions of feed particles and classified ones by the wet cyclones; Silica sand

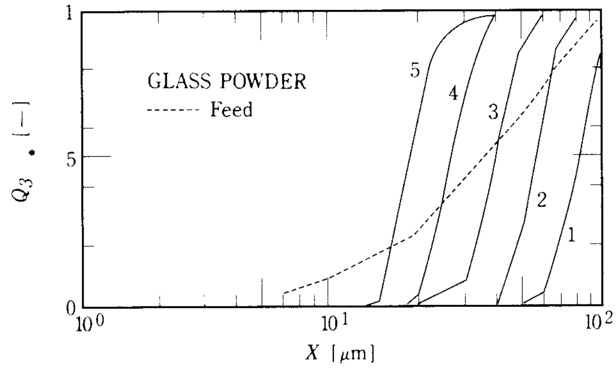

Fig. 2 Size distributions of feed particles and classified ones by the wet cyclones; Glass powder

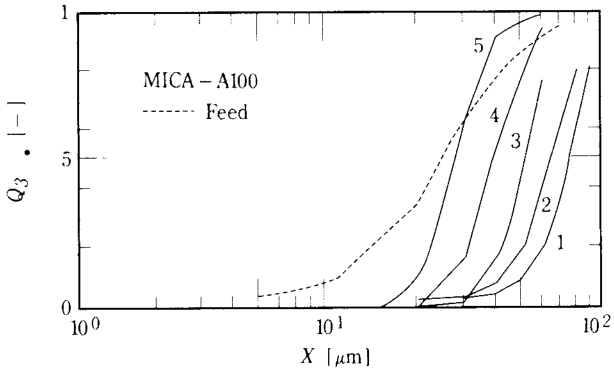

Fig. 4 Size distributions of feed particles and classified ones by the wet cyclones; Mica

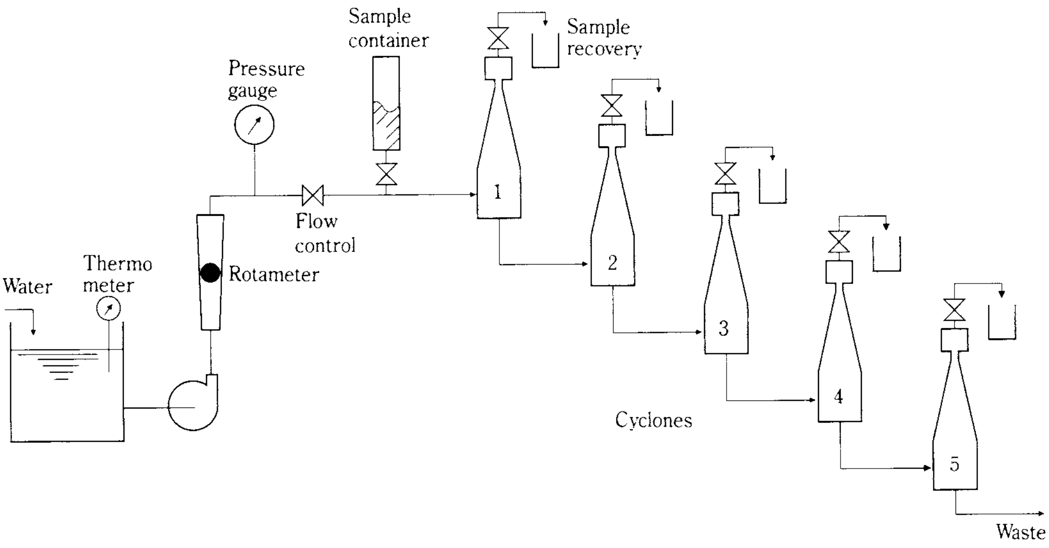

Fig. 5 Schematic diagram of experimental apparatus; CYCLOSIZER

3. Experiment results and observations

3.1 Classification characteristics of the cyclone

Fig. 1 shows, by solid lines, the particle size distribution of glass beads collected at each cyclone. In the Figure, the critical particle diameters X_{lim} of each cyclone, specified before classification are shown by arrows. X_{lim} is determined according to the specified operation conditions[6, 7] (Appendix) and in the case of the used glass beads, X_{lim} was the cut off diameter of approximately 99% oversize. For comparison, the cumulative under size distribution calculated from classified particle mass was plotted against X_{lim} and this roughly coincided with that of the supplied particles. Also, the geometrical standard deviation of classified particles was 1.16 – 1.22, showing that an extremely strict classification was made. From the above results, it was shown that a highly accurate classification was possible with the cyclone used for this experiment and at the same time, its classification performance for spherical particles could be estimated by applying Stokes resistance rule.

Figs. 2, 3, and **4** show the size distribution of collected particles when aspherical particles were classified.

3.2 Average particle diameters of classified particles

Fig. 6 shows the relation between X_{lim} set for the classification operation and 50% diameter X_{50} of the respective classified particles obtained by the gravitational sedimentation method. First, attention is focused on the relation of glass beads (GB). As shown in the Figure, the following relation for glass beads is obtained.

$$X_{50} = fX_{lim} \tag{1}$$

If the difference between the settling of spherical particles inside cyclones and free settling, such as the rotation of particles, are ignored, theX_{50} of spherical particles can be considered as being equal to the Stokes diameter inside the cyclone. This is to say, X_S is the Stokes Diameter inside the cyclone used in this experiment and can be considered as having the following relation with the operation parameter X_{lim}.

$$X_S = fX_{lim} \quad f = 1.4 \tag{2}$$

In contrast, X_{50} of the glass powder (GP) and silica sand (SS), which are aspherical, roughly satisfies the relation of Eq. (1) but the value of f is somewhat larger than that for glass beads. It is conceivable that there is some difference between the free settling and the settling inside the cyclone. This is to say that X_{50} obtained for these particles by the gravitational sedimentation is not the Stokes diameter inside the cyclone but that at the time of free settling. Furthermore, with mica (MC) which is flaky, X_{50} of cyclones 3 – 5 is fairly large compared with that of other particles. Also X_{50} of cyclones 1 and 2 show roughly similar values. Obviously, it can be assumed that the behavior of particles inside the cyclone is quite different from that of free settling.

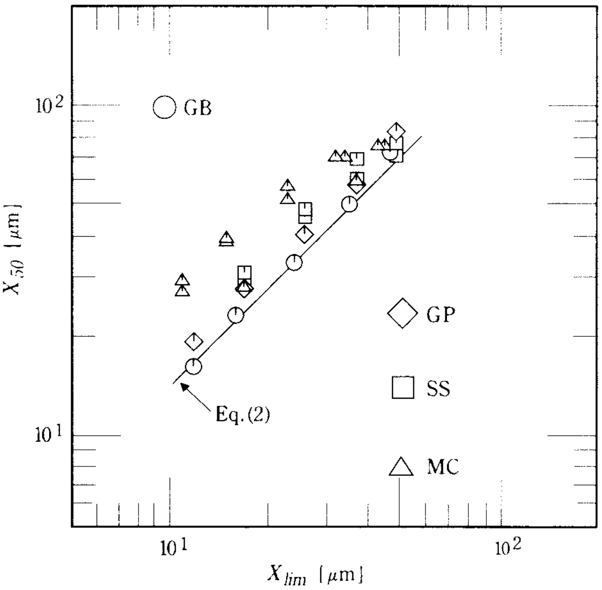

Fig. 6 Relation between cutoff diameters of the cyclones and the 50% diameters of particles classified by them

Figs 7 and **8** show SEM photos of glass powder and mica. The shape of the glass powder is massive and no characteristic change can be observed in the shape of the particles collected from upstream to downstream in the cyclones, the size being smaller but with shapes roughly similar. A similar tendency was seen in the case of silica sand. On the other hand, with mica, as seen in the photo of particles collected downstream are flaky while among the particles collected at stage 1, many particles of massive shape were observed.

cyclone 1 (× 100)

cyclone 3 (× 200)

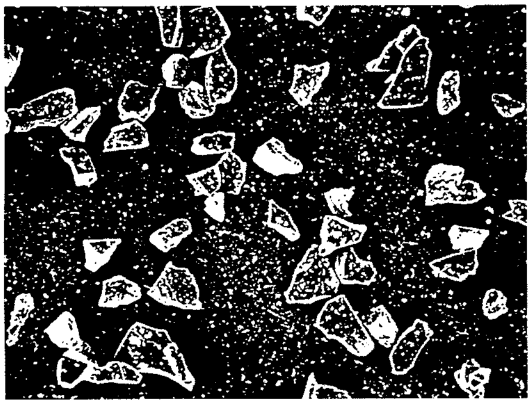

cyclone 5 (× 300)

Fig. 7 SEM microphotos of particles classified by the cyclones; Glass powder

Fig. 9 shows the relation between Heywood diameter X_H and Stokes diameter X_S. X_S was obtained using Eq. (2) with the corresponding X_{lim} and X_H was obtained from the SEM photo taken at 0° angle inclination. With massive shape silica sand and glass powder, the ratio between X_S and X_H is roughly unity but in contrast, X_H of mica is generally quite larger than X_S with the exception of stage 1. Moreover, the X_H in the first stage of the cyclone shows a smaller value than the values for particles collected at the 2nd and 3rd stages.Also the relation of Feret diameter to the Stokes diameter for all specimens, showed a tendency similar to the case of the Heywood diameter.

The above results contain some important implications with respect to shape classification.Firstly, as shown in **Fig. 9**, particles with the same value of Heywood diameter may differ in settling speed in the cyclone. This supports the possibility of making dynamic shape classification after classifying by sieving. Furthermore, according to the results shown in **Fig. 6**, it is found that although the Stokes diameter X_{50} may be the same at the time of free settling, depending on the particle, a particle may have a different sedimentation diameter X_S in the cyclone. Also, as shown in **Figs. 7, 8,** and **9,** a difference is clearly seen in their geometrical shapes. In other words, particle groups which have been

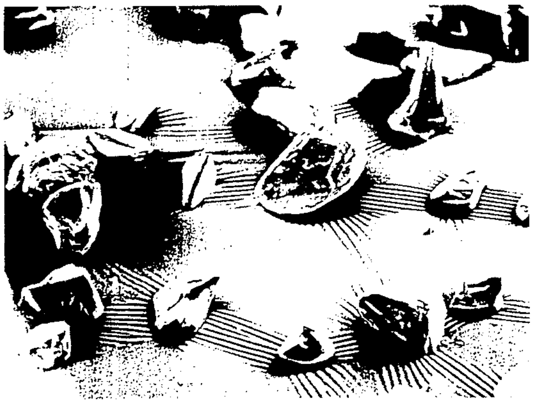

cyclone 1 (× 100)

cyclone 3 (× 100)

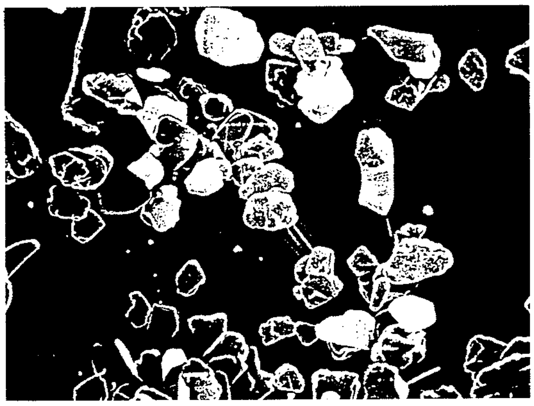

cyclone 5 (× 100)

Fig. 8 SEM microphotos of particles classified by the cyclones; Mica graded by gravitational sedimentation may possibly be classified further in the cyclone. For example, X_{50} of mica particles which may be obtained in cyclone 1 and cyclone 2, or of mica particles which may be obtained in cyclone 3, and of silica sand and glass powder which may be obtained in cyclone 2 may roughly be the same and therefore correct classification by gravitational sedimentation is impossible. In contrast, their X_S differs and therefore they can be classified by cyclones due to the difference in particle shape. This is to say, the possibility of shape separation by rotary flow is implied.

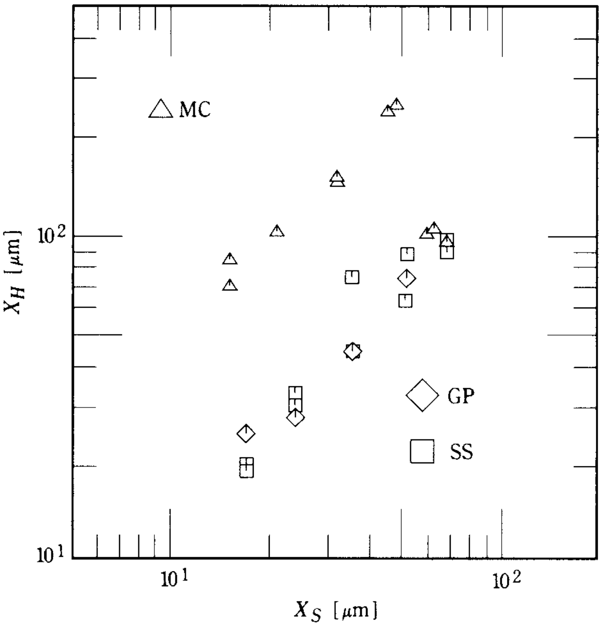

Fig. 9 Relation between Stokes diameter in the cyclones given by Eq. (2) and the Heywood diameter of particles classified by the wet cyclones

3.3 Free settling characteristics and particle shape

First, the case where rotating bodies having a uniform size freely settle in various orientations is studied. The settling velocity u_{st} of a particle settling in the direction of gravity with its rotating axis at an angle of ϕ can be obtained using the following equations[8, 9],

$$u_{st} = \Delta\varrho V_p g K_\phi / 3\pi\mu C \qquad (3)$$

$$K_\phi = K_r \sin^2\phi + K_f \cos^2\phi \qquad (4)$$

where, C is the representative diameter, V_p the particle volume, and $\Delta\varrho$ the density difference between the particle and fluid. Also, K_r and K_f are fluid resistance coefficients for various shapes and in the case of a rotating body, they are obtained using the Gans function for the particle settling in vertical and parallel to the respective rotating axis[10, 11]. The average value $\overline{X}_{st}$ of Stokes diameter X_{st} is obtained using the following equation when the probability of orientation is considered,

$$\overline{X}_{ST} = \int_{X_{min}}^{X_{max}} X_{st} P(X_{st})\, d X_{st} \qquad (5)$$

where, $P(X_{st})$ is the probability density function of X_{st} of the orientation of particles. When particles orientate randomly, $P(X_{st})$ satisfies the following equation.

$$P(X_{st})\, dX_{st} = \sin\phi d\phi \qquad (6)$$

First, particle settling models assuming random orientations of silica sand and glass powder are compared. For a prolate spheroid as a model particle, with C to be the major axis length 2a, the average Stokes diameter is obtained using the following equation[12],

$$\overline{X}_{st} = c\left[\sqrt{K_f} + \frac{K_r}{\sqrt{K_f - K_r}} \ln \frac{\sqrt{K_f} + \sqrt{K_f - K_r}}{\sqrt{K_r}}\right] \qquad (7)$$

where, 2c is the minor axis length, K_r and K_f are obtained using the following equations,

$$K_r = \left[\frac{3\zeta}{8(\zeta^2-1)} \quad \frac{2\zeta^2-3}{\sqrt{\zeta^2-1}} \ln\{\zeta + \sqrt{\zeta^2-1}\} + \zeta\right] \qquad (8)$$

$$K_f = \left[\frac{3\zeta}{(\zeta^2-1)} \quad \frac{2\zeta^2-1}{\sqrt{\zeta^2-1}} \ln\{\zeta + \sqrt{\zeta^2-1}\} + \zeta\right] \qquad (9)$$

where ζ is the axis ratio a/c (>1) of the spheroid. **Fig. 10** shows the relation between the evaluated value $X_{st,estm}$ of Eqs. (7), (8), and (9) and the experimental value $X_{st,meas}$ ($= X_{50}$). Although some dispersion is seen, no substantial discrepancy is observed and therefore it can be considered that these particles can be approximated to prolate spheroids.

Next, the case of mica is considered. Mica is obviously of a flaky shape and therefore a disk particle is considered as its model. Assumed to be a disk with X_H as the diameter and t as the thickness obtained from an image analysis, the representative diameter C is set as X_H. The average diameter is obtained from Eq. (5) using the following equations.

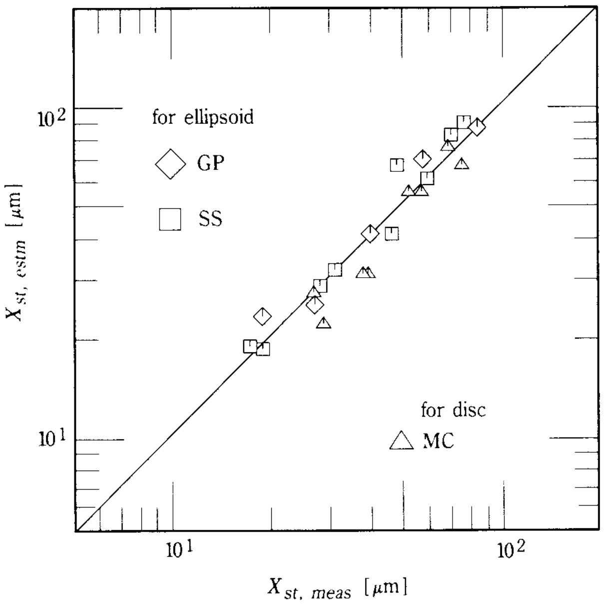

Fig. 10 Comparison of Stokes diameter obtained by photo-extinction sedimentation with that estimated by Eqs. (7) and (10)

$$\bar{X}_{st} = \sqrt{\frac{3\eta}{2}\,\frac{t}{2}}\left[\sqrt{K_f} + \frac{K_r}{\sqrt{K_r - K_f}}\left\{\frac{\pi}{2} - \arcsin\sqrt{K_r/K_f}\right\}\right] \tag{10}$$

$$\eta = X_H/t \tag{11}$$

For K_r and K_f, the Gans function for a disk is used. When flatness η is constant, according to Eq. (10), $\bar{X}_{st}$ is proportional to X_H. On the other hand, when the thickness is constant, it is roughly proportional to $\sqrt{X_H}$. The above relations are compared in **Fig. 10.** Substituting the thickness obtained from a SEM photo in Eq. (10), we estimated the Stokes diameter. Since the estimated value $X_{st,\,estm}$ was roughly close to the experimental value, the Stokes diameter at the time of free settling of classified mica can be estimated using Eq. (10). Also, it can be considered that the orientation of flaky particles settling freely was random.

3.4 Dynamic shape coefficient during rotary flow

As mentioned before, since the free settling of irregular shaped particles can roughly be described by Eq. (5) which assumes random orientation, the dynamic shape factor $\varkappa_F$ can be obtained using the following equation,

$$\varkappa_F = (\bar{X}_{st}/X_{sp})^2 \tag{12}$$

where X_{sp} is the equal volume sphere equivalent diameter. By following this definition, the dynamic shape factor $\varkappa_c$ during rotary flow is expressed by the following equation.

$$\varkappa_c = \frac{\text{(Sedimentation velocity during rotary flow)}}{\text{(Sedimentation velocity of equal volume sphere)}} = \{(X_{st}\ \text{during rotary flow})/X_{sp}\}^2 \tag{13}$$

X_{st} during rotary flow can be considered as X_{st} obtained from Eq. (2) for an optional operation condition X_{lim}. Therefore, the difference between the free settling of each particle and the settling inside the cyclone can be evaluated using the following equation.

$$\varkappa_c/\varkappa_F = (X_s/\bar{X}_{st})^2 \tag{14}$$

Fig. 11 shows the relation between $\bar{X}_{st}$ $(= X_{st,\,estm})$ estimated with Eq. (5) and X_s. The aspect ratio ζ given by substituting the projected images of glass powder and silica sand by inertial ellipsoids is 1.1 – 1.3 while the flatness η of mica of cyclone 3 – 5 was 15 – 25. Therefore it is thought that the behavior of aeolotropic particle having a larger aspect ratio during rotary flow depends more strongly on its shape and that the difference with free settling becomes greater. In other words, it can be assumed that flaky particles exhibit a peculiar orientation in rotary flow and by utilizing orientation, it is believed that shape classification by rotary flow is possible.

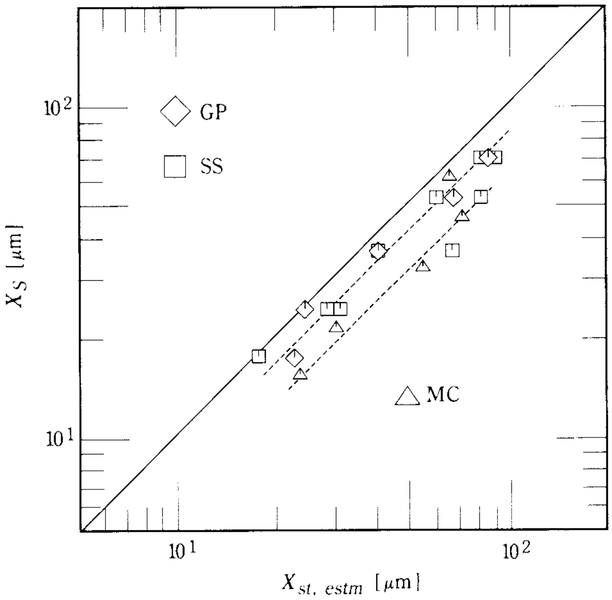

Fig. 11 Relation between Stokes diameter in the cyclones and that estimated with Eqs. (7) and (10).

4. Conclusion

To clarify the possibility of shape separation of fine particles by rotary flow, classification of aspherical particles was conducted using a wet cyclone with extremely sharp classifying characteristics and a study was made of the effect of particle shape on the dynamic behavior of particles. As a result, the following conclusions were reached.

1) The Stokes diameter of aspherical particles in free settling can be estimated by using Gans functions or dynamic shape coefficients and it is believed that the orientation at the time of free settling is random.
2) From the fact that the dynamic behavior of flaky particles in a rotary flow depends greatly on its shape compared with massive shape particles, the possibility of classification between flaky particles and massive shape particles by rotary flow is implied.
   Regarding the orientation of particles inside a cyclone, further detailed clarification as necessary hereafter by observations of sedimentation.

Finally, we would like to mention that this study was made possible with the great cooperation of Mr. Koji Ishimaru, 4th year student (at the time) in the Mechanical Engineering Dept., Hosei University. Also we acknowledge the cooperation of Mr. Shinichi Itoh of the Material Resources Dept. of our institute, NIRE, in the operation of cyclones. Our gratitude to them is extended.

Appendix

The cutoff diameter X_0 of each cyclone when quartz (specific gravity 2.65) is classified under standard operation conditions (20°C water supplied at a rate of 11.6 liters/min.) is obtained based on the results[6] of Kelsall et al.[7] The general cutoff diameter X_{lim} can be obtained using the following equation when fluid viscosity, particle density, flow rate and classification time are considered.

$$X_{lim} = f_1 f_2 f_3 f_4 X_0 \tag{A-1}$$

When Stokes resistance is assumed, the effects of the fluid viscosity μ and the particle fluid density difference $\Delta\varrho$ are given by:

$$X = (\mu/\mu_0)^{1/2} X_0 = f_1 X_0 \tag{A-2}$$

$$X = (\Delta\varrho_0/\Delta\varrho)^{1/2} X_0 = f_2 X_0 \tag{A-3}$$

where, subscript *0* indicates standard conditions. Also the following result was obtained by Kesall et al. with respect to the effect of flow rate Q.

$$X = (Q_0/Q)^{1/2} X_0 = f_3 X_0 \tag{A-4}$$

Furthermore, the effect of classification time can be obtained as follows as a function of the empirical parameter f_4.

$$X = f_4 X_0 \tag{A-5}$$

We obtain eg. (A-1) considering factors f_1, f_2, f_3 and f_4, and X_{lim} can be calculated.

Nomenclature

a	: large semi-axis of an ellipsoid	(m)
C	: characteristic dimension of a particle	(m)
c	: one semi-axis of an ellipsoid	(m)
g	: gravitational acceleration	(m/s^2)
K_f, K_r	: resistance coefficients along the translation axes of a particle or an ellipsoid given by Gans' function	(−)
Q_3	: cumulative undersize distribution	(−)
t	: thickness of a particle	(m)
u_{st}	: Stokes terminal velocity of a particle	(m/s)
V_p	: volume of a particle	(m^3)
X	: diameter	(m)(μm)
X_H	: Heywood diameter obtained from projected area	(m)
X_{lim}	: cutoff diameter of a cyclone	(m)
X_s	: Stokes diameter inside a cyclone	(m)
X_{sp}	: equivalent spherical diameter	(m)
X_{st}	: Stokers diameter	(m)
X_{50}	: 50% diameter obtained by gravitational sedimentation	(m)
$\Delta\varrho$	: density difference between a particle and fluid	(kg/m^3)
ζ	: anisometry of an ellipsoid	(−)
η	: flatness of a particle	(−)
$\varkappa_F$, $\varkappa_c$	: dynamic shape factors for free settling and settling inside a cyclone	(−)
μ	: fluid viscosity	(Pa•s)

Subscripts

estm : estimated by using Eq. (5)
meas : measured

Superscript

− : mean

References

1) Moro, T., H. Iwata and H. Ohya: ''Report on shape separation techniques of solid particles'', National Inst. for Resources and Environ. (1989)
2) Murali, C., B. Pitchumani and N. N. Clark: *Int. J. Min. Pro.*, **18**, 237 (1986)
3) Horvath, H.: *J. Aerosol Sci.*, **10**, 309 (1979)
4) Miwa, S.: ''Kagaku Kogaku 2 (Ed. by J. Fujita and H. Tohata)'', p. 342, Tokyo Kagaku Dojin (1972).
5) Goldsmith, H. L. and S. G. Mason: ''Rheology, Theory and Application'', Vol. 4, Chap. 2, Academic Press (1967)
6) Kelsall, D.F. and C.H. McAdam: *Trans. Inst. Chem. Engrs.*, **41**, 84 (1963)
7) Warman International PTY. LTD.: ''CYCLOSIZER Instruction Manual'' (1965)
8) Brenner, H., *Chem. Eng. Sci.*, **18**, 1 (1963)
9) Blumberg, P.N. and C.A. Mohr: *AIChE J.*, **14** 331 (1968)
10) Gans, R.: *Sitzber math – physk Klasse Akad. Wiss. Munchen*, **41**, 191 (1911)
11) Heiss, J. H. and J. Coull: *J. Chem. Eng. Progr.*, **48** 133 (1952)
12) Endoh, S., Y. Kuga and H. Iwata: Proc. Ann. Meeting of Soc. Powder Technol. Japan, p. 173 (1991)

A New Method for Measurement of Powder Characteristics Based on Reentrainment Phenomena†

Hiroaki Masuda, Shuji Matsusaka, and Koreyoshi Imamura
*Dept. of Chem. Eng., Kyoto Univ.**

Abstract

A new method has been developed to measure and evaluate the operational powder characteristics for fine particle processing based on the reentrainment phenomena. Experiments on particle reentrainment were carried out using an accelerated air flow for 21 different test powders. Both the reentrainment fluxes, which were measured by an electrostatic method, and the average air velocities were automatically sampled by a computer. The sampled data were processed to obtain the reentrainment profiles as a function of the average air velocity. The cumulative reentrainment efficiencies were also obtained and represented as a function of the wall shear stress.

It was found that fine particles having tendencies to form large aggregates were reentrained mainly in the early stage of the measurement when the flow velocity was as low as 5 $m\cdot s^{-1}$*. Also, the mass ratio of the reentrained large aggregates to the total particles was used to obtain information on the particle-particle (cohesion) or particle-wall interactions (adhesion). On the other hand, the cumulative reentrainment efficiency-curves must be applied to determine the operational conditions controlling the amount of adhered particles in various aerosol processes.*

1. Introduction

The quality and functions of industrial products using fine particles can be enhanced with the use of smaller particles. However the reduction in particle size increases adhesion between particles or between particles and wall surfaces and this reduces the operational qualities. Compared to the wet process, the reduction of adhesion in the dry process is difficult and especially with aerosol operation, the effect of air flow in addition to the matter of adhesion complicates the problem. For example, when fine particles deposit on inner walls of equipment by turbulent diffusion, the primary particles retain and form aggregate particles there owing to the effect of their adhesion and when the separation strength due to fluid resistance becomes stronger than the adhesion strength of the aggregate particles, reentrainment is induced1). This phenomenon is a problem which relates to almost all aerosol operations such as dust collection, dispersion, classification, pneumatic conveying, etc. The reentrainment mechanism, at first sight, may seem to be very simple but when an actual attempt is made to obtain the time course of reentrainment as a function of the adhesion strength distribution of the aggregate particles or the separation strength within the turbulence boundary layer, even an approximate analysis is difficult. Therefore, studies in the past on reentrainment mainly centered on clarifying its mechanisms and on making models1-10). However the estimation of the various reentrainment phenomena for each powder using such studies alone is difficult and how powder characteristics are to be evaluated remains an issue for future clarification.

Obtaining characteristics relating to adhesion strength is possible by measuring the adhesion strength of primary particles by a centrifugal method or by measuring the stress through various destructive tests of the powder layer. However, reentrainment

---

* Yoshida-honmachi, Sakyo-ku, Kyoto 606-01 Japan

† This report was originally printed in *J. Soc. Powder Technology, Japan.* **29**, 897 (1992) in Japanese, before being translated into English with the permission of the editorial committee of the Soc. Powder Technology, Japan.

is controlled by the balance between the adhesion strength of particles and the separation strength caused by an air flow, and studies must be made on the separation strength. When particle reentrainment is analyzed using a stress model, the separation strength can be equated to the product of wall shear stress caused by an air flow and the dimensionless form factor relating to reentrainment[10] but it is impossible to estimate theoretically the values of form factors for each powder. However, it is possible to obtain practical operational powder characteristics including form factors by measuring the wall shear stress which corresponds to reentrainment.

In the present study, fine particles deposited on a wall surface were reentrained by a continuous increase of the air velocity and the reentrainment phenomena for each type of powder were discussed using adhesion and aggregation properties. Furthermore, basic studies were performed in order to apply the relation between reentrainment and wall shear stress as a new method for measuring operational powder characteristics.

2. Test equipment and measuring method

Figure. 1 shows the structural outline of the test equipment. This equipment reentrains small amounts of powder attached to wall surfaces by an air flow. From the point of practical application, the equipment was made compact and data were automatically analyzed by digital processing. The amount of powder required for one measurement was less than several milligrams and the required measuring time was about 15 minutes.

Clean compressed air was used for particle reentrainment, and the electromagnetic valve for the air flow was controlled by a personal computer to increase the flow velocity at a constant rate. The average air velocity in the test section was obtained from the output signal of the mass flowmeter using the personal computer. For arithmetic processing, the output signal was calibrated by a volumetric type gas meter in advance and compensation calculation was incorporated. Aerosol discharged through the test section was evacuated into a reentrainment particle detector and the reentrained amount per unit time and area was obtained. Namely, the particle reentrainment flux could be obtained from the value of minute electric current generated when reentrained particles collided with the detection tube[11]. Since the sensitivity of the electrostatic detection method is high, the method is especially suitable for detection of low concentration aerosol particle flow. A short stainless steel tube (JIS SUS 304), 70 mm long with an inner diameter of 6 mm, was used as a detection tube. Since stainless steel has a hard oxide surface film, it is superior in electrostatic stability[12]. Also, to avoid deviation of the standard values of the generated electric current due to changes in the collision velocity of reentrained particles, it was necessary to maintain a constant average air velocity inside the detection tube. The test section of this equipment and the detector are not connected by piping and the setting was made so that the suction flow rate into the detector was greater than the maximum flow rate of compressed air passing through the test section. The minute electric current generated at the detector was amplified and then converted to voltage and automatically sampled as digital signals. The sampling cycle was 0.1 second and sampling was taken at 8000 points per one measurement (not less than 50 points while the average flow velocity increases up to 1 m•s^{-1}). The minimum digital input unit of the generated electric current was 0.05 pA and a maximum of 100 pA could be measured. The background in a room in normal conditions was not more than 0.05 pA.

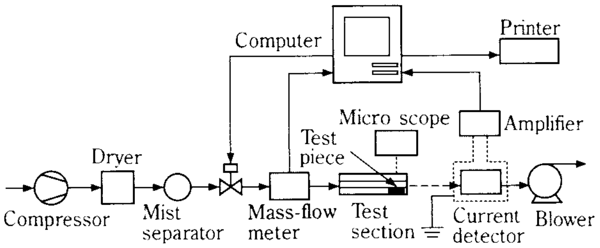

Fig. 1 Experimental apparatus

The test section consisted of a rectangular channel (width 8 mm, height 1 mm, total length 135 mm) made of stainless steel with a glass window on top. The test piece on which particles were deposited was installed behind a 100 mm fore-flow region at the same height as that of the inner surface of the channel. The selection of the test piece material was optional but here, a general purpose stainless steel (JIS SUS 304) was used with a normal machined surface finish (center line average roughness of 0.1 ~ 0.2 μm). As shown in **Table 1**, the test powders were the micron order powders for industrial testing (JIS Z8901) and also included a wide selection of others such as alumina abrasives, metals, and plastics. Among the powders, inorganic oxides which do not change in quality in an oven (at 120°C) were

Table 1 Test powders used

No.	Material	D_{p50} (µm)	$\varrho_p \times 10^{-3}$ (kg·m^{-3})	$W/A \times 10^3$ (kg·m^{-2})
1	Quartz powder (JIS Z8901-3)	7	2.7	1.7 ~ 4.6
2	Talc (JIS Z8901-4)	8	2.8	1.7 ~ 2.3
3	Talc (JIS Z8901-9)	4	2.8	1.7 ~ 4.0
4	Fly ash (JIS Z8901-5)	15	2.2	3.4 ~ 11.7
5	Fly ash (JIS Z8901-10)	5	2.2	3.4 ~ 8.6
6	Kanto loam (JIS Z8901-8)	7	3.0	1.1 ~ 5.7
7	Kanto loam (JIS Z8901-11)	2	3.0	2.3 ~ 4.6
8	Calcium bicarbonate (JIS Z8901-16)	4	2.8	1.7 ~ 4.0
9	Calcium bicarbonate (JIS Z8901-17)	2	2.8	1.1 ~ 2.3
10	Alumina (APPIE standard powder no.1)	3	4.0	1.7 ~ 3.4
11	Alumina (APPIE standard powder no.2)	5	4.0	1.7 ~ 4.0
12	Alumina (CB-A05; spherical particle)	3	4.0	1.7 ~ 2.9
13	Alumina (WA #320)	44	4.0	5.7 ~ 17.2
14	Alumina (WA #1000)	17	4.0	3.4 ~ 10.9
15	Alumina (WA #8000)	1	4.0	2.9 ~ 4.0
16	Antimony trioxide	7	5.2	5.7 ~ 13.2
17	Antimony trioxide (fine)	4	5.2	0.4 ~ 11.5
18	Copper	20	8.9	1.7 ~ 3.4
19	Toner	12	1.2	0.6 ~ 1.7
20	Polymethyl methacrylate (PMMA)	7	1.1	1.7 ~ 4.0
21	Polytetrafluoroethylene (PTFE)	30	2.2	2.9 ~ 12.1

dried for not less than 12 hours before their use. Deposition of particles on the test piece was carried out with the help of a sieve. With consideration to screening a suitable amount of micron order particles by normal vibrations, the openings were set at 74 µm (200 mesh). A test piece was cleaned with ethanol and air dried, then particles were dropped under gravity onto the center of the test piece (width 6 mm by length 30 mm). The reentrainment test was then conducted immediately.

3. Experimental results and discussion

3.1 Characteristics of equipment

The flow near the wall surface inside the channel is especially important since it is directly related to the particle reentrainment. In general, flow near the wall surface is analyzed by using friction velocity u^* defined by the following equation.

$$u^* = \sqrt{\tau_W/\varrho} \tag{1}$$

where τ_W is the wall shear stress and ϱ is the air density. The wall shear stress is proportional to the separation strength relating to particle reentrainment$^{10)}$, and it is necessary to obtain the channel flow characteristics of the equipment (relation between wall shear stress and average air velocity) in advance. The wall shear stress τ_W can be obtained using the following equation.

$$\tau_W = \Delta p D_e/(4L) \tag{2}$$

where Δp is the pressure loss in section L, and D_e is the hydraulic diameter of the channel. Pressure taps were attached at the mounting position of the test piece and pressure loss was measured by a diaphragm type differential pressure gauge. As shown by the solid line in **Fig. 2**, the wall shear stress is divided into two zones and both can be approximated by a function of the average air velocity. The obtained functions were incorporated in the program and used for data analysis. For reference, the results of the Hagen-Poiseuille equation and Blasius empirical formula applied respectively to laminar flow and turbulent flow zones are shown by the two broken lines.

3.2 Observations of particles on a test piece

Figure 3 shows the particles deposited on the test piece. As for Kanto loam (JIS Z8901-8) having small mass median diameter, large aggregates in an insular pattern are conspicuous. On the other hand, in alumina WA #320 having large mass median dia-

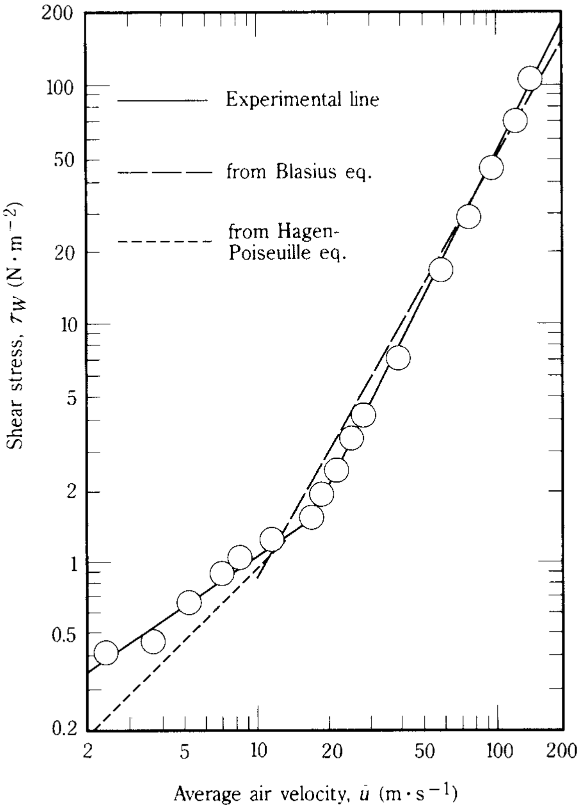

Fig. 2 Characteristic of flow

meter, almost all of them are primary particles, not aggregates.

Figures 4 and **5** give the progressive process of reentrainment of fine particles of Kanto loam (JIS Z8901-8) and fly ash (JIS Z8901-5) as typical examples. The basic reentrainment tendency of fine particles is similar and at low air velocity, relatively large aggregate particles are vigorously reentrained from insular aggregates and when the average air velocity reaches 20~30 m•s^{-1}, hardly any large aggregates are seen on the test piece. With the rise of air velocity, successive reentrainments of small aggregate particles continue. Reentrainment of primary particles or very minute aggregate particles becomes difficult and even when the average air velocity exceeds 100 m•s^{-1}, an extremely small residue of particles remain. However, there is a difference in the degree of reentrainment of aggregate particles depending on the type of the powder. Furthermore, in cases where hardly any aggregate particles are on the test piece from the beginning and only relatively large primary particles exist, such as with alumina WA #320, reentrainment progresses in a relatively mild manner.

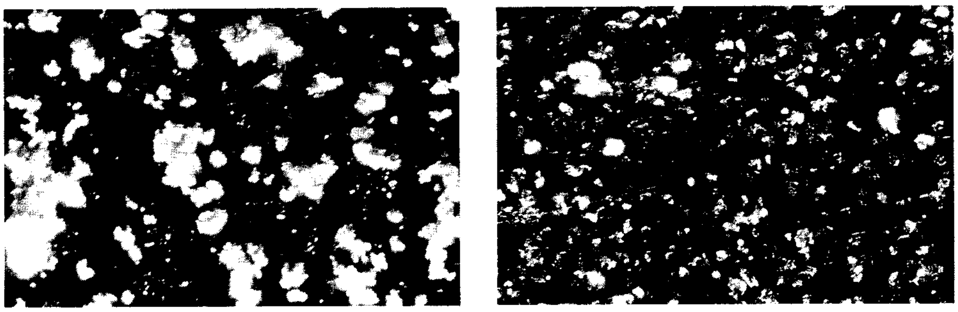

(1) Kanto loam (Z8901-8)
D_{p50} = 7µm, W/A = 5.7 × 10^{-3}kg · m^{-2}

(3) Copper
D_{p50} = 20µm, W/A = 2.9 × 10^{-3}kg · m^{-2}

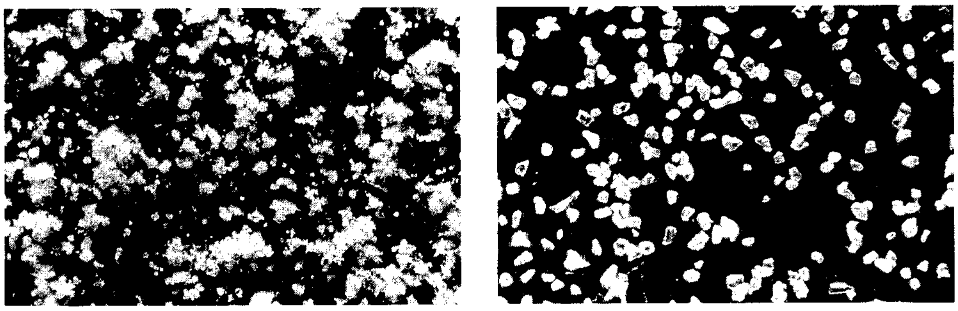

(2) Fly ash (Z8901-5)
D_{p50} = 15µm, W/A = 1.17 × 10^{-2}kg · m^{-2}

(4) Alumina (WA #320)
D_{p50} = 44µm, W/A = 1.21 × 10^{-2}kg · m^{-2}

0 500µm

Fig. 3 Photomicrographs of test powder adhering to the test piece

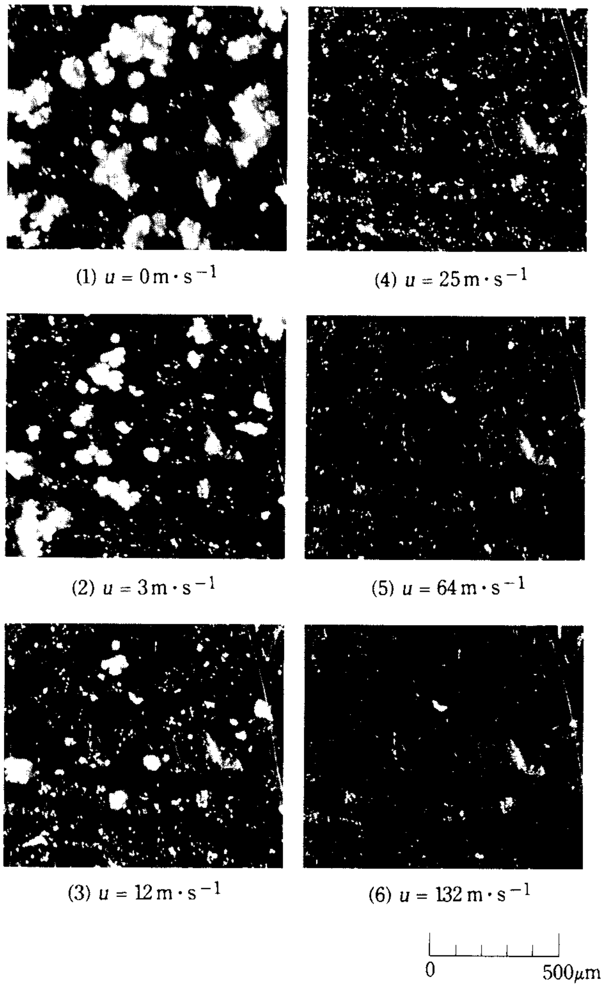
(1) $u = 0\,\mathrm{m \cdot s^{-1}}$
(2) $u = 3\,\mathrm{m \cdot s^{-1}}$
(3) $u = 12\,\mathrm{m \cdot s^{-1}}$
(4) $u = 25\,\mathrm{m \cdot s^{-1}}$
(5) $u = 64\,\mathrm{m \cdot s^{-1}}$
(6) $u = 132\,\mathrm{m \cdot s^{-1}}$

Fig. 4 Photomicrographs of particles remaining on the surface (Kanto loam, JIS Z8901-8)

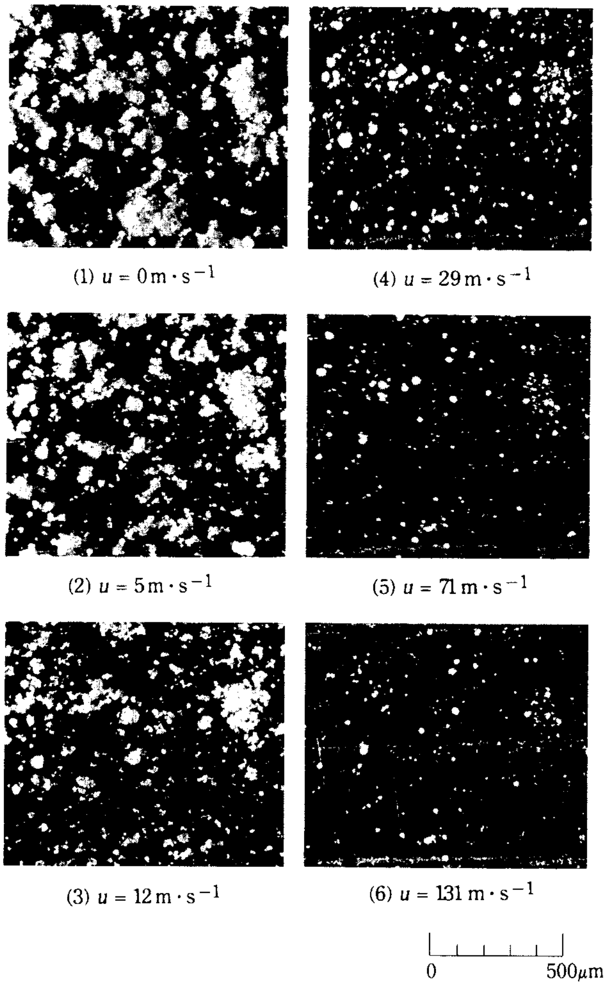
(1) $u = 0\,\mathrm{m \cdot s^{-1}}$
(2) $u = 5\,\mathrm{m \cdot s^{-1}}$
(3) $u = 12\,\mathrm{m \cdot s^{-1}}$
(4) $u = 29\,\mathrm{m \cdot s^{-1}}$
(5) $u = 71\,\mathrm{m \cdot s^{-1}}$
(6) $u = 131\,\mathrm{m \cdot s^{-1}}$

Fig. 5 Photomicrographs of particles remaining on the surface (Fly ash, JIS Z8901-5)

3.3 Measurement results of generated electric current

Taking the reentrainment test of alumina abrasives as an example, **Fig. 6** shows the output results of generated current with elapsed time when reentrained particles collide with the detection tube. In the bottom graph of the figure, the time course of the average air velocity is shown. Pulse current corresponding to momentary reentrainment is detected, but actually, since multiple particles collide simultaneously inside the detection tube, a condition in which pulse currents are cumulative is measured. Therefore, the generated current corresponds to the particle reentrainment flux on the test piece and reentrainment tendency can be derived from the overall increase and decrease of the generated current. Furthermore, information on reentrainment can be obtained from the momentary variation of the generated current. This is to say, generated current with a large variation indicates an interrupted or uneven reentrainment while conversely, a small variation in the generated current indicates that a continuous and uniform reentrainment is occurring. Basically, the generated current becomes larger because particles are more readily reentrained with an increase in flow rate but when reentrainment continues further, the amount of particles remaining on the test piece is reduced and therefore, the current gradually becomes smaller. As will be explained next, it was found that the generated current displayed a number of patterns depending on the characteristics of the powder.

Figure 6 shows the results of a reentrainment test of particles having the same quality (alumina, WA) but with three different mass median diameters (D_{p50} = 1, 17, 44 μm). With WA #8000 which has a small mass median diameter (D_{p50} = 1 μm), the generated current varies greatly at low air velocity but when this condition ends with the air velocity becoming higher, a minute current continues to be

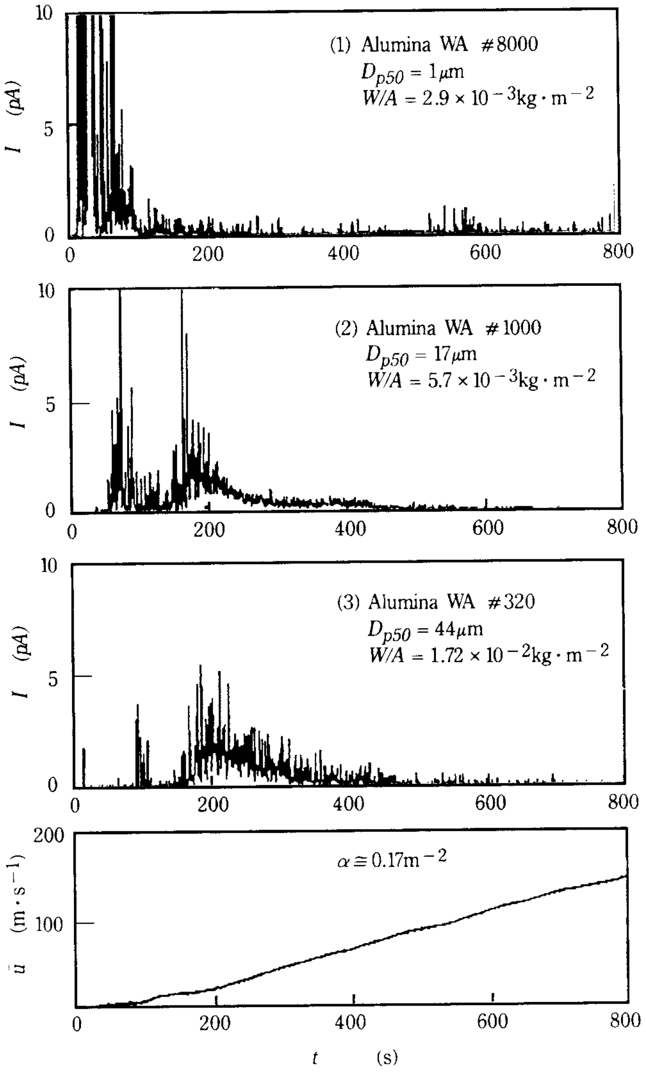

Fig. 6 Generated currents and average air velocity as a function of time elapsed

generated. As described in section 3. 2, the generated current at low air velocity corresponds to a vigorous reentrainment of relatively large aggregate particles. The generated current when the air velocity is high corresponds to the reentrainment of small aggregate particles but here, the quantity is extremely small. Even with WA #1000 having a slightly larger mass median diameter (D_{p50} = 17 μm), generation of current at low air velocity is observed but compared with WA #8000, the value is small. However when the air velocity becomes higher, the current again starts to increase and eventually, decreases slowly. At this time, a similar increasing and decreasing tendency is observed in the lower limit value of the generated current at each moment, this is because a pulse form current keeps on being generated and indicates that small aggregate particles or primary particles are continuously reentrained. With WA #320 (D_{p50} = 44 μm) which has an even larger mass median diameter, there are hardly any aggregate particles from the beginning (refer to **Fig. 3** (4)), and generation of current corresponding to the reentrainment of primary particles is clearly observed. In this way, the difference in primary particle diameters affects the aggregating characteristics and it was confirmed that the adhesion and aggregating state of powder on a test piece affect the time course of the generated current.

Now, when time integration of the generated current is performed, a electric charge corresponding to reentrainment quantity is obtained and when this electric charge is made dimensionless as in the following equation, the cumulative reentrainment efficiency η can be obtained.

$$\eta = \int_{o}^{t} Idt / \int_{o}^{t_e} Idt \qquad (3)$$

where t_e is the time up to the completion of the measurement. With regard to the alumina abrasive mentioned above, the output results of the relation between cumulative reentrainment efficiency and average air velocity are shown in **Fig. 7**. In this test, the condition of dynamic reentrainment in which the average air velocity continues to increase was measured and strictly speaking, the effect due to the delay of the reentrainment is included in the cumulative reentrainment efficiency η[8-10]. The value of η for the respective powders increases in accordance with the increase in average air velocity but a difference in the increasing tendency is observed with different mass median diameters. Here, the ratio of reentrained particles at low air velocity against total particles is defined as η_L. η_L marked

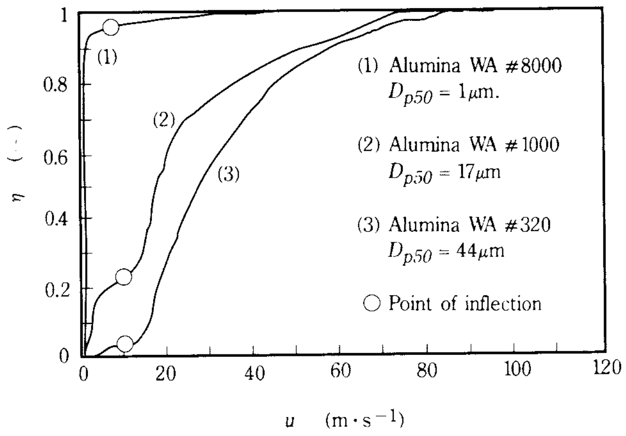

Fig. 7 Relationship between cumulative reentrainment efficiency η and average air velocity $\bar{u}$

by ○ in **Fig. 7** is the cumulative reentrainment efficiency at the inflection point. A notable difference is seen in η_L with η_L = 0.95 for WA #8000 (D_{p50} = 1 μm), η_L = 0.25 for WA #1000 (D_{p50} = 17 μm), and η_L = 0.05 for WA #320 (D_{p50} = 44 μm). In general, it is considered that reentrainment of particles having smaller mass median diameters becomes more difficult, but this should be applied only to the reentrainment of primary particles from a wall surface. It must be considered that as particle diameters become smaller, large aggregate particles are more readily formed. It is hinted that unless this is considered, results contrary to predictions may be obtained. Also, it can be predicted that the initial state may vary depending on the adhered amount of powder on the test piece but within the range of the adhered amount shown in **Table 1**, no apparent effect was observed. It is thought that this is because the effect of expansion of the area occupied by the powder on the test piece is greater than the effect of the powder being stacked in the vertical direction when the powder amount is increased. Of course, when the adhered amount becomes so great that the surface of the test piece can no longer be seen, the adhered amount will greatly affect the reentrainment. Furthermore, the reentrainment of relatively large aggregate particles is seen at low air velocities of not more than 5 m•s^{-1} and reentrainment of small aggregate particles or primary particles starts to progress when the air velocity exceeds 10 m•s^{-1}. As shown in **Fig. 2**, the flow at the test section changes greatly at a velocity of 19 m•s^{-1} but no notable change in the reentrainment is seen at this velocity in **Fig. 7**. Therefore, these reentrainment results are not characteristic of the equipment and can be applied to evaluate the operational characteristics of powder.

Next, the derivative of cumulative reentrainment efficiency η by $\bar{u}$ is shown in **Fig. 8** against the average air velocity $\bar{u}$. This figure corresponds to the relation shown in **Fig. 6**. Here, the entire reentrainment profile which was hidden by the momentary generated current changes and which could not be observed in **Fig. 6** can be clearly seen.

3.4 Results relating to reentrainment of various powders

The reentrainment tendency of powder with differing mass median diameters was studied in the previous chapter and here, the reentrainment of various powders with a narrow range of mass median diameters of 4 ~ 7 μm is studied. **Figure 9** shows the generated currents of 5 kinds of powders as a function of the elapsed time. Depending on the kind of powder, the generated current value differs greatly and therefore, a simple comparison of the particle reentrainment is impossible but differences can be seen in the time course of the generated currents. **Figure 10** shows $d\eta/d\bar{u}$ obtained from the cumulative reentrainment efficiency η of Eq. (3). With Kanto loam (JIS Z8901-8) and calcium bicarbonate (JIS Z8901-16), it is seen that reentrainment of aggregate particles at low air velocity is dominant while the proportion of aggregate particles at low air velocity diminishes in the order of talc (JIS Z8901-9), fly ash (JIS Z8901-10), and alumina (APPIE standard no. 2). These are typical results and these profiles are roughly simulated with other fine particles. Next, the output results of the cumulative reentrainment efficiency η are shown in **Fig. 11**. Here, to eliminate the effect of the size of the test channel and to apply to industrial equipment, the wall shear stress τ_w instead of the average air velocity $\bar{u}$ was used for the abscissa. The respective curves show the characteristics relating to reentrainment. It is seen that when special conditions to prevent all fine particles in the order of microns from adhering to the wall are required, the wall shear stress must be made

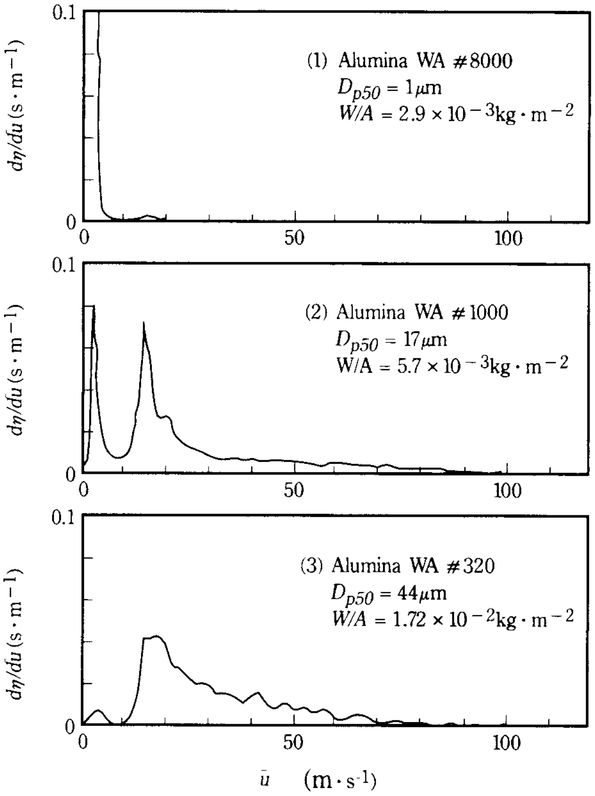

Fig. 8 Reentrainment efficiency distributions as a function of average air velocity

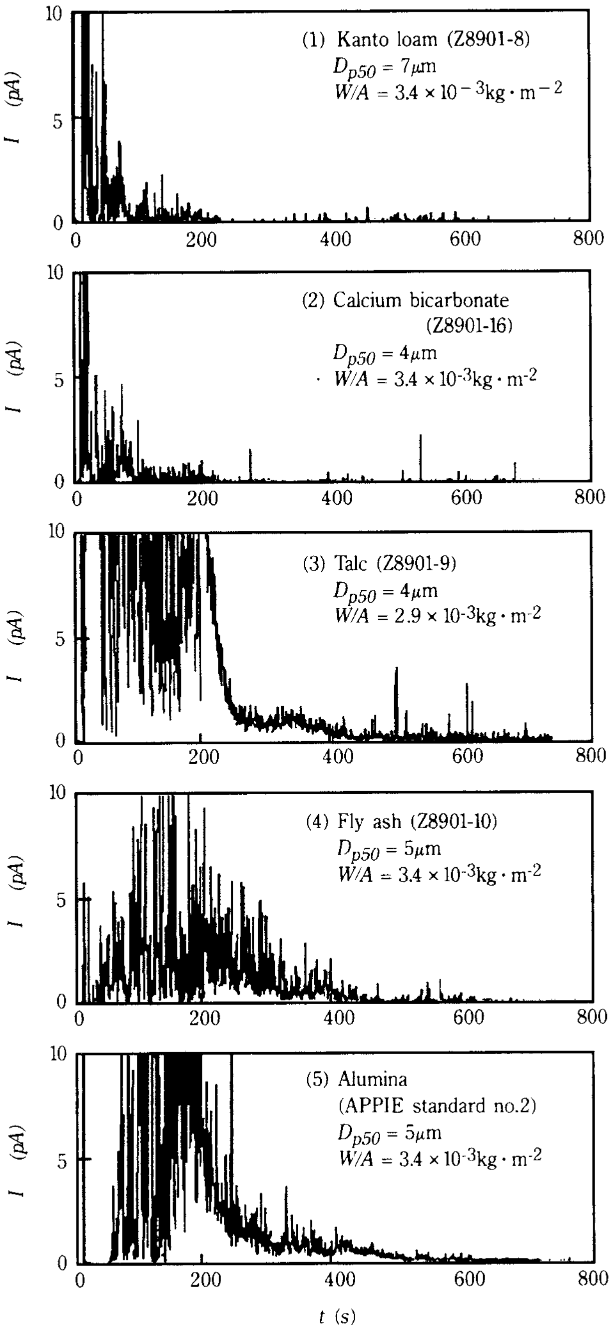

Fig. 9 Generated currents as a function of time elapsed ($\alpha \cong 0.17$ m•s^{-2}).

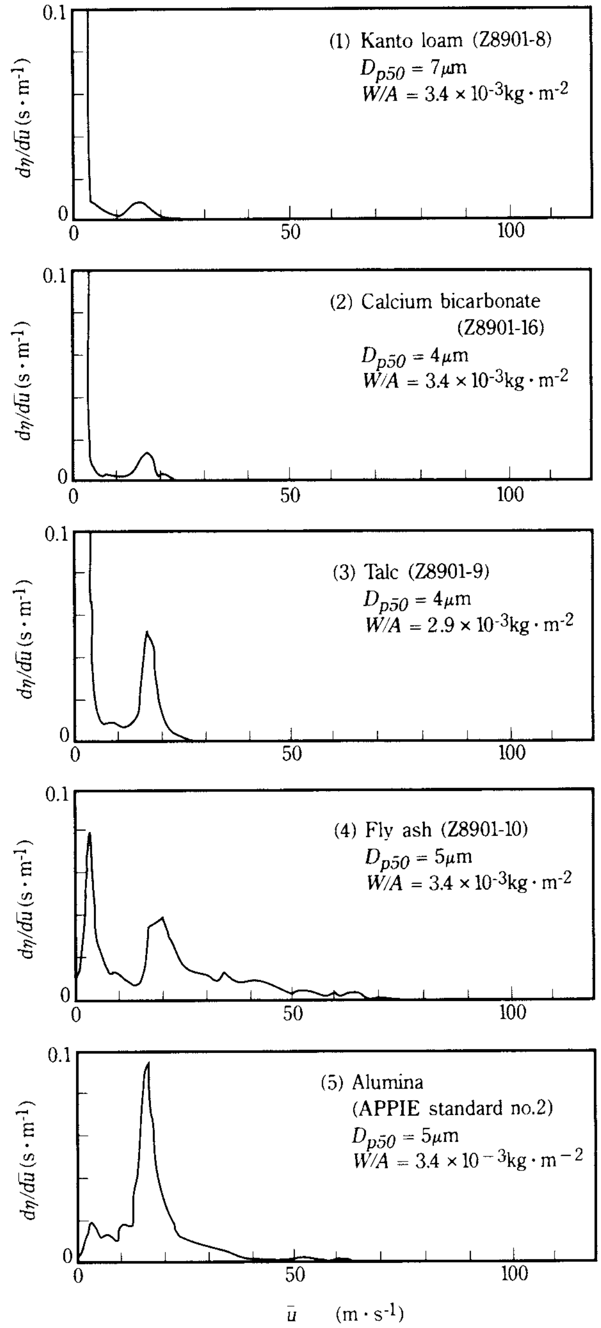

Fig. 10 Reentrainment efficiency distributions as a function of average air velocity

extremely large. However, it is important to control the adhered amount in general powder processes and the characteristic curve shown with the cumulative reentrainment efficiency η is effective in selecting such conditions. For example, to reduce the adhered amount of powder to $1/n$ of the actual amount, shear stress corresponding to η_1 must be selected as the new condition instead of η_0. The following relation is seen between η_1 and η_0.

$$\eta_1 = 1 - (1 - \eta_0)/n \tag{4}$$

In this test, reentrainment of aggregate particles was mainly targeted and **Fig. 12** summarizes the proportion η_L of reentrainment of large aggregate particles at low air velocities for all tested powders. A certain degree of scatter is seen but the characteristics of each powder are displayed and it can be considered that η_L is a characteristic including both aggregating and reentraining properties. This shows that as η_L approaches unity, reentrainment at low air velocity becomes easier. This is to say that with

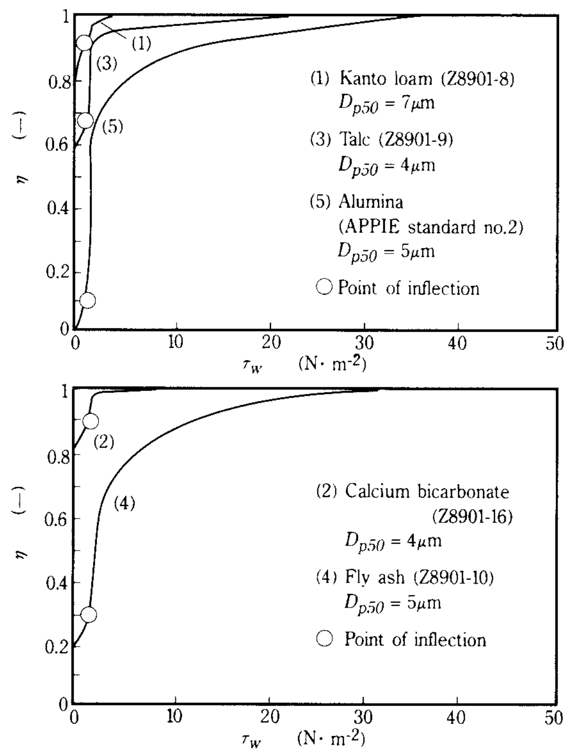

Fig. 11 Relationship between cumulative reentrainment efficiency η and wall shear stress τ_w

such powder, the adhesion properties between particles are strong and large aggregate particles are readily formed. Conversely, $\eta_L \simeq 0$ corresponds to a powder for which the adhesion between aggregate and wall occurs more strongly than the adhesion between aggregate and aggregate. In particular, those with extremely high aggregating properties ($\eta_L \simeq 1$), and on the other hand, those with low aggregating properties ($\eta_L \simeq 0$) have fairly good reproducibilities.

Finally, a study was carried out on the applicability of the electrostatic detection method for the respective powders. **Figure 13** shows the electric charge per unit mass of tested powders q/W_r. There are powders having a positive polarity and others having a negative polarity. It is thought that **Fig. 13** illustrates a kind of an electrostatic series. The test powders include metals and plastics in addition to inorganic oxides, and q/W_r reaches a value of the order of $10^{-5} \sim 10^{-2}$ C•kg^{-1}. It was possible to detect all of these sufficiently.

The adhesion state of particles to the wall differs depending on how the particles are made to deposit on the test piece and this should affect the reentrainment. Here, a most convenient screening method was adopted and it was possible to evaluate the difference in aggregate conditions by mass median diameter, and it is thought that this is a practical method for processes in which gently deposited aggregate particles are reentrained. However, it is necessary to review the deposition method of the

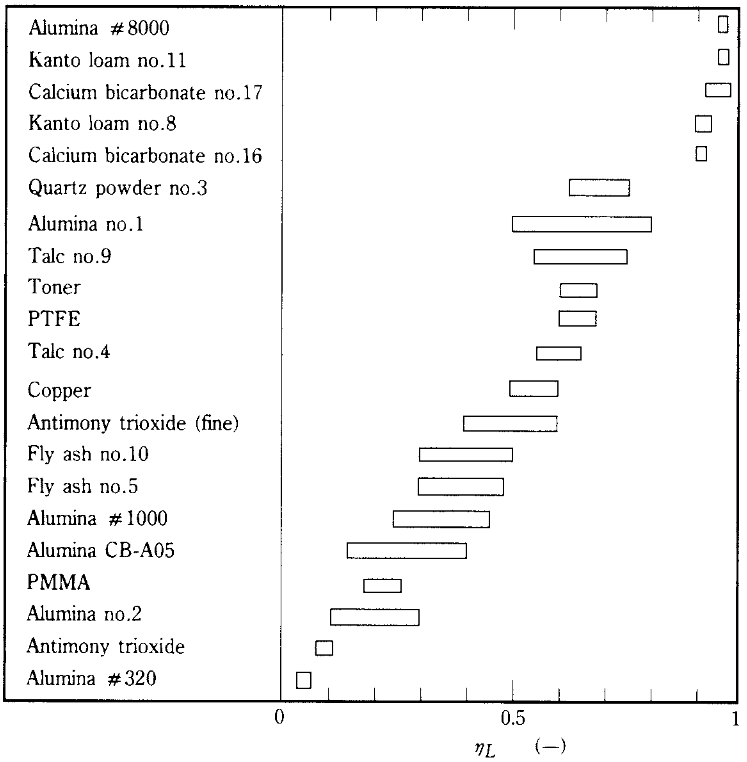

Fig. 12 Mass ratio of reentrained large aggregates to total particles (cf. Table 1)

particles in accordance with the process applied. Namely, depositing conditions such as dispersion efficiency, particle inertia and wall surface material as well as the ambient conditions such as temperature, humidity which are as close as possible to those in the actual process should be selected. It is not so difficult to take measurements using an deposition method which fulfills these conditions and data analysis can be applied successfully using the method which we have described in this paper. Depending on the deposition method, it may be possible to grasp the mutual relation between particles (cohesion), and between particles and wall surface (adhesion) more clearly. In this regard, further detailed studies are scheduled for the future.

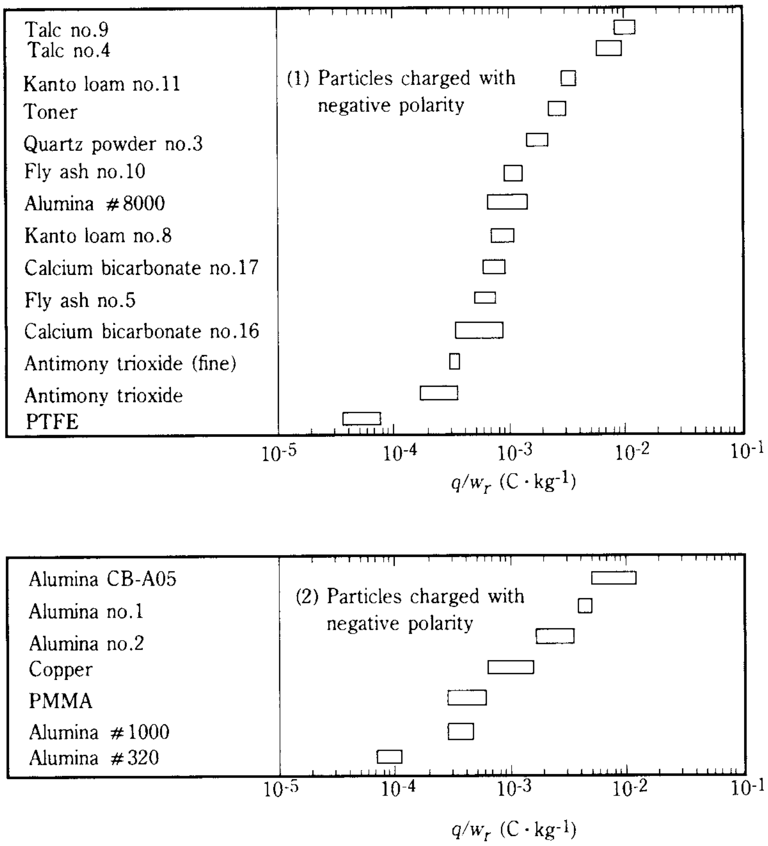

Fig. 13 Characteristics of particle electrification (cf. Table 1)

4. Conclusion

Using methods to increase the air velocity successively, reentrainment tests of various powders were conducted and the following conclusions were reached.

(1) It is possible to obtain reentrainment profiles from the generated current values by the electrostatic method and it was found that reentrainment could be generally divided into an uneven reentrainment of the relatively large aggregate particles at low air velocity and a uniform reentrainment of the small aggregate particles or primary particles at high air velocity.

(2) Aggregating properties become stronger as the size of the mass median diameter becomes smaller with reentrainment at low air velocity being dominant but depending on the type of powder, great differences are observed in aggregating and reentraining properties.

(3) It is possible to obtain the electric charge corresponding to the reentrainment quantity from time integration of generated current and it is possible to obtain the cumulative reentrainment efficiency by making the generated current dimensionless using the total electric charge corresponding to the total reentrainment quantity. This relation between the cumulative reentrainment efficiency and the wall shear stress gives a powder characteristic curve relating to reentrainment and by using this curve, conditions of the air flow for controlling the powder amount adhering to the wall surface can be selected.

Nomenclature

A	: area covered by deposited particles	(m^2)
D_e	: hydraulic diameter of rectangular channel	(m)
D_{p50}	: mass median diameter	(m)
I	: generated electric current	(A)
L	: distance between pressure taps	(m)
n	: variable in Eq. (4)	(−)
Δp	: pressure loss	(Pa)
q	: total charge	(C)
t	: time	(s)
t_e	: measuring time	(s)
$\bar{u}$	: average air velocity	($m{\bullet}s^{-1}$)
u^*	: friction velocity	($m{\bullet}s^{-1}$)
W	: mass of deposited particles	(kg)
W_r	: mass of reentrained particles	(kg)
α	: air acceleration	($m{\bullet}s^{-2}$)
η, η_0, η_1	: cumulative reentrainment efficiency	(−)
η_L	: mass ratio of large aggregates to total particles	(−)
ρ	: air density	($kg{\bullet}m^{-3}$)
ρ_p	: particle density	($kg{\bullet}m^{-3}$)
τ_w	: wall shear stress	($N{\bullet}m^{-2}$)

References

1) Ikumi, S., H. Wakayama and H. Masuda: *Kagaku Kogaku Ronbunshu,* **12,** 589 (1986)
2) Kousaka, Y., K. Okuyama and Y. Endo: *J. Chem. Eng. Japan,* **13,** 143 (1980)
3) Masuda, H., S. Matsusaka and S. Ikumi: *Kagaku Kogaku Ronbunshu,* **11,** 48 (1985)
4) Kanaoka, C., H. Emi, N. Kikukawa and T. Myojo: *J. Soc. Powder Technol., Japan,* **24,** 233 (1987)
5) Reeks, M. W., J. Reed and D. Hall: *J. Phys. D: Appl. Phys.,* **21** 574 (1988)
6) Wen H.Y. and G. Kasper: *J. Aerosol Sci.,* **20,** 483 (1989)
7) Wang. H.C.: *Aerosol Sci. Technol.* **13,** 386 (1990)
8) Matsusaka, S., T. Aoyagi and H. Masuda: *Kagaku Kogaku Ronbunshu,* **17,** 1194 (1991)
9) Matsusaka, S., Y. Nakamura and H. Masuda: *J. Soc. Powder Technol., Japan,* **29,** 110 (1992)
10) Matsusaka, S. and H. Masuda: *J. Soc. Powder Technol., Japan,* **29,** 530 (1992)
11) Masuda, H., T. Komatsu and K. Iinoya: *AIChE J.,* **22,** 558 (1976)
12) Masuda, H.: *Kagaku Kogaku,* **54,** 431 (1990)

A Study on the Formation of Cu-Al_2O_3 Composite Particles by Mechanofusion

A Consideration on the Formation relating to the Effects of Vacuum and Temperature Increase of Particle Surfaces†

Hisashi Kaga and Yoshihiro Taya
*Hokkaido Industrial Technology Center**
Yoshikazu Hamaguchi, Hiroshi Katayama and Ken-ichi Mukaida
*Muroran Institute of Technology***

Abstract

A mechanofusion apparatus which can operate at a high vacuum pressure of the order of 10^{-2} *Pa was developed. Using this apparatus, formation of Cu composite with* Al_2O_3 *core particles was conducted. The rate of progress of composite formation was low under atmospheric or low vacuum conditions but under a high vacuum or in an Ar displaced atmosphere, such formation was remarkably accelerated. Namely, it was found that composite formation is greatly accelerated by lowering the oxygen partial pressure. Following oxygen analysis of the Cu covering layer of composite particles by AES, it was found that with a higher atmospheric pressure, the oxygen amount became higher and oxygen penetrated into the interior.*

As a result of microstructure observations of the composite particles to which extended mechanofusion processing and chemical etching had been applied, grain boundaries were observed in the Cu covering layer which may imply that the Cu particle surface becomes exposed to high temperature as more sintering occurs. This microstructure is very similar to the structure of Cu after high temperature annealing. The individual particle surface temperatures during mechanofusion was estimated as being around 1000 K from the experimental results of sintering behavior of cold pressed Cu.

1. Introduction

Composite particles are becoming popular as a raw material for producing new materials[1]. Mechanical processes are attracting an attention for producing these composite particles. Among these processes, research relating to composite formation by the mechanofusion method has been aggressively studied because of its flexibility to wide variety of raw materials, and of possibility of adding novel characteristics to the material[2-4].

It is known that the surface temperature of powders becomes extremely high during mechanofusion[5]. However, only a few research attempts have been made to quantify the temperature increase of particle surfaces[6,7] as well as the effect of the atmosphere on mechanofusion. It will be necessary to clarify the effect of the atmosphere on the formation of composite particles to advance the development of highly functional composite particles and the industrialization of the mechanofusion process.

In this report, we discuss the formation of composite particles consisting of *Cu* adhering particles and Al_2O_3 core particles by mechanofusion in vacuum. The effect of atmospheric pressure on composite formation was examined through the evaluation of the specific surface area. Also a consideration was made on the role of vacuum through analyzing the components of the top surface layer of the composite particles and the behavior of the rate of progress of composite formation in vacuum, argon, and hydrogen atmospheres. The temperature rise of the particle surface layer during the mechanofusion process was

---

* 379 Kikyo-cho Hakodate, Hokkaido 041, Japan

** 27-1 Mizumotocho Muroran, Hokkaido 050, Japan

† This report was originally printed in *J. of Japan Society of Powder & Powder Metallurgy*, **39**, 1124, 1129 (1992) in Japanese, before being translated into English with the permission of the editorial committee of the Soc. of Powder & Powder Metallurgy.

quantified by considering the sintering behavior of *Cu* particles. On the basis of these results, the role of the mechanofusion atmosphere on promoting composite formation was studied.

2. Experimental

2.1 Vacuum mechanofusion apparatus

Based on a mechanofusion apparatus, model AM-15F, made by the Hosokawa Micron Corporation, a high vacuum mechanofusion apparatus was developed. A schematic drawing of this apparatus is shown in **Fig. 1**. It is composed of a fixed inner piece and a rotating casing etc. A structure to prevent the ingress of powders into the evacuating system was introduced, making it capable of direct evacuation of the inside of the casing. Magnetic seals were used as vacuum seals for the rotary part. This apparatus maintains a high vacuum of the order of 10^{-2} Pa during mechanofusion. The maximum quantity of powder which can be charged is 150 cc. A thermocouple imbedded at a depth of 5 mm from the surface of the inner piece which comes into contact with the powder gives continuous reading of the temperature during the mechanofusion process (hereinafter called the inner piece temperature).

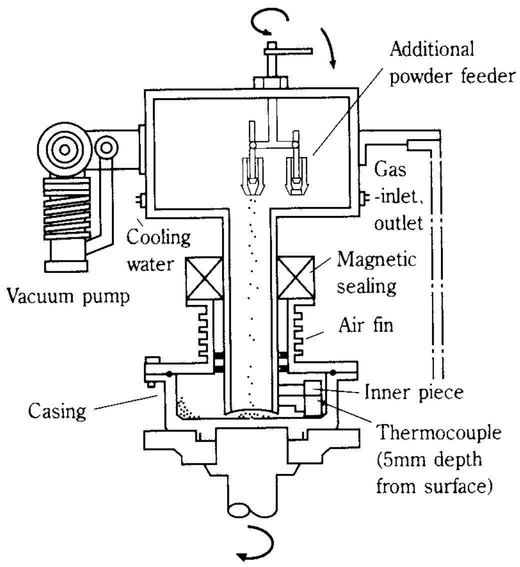

Fig. 1 Schematic outline of vacuum mechanofusion apparatus

2.2 Surface analyses of the composite particle

The raw material powder used for composite formation consisted of spherical core particles of Al_2O_3 having an average particle diameter of 45 μm, and attached *Cu* particles having an average diameter of 0.2 μm. One hundred grams of the mixed powder of 10 mass% *Cu*-90 mass% Al_2O_3 were charged in the casing and after evacuation was made to the specified pressures of 1.0×10^5 Pa, 5.3×10^2 Pa, and 5.3×10^{-2} Pa, mechanofusion processing was initiated. In addition to this, powders were charged and after the specified pressures were reached, the atmosphere was replaced by with *Ar* or hydrogen gas set at specified pressures, then mechanofusion processing was initiated. Thereafter, from the composite formation behavior, the role of vacuum was studied. The mechanofusion conditions were as follows: a casing revolving velocity of 800 *rpm*, a mechanofusion time of 3.6 *ks*, and a space between the inner piece and the casing of 3.5 mm.

The specific surface areas of the mechanofused composite powder was measured by the BET one point method using FLOWSORB II 2300 made by Shimadzu Co., Ltd. and the progress of the composite formation was evaluated. Constituent of the top surface layer of the composite particles was analyzed by using an Auger analysis apparatus JAMP-7000 made of JEOL Ltd.

2.3 Test of increase of particle surface temperature

Tests to study the temperature of particle surface layers were conducted as follows. Attaching *Cu* particles having an average particle diameter of 2.4 μm were used because of easy observation of their micro-structure of the surface layer, and the above mentioned spherical Al_2O_3 particles having an average particle diameter of 45 μm were used as core particles. The composite formation tests were conducted with the mechanofusion time set at 3.6 *ks* and 10.8 *ks*. The mechanofused composite particles were etched in an aqueous solution (5% HCl + 1% $FeCl_3$) and the surface structure was observed with a SEM.

In regard to sintering behavior, *Cu* powder for attaching *Cu* particles were used to produce a compact specimen having a diameter of 20 mm and a thickness of 3 mm by press compacting at room temperature. The press load for compacting was 14 *kN*. This specimen was heated rapidly in a vacuum oven and then the density of the sintered specimen was measured. The sintering test was repeated by several temperatures. Also an observation by a SEM was conducted and the sintering temperature of the specimen was specified. In regard to the heat maintenance time, the time during which the individual particles were actually subjected to dynamic action in the space between the inner piece and the casing was calculated and this calculated time was applied.

3. Results and discussions

3.1 Effect of atmosphere

Figure 2 shows the changes of the inner piece temperature and the BET specific surface area with the atmospheric pressure during mechanofusion. **Figure 2** shows the results after 3.6 *ks* mechanofusion for 10 mass%*Cu*-90 mass% Al_2O_3 mixed powder, and the open circle ○ in the Figure denotes results in air while the solid circle ● denotes results in the *Ar* atmosphere. The inner piece temperature tends to decrease with the increase in the atmospheric pressure. With the exception of the case with a high vacuum of 5.3×10^{-2} Pa, the temperature in the *Ar* atmosphere is slightly higher, than in air. However, when compared with the case of *Cu* core particle and Al_2O_3 adhering particles[8,9], the temperature difference with the atmospheric pressure is very small.

In air, the specific surface area increases with the atmospheric pressure indicating that the formation of composites becomes more difficult in high pressure regions. On the other hand, in the *Ar* atmosphere, the extent of the BET specific surface area increase with a pressure increase is extremely lower. Under a high vacuum of 5.3×10^{-2} Pa, the BET specific surface area does not differ between the air atmosphere and the *Ar* atmosphere but with an increase in pressure, the difference increases. That is to say, it was found that composite formation is greatly accelerated under a low vacuum of 5.3×10^{2} Pa and under an atmospheric pressure of 1.0×10^{5} Pa in an *Ar* atmosphere. No effect at all of *Ar* atmosphere to accelerate composite formation was observed under a low pressure (high vacuum) of 5.3×10^{-2} Pa, but the effect increased greatly as the atmospheric pressure became higher than this pressure.

Composite particles formed by mechanofusion under a normal atmospheric pressure of 1.0×10^{5} Pa showed a brownish black color, but composite particles formed by mechanofusion in the *Ar* atmosphere at the same atmospheric pressure had a reddish copper color. Therefore, acceleration effect of the composite particle formation of the *Ar* atmosphere corresponds to the effect of a partial pressure of oxygen decrease. It is believed that oxidation of *Cu* plays an important role in accelerating composite particle formation. The reason why the Ar atmosphere of a pressure of 5.3×10^{-2} Pa shows no effect can be that oxidation does not occur to such an extent as to obstruct composite formation at 5.3×10^{-2} Pa or under, or that the decrease in oxygen partial pressure does not occur due to the impurity oxygen in the *Ar* gas.

Since oxidation of *Cu* is important in this way, SEM observation results of composite particles after mechanofusion processing of particles in air, argon, and hydrogen under atmospheric pressure of 5.3×10^{2} Pa are shown in **Fig. 3**. In air as shown in **Fig. 3** (a), a granular *Cu* particles at the initial stage of composite formation process are observed. In the Ar atmosphere (b), the smooth covered area by *Cu* increases and composite formation accelerates. In the hydrogen atmosphere (c), irregularities become small, the covered area increases with a further progress of smoothing, and composite formation has progressed compared with (b). When the atmosphere is replaced by *Ar*, the oxygen partial pressure is smaller and composite formation is more advanced as shown in **Fig. 3** (b) than in air as shown in **Fig. 3** (a). In the hydrogen atmosphere (c), the reducing effect of hydrogen combined with the decrease in the oxygen partial pressure promotes composite formation. The oxidation preventing effect of atmosphere is important in promoting composite formation.

It is believed that the oxidation of *Cu* obstructs the adhesion among *Cu* particles, and among *Cu* and Al_2O_3 core particles. Adhesion must occur through *Cu* oxides which prevent the formation of a strong adhesive covering layer.

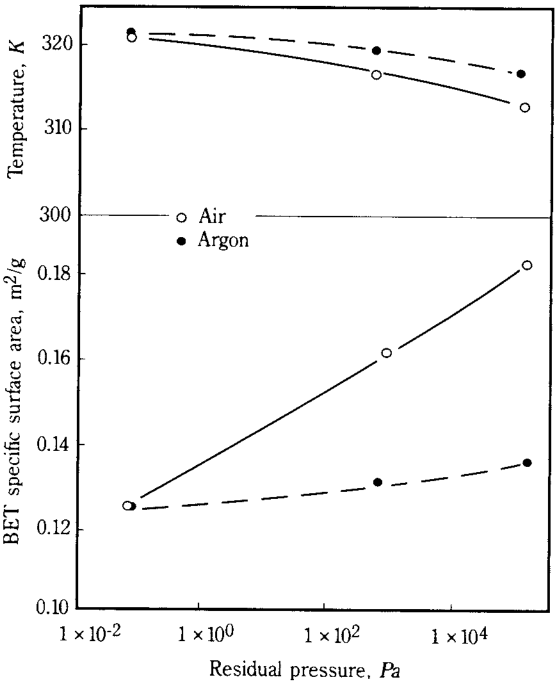

Fig. 2 Effect of the pressure of the atmosphere on BET specific surface area and inner piece temperature.

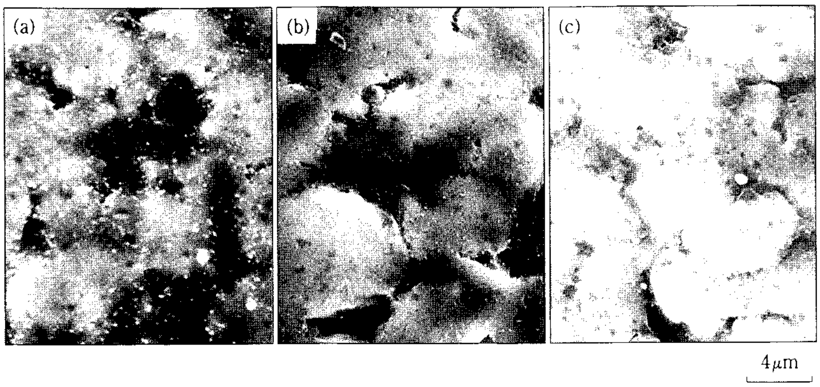

Fig. 3 SEM surface micrographs of a composite particle. (3.6 ks, 5.3 × 10^2 Pa) (a) Vacuum, (b) Argon, (c) Hydrogen

3.2 Surface analysis of composite particles

Figure 4 shows the AES spectrum of composite particles mechanofused at 5.3×10^{-2} Pa for 3.6 *ks*. As can be seen in **Fig. 4** (a), in addition to *Cu* of the attached particle, *O*, *C*, and *Al* (with an arrow) are detected. Carbon peak is due to contamination by organic impurities. It is in agreement with the gas analysis during the mechanofusion process⁸⁾. The peak of *Al* derives from the Al_2O_3 core particle, and the peak of *O* is due to oxygen presented in Al_2O_3, *Cu* oxide or *Cu*. In regard to *O*, mention is made later and the *Al* peak due to Al_2O_3 is described here. As reasons for the detection of Al_2O_3, two points may be considered; one is the detection of *Al* from the exposed part of the Al_2O_3 core particle within the *Cu* covering layer inside the beam diameter and the other is the mixed presence of Al_2O_3 in the covering layer.

However, for the former reason, as shown in **Fig. 4** (b), experimental results show the presence of a layer in which the *Al* peak is not detected during Ar ion sputtering before reaching the core particle phase. Judging from this result, the peak of *Al* in the composite particle surface layer cannot be conceived as *Al* from the exposed part of the Al_2O_3 core particle. The sputter conditions in **Fig. 4** (b) are: accelerating voltage of the primary electrons in the AES analysis is 5 *kv*, the ion energy is 3 *kv*, the ion current density is 150 $\mu A/cm^2$, and the sputtering rate for *Cu* is 3.5 Å/s estimated from the sputtering rate for SiO_2.

The result that Al_2O_3 was detected in the *Cu* layer is an interesting phenomenon for the study of the composite formation process and also in considering the characteristics of composite particles. The mechanism of this Al_2O_3 mixing into *Cu* phase is not clear. It is thought that Al_2O_3 abraded powder generated by friction etc. between core Al_2O_3 particles, and between Al_2O_3 and *Cu* particles during the mechanofusion process mixes with *Cu*. It is believed that composite formation progresses in the initial stage with repeated joining by adhesion friction of *Cu* to Al_2O_3 and repeated separation, and by imbedding of abrasion powder generated by abrasion between Al_2O_3 particles into attached or attaching *Cu* powder.

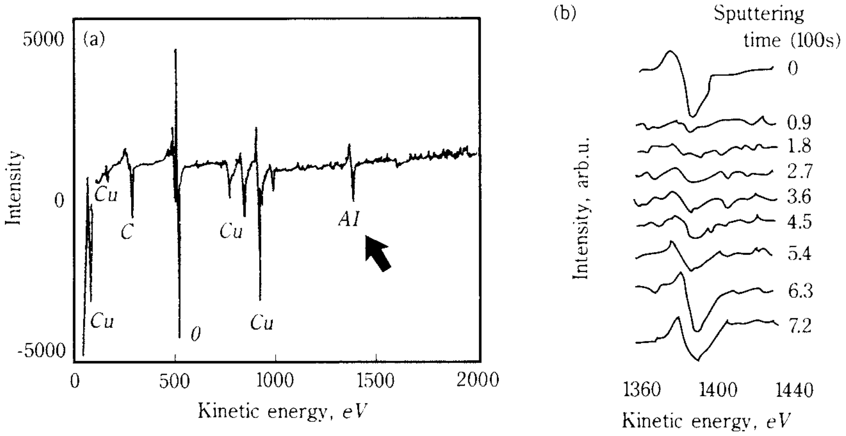

Fig. 4 AES spectra of the composite particle. (a) Surface spectrum (b) Spectra change with sputtering time

Composition depth profile of composite particles mechanofused in air at a pressure of 1.0×10^5 Pa analyzed by AES is shown in **Fig. 5**. The sputtering conditions were the same as those in **Fig. 4** (b). In the short sputtering time region in **Fig. 5**, namely in the top surface layer, a densifying of *O* and *Al* is observed. In this region, *Cu* decreased. As mentioned above, *O* peak arises from *Cu* oxide, oxygen in *Cu*, and *O* from Al_2O_3. Only the oxygen intensity relating with *Cu* must be derived. The oxygen depth profile was obtained by subtracting the *O* quantity of Al_2O_3 from the *O* content in **Fig. 5**. The AES peak strength ratio between *Al* and *O* in Al_2O_3 was obtained, and *O* corresponding to *Al* was deducted.

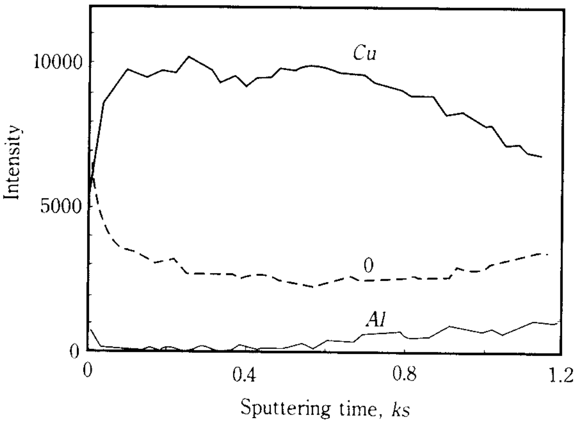

Fig. 5 AES depth profiles of composite particles mechanofused at 1.0×10^5 Pa.

Figure 6 shows the oxygen quantity obtained in this way plotted against the sputtering time. With the lapse of sputtering time, the oxygen quantity decreases to a stable value at a certain depth. However the depth at which the value becomes constant varies depending on the atmospheric pressure during mechanofusion. As the atmospheric pressure becomes higher, the depth at which the value becomes constant increases. The degree of oxygen densification decreases with lowering atmospheric pressure, and moreover the densification is limited to the very top surface layer. In composite particles treated at the maximum pressure of 1.0×10^5 Pa, the oxygen content at the surface is high and densification of oxygen is seen even inside the particle. Consequently, the effect of low atmospheric pressure on the composite formation promotion mentioned in **Fig. 2** can be substituted by oxygen partial pressure.

These composite particles were placed on a *Cu* mesh and flattened to 12 × 12 mm by a press load of 50 *kN*, then subjected to an XPS analysis. The external appearance of the surface of the composite particles after pressing is shown in **Fig. 7**. In contrast with the superior ductility and malleability of *Cu* of the composite particle surface produced under a pressure of 5.3×10^{-2} Pa, numerous micro-cracks were observed on the surface layer of composite particles produced under 1.0×10^5 Pa.

Although omitted in this paper, it was found from the results of an XPS analysis that the *Cu* condition changed its oxidation state in the order of *CuO*, Cu_2O, and *Cu(O)* from the surface layer. Compared with those produced under 5.3×10^{-2} Pa, composite particles produced under 1.0×10^5 Pa had a thicker oxide layer of *CuO*, Cu_2O and such. This result agrees well with the generation of micro-cracks on composite particles produced under 1.0×10^5 Pa in **Fig. 7**.

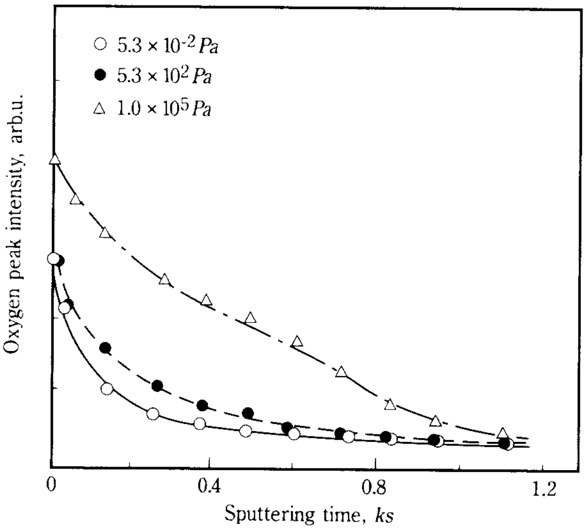

Fig. 6 Variation of Auger oxygen peak intensity with sputtering time for the composite particles mechanofused at different pressures.

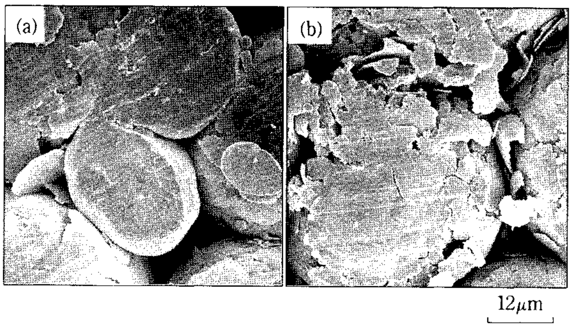

Fig. 7 SEM surface micrographs of the composite particles compressed by cold press.

3.3 Observation of the particle surface temperatures

3.3.1 Observation of the composite particle surface

Composite particles from 10 mass%*Cu*-90 mass% Al_2O_3 mixed powder were chemically etched, and then the microstructure was observed through a

SEM. **Fig. 8** shows the results. With a mechanofusion time of 3.6 *ks* in **Fig. 8** (a), the exposed part of an Al_2O_3 core particle can be observed owing to the intrinsic concavities without *Cu* covering, or due to elution of *Cu* by corrosion of the *Cu* covering layer. Also the boundary between particles show waviness. In contrast, with 10.8 *ks* in **Fig. 8** (b), a standard-type grain boundaries like those seen after heating of *Cu* by ingot making process, entirely different from the *Cu* particle shape of the raw material, were observed10). It is thought that the reason for grain boundary formation is considered as follows; the *Cu* particles adhere to the core particles, and to each other during mechanofusion, then after heated by the friction between particles, together with occurrence of plastic deformation by processing, sintering between particles progresses, and as a result grain boundaries are formed.

It is not clear whether these crystal grains originate from initial *Cu* particles or whether they are crystal grains formed after recrystallizing. Considering the fact that the crystal grains are isotropic and are not of a mixed structure containing fine crystal grains, it can be assumed that the crystal grains were subject to repeated isotropic processing and temperature increases. As shown in **Fig. 8** (a), the formation of such linear grain boundaries is not attained with a mechanofusion processing time of 3.6 *ks*.

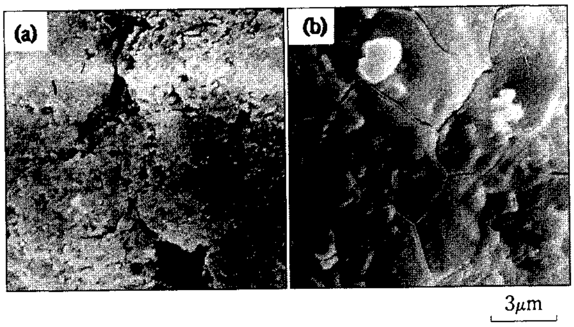

Fig. 8 Surface microstructures of composite particles after chemical etching.
(a) 3.6 ks, (b) 10.8 ks

3.3.2 Effect of Mechanofusion time

To form a micro-structure as shown in **Fig. 8** (b), the mechanofusion time is an important factor. Here we discuss the time during which powder being mechanofused is subjected to the actual dynamic action between the inner piece and the casing. Hereafter the time is designated as actual mechanofusion time.

Figure 9 shows a schematic drawing of the rotating casing and the inner piece. **Figure 9** (a) shows a conceptual drawing of the casing and the inner piece and also the scraper, while **Fig. 9** (b) shows an enlarged drawing of the casing and the inner piece section. Powder is subjected to dynamic actions such as compressing, shearing, and friction, and the compacted powder is scraped from the casing by the scraper, pressed against the inner wall of the casing by the centrifugal force, again subjected to dynamic action between the casing and the inner piece, and composite formation of particles occurs11,12).

Next, the actual mechanofusion time is calculated. The contact angle θ of the powder being worked on the casing periphery is expressed by equation (1).

$$\theta = \ell / 2\pi R \quad \cdots\cdots (1)$$

Here, ℓ is the contact length, and R is the radius of curvature of inner piece.

The contact length ℓ in a loaded condition with 100 grams of 10 mass% *Cu*-90 mass% Al_2O_3 mixed powder was measured to be 12 mm. R was 42 mm. By calculating θ from these values, θ = 0.045 (rad) was obtained.

The actual mechanofusion time t with respect to the mechanofusion time t_0 is approximated by equation (2).

$$t \fallingdotseq \theta \bullet t_0 \quad \cdots\cdots (2)$$

The actual mechanofusion time in this study, calculated t = 0.16 *ks*, 0.48 *ks* using equation (2) and t_0 = 3.6 *ks*, 10.8 *ks*.

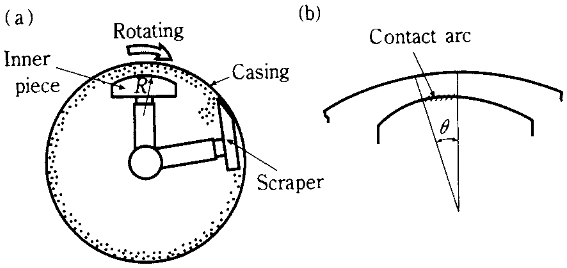

Fig. 9 Schematic diagrams of the mechanofusion process.

3.3.3 Sintering behavior of attached *Cu* particles

On the basis of these actual mechanofusion time and the sintering behavior of the attached *Cu* particles, a study was made of the temperature increase during mechanofusion. Using *Cu* powders having average particle diameters of 0.2 μm and 2.4 μm, a disk shaped compact was made by cold pressing. The 0.2 μm powder, used for the surface analysis, was used for comparison as well. After heating the disk compacts for the actual mechanofusion time $t = 0.16$ *ks* ($t_0 = 3.6$ *ks*) and $t = 0.48$ *ks* ($t_0 = 10.8$ *ks*), the sintering temperature of *Cu* powders was estimated by obtaining the bulk density variation.

Since wavy grain boundaries are seen at $t_0 = 3.6$ *ks* ($t = 0.16$ *ks*) in **Fig. 8** (a), it is assumed that sintering between particles did not occur. On the other hand, at $t_0 = 10.8$ *ks* ($t = 0.48$ *ks*) in **Fig. 8** (b), the microstructure is the same as that produced by normal methods such as ingot making. It is believed that a sintering action occurred due to thermal diffusion of *Cu*, accompanying a temperature increase of the particle surface during mechanofusion. Therefore by estimating the temperature at which sintering does not occur at $t = 0.16$ *ks* and at which sintering occurs at $t = 0.48$ *ks*, it is possible to estimate the particle surface temperature during mechanofusion.

Figure 10 shows the density variation resulting from these heating temperatures. With the compacts having an average particle diameter of 0.2 μm, sintering started at 773 *K* but in contrast, with those having a particle diameter of 2.4 μm which were used for the microstructure observation shown in **Fig. 8**, sintering began at around 973 *K*. However, between the maintenance time $t = 0.16$ *ks* and $t = 0.48$ *ks*, considerable difference in sintering starting temperatures for both powders could not be observed.

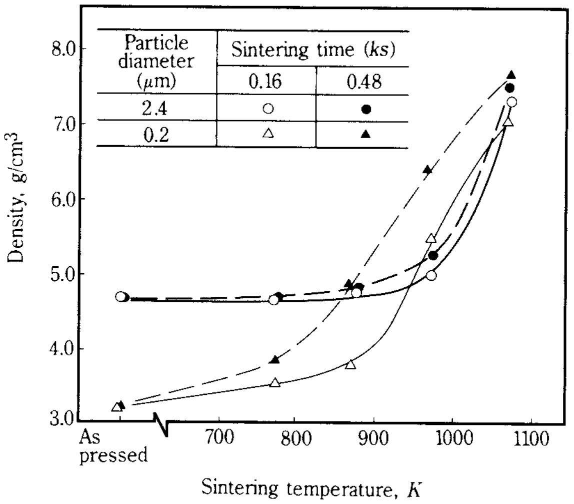

Fig. 10 Variation of apparent density of the *Cu* compact with sintering temperature.

Figure 11 shows the SEM surface observations of a sintered body using of 2.4 μm. **Figure 11** (a) and (b) show the surface with a sintering time (corresponding to t) of 0.16 *ks*, while **Fig. 11** (c) and (d) show the surface with a sintering time of 0.48 *ks*. As can be clearly seen in **Fig. 11**, with a heating time of $t = 0.16$ *ks*, sintering does not occur at a sintering temperature of 973 *K* in (a) but begins at a sintering temperature of 1073 *k*. On the other hand, with a heating time of $t = 0.48$ *ks*, sintering does not occur at a sintering temperature of 873 *k* in **Fig. 11** (c) but occurs at 973 *K* in (d).

Consequently, from the results of **Fig. 10** and **Fig. 11**, the maximum temperature at which sintering does not occur with $t = 0.16$ *ks* is 973 *K*, while the sintering starting temperature with $t = 0.48$ *ks* is 973 *K*. From these results, it is assumed that the particle surface temperature rises to around 973 *K* during the mechanofusion to produce composite particles shown in **Fig. 8**.

However the sintering behavior in the present experiment was analyzed to obtain the sintering temperature of a compact made by pressing under room temperature by static heating. In the actual mechanofusion processing, the sintering conditions are dynamic in which processing and heating are simultaneously performed. The actual sintering temperatures are probably lower than the sintering temperatures obtained in **Fig. 10** and **Fig. 11**. Of course, the degree of temperature rise differs depending on the mechanofusion conditions and on the used raw material powder. A systematic study in these connections will be necessary.

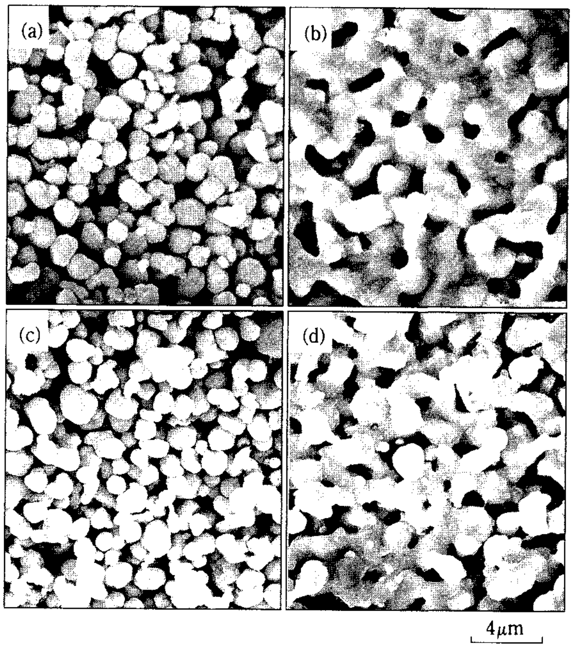

Fig. 11 Change in appearance of *Cu* compacts with sintering time and temperature
(a) $t = 0.16$ *ks*, $T = 973$ *K*, (b) $t = 0.16$ *ks*, $T = 1073$ *K*
(c) $t = 0.48$ *ks*, $T = 873$ *K*, (d) $t = 0.48$ *ks*, $T = 973$ *K*

Up to the present, it has been reported that the temperature of particle surface increases during mechanofusion[3]. Although this matter is important from the viewpoint of the composite formation mechanism and for the development of suitable processing techniques, studies in this connection have been few because of the difficulty of measurements. Mizota et al[6] derived the particle surface temperature rise when attaching TiO_2 particles to PMMA core particles from the changes in the color tones of TiO_2 caused by heating. They reported that the particle surface temperature rises to 573 K or higher. Also Nogi et al[7] used standard free energy of formation for oxides, and from the oxygen contents in Mo and Si powder during mechanofusion, estimated the temperature of the particle contact surface to be within the range of 593 K to 1703 K.

The temperature estimated from the sintering behavior in the present study was around 1000 K and being within the temperature range estimated by Nogi et al. However, the above mentioned dynamic factors or mechanochemical reaction factors are not considered both in the present study and in the study by Nogi et al. Hereafter,further studies will be required, including studies by quantitative treatment. As mentioned above, the direct measurement of the particle surface temperature during mechanofusion is extremely difficult. It will be necessary to estimate the particle surface temperature by various methods and conduct comparative studies of the results.

In this way, a temperature rise to around 1000 K in atmosphere comprises a temperature range in which notable oxidation of Cu occurs. From the viewpoint of suppressing oxidation in the promotion of composite particle formation, the role of vacuum atmosphere control can be regarded as highly important.

4. Conclusion

The following results were obtained through experiments relating to composite particle formation of Cu and Al_2O_3 using a vacuum mechanofusion apparatus and through surface analysis of such composite powders.

1) The effect of Ar atmosphere was extremely significant in promoting composite particle formation in atmosphere and under a low vacuum. However Ar atmosphere was hardly effective under high vacuum.
2) Oxygen densification was found in the surface layer of the composite particles. The degree of oxygen densification changed with the atmospheric pressure during mechanofusion. As the pressure increased in the air atmosphere, the quantity of oxygen increased and the densification depth grew large.
3) From observation of the microstructure of the Cu covering layer, and from the sintering behavior of the Cu particles, it was clarified that the temperature of the particle surface layer rises to around 1000 K during mechanofusion.
4) As an effect of vacuum in promoting composite formation, a reduction in the oxygen partial pressure is produced. While the surface temperature rise of particles during mechanofusion induces oxidation of the covering Cu particles. However oxidation of Cu is suppressed in vacuum, and as a result, it was found that composite formation is promoted.

Acknowledgement

The authors wish to express their deep gratitude to Associate Professor Tadashi Momono of the Muroran Institute of Technology and to Associate Professor Hajime Konishi of the Shinshu University for their guidance and advice, to Chief Researcher Katsumasa Yabe of the Hokkaido national Industrial Research Institute for his cooperation in XPS analysis, and to Chief Researcher Yuji Nagasawa of JEOL Ltd. for his cooperation in AES analysis.

References

1) Takahiro Fujii, Kaoru Gonoi and Eiki Takeshima: KOGYO ZAIRYO (*Industrial Material*), **38** (1990) No.11, p.43.
2) Tamotsu Senna: FUNTAI KOGAKU (*Powder and Particle Technology*), issued by the Chemical Association, published by Maki Bookstore (1987) p.160.
3) M. Alonso, M. Satoh and K. Miyanami: Powder Technology, **59** (1989) p.45.
4) Makio Naito:FUNTAI To KOGYO (*Powders Sci. and Eng.*) , **21** (1989) p.77.
5) Tohei Yokoyama: The Micrometrics, No.35 (1991) p.94.
6) Keiko Mizota, Shinichiro Fujita, and Tamotsu Senna: Material Science and Engineering, **B10** (1991) p.139.

7) Kiyoshi Nogi: The 2nd Hosokawa Powder Symposium, Powder Technology Discussion Meeting, (1991) p.7.
8) Hisashi Kaga, Yoshihiro Taya, Isao Shimono, Hiroshi Katayama: J. Jpn. Powders and Powder Metall., **39** (1992) p.546.
9) Hisashi Kaga, Yoshihiro Taya, Hiroshi Katayama, Yoshikazu Hamaguchi: J. Jpn. Soc. Powders and Powder Metall., **39** (1992) p.553.
10) Masahiro Kitada: SHOKYU KINZOKUGAKU (*Beginner's Metal Science*), Agne (1991) p.110.
11) Makio Naito, Masahiro Yoshikawa, Toshinari Tanaka, Hikari Kondo:J. Soc. Powder Technology, Jpn., **29** (1992) p.434.
12) Koichi Tanno, Tohei Yokoyama, Kiyoshi Urayama: J. Soc. Powder Technology Jpn., **27** (1990) p.153.

Removal of Fine Particles from Wafer Surface by Pulse Air Jets †

Yoshio Otani, Hitoshi Emi and Tetsuya Morizane
*Department of Chemistry and Chemical Engineering, Kanazawa University**
Jisaku Mori
*Department of Mechanical Engineering, Toyama National College of Technology***

Abstract

Removal of fine particles from wafer surface by air jets was experimentally investigated in order to seek an effective surface-cleaning method which uses no cleaning liquids. Monodisperse polystyrene latex particles with diameter between 0.25 and 3.3μm were deposited on a silicon wafer by gravitational settling and removed by air jets from a rectangular nozzle. Particles were blown off the moment the air jet struck the wafer surface, and afterwards no particle reentrainment occurred. This suggests that the sequential pulses of air jets are effective for the removal of fine particles. By exposure of wafer surface to sequential pulse air jets, particles with a diameter as small as 0.25μm were almost completely blown off the surface. The experimental results also indicated that the removal efficiency of particles per pulse air jet, which is the ratio of number of particles reentrained during an air jet exposure to that before the exposure, is kept constant for each exposure to sequential pulse air jets.

1. Introduction

Wet cleaning methods with ultra-pure water and other cleaning liquids are most commonly used to remove particles from wafer surfaces. However, wet cleaning methods have several drawbacks, such as recontamination of the surfaces by dissolved chemicals during rinsing and drying process, water marks, COPs (crystal originated particles), etc. Furthermore, wafers are usually processed under high vacuum condition so that the adsorbed water on wafer surface is claimed to cause some defects in the products. Therefore, most of the problems arising in the wet cleaning method seem to ensue from the use of liquids itself. The present work aimed at developing an effective dry cleaning method without using liquids or solvents, and studied the limitations of air blowing method for wafer surface cleaning.

Reentraiment of particles from surfaces has been studied mainly from the viewpoint of particle's dynamic behavior, for instance, resuspension of particles from powder layers[1,3,4,6], reentrainment of particles from walls[2], and they were recently reviewed by Masusaka *et al.*[5] However, few data have been reported on the reentraiment of particles with diameter smaller than several micrometers, and no previous studies have been conducted from the viewpoint of surface cleaning. Therefore, only limited knowledge can be obtained on how surface material, air jet velocity, particles size, and particle material affect the removal efficiency. In the present work, as a fundamental study for developing a dry cleaning method, the influences of particle condition (mainly particle size) and air jet condition were experimentally investigated under well-defined condition where monodisperse spherical particles of polystyrene latex (PSL) are blown off from a smooth surface of silicon wafer.

2. Experimental setup and procedures

Since adhesion force between particles and surface is affected by many factors, we tried to conduct experiments by excluding factors such as electrostatic force and humidity effect. In preparation of particle-deposited wafer, PSL particles were neutralized by a neutralizer with ^{241}Am, and deposited on wafer surface by gravitational settling. We may use impactors to deposit particles, but the adhesion force distribution would be broader than that by the gravitational settling because of the large difference in the impaction

---

* 2-40-20 Kodatsuno, Kanazawa 920, Japan

** 13, Hongo-machi, Toyama 939, Japan

† This report was originally printed in *Kagaku Kougaku Ronbunshu,* **19**, 114 (1993) in Japanese, before being translated into English with the permission of the editorial committee of the Soc. Chemical Engineers, Japan.

velocity of particles. Further, we can deposit particles uniformly in a large region of surface by gravitational settling.

Fig. 1 shows the dimensions of acrylic nozzle used in the present work, and the whole experimental setup is shown in **Fig. 2**. Rectangular nozzle with crosssection of 5 × 0.5mm^2 was used to clean a large surface area of wafer. In the experiments, particle adhered wafer was placed on a grounded metal disc and exposed to air jet from the nozzle. The air jet blow was operated by solenoid valve controlled by a personal computer. The particle adhered wafer was prepared by using the apparatus shown in **Fig. 3**. PSL particles were generated by Collison atomizer followed by neutralization with ^{241}Am neutralizer and then introduced into a sedimentation chamber. The humidity of the aerosol stream was 20 – 25 %RH. The particle deposited wafer was stored in a desiccator for more than 12h.

Particles on the wafer were observed under an optical microscope connected to a VTR. Image of particles on the wafer before exposure to the air jet was processed with an image analyzer to obtain binary image, and stored in video memory. The image was compared with that after the air jet exposure, and the particles removed from wafer were counted. The removal efficiency of particles was obtained as the ratio of removed particles to those initially deposited on the wafer in the region of 1 × 4mm^2 around a stagnation point of air jet where the highest removal efficiency of particles was attained. The counting of particles was conducted by dividing the area into 16 regions and the number of particles counted by each run is at least 1600 before the air jet exposure.

3. Determination of experimental conditions

The present work was aimed at studying the possibility of air jet cleaning for wafer surface. Consequently, nozzle-wafer surface clearance, jet impinging angle, air jet blowing period were fixed at a constant value which gives the highest removal efficiency. The determination of the optimal conditions of the these factors are as follows.

First, removal efficiency was measured by changing the nozzle – surface clearance at a fixed jet impinging

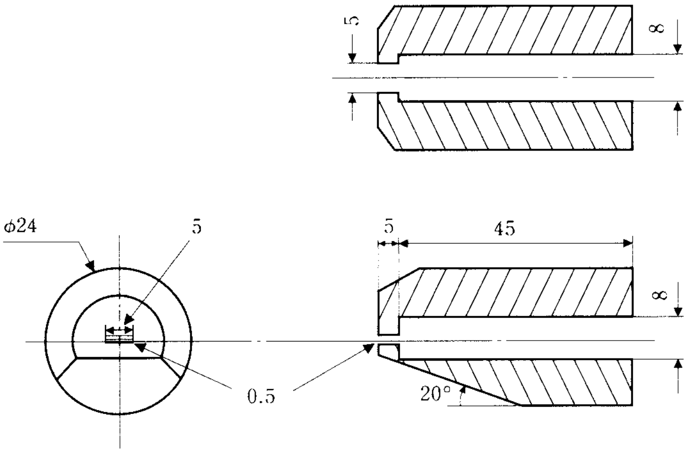

Fig. 1 Dimensions of rectangular nozzle.

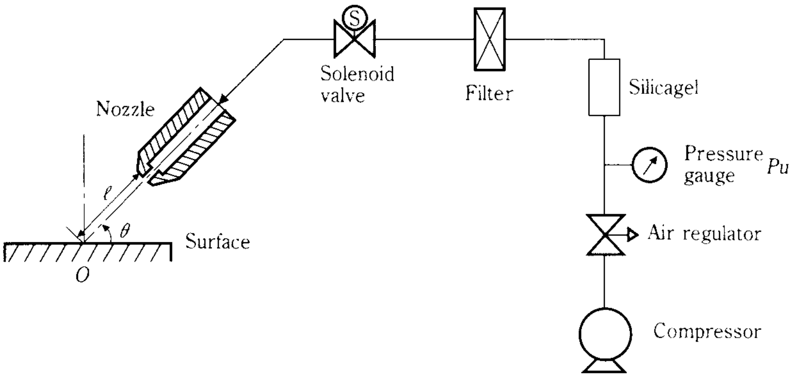

Fig. 2 Flowchart of experimental setup.

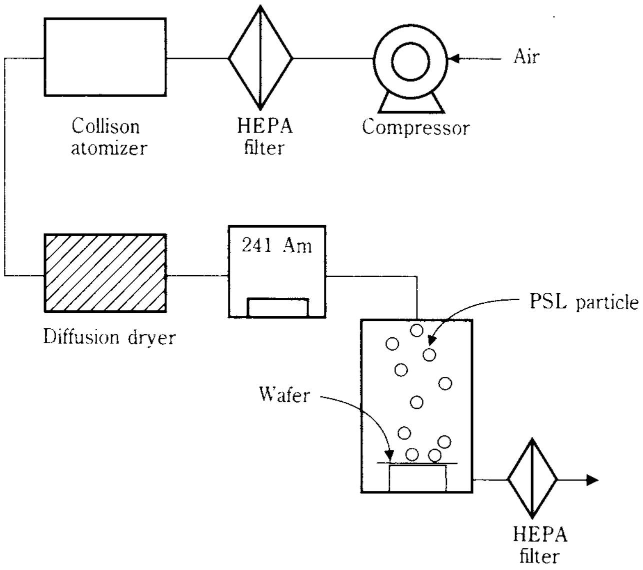

Fig. 3 Experimental setup for the preparation of particle-deposited wafer by gravitational settling.

angle and air pressure. As a result, removal efficiency was found to be constant at a clearance between 6mm and 12mm, but it decreased when the clearance was less than 6mm or greater than 12mm. Therefore, the clearance was fixed at 6mm for the rest of the experiments.

Fig. 4 shows the influence of jet impinging angle on the removal efficiency. These data were obtained by exposing the wafer for 60s to air jet with a pressure plotted on the abscissa. The figure also shows the reproducibility of the data by error bars when the jet imping angle is 90 degrees. As seen from the figure, the removal efficiency increases as the jet impinging angle becomes smaller. Further, observation of wafer surface by optical microscope showed that the wider area was cleaned by the air jet at a smaller impinging angle. Consequently, smaller impinging angle is preferable for the removal of particles. However, because of the confinement of the nozzle structure, the impinging angle was set at 30 degrees for the rest of the experiments.

In order to determine jet blowing time, time change of removal efficiency after the jet exposure was measured. **Fig. 5** shows that the removal efficiency increases to a certain value the moment the air jet blow is started and it afterwards remains almost constant, which indicates that the particles are removed instantly by the air jet blow and that the continuation of jet blow gives almost no further increase in the removal efficiency. Therefore, the duration of air jet blow was set at 1s. The result shown in **Fig. 5** actually gave us the motive for the present work, *i.e.*, one may increase removal efficiency by exposing wafer to pulsed air jets repeatedly. Hereafter, our effort was concentrated to study the effectiveness of pulsed air jets.

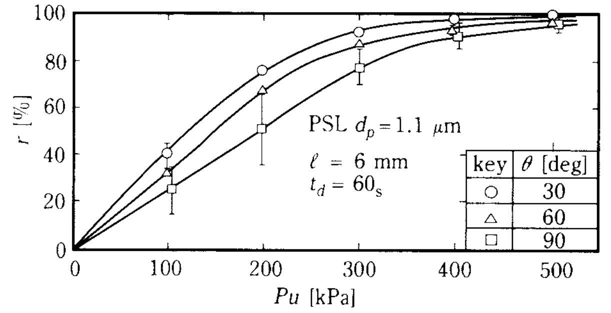

Fig. 4 Influence of nozzle angle on removal efficiency.

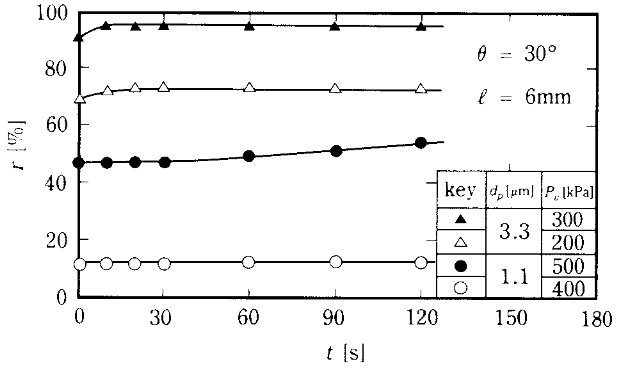

Fig. 5 Change in removal efficiency with exposure time to air jet.

The experimental conditions with relevant factors which gave the maximum removal efficiency are shown in **Table 1**. The test particle size was changed from 0.25 to 3.3μm, and the air jet pressure was between 100 to 500 kPa. Incidentally, the interval of pulsed air jet was taken to be 3s because the removal efficiency was invariant for the jet interval. 3s is the minimum time period required for air pressure to recover after the air jet blow.

Table 1 Experimental conditions

Surface material	Silicon wafer
Particle material	Polystyrene latex (PSL)
Particle diameter d_p [μm]	3.3, 2.0, 1.1, 0.55, 0.25
Air pressure (gauge) P_u [kPa]	100 ~ 500
Distance between surface and nozzle-tip ℓ [mm]	6
Jet impinging angle Θ [deg]	30
Duration of air jet t_d [s]	1.0
Jet interval t_i [s]	3.0
Relative humidity [%]	20 ~ 25

4. Removal of particles by pulse air jets

Fig. 6 shows the change in the total removal efficiency by the pulse air jets as a function of number of exposures. The figure clearly shows that the removal efficiency increases with number of air jet exposures, and that particles with diameter larger than 0.55μm are completely removed from the surface after ten exposures at a pressure of 500kPa. Removal efficiency of 0.25μm particles remains lower compared to other particles, however it increases further with increasing the number of exposures, as shown in **Fig. 7**. After a hundred exposures to the air jet with pressure of 500kPa, almost 90% removal efficiency is attained. These figures give the proof on how the repeated exposure to pulse air jet is effective for the removal of fine particles.

Removal efficiencies plotted in **Figs. 6** and **7** were the total removal efficiency, which is the number fraction of removed particles to initially deposited particles. From these figures, we may calculate removal efficiency per an exposure to pulse air jet, which is the number ratio of removed particles by a single exposure to those before the exposure. The removal efficiency per pulse air jet exposure is plotted in **Fig. 8** as a function of number of exposures. The remarkable result shown in the figure is that the removal efficiency remains almost constant during the exposures to consecutive pulse air jets. One would

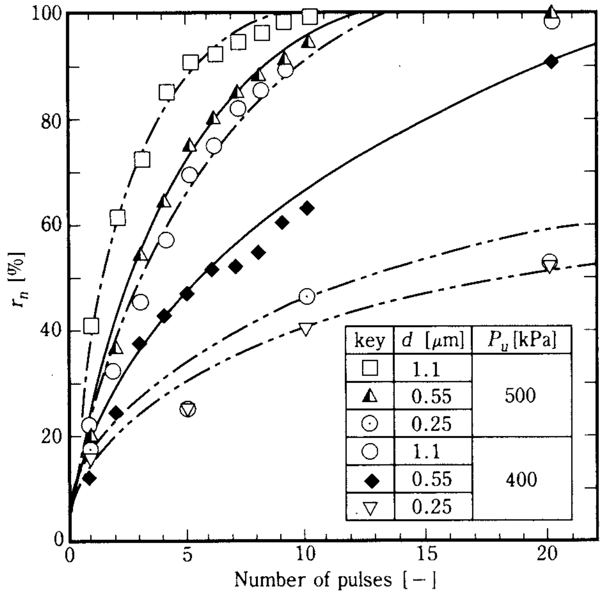

Fig. 6 Change in removal efficiency with number of pulse air jets.

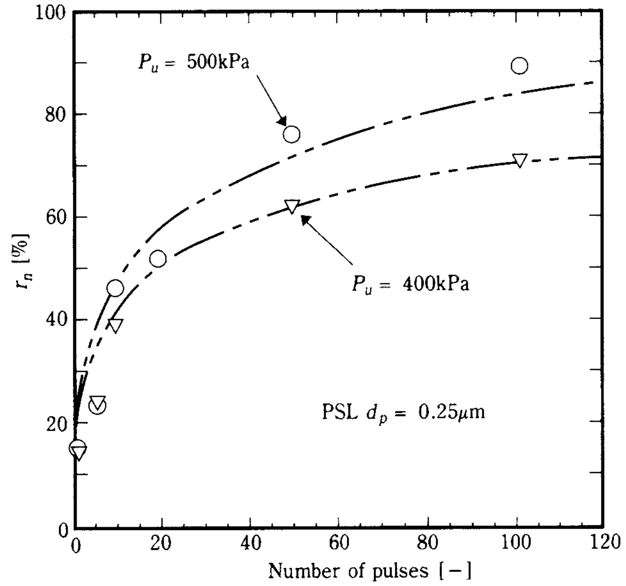

Fig. 7 Change in removal efficiency of 0.25μm particles with number of pulse air jets

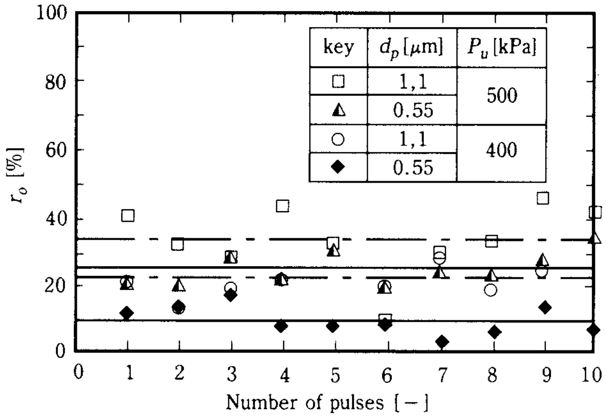

Fig. 8 Relationship between removal efficiency per pulse air jet and number of pulse air jets.

speculate that the removal efficiency should decrease with number of exposures because particles with a small adhesion force would be removed easily and thus the particles with a larger adhesion force would remain on the surface. The invariableness of removal efficiency per pulse air jet may result from preservation of adhesion force distribution, as shown in **Fig. 9**.

When the removal efficiency per pulse air jet is constant regardless of number of exposures, it can be related to the total removal efficiency by the following equation.

$$\begin{aligned} r_n &= r_0 + (1-r_0)r_0 + (1-r_0)^2 r_0 + \ldots + (1-r_0)^{n-1} r_0 \\ &= 1-(1-r_0)^n \end{aligned} \qquad (1)$$

By taking the logarithm of both sides, we obtain

$$\mathrm{In}\,(1-r_n) = n\ln(1-r_0) \qquad (2)$$

Therefore, if the fraction of particles remaining on the wafer ($1\text{-}r_n$) is plotted against number of exposures on a semi-logarithmic paper, we should obtain a straight line. In **Fig. 10**, the fractions of remaining particles are plotted on a semi-logarithmic paper to see whether the relationship given by Eq.(2) holds or not. As clearly seen from the figure, the fraction of remaining particles decreases linearly on a semi-logarithmic paper, corroborating the consistency of Eq.(2). Consequently, if the removal efficiency per pulse air jet is known, the total removal efficiency can be predicted by using Eq.(2).

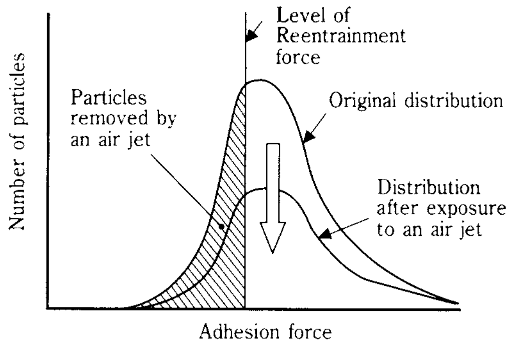

Fig. 9 Illustration of change in adhesion force distribution of particles on wafer by exposure to pulse air jet.

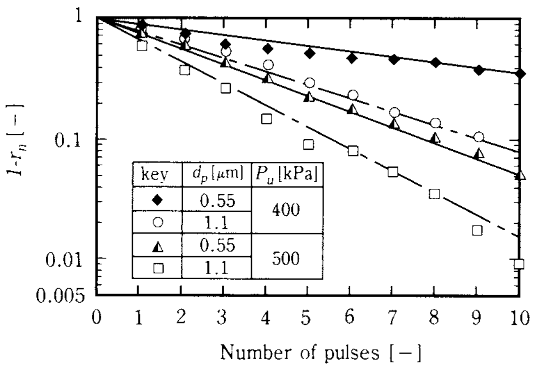

Fig. 10 Cumulative removal efficiency of particles as a function of number of pulse air jets.

Conclusions

Through the experiments on the removal of particles from wafer surfaces, the following results were obtained.

1) Reentrainment of particles occurs the moment the air jet hits the wafer surface, and further exposure of wafer to steady air jet does not bring a further increase in the removal efficiency.
2) Repeated exposure to pulse air jet can remove particles as small as 0.25μm, which cannot be blown off by the steady air jet.
3) During the repeated exposure of wafer to pulse air jets, removal efficiency per pulse air jet remains constant regardless of the number of exposures. Therefore, by knowing the removal efficiency per pulse air jet, one can predict the total removal efficiency after a given number of air jet exposures.

Acknowledgement

This work was financially supported by Grant-in-Aid, Ministry of Education, Culture and Science, Grant No.02650681. Authors also wish to thank JSR (Japan Synthetic Rubber Company) for kindly offering test particles of PSL spheres.

Nomenclature

d_p = particle diameter [m]
d_n = nozzle width [m]
l = distance between surface and nozzle tip [m]
n = number of pulse air jets [–]
P_u = air pressure upstream of nozzle (gauge) [Pa]
r = removal efficiency of particles [–]
r_0 = removal efficiency of particles per pulse air jet [–]
r_n = cumulative removal efficiency by n pulse air jets [–]
t_i = interval between pulse air jets [s]
t_d = duration of pulse air jet blow [s]
Θ = jet impinging angle on surface [deg]

Literature cited

1) Ikumi, T., H. Wakayama and H. Masuda: *Kagaku Kogaku Ronbunshuu,* **12**, 589 (1986)
2) John, W., D.N. Fritter and W. Winklmayr: *J. Aerosol Sci.,* **22**, 723 (1991)
3) Masuda, H., S. Matsusaka and T. Ikumi: *Kagaku Kogaku Ronbunshuu,* **11**, 48 (1985)
4) Matsusaka, S., A. Aoyagi and H. Masuda: *ibid.,* **17**, 1194 (1991)
5) Matsusaka, S. and H. Masuda: *J. of Society of Powder Thchnol.* Japan, **29,** 530 (1992)
6) Matsusaka, S., Y. Nakamura and H. Masuda: *ibid.,* **29**, 110 (1992)

High-pressure Cold Isostatic Pressing of Ultra-fine Oxide Powders†

Hidehiro Kamiya, Chiaki Nakayama and Genji Jimbo**
*Department of Chemical Engineering, Nagoya University**

Abstract

Fine Al_2O_3, MgO and SiO_2 powders of various sizes were consolidated into a dense and uniform structure by high-pressure cold isostatic pressing. Although the average particle diameter was less than 21 nm, Al_2O_3, MgO and SiO_2 powder compacts were compressed to 60% of their theoretical density by cold isostatic pressing at 1 GPa, because the open and strong aggregate structure collapsed under the cold isostatic pressure. The pore size of these compacts decreased below the primary particle size. Especially, in the case of MgO powders, the maximum relative density increased to 80% and the ratio of pore size to primary particle size was less than 20%. However, in the case of Al_2O_3 powders, whose size was more than 100 nm, a slight increase in relative density and decrease in pore size in the compacts occurred with an increase in isostatic pressure up to 1 GPa. In the case of particles larger than 100 nm and high-hardness materials, high cold isostatic pressure was not effective in increasing the packing density.

The mean vertical force and compressive stress at the contact point between particles in compacts and the maximum tensile stress in a particle during isostatic pressing were estimated using Rumpf's and Hertz's equation. Because these stresses were smaller than the hardness and tensile strength of Al_2O_3 or MgO materials, no viscous deformation or fracture of particle took place during compacting. The relations between the ratio of mode pore diameter to particle diameter and the relative density of Al_2O_3, MgO and SiO_2 compacts agreed with those of spherical and monosized particle beds. The main mechanism of densification of compacts during isostatic pressing was the collapse of aggregates and rearrangement of particles.

1. Introduction

To improve the sintering qualities of inorganic type powders used in ceramics etc., and to obtain ceramics with a fine structure at low sintering temperatures, the reduction of particle size of raw material powders, and the increase in the physical activities of non-crystal or of particles without complete cyrstalization are effective[5)]. However ultra-fine particles with a particle size of 0.1 μm or less readily form a strong and coarse aggregate structure in general and compacting of a dense, uniform structure is difficult. Therefore refinement and high activation of particles does not necessarily lead to obtaining dense sintered compacts under low temperature conditions.

It is believed that pH control in water and colloid scientific methods using surface active agents are effective in collapsing and dispersing the strong aggregate structure of ultra-fine particles[7,13,15)]. However with ultra-fine particles of less than 100 nm, the dispersion of aggregates by these methods is extremely difficult and this has not been successful except for cases of particles with special surface conditions such as SiO_2 fine particles, formed from metallic alkoxide[6)]. Another effective method to collapse aggregate structures of ultra-fine particles is by compacting using ultra high pressure. Gleiter et al[4,8)] compacted a gaseous phase ultra-fine particle to several nm particle diameter formed under a very high vacuum of 10^{-6} torr by applying a maximum of 5 GPa uniaxial pressure, and succeeded in producing a dense bulk body (nanocrystalline) with a crystal particle size of several nm without sintering. However this method used by Gleiter et al requires a large scale apparatus

---

* Furo-Cho, Chikusa-ku, Nagoya, 464-01 Japan

** Now with Tokyo University of Agri. & Tech., Koganei, Tokyo 184 Japan

† This report was originally printed in *Kagaku Kougaku Ronbunshu*, **19**, 220 (1993) in Japanese, before being translated into English with the permission of the editorial committee of the Soc. Chemical Engineers, Japan.

involving high costs and since it is by uniaxial compacting, a uniform structure cannot be obtained. Therefore, as reported previously⁶⁾, the authors produced a granulated powder resembling a closely packed structure by the spray drying method from spherical mono-dispersed silica fine particles of not more than 0.1 μm, formed from metallic alkoxides by isostatic pressing at 1 GPa, and obtained a Green body with a maximum relative density of 78%.

Furthermore, the authors heat treated mullite precursor ultra-fine particles of not more than 10 nm, synthesized from metallic alkoxide at not more than 1000°C by which the amorphous phase remains and the particle size hardly increases, then conducted isostatic pressing at 1 GPa⁵⁾. As a result, a Green body with a relative density of 60 – 70% was obtained, and at a sintering temperature less than the liquid phase formation temperature of 1,500°C which is lower by 200°C than normal, the density was increased to 98% and above to obtain a mullite sintered compact with an average crystal particle size of not more than 100 nm. High activity ultra-fine particles were prepared and using a method to collapse the aggregate structure by a high pressure of 1 GPa, a ceramic (nano structure sintered compact) having an ultra-fine structure, sintered and densified at a relatively low temperature was produced. However the ultra-fine particles synthesized from metallic alkoxide possessed better dispersion qualities in water compared with particles produced by other methods and even though made of ultra-fine particles, they aggregate very much. In this report, to study whether the aggregate structure of ultra-fine particles made by other methods or from other materials would collapse by isostatic pressing and whether improvement of densification or sintering qualities of compacts could be obtained, ultra-fine particles of oxides with various diameters, made by various methods and from raw materials other than metallic alkoxides were used. Then the particle size and particle material which affect the densification process of compacts following an increase in isostatic pressure were studied and a quantitative study of the densified structure was attempted.

2. Experiments

Three kinds of oxide type fine particles, Al_2O_3, MgO, and SIO_3 were used. Their specific surface area (S_W), density (ϱ_T), specific surface area converted diameter (d_B) calculated using Eq. (1) and crystal structure are summarized in **Table 1**.

$$d_B = 6000/(S_W \varrho_T) \tag{1}$$

The specific surface area was measured by the BET method by nitrogen adsorption while the crystal structure was measured by an X ray analysis method (XRD method). Al_2O_3 (I) is α-Al_2O_3 (Made by Showa Denko, AL160SG) made by de-alkalizing the powder obtained by the Bayer method, while Al_2O_3 (II) to (IV) are high purity Al_2O_3 (Made by Daimei Chemical, TM-D, TM-100, and TM-300) obtained by thermal decomposition of $NH_4AlCO_3(OH)_2$. I and II whose specific surface area equivalent particle diameters (d_B) are not less than 100 nm, are γ-Al_2O_3 (trigonal system) while III and IV of 12.2, and 5.6 nm are γ-Al_2O_3 (cubic system). It has been confirmed that γ-Al_2O_3 is rearranged by differential thermal analysis to α-Al_2O_3 at a temperature of around 1150°C. Ob-

Table 1 Powder properties of raw materials.

(A) Al_2O_3

Sample No.	S_W [m²/g]	ϱ_T [g/cm³]	d_B[nm]	purity [%]	phase
I	5.6	3.98	269	99.4	Trigonal ($\alpha-Al_2O_3$)
II	14.0	3.98	108	99.99	Trigonal ($\alpha-Al_2O_3$)
III	134	3.67	12.2	99.99	Cubic ($\gamma-Al_2O_3$)
IV	290	3.67	5.6	99.99	Cubic ($\gamma-Al_2O_3$)

(B) MgO

Sample No.	S_W [m²/g]	ϱ_T [g/cm³]	d_B[nm]	purity [%]	phase
I	8.4	3.58	199	99.9	Cubic
II	18.0	3.58	94	99.9	Cubic
III	37.0	3.58	45	99.9	Cubic
IV	168	3.58	10	99.9	Cubic

(C) SiO_2

Sample No.	S_W [m²/g]	ϱ_T [g/cm³]	d_B[nm]	purity [%]	phase
I	128	3.20	21	99.9	amorphous
II	284	3.20	9.6	99.9	amorphous

servation by an electron microscope shows that all the particles are aggregated but the primary particle sizes are relatively uniform.

MgO were all particles obtained by vapor oxidation of magnesium (Made by Ube Kosan, 2000A, 1000A, 500A, and 100A) with particle size controlled by the reaction conditions[10]. Observations by an electron microscope confirmed that MgO (I) consisted of a mixture of particles of around 0.1 – 0.5 μm formed into a cubic shape and fine particles of several 10 nm. Even with MgO (II) and (III), the particle diameters are smaller than those of MgO (I) but cubic shape particles were observed[10]. MgO (IV) did not contain cubic particles and consisted only of fine particles and a relatively uniform particle size distribution was observed. The particle size distribution is fairly widespread compared with Al_2O_3 but the specific surface area converted diameter (d_B) was taken as representative of the particle diameter.

SiO_2 was made by hydrolysis in oxyhydrogen flame of a volatile silane compound (Made by Nippon Aerosil, AEROSIL-130, 380). The specific surface area equivalent particle sizes were 21, 9.6 nm and the fine particles were amorphous. Seen by an electron microscope, they were similar to Al_2O_3 (III), (IV) and MgO (IV) in that they were ultra-fine particles with a relatively uniform particle size.

The raw material powders were put in a metal mold of 20 nm and preparatory uniaxial compacting was performed for 3 minutes at 6.2 MPa. Then under conditions ranging from 0.05 to 1 GPa, isostatic compacting was conducted for 3 minutes. The powder density and pore size distribution of the compacts were evaluated by the mercury press method.

3. Results

3.1 Changes in compact density by isotropic high pressure compacting

Figs. 1(a) and **(b)** show the relation between the isostatic compacting pressure and the relative density after compacting (ϱ_G/ϱ_T). Out of the four types of Al_2O_3 particles, Al_2O_3 (I) and (II) whose particle diameters were not less than 100 nm reached a relative density of 46.7% in the uniaxial compacting stage $(p_C = 0\ GPa)$. However the increase in density accompanying an increase in pressure was slight and even when a pressure up to 1 GPa was applied, a density increase of only around 10% compared with the case of metal mold forming was observed. On the other hand, with γ-Al_2O_3 III and IV with a particle size of 12.2 and 5.6 nm, the relative density at 60% was reached, roughly comparable to that of (I) and (II). With any of the powders, the relation between the relative density (ϱ_G/ϱ_T) and the compacting pressure was linear on a semi-logarithmic graph like the following equation using constants a and b.

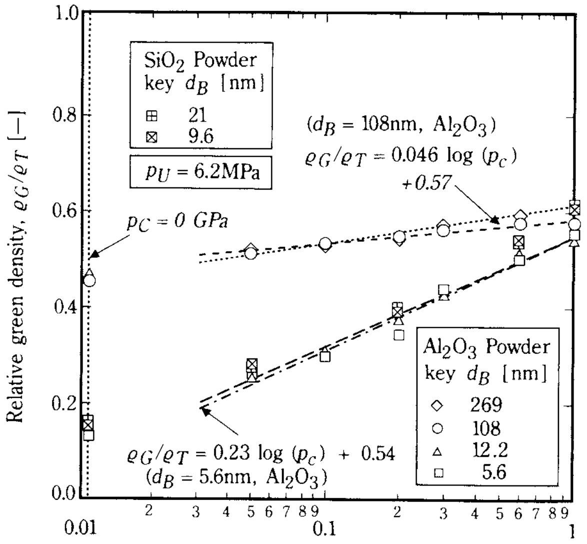

(a) Al_2O_3 and SiO_2 powders

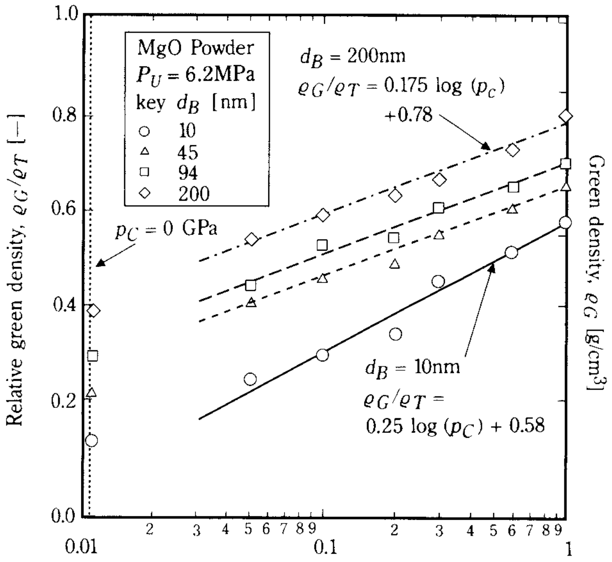

(b) MgO powder

Fig. 1 Change in the relative density of compacts with cold isostatic pressure. Uni-axial pre-pressing pressure (p_U) was 6.2 MPa.

$$\varrho_G/\varrho_T = a \log(p_C) + b \qquad (2)$$

The slope with (I) and (II) was about 0.05 but with (III) and (IV), it was about 0.25 or fivefold more. In the Figure, the results on SiO_2 of particle diameters 21, 9.6 nm are also shown and they roughly coincide with the results of Al_2O_3 (III) and (IV).

In the case of Al_2O_3 (I) and (II) for which the particle size was not less than 100 nm, the application of pressure was not very effective in increasing the density of compacts. Even with SiC and the like which are non-oxide particles, results with which isostatic pressures up to 900 MPa were applied have been reported[1,2], but since the particle size was around 100 nm and above, a notable density increase following the application of pressure was not observed. However with fine particles of 2, 30 nm and less, the application of isostatic pressure was extremely effective in increasing the compact density, not only for Al_2O_3 but for SiO_2 and for those shown in **Fig. 1(b)** such as MgO. Even with a pressure of 1 GPa, the density increase limit was not reached and with a pressure increase above 1 GPa, further densification can be expected.

Also with MgO, the slope was the steepest in the relation between the relative density of the smallest particle size MgO (IV) and pressure (**Fig. 1(b)**). Also, it roughly coincides with the relation between compact pressures of Al_2O_3 (III), (IV), SiO_2 and their relative density, while for particle sizes of not more than 21 nm, the effect of material was hardly observed in the relation between the compact pressure and the relative density (ϱ_G/ϱ_T). On the other hand, when the particle size was 45 nm (III), although not as conspicuous as with Al_2O_3, the slope compared with that of (IV) became somewhat flatter. With MgO (I) and (II) with an even larger particle size, the slope hardly changed. As the particle size became larger, the relative density following uniaxial compacting became higher and the slope did not become flat as much as that for Al_2O_3 and therefore, under a pressure condition of 1 GPa, the maximum relative density of MgO (I) reached 80%. In the case of MgO, even with a particle size of 100 nm and above, the slope in the relation between the relative density and pressure, as with Al_2O_3, was of a mechanism where as it did not become flatter compared with that of ultra fine particles with particle size of 21 nm and less, and the following 2 points are conceivable for this mechanism. The first is that for MgO (I) to (III), the particle size distribution is widespread and therefore the mechanism where small particles intrude into the space of large particles effectively functions even in high pressure stages. Secondly, the hardness of MgO is lower compared with that of Al_2O_3 and MgO is more liable to plastic deformation whereby deformation develops at the particle contact points under high pressure conditions. When the densification mechanisms of compacts in the pressurizing process change following a rearrangement of particles to the second mechanism which is a deformation of particles, a change is seen in the slope of Equation (2) and it was reported that it could not be approximated by one straight line[11]. However within the stress scope of the present study, no change was observed in the slope even under high pressure conditions near 1 GPa and both slopes of MgO and Al_2O_3 were approximated by a single straight line. Consequently, in the densification mechanism, the rearrangement of primary particles is dominant within the stress scope of the present study and it can be presumed that densification by plastic deformation of particle contact points is not dominant. The particle distribution of MgO (I) – (III) compared with that of Al_2O_3 (I), (II) is more widespread and it is believed that because the mechanism of small particles intruding into the space of large particles functions effectively, the relative density increases. To observe these mechanisms, attention was focused on the pore size distribution to study the changes in the compact structure during isostatic pressure application.

3.2 Changes in pore size distribution in compacts during pressure application

Figs. 2(a) and **(b)** show changes of pore size distribution accompanying the increase in isostatic compacting pressure of Al_2O_3 (II) and (III). During the metal mold forming stage, $(p_C = 0\ PGa)$, pores larger than the primary particle size $(d_B = 108\ nm)$ were present in Al_2O_3 (II) but by applying a low isostatic compacting pressure of only 0.05 GPa, pores larger than the primary particle size became hardly observable (**Fig. 2(a)**). Even by increasing the compacting pressure, not only the pore volume but the pore diameters were not appreciably reduced. With powders having a particle size of 100 nm or larger, almost all aggregate structures collapse under a relatively low pressure and a dense compact structure is acquired. Since a dense primary particle arranged structure already exists in the low pressure stage, rearrangement of particles is minimal even with an increase in pressure. It is thought that the near completion of particle rearrangement in the low pressure stage which is the densification mechanism of compacts, is the reason for the flat slope angle of Al_2O_3 (I) and (II) in **Fig. 1(a)**.

On the other hand, with Al_2O_3 (III) having ultra-

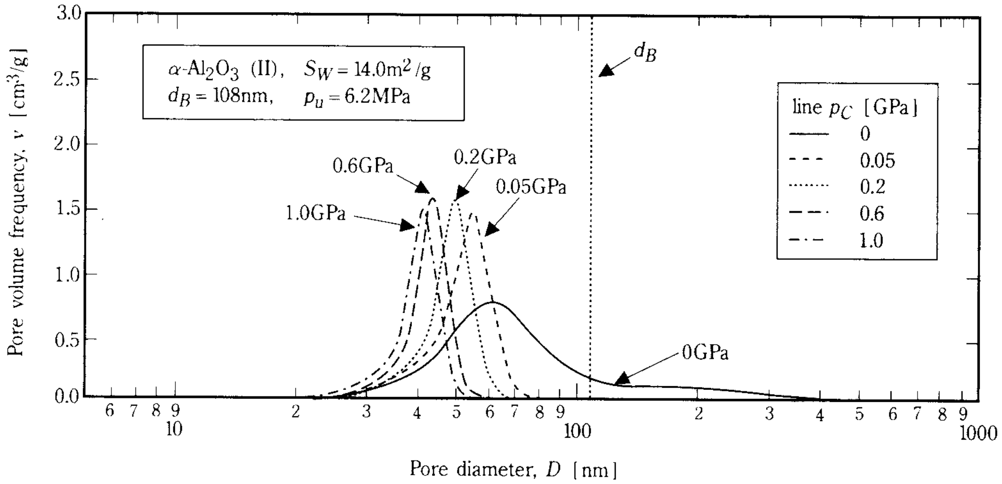

(a) d_B = 108nm, S_w = 14m²/g

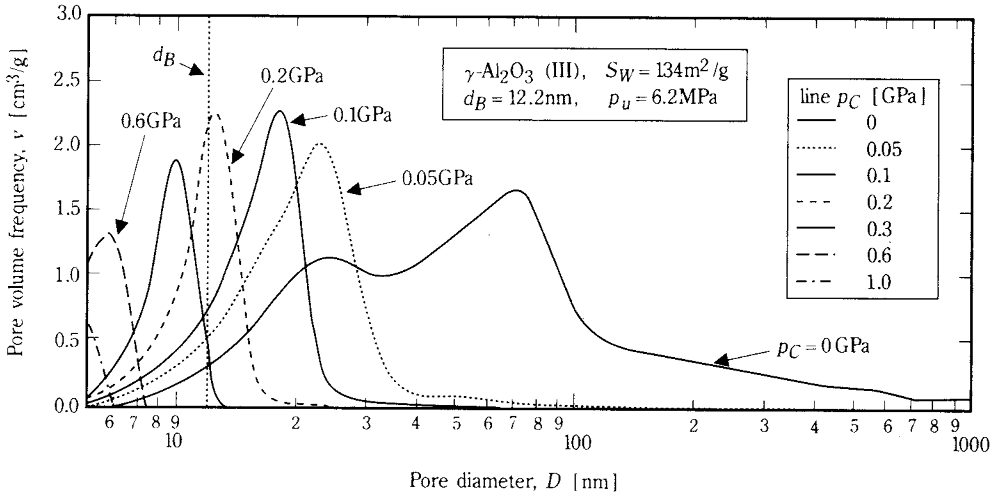

(b) d_B = 12.2nm, S_w = 134m²/g

Fig. 2 Pore size distribution in compacts of Al_2O_3 powders measured by mercury porosimetry

fine particles with primary particle size of 12.2 nm, pores with sizes 10 times larger than the primary particle size exist in the low pressure stage, indicating that aggregate structures have not collapsed (**Fig. 2(b)**). However with an increase in pressure, the pore diameters decrease and at 0.3 GPa, the pore diameters become about the same as the primary particle diameters. Then under high pressure conditions of 0.6 GPa and above, the pore diameters become smaller than the primary particle diameters. Aggregate structures of ultra-fine particles of around 20 nm and smaller do not collapse under low pressures but with an increase in pressure, they collapse and become deformed. At 1 GPa, the mode pore size is smaller than 6 nm which is the measurement limit set for the mercury pressure fitting method adopted in this report, and reaches a size 60% or less of the primary particle diameter (d_B) which does not differ much from the ratio between the d_B in the case of Al_2O_3 (I) and (II) particles 100 nm or bigger and mode pore size. Consequently, it is thought that the arranged structures of primary particles of 12.2 nm and 108 nm are approximately the same under high pressure conditions of 1 GPa.

Also in the case of MgO (I), the pore diameters are roughly smaller than the primary particles' diameters and are of a dense structure in a relatively low pressure stage (**Fig. 3**). Although the powder is of a relatively large particle size of 200 nm compared with Al_2O_3 (I), the mode pore size is conspicuously reduced with an increase in pressure. Also with MgO (II) and (III), the pore diameters become smaller in proportion with an decrease in particle size but a tendency similar to that of

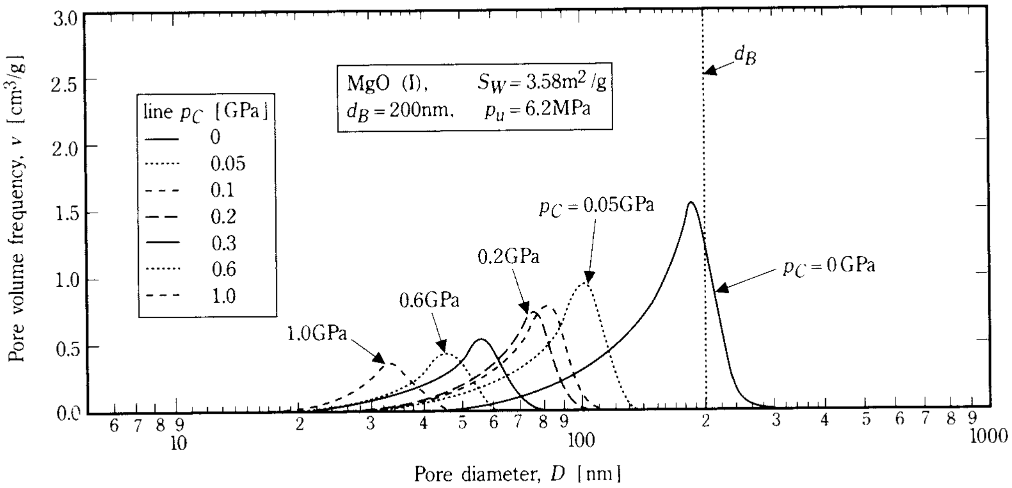

Fig. 3 Pore size distribution in compacts of MgO powders measured by mercury porosimetry. Estimated mean particle size was 200 nm

MgO (I) was obtained. With MgO (IV), as with Al_2O_3 (III), pores with diameters several times larger than the primary particles' diameter are present under low pressure conditions but the pore diameters decrease with an increase in pressure and at 1 GPa, open pores larger than 6 nm are hardly observable.

In regard to powders on which experiments were made, the ratio between the mode pore size (D_m) and the primary particle size (d_B) under various pressure conditions was obtained and the relations with the compacting pressure are shown in **Figs. 4(a)** and **(b)**. With Al_2O_3 (I) and (II) (d_B = *269, 108 nm*), in which the compact relative density does not change much with high pressure applications, a reduction down to around $D_m/d_B = 0.6$ was seen under low pressure conditions of 0.05 GPa. However even by applying a higher pressure of 1 GPa, D_m/d_B drops only to 0.4, indicating that the packed structure of particles does not change much (**Fig. 4 (a)**). On the other hand, with Al_2O_3 (III) or SiO_2 (I), (II) and MgO (IV), which consist of fine particles of 100 nm and less, $D_m/d_B >> 1$ at a low pressure stage but from around 0.3 GPa, the mode pore size became smaller than the particle size and at 1 GPa, it reached the same level as that of Al_2O_3 (I) and (II) (d_B = *269, 108 nm*) of $D_m/d_B = 0.4$. The relation between D_m/d_B and the compacting pressure also was approximated by a nearly straight line on a logarithmic graph and compared with Al_2O_3 (I) and (II), the slope of fine particles of around 10 nm particle size was about 5 times steeper. Also in the relation between the compact density and pressure shown in **Fig. 1**, the slope differed by about 5 times, roughly coinciding with the above. In the case of MgO (I), (II) and (III), the

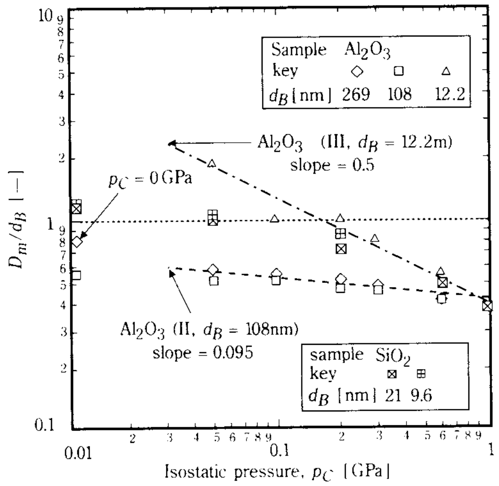

(a) Al_2O_3 and SiO_2 powders

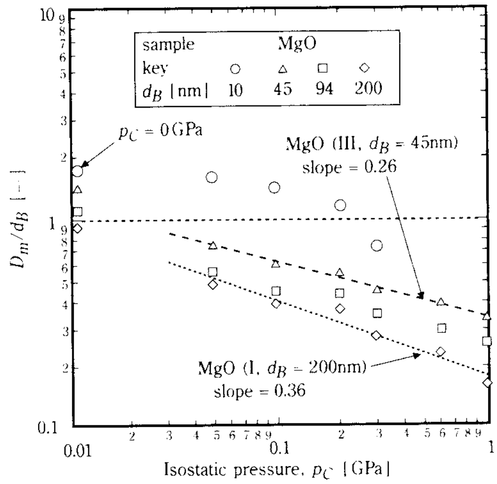

(b) MgO powders

Fig. 4 Ratio of mode pore size in powder compacts to mean particle diameter with cold isostatic pressure.

mode pore size decreased with an increase in pressure and the slope indicated in the Figure by a straight line shows an intermediate value between that of Al_2O_3 (I), (II) and Al_2O_3 (III). As a result, D_m/d_B at 1 GPa decreased down to 0.2 or less.

Since a correlation is observed between the isostatic compacting pressure and the mode pore size as well as the compact density, the relation between the relative density (p_G/p_T) and D_m/d_B is shown in **Fig. 5**. Under low pressure conditions with a relative density not exceeding 0.3, some dispersion of D_m/d_B values may occur depending upon the particles but when high pressure is applied and the relative density becomes 0.5 or more, hardly any difference between particles is observed and the relation can be approximated by a straight line of slope -2 as shown in the Figure.

This result was compared with the packed structure of spherical mono-dispersed particles. It was assumed that the diameter of spheres which are in the air gap formed by the respective particles and which come into contact with each particle corresponds with the pore mode diameters. **Table 2** summarizes the ratios *(D/d)* between the particle diameters of each structure and the diameter of spheres which inscribe each particle as well as the relative densities. When the results in **Table 2** overlapped with those of **Fig. 5**, the experiment values roughly coincided with the pore diameter/particle diameter ratio up to the packed model structure and the compact relative density. The slope gradient became approximately -2 and the spherical mono-dispersed particles *D/d* coincided with the fine particles D_m/d_B used in this study. The specific area converted particle size and mode pore sizes were both affected by the particle size distribution. However since both the converted particle size and the pore diameters were about the same, the effect due to the particle size distribution was offset and it was thought that they roughly coincided with the case of spherical mono-dispersed particles. Also in the case of MgO (I) where the relative density reached a maximum of 80%, approximation was made by the straight line in the Figure. If it is to be assumed that densification progressed by mechanisms such as the deformation of primary particles, it can be presumed that the distribution would divert from this straight linerelation. Therefore it is thought that densification progresses through a particle rearrangement mechanism.

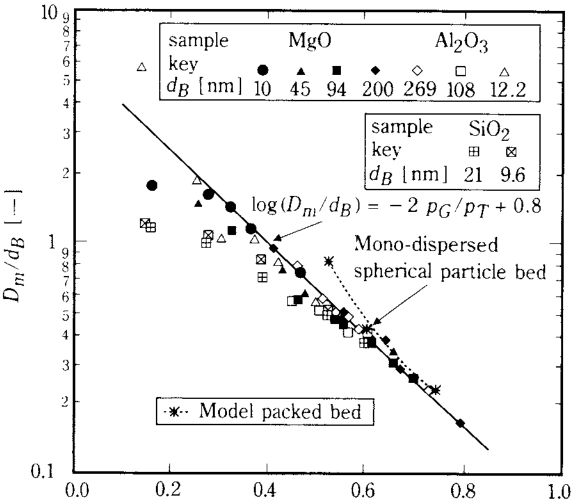

Fig. 5 Relations between ratio of mode pore size in powder compacts to mean particle diameter and relative density of powder compacts. Results of model packed bed using spherical and monosized particle were added

The study on compact structure was organized by focusing on mode pore size and next, the mode pore size distribution was studied. As shown in the example given in **Fig. 6**, the pore size distribution can be approximated by Gauss distribution (Eq. 3) and not by the kind of particles or compacting conditions.

$$\nu = k_1 \exp\{(D - D_m)^2/k_2\} \qquad (3)$$

Here, k_1 is the pore volume frequency (ν) when the pore diameter *(D)* is equivalent to Dm and corresponds to the height of the peak value of the pore diameter distribution while k_2 indicates the spread of distribution. To study the correlation between the respective parameters, the parameters were estimated from the pore diameter distribution of compacts obtained in this study and **Fig. 7** shows the results of the relations between k_2 and the mode pore size (D_m). The relation between the two is roughly a proportional relation and can be approximated by the straight line $(k_2 = 0.2\ D_m)$ in the Figure. Especially in the case of MgO, a good straight line relation exists and with changes in pore size distribution form

Table 2 **Ratio of pore channel diameter to particle size and relative density of model packed beds for monosized spherical particles**

Packing structure	Simple cubic	Body-centered cubic	Hexagonal close packing
Relative density	0.524	0.605	0.741
D/d	0.732	0.414	0.225

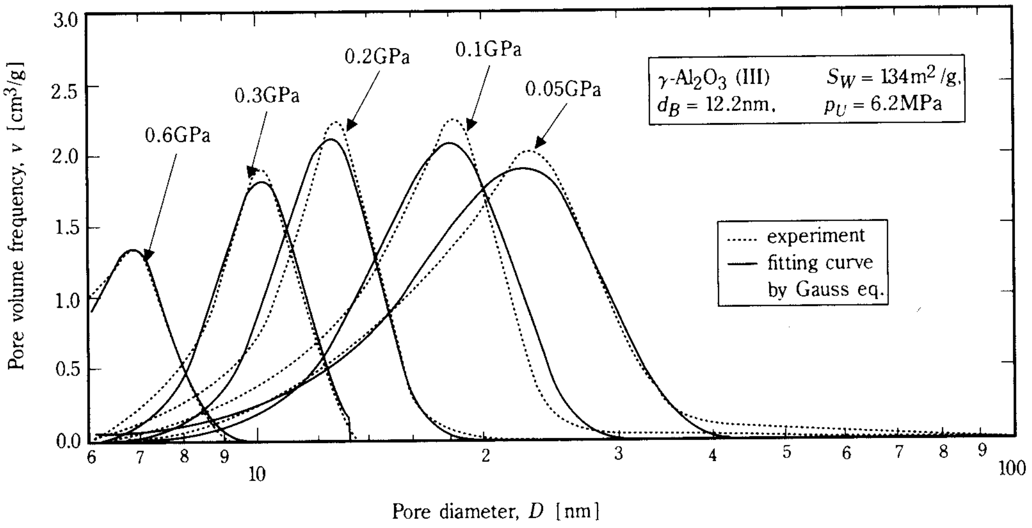

Fig. 6 Examples of curve fitting results for pore size distribution in compacts by Gauss distribution function (Eq. 2)

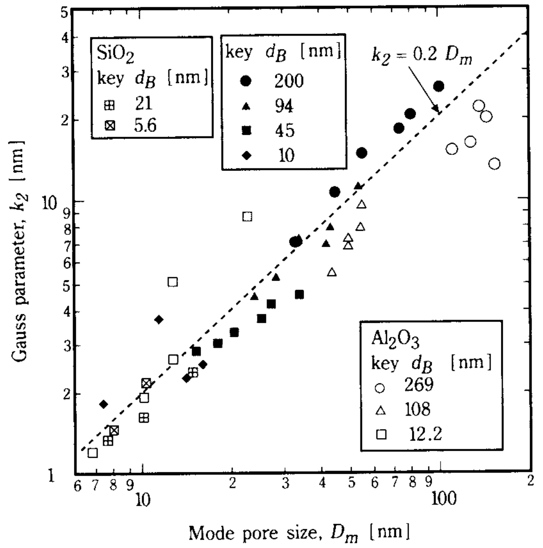

Fig. 7 Relations between parameter k_2 Eq. (2) and mode pore size in compacts

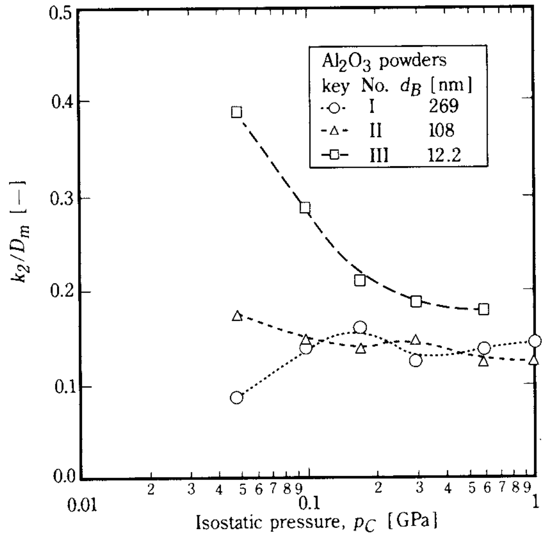

Fig. 8 Change in the ratio of parameter k_2 in Eq. (2) to mode pore size in Al_2O_3 powder compacts with increase of cold isostatic pressure

during the process of compacting with a slight pressure increase, only the mode pore size decreases, resulting in densification.

On the other hand, with Al_2O_3, the mode pore size (D_m) and k_2 are not necessarily proportional and as shown in **Fig. 8**, with Al_2O_3 (III) which consists of ultra-fine particles, k_2/D_m decreased with the application of compacting pressure and the distribution form changed. Also with Al_2O_3 (IV), the pore sizes reached 6 nm or less with a pressure of 0.2 GPa or higher and although this is not shown in **Figs. 7** and **8**, a change in pore size distribution form was conspicuous. It is believed that with ultra-fine particles of Al_2O_3, the aggregate structure remaining from the low pressure stage gradually collapses during the pressurizing process and therefore changes in the pore size distribution form could be seen.

4. Discussion

In regard to the densification mechanism produced by isostatic high pressure compacting of ultra-fine particle packed beds, the rearrangement of particles following the collapse of the aggregate structure or elastic deformation at the particle contact point and collapse of the particles themselves can be considered. From the results shown in **Fig. 5**, it can be presumed that the rearrangement of particles is dominant in the densification mechanism but by computing the compression stress at the particles' contact point as well as the tensile stress inside the particles during the pressure application process and by comparing the hardness of the particles with the collapsing strength, a quantitative study on the possibility of particle deformation and collapse was made. When isostatic stress (p_C) is applied on particle compacts, the force (P) generated at the particles' contact point may be obtained using the following equation if the packed bed is a uniform and isotropic random bed[12,16].

$$P = p_C d_B^2\, \varepsilon/(1 - \varepsilon) \tag{4}$$

Where, ε is the air gap ratio of the compact and from **Fig. 1**, the compact density is proportional to the logarithm of the isotropic stress (p_C); therefore ($\varrho_G/\varrho_T = 1 - \varepsilon = a \log P_c + b$). Equation (4) can be rewritten as Equation (5) using constants a and b.

$$P = p_C d_B^2 \{1 - (a \log p_C + b)\}/(a \log p_C + b) \tag{5}$$

In the case of ultra-fine particles, aggregate bodies may be present and the assumption of a uniform isotropic random structure may not be satisfied. However, from the measurement results of pore size distribution in **Fig. 3**, it can be seen that aggregate structures are nearly collapsed under high pressure conditions of 0.2 GPa and above, and there is a difference in force between the inside and the surface of the aggregate structure even in the low pressure stage but by assuming that P of Equations (4) and (5) is an average value, it is believed that such assumption is justified. **Fig. 9** shows the results obtained by deriving the constants a and b for each powder of **Fig. 1** and converting the force which acts on the contact points. As the particles become larger, the contact points in the compacts become fewer and therefore the force that acts on the contact points becomes greater. Also, the slopes in the Figure have all a gradient smaller than 1 and the forces applied as compacting pressure and at contact points are not proportional. Also with Al_2O_3 (III) and (IV) and MgO (IV) in which the primary particle sizes are not larger than 15 nm, the force acting on the contact points hardly changes at pressures of 0.03 GPa or less and it can be seen that the force which was applied by rearrangement of particles is dispersed.

Next, the average stress generated at the particle contact point by force (P) was estimated[9, 14]. Assuming a spherical particle, the particle contact point is subject to an elastic deformation due to force (P) as shown in **Fig. 10(a)** and the elastic displacement (Δ) is expressed by the following equation using Hertz formula.

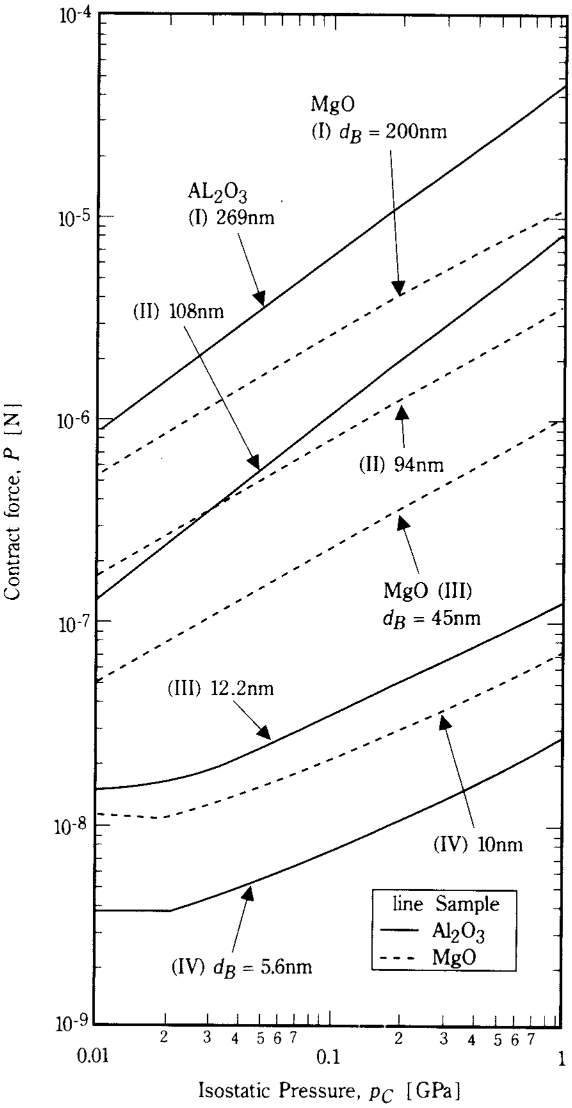

Fig. 9 Estimated mean force at contact point between particles in compacts according to Rumpf's equation (Eq. 3)

$$\Delta = \{9P^2 (1 - \nu^2)^2/(2\, d_B Y^2)\}^{1/3} \tag{6}$$

Where, ν is Poisson's ratio and Y is Young's modulus. To evaluate the elastic deformation characteristics of the particle from its hardness, the area (A) of the osculating circle following elastic deformation is obtained geometrically using the following equation.

$$A = \pi r^2 = \pi\, (\Delta d_B/2 - \Delta^2/4) \tag{7}$$

The displacement amount at the contact point is calculated using Equation (6) and the results of the calculation of P/A as the simplified mean stress at the contact point by applying Equations (5) and (7) of P/A is given in **Fig. 10 (b)**. For Poisson's ratio and

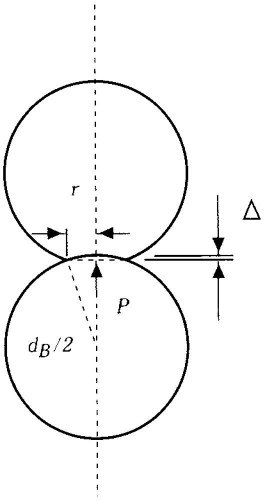

(a) Scheme of contact point between particles.

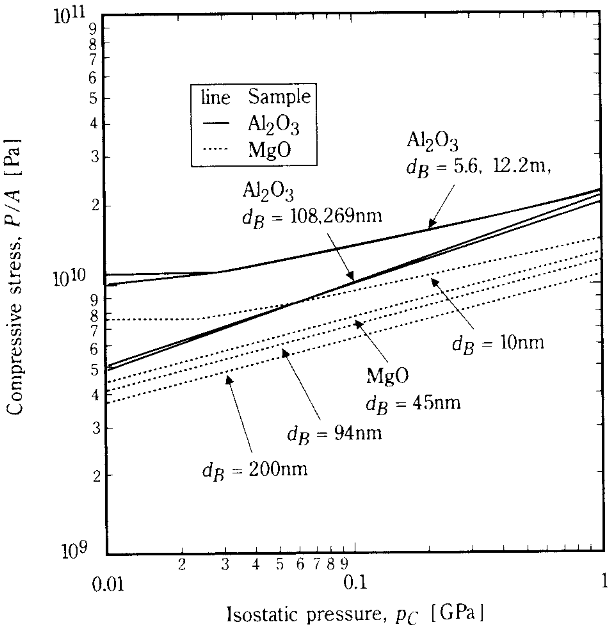

(b) Estimated mean compressive stress at contact point by Equation (5) and (7).

Fig. 10 Estimation of elastic deformation and mean compressive stress at contact point between particles.

Young's modulus, $\nu = 0.25$, $Y = 420$ MPa for Al_2O_3, and $\nu = 0.25$, $Y = 248$ MPa for MgO were used[3]. The mean stress at the particle contact point differed somewhat depending on the type and size of particles, but it remained within the range of 4 GPa to 20 GPa. Since the hardness of particles is around 25 GPa for Al_2O_3 and 15 GPa for MgO[3], P/A had about the same value as the hardness value or was slightly lower. Although the contact points may be plastically broken down locally, the stresses at the contact surfaces were nearly the same as the hardness and an occurrence of a plastic deformation larger than the value of Δ obtained from the elastic displacement is inconceivable. **Table 3** shows the ratio between the displacement amount Δ at 1 GPa for each powder obtained from Equation (6) and the particle size. The deformation amount at a contact point was estimated to be about 3% of the particle size at the most. With a plastic deformation of this magnitude, it is thought that the effect of the deformation of a particle contact point on the pore size between particles, on the increase in compact density, or on making the pore size finer is slight.

Finally, the effect due to fracture of particles was studied. By applying a compression force (P) to the particle contact points, the tensile stress (σ_T) generated near the particle contact point was obtained using the following equation[14].

$$\sigma_T = \{(1 - 2\nu)/3\}\{3P/(\pi r^2)\}$$
$$= \{(1 - 2\nu)/2\}\ (P/A) \qquad (8)$$

The tensile stress generated near the particle contact point obtained using this equation was $(1 - 2\nu)/2$ times the mean compression stress and when $\nu = 0.25$ was used, it became 1/4 times. In **Table 3**, the tensile stresses of the corresponding powders at 1 GPa, obtained using Equation (8), are shown but they are within a range of 2.5 – 5 GPa. This value, compared with the theoretical strength of alumina monocrystals, $(\sigma_{th} - E/10 = 42$ GPa)[17] or with the actual measured value (15 GPa)[17] of the tensile strength of alumina monocrystal whiskers, is sufficiently small. The tensile stress obtained using Equation (8) is generated within a depth range of about twice the contact radius r of the particles from the particle contact surface and rapidly decreases inside the particle[14]. The contact radius r at a compact pressure of 1 GPa was obtained geometrically using the following Equation and the calculated results are shown in **Table 3**.

$$r = (\Delta d_B/2 - \Delta^2/4)^{1/2} \qquad (9)$$

In either case, the contact radius r is about 10% of the particle diameter and even with Al_2O_3 which has the largest particle size, it is 28 mm. From the Weibull theory[17] in which the material strength is dominated by the maximum defect in the material, the maximum defect length c which is concerned with fractures near the particle contact point due to the generated tensile stress σ_T is assumed to be equivalent to a range of about 2r within which the maximum tensile

Table 3 **Estimated deformation of particle, tensile stress and tensile strength at contact point. Isostatic pressure was equal to 1 GPa.**

Samples	Al_2O_3				MgO			
d_B [nm]	269	108	12.2	5.6	200	94	45	10
Δ/d_B [%]	2.2	2.4	2.6	2.6	1.8	2.3	2.7	3.3
σ_T [GPa]	4.9	5.0	5.3	5.3	2.6	2.9	3.2	3.5
r [nm]	28	12	1.4	0.63	19	10	5.2	2.7
σ_e [GPa]	10	15	42	42	12	17	23	32

strength is generated. From this assumption, the fracture strength σ_e near the contact point was estimated from the following equation.

$$\sigma_e = K_{IC}c^{1/2}/1.26 \qquad (10)$$

Where, K_{IC} is the critical stress intensity factor for brittle materials and the value differs depending on the literature and measuring method but since a value of around 2 ~ 4 $MNm^{3/2}$ for Al_2O_3, and 3 $MNm^{3/2}$ for MgO was obtained, 3 $MNm^{3/2}$ was used. **Table 3** shows the results of the calculation of the fracture strength near the contact point σ_e with $c = 2r$. For Al_2O_3 (III) and (IV), since $\sigma_e > \sigma_{th}$ was obtained, $\sigma_e = \sigma_{th}$ was used. From this result, it can be estimated that the strength near the fine particle contact point of 1 μm and less used in this report was not lower than 10 GPa which is close to the theoretical strength. Consequently, it can be considered that with a generated stress of several GPa, fracture of particles hardly occurs.

Observations of compacts using an electron microscope were made on compacts of Al_2O_3 (II) and MgO (I) which are of relatively large particle size. Their particle shapes were maintained even under isostatic high pressure compacting conditions of 1 GPa and no notable particle fracture or deformation was observed. The relation between the relative density shown in **Fig. 5** and the mode pore size/particle size coincided with the model packed structure of spherical mono-dispersed particles and in consideration of this, there was little possibility of substantial plastic deformation or particle fracture occurring at contact points even under high pressure conditions. It is thought that densification occurred by rearrangement of primary particles following the collapse of aggregate structures.

5. Conclusion

Using ultra-fine particles of Al_2O_3, MgO, and SiO_2 of various particle sizes, isostatic high pressure compacting under pressures of up to 1 GPa was conducted and from the results obtained through evaluation and analysis of the compacting characteristics and compact structures, the following conclusions were reached.

1) Isostatic high pressure of 1 GPa is extremely effective for the densification of ultra-fine particle compacts with particle sizes of 15 nm and less, irrespective of the type of powder. Strong and coarse aggregate structures completely collapse under high pressure, and the relative density increased up to a maximum of 60%. It was also possible to make the pore size inside the compact smaller than the primary particle size.
2) With Al_2O_3 powders of 100 nm and a larger particle size, the density and pore size did not change appreciably with an increase in pressure. High pressures of 0.6 GPa or above were not very effective for the densification or for making air gaps in compacts smaller. On the other hand, with MgO powders, even for particle sizes of 100 nm and above, increased densification and reduction in pore size were seen with an increase in pressure and a maximum relative density of 80% and a reduction to 20% or less of the mode pore size with respect to the specific surface converted diameter were achieved.
3) The relation between the mode pore size/primary particle size ratio and the compact relative density was roughly approximated by a single straight line on a semi-logarithm graph. Also, by estimating the force applied at the particle contact points, the generated stress, and the maximum tensile stress generated inside the particles, and by making comparisons with the particle strength and the particle fracture yield value, it was confirmed that no notable plastic deformation or particle fracture phenomena at the contact points had occurred. Consequently, within the experiment scope of this study, densification was enhanced by the primary particle rearrangement mechanism following the collapse of aggregate structures.

[Acknowledgements]

Gratitude is expressed for the support provided for this study by "the Toden Memorial Scientific Technology Research Center Foundation research assistance", and "the Ministry of Education Scientific Research subsidy (General Research A)".

Nomenclature

A = area of contact circle between particle [nm^2]
a = parameter in Eq. (3) [—]
b = parameter in Eq. (3) [—]
c = maximum flow length in contact area of particle [nm]
D = pore diameter in compacts [nm]
d = particle diameter [nm]
d_B = mean particle diameter estimated from specific surface area by BET method [nm]
D_m = mode pore diameter in compacts [nm]
k_1 = parameter in Gauss equation [cm^3/g]
k_2 = parameter in Gauss equation [m^2]
K_{IC} = critical stress intensity factor for brittle material [MNm$^{-2/3}$]
P = force at contact point between particles in compacts [N]
p_C = cold isostatic pressure [GPa]
p_U = pressure of uni-axial pre-pressing [GPa]
r = radius of contact circle between particles [nm]
S_W = specific surface area by BET method [m^2/g]
v = pore volume frequency [cm^3/g]
Y = Young's modulus [MPa]
Δ = deformation at contact point between particles [nm]
ε = porosity in powder compacts [—]
ν = Poisson's ratio [—]
σ_e = estimated tensile strength of contact area of particle [Pa]
σ_T = tensile stress in particle [Pa]
σ_{th} = theoretical tensile strength of materials [Pa]
ϱ_G = density of powder compacts [kg/m^3]
ϱ_T = powder true density [kg/m^3]

Literature cited

1) Abe, O., S. Kanzaki and H. Tabata: *J. Ceram. Soc. Jpn.*, **97**, 32-37 (1989)
2) Abe, O., S. Aoki, S. Kanzaki and H. Tabata: *ibid.*, **97**, 432-38 (1989)
3) "Fine Ceramics Jiten", (1987), Gihoudou Shuppan, Japan
4) Horvath, J., R. Birringer and H. Gleiter: *Solid State Communication*, **65**, 319-22 (1987)
5) Kamiya, H., H. Suzuki, T. Ichikawa and G. Jimbo: *Ceramic Eng. and Sci. Proc.*, **13** (7-8), 563-70 (1992)
6) Kamiya, H., H. Suzuki, D. Kato and G. Jimbo: *J. Am. Ceram. Soc.*, **76** (1), (1993) in press
7) Kumagai, M. and G.L. Messing: *ibid.*, **68**, 500-05 (1985)
8) Karch, J., R. Birringer and H. Gleiter: *Nature*, **330**, 556-58 (1987)
9) Mindlin, R.D. and N.Y. New York: *J. Applied Mechanics*, 259-65 (1949)
10) Nishida, A., A. Ueki and H. Masuda: *J. Mat. Sci. Jpn.*, **36**, 1157-61 (1987)
11) Reed, J.S.: "Introduction to the Principles of Ceramics Processing", p.339, John Wiley and Sons, New York (1982)
12) Rumpf, H.: *Chem. Ing. Tech.*, **42**, 538-40 (1970)
13) Sacks, M.D. and T.Y. Tseng: *J. Am. Ceram. Soc.*, **67** (8), 526-32 (1984)
14) Timoshenko, S.P., and J.N. Goodier: "Theory of Elasticity, Third Edition", pp.409, McGraw Hill (1970)
15) Tseng. T.Y. and M.D. Sacks: *J. Am. Ceram. Soc.*, **71**, 841-44 (1988)
16) Tsubaki, J. and G. Jimbo: *Powder Technology*, **37**, 219-27 (1984)
17) Yokobori, T.: "Zairyou Kyodogaku", p.9, Iwanami Zensyo, (1974)
18) Kirchener, H.P.: *Eng. Fract. Mec.*, **10**, 283-88 (1978)

Dispersion and Compounding Process of Particulate Ag and Fine Ni Powder Using a High-speed/High-shear Mill[†]

Munetake Satoh, Takahiko Yamashita and Kei Miyanami
Department of Chemical Engineering, Faculty of Engineering, University of Osaka Prefecture[*]
Kenji Higashi and Shinji Tanimura,
Department of Mechanical Engineering, Faculty of Engineering, University of Osaka Prefecture[**]
Hayato Inada and Koji Tsuji
Materials Research and development Laboratory, Matsushita Electric Works[***]

Abstract

A dry powder coating method has been applied to develop high-performance contact-materials for the electrical industry. Using a high-speed/high-shear type of mill, the despersion and compounding process of particulate Ag and nano-meter-size Ni powder were investigated. The transformation of the particles throughout the process was shown by the torque and temperature curves during the treatment in the mill. The optimum operating conditions for both dispersion of fine particles into the matrix and sintering process were discussed based on the physical properties of bulk powders and sintered composite.

1. Introduction

Electrical contacts are used in relays, magnetic switches, contact circuit breakers and similar current-switch devices. Silver-based alloys have been used extensively as electrical contact materials in current switching devices because of their properties of conductivity and resistance to corrosion, fusion and mechanical wear. Silver-nickel system contacts, well known as materials of high workability, high reliability and low contact resistance, are used as media for weak current contacts. The suitable range of nickel concentration needed in silver matrix to give the required mechanical strength and electrical properties is around 10 wt%. However, there are difficulties in controlling the nickel concentration in silver phase appropriately and dispersing the finer component in the matrix by ordinary metallurgical processes, because the silver-nickel system exhibits very low mutual solubility in all temperature ranges, as seen from the equilibrium state diagram.

The compaction of simple mixed powders and coated particles or ordered mixtures is a normal compounding method, offering wide applications in the preparation of new materials, which might circumvent these difficulties.

In the present study, a powder mixing and coating method in dry state incorporating partial mechano-fusion was applied to disperse the fine particles at the desired proportion within the matrix formed by coarse *Ag* particles using a high-speed/high-shear mill. The mixing and compounding processes and suitable operating conditions were assessed by measuring the color change of the mixture and the characteristic curves of torque change with operating time.

2. Materials and experimental method

2.1 materials: In this experiment, silver(*Ag*) particles with an average diameter of 5μm were used as the matrix and fine nickel powder(*Ni*) with a mean diameter of 0.02 μm as the filler. *Ni* powder is cohesive (poor flowability) and has a tendency of forming agglomerates. The total proportion of the *Ni* component was controlled at a constant value of 10wt% considering mechanical strength and electrical properties.

2.2 Experimental method: Figure 1 illustrates the series of processes from compounding the starting powder materials to obtaining the hot pressed test piece. In the first place, measured amounts of *Ag* particles and *Ni* powder were mixed using a ball

---

[*] 1-1 Gakuen-cho, Sakai Osaka 593, Japan
[**] 1-1 Gakuen-cho, Sakai Osaka 593, Japan
[***] 1048 Kadoma, Osaka 571, Japan
[†] This report was originally printed in *J. of Japan Society of Powder & Powder Metallurgy*, **40**, 299 (1993) in Japanese, before being translated into English with the permission of the editorial committee of the Soc. Powder & Powder Metallurgy.

mill to obtain a homogeneous dispersed state and a partially coated state of *Ni* onto the surface of *Ag* particles. After preliminary mixing, the mixture was introduced into the vessel of high-speed/high-shear mill and compounding was carried out in an inert atmosphere of *Ar* gas and under different operating conditions. The schematic illustration of the mill and measuring system is shown in **Figure 2**. The clearance between the rounded inner piece and the vessel wall was set at 3.0 mm. One mm zirconium beads were used as a medium to prevent fine powders from sticking to the vessel wall and to the rounded inner piece, so as to improve the dispersion effects of *Ni* powder and the shear and compression effects between *Ag* particles and *Ni* powder. The amount of beads was· determined so as to form 3 mm of packed beads layer around the inner side wall of the vessel under centrifugal force. The packing ratio of powder mixture within the void volume of the beads layer is defined by the following equation:

packing ratio(V/V_E) = powder volume/void volume of the beads layer

where, the value of V_E is taken with the assumption of dense packing state.

Transformation of the particles throughout the compounding process was assessed by the lightness of the mixture, change of power consumption with time, temperature change, specific surface area of compounded particles, aspect ratio of processed particles, compressibility parameter, C[(dense packed density − loose packed density)/(dense packed density)] as a flowability index, and SEM photograph. Compounded particles thus obtained were formed and sintered in vacuum under the following conditions: sintering temp. at 1123K, 3600 seconds for temperature rise and 7200 seconds of sintering time. Hardness(*HV*) and shrinkage ratio (change of density before and after sintering) were measured to evaluate the compounding processes and composite properties.

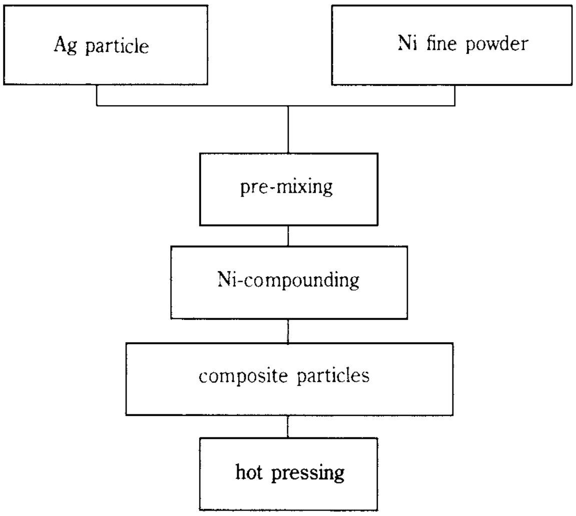

Fig. 1 Ag-Ni contact manufacturing process

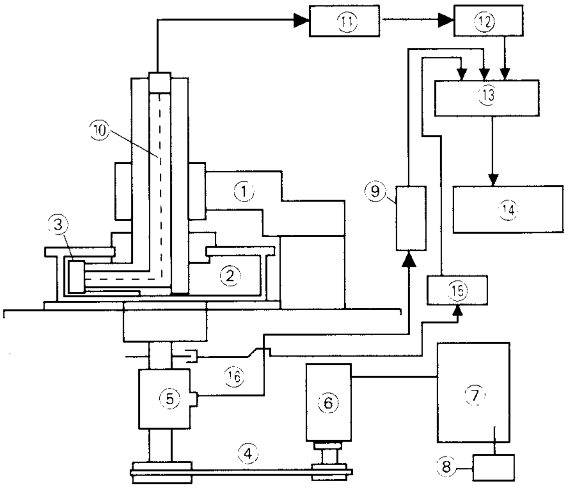

① arm
② chamber
③ inner piece
④ belt
⑤ torque meter
⑥ motor
⑦ inverter
⑧ speed controller
⑨ strain amplifier
⑩ thermocouple
⑪ thermometer
⑫ DD amplifier
⑬ A/D converter
⑭ personal computer
⑮ F/V converter
⑯ tachometer

Fig. 2 Schematic illustration of high-speed/high-shear mill

3. Results and discussion

3.1 Compounding process

Prior to the compounding experiments, a preliminaly study was carried out on the effect of high-speed, high-shear treatment on the binary mixture of *Ag* and *Ni* with zirconium beads. **Figure 3** shows the relationship between the torque, T, loaded on the driving shaft and the rotational speed, N, of the mill measured under the condition of constant charge ratio (powder and beads) and low temperature during the initial mixing period of the operation, before coating or compositing. The torque increased exponentially with the rotational speed. From this behavior, it is clear that a strong compressive force is required to pass the material through the clearance between the rounded inner piece and the wall.

The variation in torque and temperature with time during mixing at varying rotational speeds and packing ratios (V/V_E) are shown in **Figure 4**. In the case of a high speed and V/V_E = 1.0, the torque increased immediately after the mill was set in motion, passed through a maximum, then decreased gradually to attain a steady value. The temperature-time curve (dotted line, *T*) showed in general the same pattern as the torque curve but the peak value appeared after the torque peak occurred and the peak value was not much larger than the value at the equilibrium state. On the other hand, in low speed operation at V/V_E = *0.5*, the torque changed in easy undulations and the temperature curve increased monotonically, failing to show any peak. On passing through the narrow clearance between the inner piece and the vessel wall, the mixed powder layer including beads is compressed adiabatically at that moment and as a result of exothermic phenomena, fine *Ni* powders are fixed onto the surface of large *Ag* particles and enter the matrix. This compounding mechanism might be confirmed by evaluating the surface condition of the powder.

Figure 5 shows the typical variations with time of the color (lightness *L*, measured by a colorimeter: Minolta CL-100) of the mixture and flowability index (compressibility parameter, *C* measured by powder tester: Hosokawa micron). The lightness value of the premixed powder is 33 (dark gray) and as seen in the figure, the mixture becomes progressively lighter (metalic gray). The compressibility, *C* combines various different kinds of physical properties of particles and *C* is used as one of the indices representing the flowability of powder beds. In this experiment, *C* indicates the maximum when the adhered fine *Ni* particles are fixed on the *Ag* surface and the surface roughness of the *Ag* attains the maximum.

These characteristic curves of *L* and *C* are very useful for the analysis of the change in the surface condition of the powder throughout the compounding process. The shearing and compression forces acting upon the powder stabilized the adhered fine particles of *Ni* on the *Ag* particles. Eventually, part of these fine particles penetrates into the *Ag* matrix, thus decreasing the number of exposed black fine particles. Friction between *Ag* particles provokes further smoothing of their surface, and the external surface of the *Ag* particles reappears (increasing lightness and improving flowability). To confirm the series of compounding process, the variations in specific surface area, *A*, measured by the BET method and the aspect ratio, *ℓ/Lp* (=breadth/length) of the compounded particles are plotted in **Figure 6**. The specific surface area decreases with time. The aspect ratio decreases once, and then, increases again. This result shows the deformation process of the matrix particles by high-shear and high-stress during the compounding operation, i.e. in the initial stage, flattened elliptic particles are transformed into spheres by a sort of kneading effects accompanying the rolling and folding mechanisms without breaking into fine pieces.

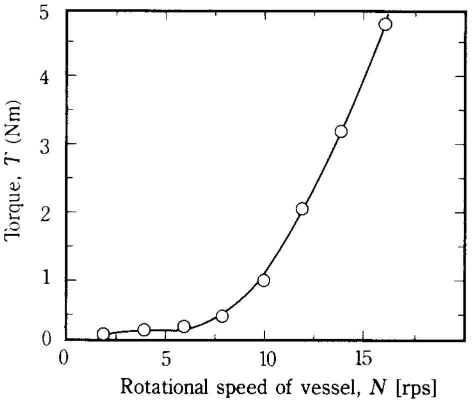

Fig. 3 Relationship between torque and rotational speed

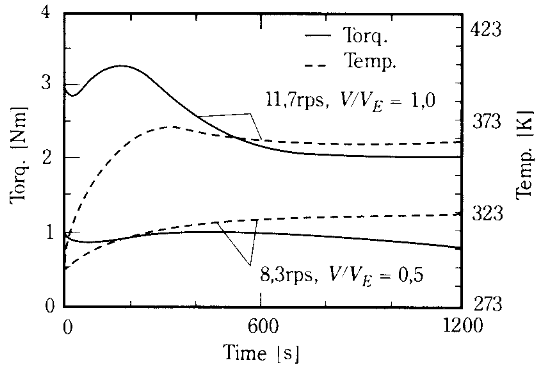

Fig. 4 Variations in torque and temperature with operating time

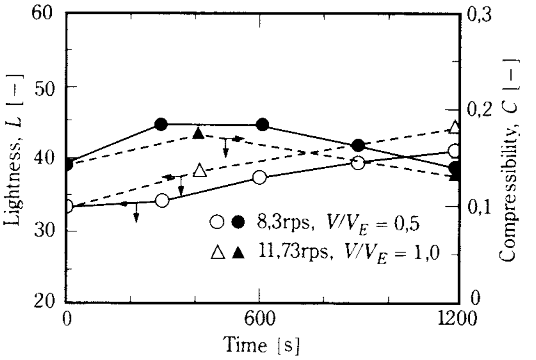

Fig. 5 Changes in lightness (○, △) and compressibility (●, ▲) of mixture with operating time

3.2 Physical properties of compounded particles

The average hardness values H_V (measured with micro-Vickers-hardness meter) at the cross-section of 20 particles of each sample obtained under different operating conditions are plotted against the lightness in **Figure 7**. The relation between the hardness and the lightness is considered to be linear with the experimental conditions as seen in this figure. And particles which showed both higher values of lightness and hardness corresponded to the product processed under the condition of a higher rotational speed of the mill. It is clear that the measurement of the lightness of a powder mixture during operation is useful to evaluate the degree of strength of the composite by dispersion of fine particles into the matrix.

The external appearance and internal micro-structure of composite particles (having the maximum value of hardness marked ■ in the **figure 7**) are shown in SEM **Photo-1** (a) and (b). As seen in picture (a), the mixture of metal powders formed agglomerates with an average diameter of 20 μm. It was confirmed that fine *Ni* powder was dispersed into the matrix of *Ag* particles in a nano-scale order (*Ni* corresponding to the gray color part in the cross-section of the composite particle shown in picture (b)). On the other hand, the composite processed under the conditions of low shearing rate indicated a lower hardness value because of insufficient dispersion of *Ni* fine particles.

3.3 Effect of compounding process on the density of sintered material

The compounded particles were formed into a tablets (10mm in diameter) using a cylindrical die under different pressures.Sintering of the tablets was carried out under the conditions of 10^{-6} torr in vacuum at 1173K.

The densities of the tablets before and after sintering were measured to evaluate the shrinking ratio, i.e. reduction of voids and flaws in the material. The shrinking ratio was defined by the following equation:

$$\text{shrinking ratio} = [(\varrho_S - \varrho_o)/\varrho_S] \times 100$$

where, ϱ_o: density before sintering, ϱ_S: density after sintering. With a positive value for the shrinking ratio, the formed tablet becomes a highly dense composite after sintering. **Figure 8** shows the relationship between the shrinking ratio and the operating time. As seen in the figure, the shrinking ratio is constant up to 600s, and then, after further processing the ratio decreases, i.e. showing an expanding tendency. The expansion of compacted powders during the sintering process is an undesirable phenomenon because it may create local faults in the material such as voids, cracks, segregation of components and so on. However, it is clear that during compounding and pressing of powders, leaving micro through-holes from the inside to the surface of both agglomerated particles and compacted ones is required to release all gaseous elements adsorbed

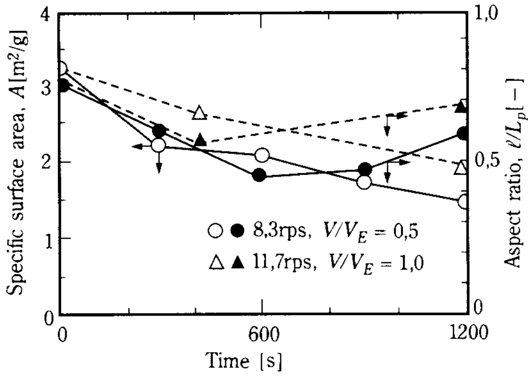

Fig. 6 Changes in specific surface area (○, △) area and aspect ratio (●, ▲) with operating time

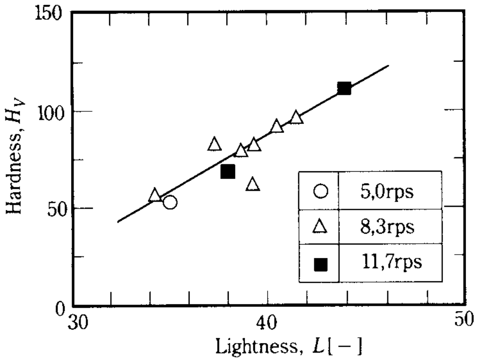

Fig. 7 Relationship between lightness and Vickers Hardness of the composite particles

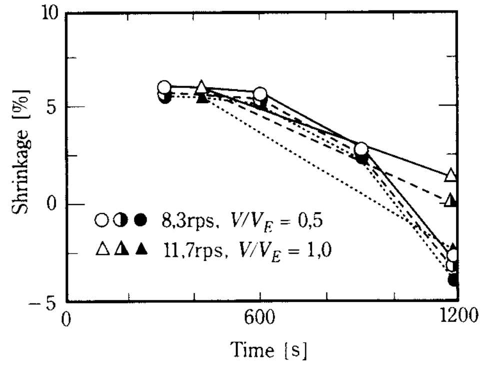

Fig. 8 Changes in shrinkage with operating time

on the internal surface.And at the final stage of the sintering process, all the micro holes and voids should disappear and the density of the sintered material needs to attain the maximum. Therefore, selection of mixing and compounding conditions becomes the key to satisfying both good dispersion state between matrix and filler, and denser sintered state. The tendency of expansion during the sintering process was promoted gradually by over-mixing or over-compounding as seen in the figure. In this experiment, the upper limit of the operating time for dispersing and compounding fine particles into large matrix particles without expansion was determined to be 1000 seconds for $V/V_E=1.0$, $N=11.7$rps and 1200 seconds for $V/V_E=0.5$, 8.3rps, respectively.

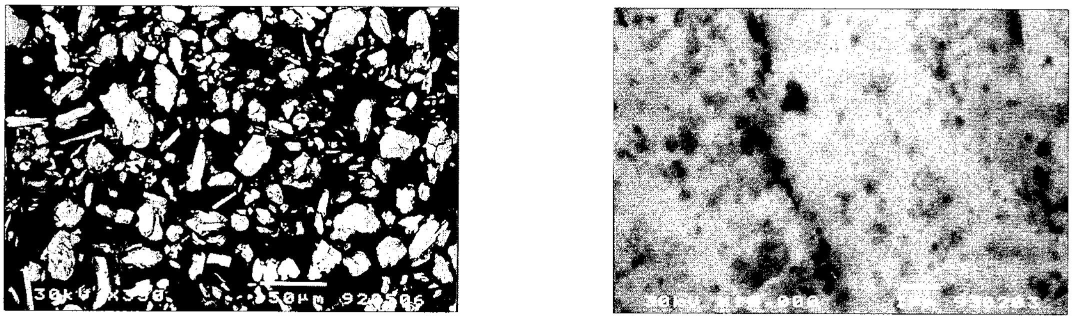

(a) SEM photograph of the composite particles

(b) cross-sectional view of the particle milled at 11.7 rps and $V/V_E = 1.0$

Photo.-1 The external apperance and internal micro-structure of composite particles

4. Conclusion

A dry process for mixing and compounding binary components of metal powders has been applied to develop high quality functional metal composites using a high-speed/high-shear type of mill. In this study, measurements of color change of the mixtures, power consumption and temperature with time are shown to be practical methods for monitoring the degree of mixing and the state of compounding during operation. It has been shown that very fine dispersion (of nm scale) of ultra fine *Ni* into *Ag* matrix can be obtained under the conditions of $N=11.7$rps and $V/V_E=0.5$, and forming and/or sintering of the compounded particles was possible.

Nomenclature

A : specific area of powder (m^2/g)
C : degree of compressibility (−)
H_V : Vicker's hardness
L : lightness (−)
L_p : length of composite particle (m)
ℓ : breadth of composite particle (m)
N : rotational speed (s^{-1})
T : torque (*Nm*), temperature (*K*)
V : powder volume (m^3)
V_E : void volume of the beads layer (m^3)
ϱ_a : density of composite after sintering (kg/m^3)
ϱ_o : density of composite before sintering (kg/m^3)

References

1) K.H.Schroder: Proc. Meet. IEEE Holm Conf. Electr. Contact Phenom., Chicago, **33**, 163 (1987).
2) M. Satoh, F. Hamano, K. Miyanami, K. Higashi, T. Ito and H. Yoshida: Proc. 2nd World Congress Particle Technology , Kyoto, **432** (1990).
3) M. Alonso, M. Satoh, K. Miyanami, K. Higashi and T. Ito: *Powder Technol.*, **63**, 35 (1990).
4) M. Satoh, K. Higashi, K. Miyanami, S. Tanimura, K. Tsuji, H. Inada and K. Kojima: *Powder Technol.*, **70**, 71 (1992).
5) K. Tsuji, H. Inada, K. Kojima, M. Satoh, K. Higashi, K. Miyanami and S. Tanimura: *J. Mater. Sci.*, **27**, 1179 (1992).
6) M. Kuntcheva, J. Dimitrov and R. Todorov: Proc. 8th Int. Conf. Electr. Contact Phenom., Tokyo, 523 (1976).

Fine Particle Separation by Revised Type Air-Cyclone Classifier †

Hideto Yoshida, Tatsuya Saeki, Toshiyuki Fujioka,
Tetsuya Ueda and Tadashi Fuyuki**
Dept. of Chem. Eng., Hiroshima Univ., *

Abstract

Experimental and theoretical studies were conducted on the separation of submicron powder using a revised type of cyclone. The cyclone has a movable inlet guide plate at the inlet section, and 50% cut size is controlled from 0.45 to 0.75 μm by changing the inlet clearance of the guide plate. But the 50% cut size increases again with a very narrow inlet clearance of the guide plate, because the radial velocity of particles decreases and fluid turbulence increases under such condition.

The 50% cut size decreases to about 0.4 μm when both the inlet guide plate and the blowdown method are used. The partial separation efficiency with a spiral-inlet cyclone is higher than a cyclone with tangential inlet, and the 50% cut size decreases with a highly polished inside wall surface.

Introduction

Cyclones are widely used as a separation apparatus for solids and gases, and for solids and liquids since their structure is simple and they can be installed at low cost. Recently, with improvements in the dimensions of the various parts of the cyclone, classification of sub-micron order particles with fairly high precision evaluation, which is not feasible by conventional cyclones, has become possible.

However, the changing of 50% cut size of cyclones generally requires changing the inlet flow velocity or the cyclone diameter and in actual practice, may entail difficult operation.

This report describes experiments using a new prototype of cyclone, fitted with an arc shaped sliding guide plate at the cyclone inlet which allows 50% cut size changes by simple external control. In addition, with the object of studying the effect due to the inlet shape and to the degree of roughness of the inner wall surface on the collection of finer particles, a study was made on the classification characteristics with the combined use of the guide plate and blowdown method. This report is made on some of the interesting knowledge gained.

1. Experiment apparatus and methods

Fig. 1 shows the schematic drawing of the experimental apparatus. The diameter of the cyclone was set at 72 mm and the dimensions of the parts were based on a shape which proved superior in classification performance in experiments conducted by Iinoya et al[1-3]. Namely, it features a total circumferential spiral-inlet type with a dust box diameter larger than the outlet pipe diameter.

The partial separation efficiency η was measured by applying the centrifugal sedimentation method (Shimadzu, SA-CP3) to the particle size distribution of the corresponding collected powder and calculated using the following equation with respect to the collected amount percentage. The particle size distribution and weight of the feed powder was obtained by considering the total weight and weight ratio of the total collected powder.

$$\eta = \frac{\Delta W_C + \Delta W_B}{\Delta W_C + \Delta W_B + \Delta W_F} \qquad (1)$$

In the above equation, Δ is the value within the finite particle size range and ΔW_C, ΔW_B, ΔW_F, are respectively the collected dust mass within the finite particle size range of the coarse powder side, blowdown side, and fine powder filter side. Since deposits of particles were seen on the inner wall of the cyclone, such particles were brushed off and added to the coarse powder side. Also a ring nozzle type disperser (made by Nisshin Engineering Co.)

---

* 4-1 Kagamiyama, 1-Chome, Higashi-Hiroshima-Shi 724, Japan

** Nisshin Flour Milling Co., Ltd., Technical Res. Center, Tsurugaoka 5-3-1, Ohi-machi, Iruma-Gun Saitama 354, Japan

† This report was originally printed in *Kagaku Kougaku Ronbunshu*, **19**, 476 (1993) in Japanese, before being translated into English with the permission of the editorial committee of the Soc. Chemical Engineers, Japan.

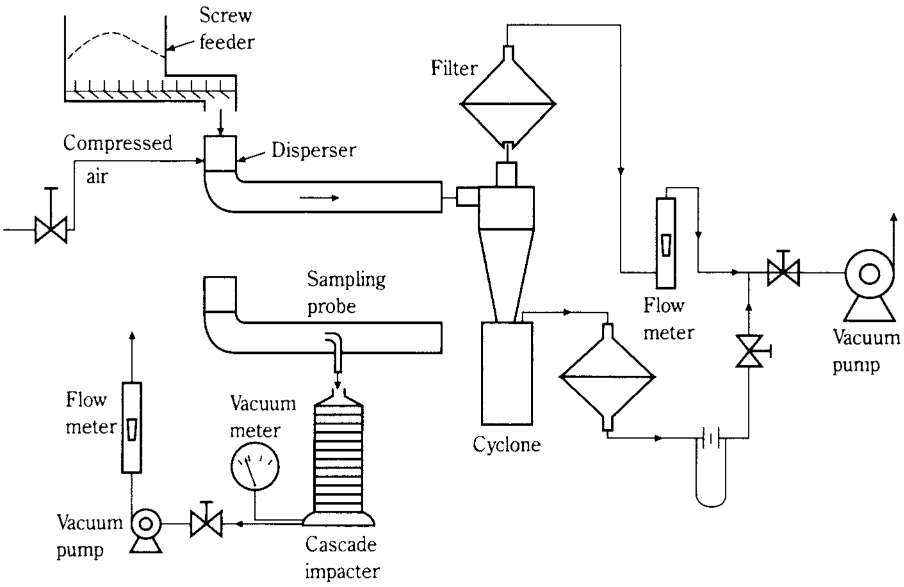

Fig. 1 Experimental apparatus of cyclone classifier

was installed downstream after the screw feeder and using an impactor at the cyclone inlet, the degree of particle dispersion was checked in order to conduct experiments under favorable dispersion conditions$^{4)}$. The test powder was Kanto loam (JIS No. 11).

Fig. 2 shows the dimensions of the respective parts of the cyclone. Stainless steel was used for the manufacture of the cyclone. The inner walls were buff polished to a mirror finish to reduce attenuation of circumferential velocity and to collect finer particles.

As shown in **Fig. 3**, the cyclone used in this study featured an arc shaped guide plate inserted in the upper inlet section of the cyclone with the guide plate sliding in the circumferential direction to enable a variation in the 50% cut size. In a normal condition, the guide plate tip is at position A. With the guide plate at positions B, C, and D, the fluid velocity at the tip section increases and also the particle travelling distance in the radial direction toward the cylindrical wall is shortened and therefore it was thought that finer particles could be collected. In experiments, the distance b between the guide plate tip and the cylindrical inner wall was varied over a range of 4 to 17 mm. Experiments were conducted with different flow velocities at the guide plate tip with a velocity of 22 (m/s) at position A and 92 (m/s) at position E, but the total flow volume at the inlet was kept constant at 0.80 (m^3/min.).

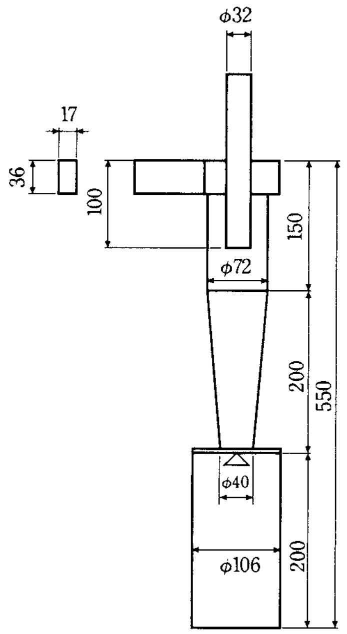

Fig. 2 Dimensions of the cyclone

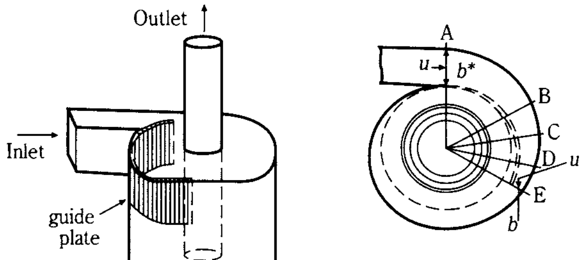

	A	B	C	D	E
b (mm)	17	12	8	6	4
u (m/s)	22	31	46	61	92

Fig. 3 Cyclone inlet with inlet guide plate

2. Experimental results and observations

To examine the degree of particle dispersion at the cyclone inlet, a low pressure type cascade impactor (made by Tokyo Direct Co. , Model LP-20, total 12 stages) was used to measure the particle size distribution. Also particle size measurements were taken using a liquid centrifuge method on coarse particles collected by the cyclone and on particles at the fine powder side filter section, and by estimating the inlet particle size, experimental results obtained through the two measuring methods were compared and are shown in **Fig. 4**. The results roughly match each other and it can be considered that the particles at the cyclone inlet are almost completely dispersed. This is perhaps due to the good dispersion properties of the feed powders, the use of a ring nozzle type disperser, and to low particle concentration under which the experiment was conducted.

Next **Fig. 5** shows the results of the effect due to the difference in the cyclone inner wall condition on partial separation efficiency.

The guide plate was set at position A (normal position) and experimental results were compared with buff polished mirror surface inner wall and with unpolished inner wall. With the polished wall, the 50% cut size was around 0.7 μm while with the unpolished wall, the 50% cut size was larger at approximately 1.0 μm. This is perhaps due to the reduction in fluid friction loss near the inner wall surface with the buff polished wall, allowing more collection of fine particles. Hereinafter, all results in this report are for those obtained with the polished wall.

Next, the effect due to the difference in cyclone inlet shape on partial separation efficiency was studied. Experimental results are shown in **Fig. 6**. The guide plate was set at position A as shown in **Fig. 3** and a comparison was made between the tangential inlet type and the total circumferential spiral-inlet type with all other conditions being the same. The 50% cut size was roughly the same for both types but in the area with particle size of 1 μm and above, the spiral-inlet type exhibited a higher partial separation efficiency than the tangential type. The reason for this is thought to be due to the difference between the two types in air flow conditions near the cyclone inlet. With the spiral-inlet type, the occurrence of turbulence where the air flow of the inflow section converges with the air flow after one rotation is low while with the tangential

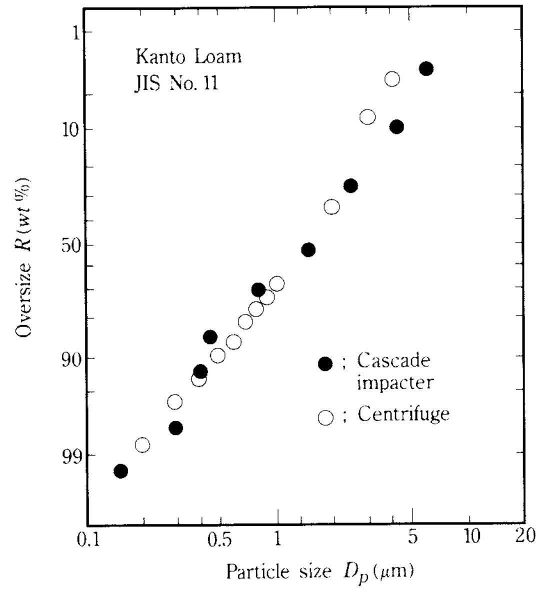

Fig. 4 Particle size distribution measured by cascade impactor and liquid centrifuge

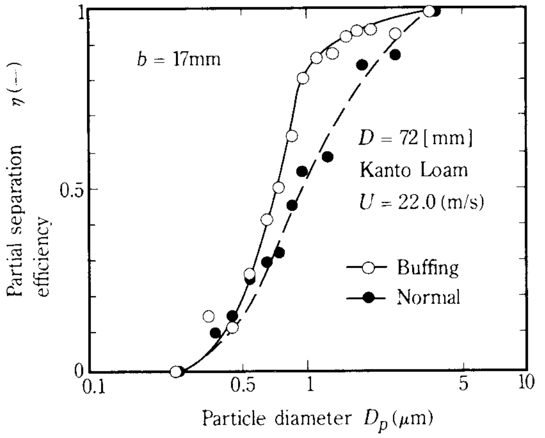

Fig. 5 Effect of cyclone wall with and without polishing on partial separation efficiency

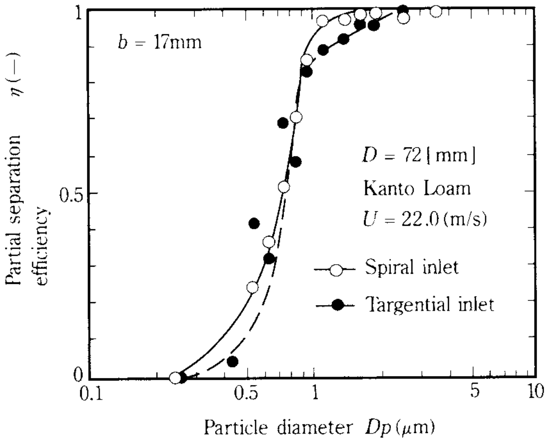

Fig. 6 Effect of cyclone inlet shape on partial separation efficiency

inlet type, the two flows converge at a greater angle and it is presumed that occurrence of turbulence is greater. It has been clarified by the results[6] of numerical analysis made by the authors that coarse particles with a particle size of 1 μm and above are mainly collected near the upper cylindrical part and since occurrence of turbulence is less in the coarse particle collecting section of the spiral-inlet type, it is thought that partial separation efficiency in the high inertial region is higher with the spiral-inlet type.

The above experiments proved that in order to decrease the 50% cut size of the cyclone, it is necessary to buff polish the inner walls to provide a mirror finish and adopt the total circumferential spiral-inlet type for the inlet. Next, a study was made on the possibility of collecting finer particles and changing 50% cut size by inserting an arc shaped guide plate at the cyclone inlet and increasing the flow velocity at the guide plate tip while reducing the travelling distance of particles toward the inner wall in the radial direction.

Fig. 7 shows the experimental values of partial separation efficiency when the inlet clearance *b* from the guide plate tip to the circumferential inner wall is varied. Compared with the normal case with an inlet clearance *b* of 17 mm (**Fig. 3-A**), when the clearance is decreased to 8 mm, the 50% cut size is decreased to about 0.5 μm. Also the slope of the partial separation efficiency curve for the high inertial region becomes greater. However when the inlet clearance is decreased to the minimum value of 4 mm, the 50% cut size increases again. This is thought to be caused by the particle repulsion and by the increase in turbulence near the guide plate. However when the inlet clearance is varied from 8 to 17 mm, it can be seen that the 50% cut size changes from 0.5 to 0.75 μm.

Next, the effect of blowdown flow rate changes on partial separation efficiency was examined. **Fig. 8** shows the partial separation efficiency with the blowdown flow rate set to 5, 10, and 15% with the inlet clearance *b* set to the normal value of 17 mm. It is seen that the 50% cut size decreases with an increase in flow rate. This is believed to be caused by increased average residence time of particles inside the cyclone due to the reduced flow rate at the outlet piping and by easier suction of fine particles near the conical wall into the dust box resulting from the increase in downward velocity component of air flow near the conical wall when blowdown is applied[6].

From **Fig. 7**, it can be seen that it is possible to decrease the 50% cut size by narrowing the inlet clearance with the use of the guide plate and also according to **Fig. 8**, the 50% cut size can be decreased by conducting blowdown, and therefore considering that 50% cut size may be minimized by combining the two, the following experiment was carried out.

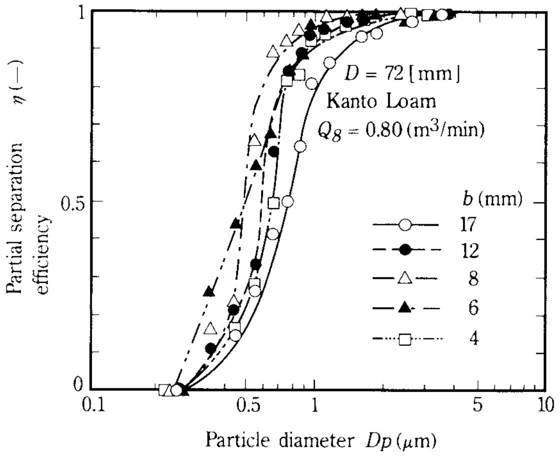

Fig. 7 Effect of the clearance of guide plate on partial separation efficiency

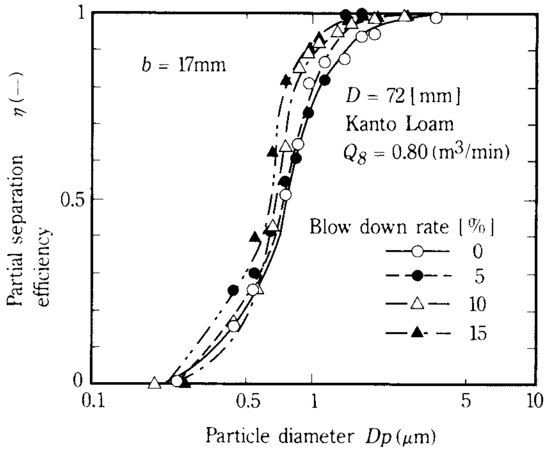

Fig. 8 Effect of blow down flow rate on partial separation efficiency

Fig. 9 shows the experimental results obtained when the combined use of the guide plate and blowdown was applied. The experiment was conducted under the conditions of cyclone inlet flow rate of 0. 80 (m^3/min.) and inlet flow velocity of u = 22 (m/s). The ○ mark in the Figure indicates the case where the inlet clearance *b* was 17 mm and the 50% cut size was approximately 0.75 μm. When the guide plate was positioned at *C* as shown in **Fig. 3**, the inlet clearance became b = 8 mm and the separation diameter decreased to 0.52 μm (marked by △ in the Figure).

Furthermore, when the blowdown method was applied with b = 8 mm, the separation diameter decreased to around 0.4 μm (marked by ▲ in the Figure.) It is found that the combined use of a guide plate and blowdown is effective for further collection of finer particles.

3. Theoretical study on changes in the separation diameter

Next, a theoretical study was made on how the 50% cut size changes when the guide plate is used. If we were to assume that particles are collected according to the horizontal separation theory[5)], the partial separation efficiency can be expressed by the following equation.

$$\eta = \frac{2\pi N U \varrho_p D_p^2 C}{18\,\mu b^*} \tag{2}$$

In Eq. (2), b^* is the inlet clearance, U the inlet fluid velocity, N the revolving number of particles in the cyclone and C the Cunningham's slip correction factor.

Fig. 10 shows a comparison between the experimental values when the guide plate is at position A of **Fig. 3** (in a normal state) and the value calculated using Eq. (2). By setting $N = 11$ in the case when the cyclone inner wall is buff polished and $N = 7$ in the case when polishing is not applied, the experiment value roughly agrees with the theoretical value. Although a difference is seen between the experimental and the calculated values in the high inertial region, this is probably due to the fact that repulsion after the particles collide with the wall and re-entrainment are not considered in the case of theoretical calculation. Also when the wall is buff polished the value obtained is higher than the normal literature's value of around $N = 5 \sim 6$, because attenuation of circumferential velocity in this experiment was suppressed by making the wall surface having a mirror finish.

Fig. 11 shows the relation between the 50% cut size and the inlet clearance b when a guide plate is used. The cyclone inlet flow rate is constant ($Q_0 = 0.80$ m^3/min.). When the inlet clearance b changes between 4 and 17 mm, the 50% cut size varies within a range of 0.5 ~ 0.75 μm. In the Figure, the calculated value obtained when it is assumed in Eq. (2) that $N = 11$ is given by the dotted line, and this shows a tendency for the 50% cut size to decrease with a reduction in the inlet clearance but the experimental value and the calculated value differ in the range where the inlet clearance is small.

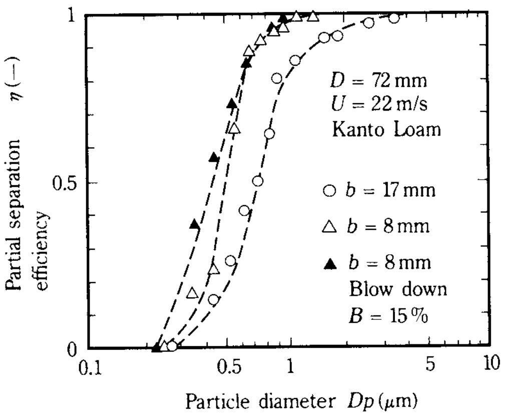

Fig. 9 Effect of guide plate and blow down on partial separation efficiency

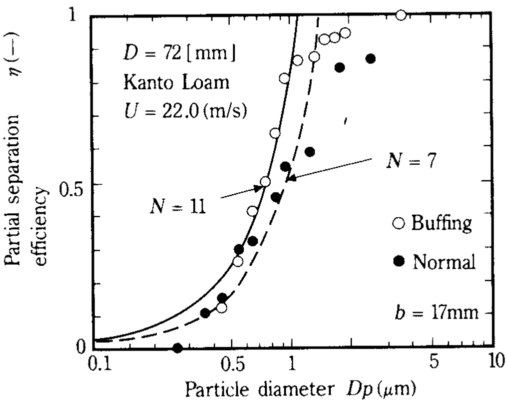

Fig. 10 Experimental results of partial separation efficiency compared with calculated results of separation theory

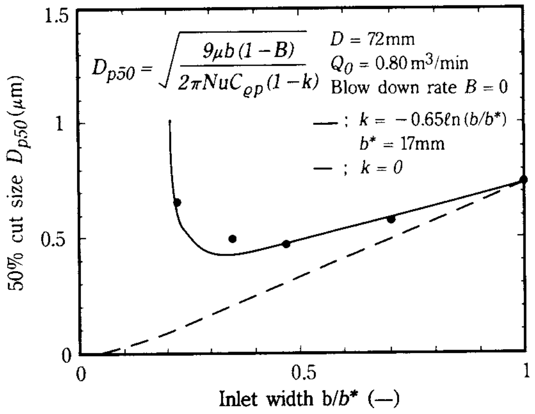

Fig. 11 Change of 50% cut size with inlet clearance of guide plate

However when the guide plate is used, calculation was made with U, b^* of Eq. (2) converted to u, b. This is to say that when the guide plate is moved and the inlet clearance set as b, the change in the 50% cut size can be calculated by substituting the fluid velocity u which can be obtained from the following equation using the continuity of the fluid in Eq. (2).

$$hb^*U = hbu \tag{3}$$

In the above equation, h is the inlet height, b^* is the normal inlet clearance of 17 mm, and U is the inlet velocity.

When the inlet clearance b is small, the difference between the experimental value and the calculated value shown by the dotted line is thought to arise because the velocity variation in the radial direction of the particle is not considered. This was studied using the following model.

When the guide plate is used, particles rapidly contract and then expand and therefore it was assumed that the following equation applies because the actual particle radial velocity decreases as shown in **Fig. 12**.

$$v_r = v_{r1} - v_r' = v_{r1}\,(1-k),\ k = v_r'/v_{r1} \tag{4}$$

However the v_r' in the above equation is the radial velocity in the opposite direction to the wall, caused by the narrowing of the inlet clearance.

On the other hand, the air flow residence time is expressed by the following equation.

$$t = \frac{2\pi RN}{u} \tag{5}$$

Also the following equation is obtained when the sedimentation distance in the radial direction of particles is set as x.

$$t = \frac{x}{v_r} = \frac{x}{v_{r1}\,(1-k)},\ v_{r1} = \frac{\tau u^2}{R} \tag{6}$$

However in Eq. (6), τ is the particle relaxation time. When the residence time t is eliminated from Eqs. (5) and (6), the partial separation efficiency can be expressed by the following equation.

$$\eta = \frac{x}{b} = \frac{2\pi NuC\varrho_p D_p^2\,(1-k)}{18\,\mu b} \tag{7}$$

Therefore, from the above equation, the 50% cut size (η = 0.5) can be expressed by the following equation.

$$D_{p50} = \sqrt{\frac{9\,\mu b}{2\pi NuC\varrho_p\,(1-k)}} \tag{8}$$

Fig. 13 shows the calculated value of k using Eq. (8) from the experimental value of **Fig. 11** to examine the relation between the velocity ratio k defined by Eq. (4) and the inlet clearance b. When the inlet clearance b becomes small, the value of k increases and it can be seen that the actual radial velocity decreases. The solid line shows the calculated value by use of the following equation and the constant 0.65 was determined by a trial and error method.

$$k = -0.65 \ln (b/b^*)$$

The solid line in **Fig. 11** is the calculated line using Eqs. (8) and (9) and roughly agrees with the experimental value. Namely, it can be said that the reason for the 50% cut size to increase again in the area of $(b/b^*) < 0.4$ with a decrease in guide inlet clearance is because the radial velocity of particles becomes smaller than v_{r1} calculated using Eq. (6).

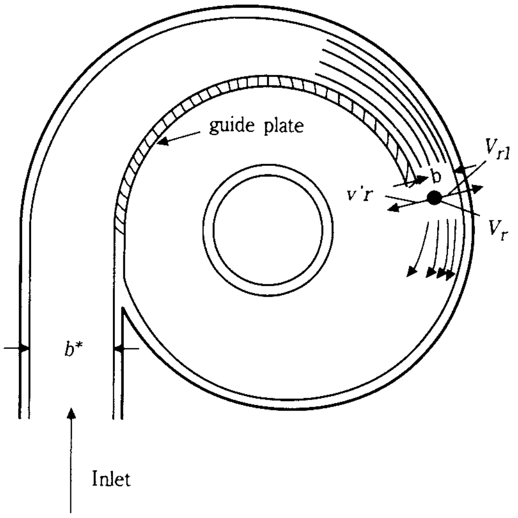

Fig. 12 Radial particle velocity with guide plate attached in the cyclone inlet

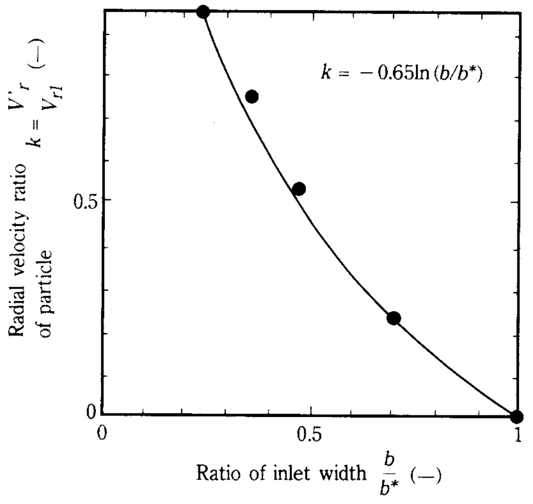

Fig. 13 Change of radial particle velocity with the ratio of inlet width of guide plate

The above study concerns the effect of the guide plate on the 50% cut size. Next, the changes in separation diameter when the guide plate and blowdown are combined are examined. When hold up inside the cyclone is set as V_S, the air flow residence time depending on whether blowdown is used or not can be approximated with the following equations.

$$\text{Without blowdown: } t = \frac{V_S}{Q_O}$$

$$\text{With blowdown: } t' = \frac{V_S}{Q_O\,(1-B)} \qquad (10)$$

Here, B in Eq. (10) indicates the blow down flow rate.

On the other hand, when the revolving number of particles in the cyclone N is assumed to be proportional to the air flow residence time inside the cyclone, the revolving number of particles in the cyclone N' with blowdown is obtained using the following equation from Eq. (10).

$$N' = \frac{N}{(1-B)} \qquad (11)$$

Therefore the 50% cut size when blowdown is applied is given by the following equation by setting N in Eq. (8) as N' and substituting in Eq. (11).

$$D_{p50} = \sqrt{\frac{9\,\mu b\,(1-B)}{2\pi N u C \varrho_p\,(1-k)}} \qquad (12)$$

Fig. 14 shows the changes in separation diameter when the guide plate and blowdown are used in combination. With an increase in the blowdown flow rate, the 50% cut size decreases but when the inlet clearance b becomes narrow in the area of $b/b^* < 0.4$, the separation diameter increases. Also, the dotted line in the Figure shows the value calculated using Eq. (12) and approximately coincides with the experimental value.

In Eq. (12), when blowdown is used, calculation was made on the assumption that N = constant but this error affects v_r', namely k. However since the experimental value of the 50% cut size and the calculated value roughly coincide, it is thought the degree of this error is small.

From the above results, it is found that for further reduction of separation diameters of conventional cyclones, the combined use of a guide plate and blowdown is desirable from both viewpoints of practicality and convenience.

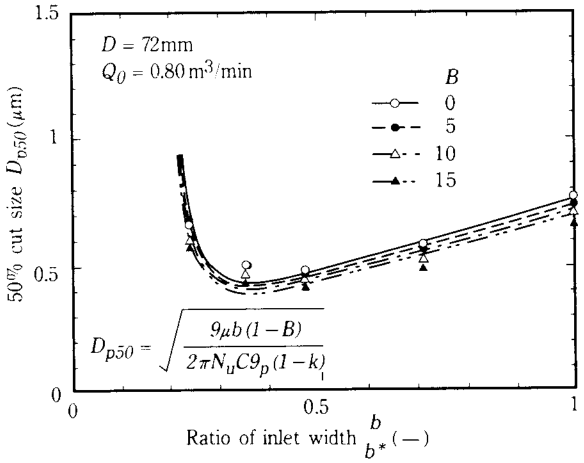

Fig. 14 Effect of blow down flow rate and inlet width of guide plate on 50% cut size

Conclusion

Experiments and theoretical studies were made on an improved type of cyclone enabling a variable 50% cut size and the following conclusions was obtained.

1) By installing a sliding arc shaped guide plate at the cyclone inlet and by reducing the inlet clearance, changing the 50% cut size within a range of 0.45～0.75 μm is possible.
2) When the guide plate inlet clearance is made extremely narrow, the 50% cut size increases. This is thought to be caused by the reduction in radial velocity to the wall direction of particles and by increased turbulence inside the cyclone.
3) To decrease the 50% cut size, the combined use of the guide plate and blowdown is desirable and under the experimental conditions of the present report, it was possible to reduce the 50% cut size down to approximately 0.4 μm.
4) A spiral type rather than a tangential type inlet shape for the cyclone increases the partial collection efficiency in the high inertial region. Also a further decrease of the 50% cut size is possible when the inner wall surface is buff polished to a mirror finish.

[Acknowledgements]

Gratitude is expressed to Koichi Iinoya, Professor emeritus of Kyoto University and Yukiyoshi Yamada of Nisshin Flour Milling Co., Ltd. for their advice.

Nomenclature

B = blowdown flow rate ratio [%]

b = width between guide plate and cyclone wall [m]

b^* = width of cyclone inlet [m]

C = Cunningham's slip correction factor [−]

D_p, D_{p50} = particle diameter and 50% cut size [μm]

h = height of cyclone inlet [m]

$k\ (= v_r'/v_{r1})$ = constant in Eq. (4) [−]

N = revolving number of particles in the cyclone [−]

N' = revolving number of particles in the cyclone with blowdown [−]

Q_o = total flow rate [m^3/s]

R = radius of cylindrical part of the cyclone [m]

t = residence time of particles in the cyclone [S]

t' = residence time of particles in the cyclone with blowdown [S]

u = fluid velocity at the tip of guide plate [m/s]

U = inlet fluid velocity [m/s]

v_r = radial particle velocity [m/s]

$v_{r1}\ (=\frac{\tau u^2}{R})$ = radial particle velocity calculated using Eq. (6) [m/s]

v_r' = radial particle velocity indicated in Fig. 12 [m/s]

x = radial sedimentation distance of particles [m]

ΔW_C, ΔW_B, ΔW_F = mass of collected particles of coarse, blowdown and fine sides respectively [g]

τ = relaxation time of particles [s]

ϱ_p = particle density [g/cm^3]

η = partial separation efficiency [−]

μ = gas viscosity [Pa·s]

Literature cited

1) Iinoya, K., C. Piao, S. Okamoto and K. Takeuchi: *J. of the Soc. of Powder Tech. Japan,* **18,** 4, 229-233 (1981)
2) Iinoya, K., T. Fuyuki, Y. Yamada, H. Hisakuni and E. Sue: *J. of the Soc. of Powder Tech., Japan,* **29,** 5, 351-355 (1992)
3) Iinoya, K., H. Hisakuni, E. Sue, T. Fuyuki and Y. Yamada: Proceedings of Second World Congress, Particle Tech., Japan, pp. 120−126, Kyoto (1990)
4) Yamada, Y., H. Murata and K. Iinoya: Proceedings of Second World congress, Particle Tech., pp. 48−54, Kyoto (1990).
5) Parker C. Reist: "Introduction to Aerosol Sci.", pp. 96−99, Macmillan Pub. Comp. (1984)
6) Yoshida, H., T. Saeki, K. Hashimoto and T. Fujioka; *J. Chem. Eng. Japan,* **24**, pp. 640−647 (1991)

Information Articles

The Symposium on Powder Technology

''The 28th Symposium on Powder Technology'' sponsored by the Council of Powder Technology was held at Sunshine City Prince Hotel, Tokyo on August 24, 1994.

The symposium focused on ''measurement'', closely related to the progress of manufacture technologies in the industrial field under the main theme, ''Powder Process On-line Measurement''. Lectures were given by the researchers and engineers active in the first line today. With the enthusiasm of more than 200 audiences closely packed in the hall and the lecturers, the meeting was a great success.

A KONA Award Special Lecture was also given by Prof. Yasuo Kousaka, Univ. of Osaka Prefecture, the winner of the 3rd KONA Award presented by the Hosokawa Powder Technology Foundation.

The 28th Symposium on Powder Technology
Powder Process On-line Measurement

Session I Vision of Measurement Technology in On-line Process

Chairmanship: Toshio Oshima (Himeji Institute of Technology)

● Progress of Realtime Measurement Technology in Powder Process	Kei Miyanami (University of Osaka Prefecture)
● Mesurement of Powder Flow Rate by Using Static Electricity	Shuji Matsuzaka (Kyoto University)
● Application of Tomograghy to Powder Process Measurement	Mitsukuni Mizuno (Aichi Institute of Technology)

Session II KONA Award Special Lecture

Chairmanship: Tetsuo Yoshida (Emeritus Prof. of University of Osaka Prefecture)

● Adhesion and Dispersion of Fine Particles	KONA awardee, Yasuo Kousaka (University of Osaka Prefecture)

Session III Practice of On-line Measurement in Powder Processes

Chairmanship: Teruaki Suzuki (Hosokawa Micron Corporation)

● Examples of On-line Measurement in Pharmaceuticals Producing Processes	Hayao Inoue (Shionogi & Co., Ltd.)
● On-line Measurement and Automatic Control of Fludized Bed Granulizer and Its Application	Toyokazu Yokoyama (Hosokawa Micron Corporation)

The 3rd KONA Award

As the winner of the KONA Award sponsored by Hosokawa Powder Technology Foundation and given to the scientists or groups who have achieved excellence in the researches related to the basic powder technologies, Prof. Yasuo Kousaka of the University of Osaka Prefecture was selected.

Prof. Kousaka achieved remarkable results in the field of powder technology and aerosol science, especially the physical characteristics of particles and their evaluation method through years of researches, widely gaining the top-grade evaluation at home and abroad.

On January 19, 1994, Mr. Masuo Hosokawa, President of Hosokawa Powder Technology Foundation handed Prof. Kousaka the KONA Award at the ceremony of the presentation held at the R&D Center, Hosokawa Micron Corporation in Hirakata, Japan.

Academic publication concerning powder technology in Japan (1993)

Journal of the Society of Powder Technology, Japan Vol. 30 (1993)

Title	Author(s)	Page
<Original Report>		
• The Removal of Deposited Particles Using a High-speed Air Jet	H. Masuda, K. Gotoh H. Fukada and Y. Banba	24 – 31
• The Effect of the Operational Condition and Core Particle Size on the Powder Composite Process by a Mechanical Method	M. Naito, A. Kondo M. Yoshikawa and T. Yokoyama	32 – 37
• The Wear Characteristics of Zirconia Ball in a Grinding Machine – The Effect of the Type of Mill, Materials of the Tank and Mechanical Properties –	K. Inui, H. Ohnishi and T. Kawanami	80 – 86
• Distribution of Contact Numbers Between Different Particles and the Precision of Estimation	H. Shinda and R. Oishi	87 – 93
• Synthesis of Ultrafine Particles by Reactions in Electrical Discharges and its Application	S. Shioji, H. Yamamoto K. Tokami and T. Nomura	94 – 100
• Study on the Deashing of Coal by the Oil Agglomeration Process – The Effect of the pH of the Disperse Medium on Deashing Efficiency –	H. Takase, K. Ikeda and M. Sugimoto	101 – 107
• The Simulation of Aggregate Packing for an Ultra-fine Powder – The Influence of the Simulated Condition on Packed Bed Structure –	H. Kamiya, E. Yagi and G. Jimbo	148 – 154
• The Simulation of Mechanochemical Chain Scisson in Organic Polymers	A. Ikekawa	155 – 161
• The Analysis of Fine Cement Particle Injection into the Ground	K. Mori	162 – 165
• An Analytical Study of Pulsation Phenomena of Granular Materials in Silos during Discharge	J. Yoshida	166 – 172
• Numerical Modeling of Convective Motion in Granular Materials	Y. Taguchi	173 – 177
• Chain-like Clustering of Fine Particles in a Magnetic Fluid	Y. Inagaki, M. Furuuchi and K. Gotoh	178 – 182
• Basic Research for the Plugging of Granular Flow	H. Sakaguchi and E. Ozaki	183 – 187
• Computer Simulation of the Flowing Behavior of Granular Materials in a Chute	J. Kano, A. Shimosaka and J. Hidaka	188 – 193
• Estimation of the Mixing Index Based on the Contact Number between Different Particles by Spot Sampling	H. Shindo	234 – 239

Title	Author (s)	Page
• Estimating the Cut Size of Needle-shaped Particles During Sieving	R. Utsumi, M. Ichikawa T. Yamamoto, T. Hata and K. Ushiki	240 – 246
• The Existence Characteristics of Two States of Thermal Stability Limits in Autoxidative Self-heating Powder Beds	Y. Nakajima, S. Furusawa H. Liang and T. Tanaka	247 – 254
• An Experimental Study of the Mechanism of Vertical Conveyance of a Bulk Solid in a Pipe Belt Conveyor System	H. Tsunakawa	255 – 267
• The Effect of Voidage on the Estimation of the Flowability of a Cohesive Powder	H. Tsunakawa	318 – 323
• Sample Preparation for Particle Size Analysis of Submicron Powders	O. Hayakawa and J. Tsubaki	324 – 329
• The Effect of the Surface Coating Ratio of a Surface Modified Particle on the Contact Potential Difference Between a Powder Bed and a Metal	H. Yoshida, Y. Iguchi, T. Matsumoto H. Masuda, H. Murata and Y. Yamada	330 – 336
• The Angular and Radial Velocities of Spherical Particles in the Centrifugal Force of a Gas	Z. Tanaka, Y. Nagano and T. Takahashi	337 – 340
• An Evaluation of the Mixing Characteristics of Solid Mixers Using Adhesive Fine Powders	M. Satoh, T. Yamashita T. Yoshida, S. Hasegawa and K. Miyanami	390 – 396
• The Dispersion State of Fine Particles in Polymer Membranes and its Application	K. Osaka, H. Nakakura and K. Shiga	397 – 402
• The Effect of Pre-mixing Time on the Kneaded State of Materials for their Toner and Chraging Characteristics	T. Teshima, K. Terashita and K. Miyanami	403 – 409
• The Influence of Agglomeration upon the Dewaxing Properties of Greenwares for Low Pressure Molding	S. Nakao, M. Saito, K. Tanaka and K. Minai	410 – 415
• The Preparation of Composite Particles with a Double Layer or with Multicomponent Dispersed Layer by a Two-step Mechanofusion Process	K. Tanno, T. Onagi, M. Naito and T. Yokoyama	416 – 422
• Characterization of the Microstructur and Disintegration Behavior of Granules	T. Ishimori and M. Senna	470 – 476
• The Effect of Air Velocity on the Flow Characteristics of the Pneumatic Conveyane of Powders	M. Futamura	477 – 482
• Efficacy and Risk of Aeration to Prevent Self-heating Powder Beds from Spontaneous Ignition	Y. Nakajima, S. Furusawa, H. Liang and T. Tanaka	483 – 489
• The Performances of Several Types of Cyclones	T. Fuyuki, Y. Yamada and K. Iinoya	490 – 495
• The Effect of the Types of Mill on the Flowability of Ground Powders	T. Oshima, Y. Zhang, M. Hirota M. Suzuki and T. Nakagawa	496 – 501

Title	Author(s)	Page
• Contamination and Sinterability of Planetary Milled Alumina	O. Abe	548 – 555
• The Mixing of Toner Composition and its Evaluation	T. Teshima, N. Yabe, K. Terashita and K. Miyanami	556 – 562
• The Simultaneous of Granulation, Grinding and Separation in a Continuous Tumbling Conical Granulator – On the Shape Evaluation of the Granules and Granulating Conditions –	M. Sugimoto, N. Yokota and H. Miyanaga	563 – 569
• The Effect of Alcohol Grinding Aids on the Ultrafine Grinding of Feldspar	M. Hasegawa and Y. Kanda	570 – 575
• Preparation of Spherical, Mullite Fine Powders by the Spray Decomposition using an Ultrasonic Atomizer	T. Ogihara, T. Yanagawa, N. Ogata K. Yoshida, Y. Saito and K. Ogawa	614 – 619
• The Separation of Irregularly-shaped Fine Particles by a Vibrating Rotating Disk	K. Yamamoto, T. Okumura and M. Sugimoto	620 – 626
• The Estimation of the Interparticle Reaction Rate by the Introduction of a Number of Contact Points in a Uni-directional Diffusion System	A. Shimizu and Y. Hao	627 – 634
• The Mechano-chemical Change of Synthetic Mordentie by Dry-grinding – Changes in the Characteristics of Cation Adsorption –	E. Kasai, H. Mimura, K. Sugiyama F. Saito, K. Akiba and Y. Waseda	635 – 640
• Using Low-grade Materials for Electrical Power Insulators – The Relationship between the Crystallinity of Raw Materials and Slurry Properties –	T. Ueda, I. Tada, H. Kitamura S. Omote and M. Nakamura	641 – 645
• Feeding Performance of a Dry Powder by a Mohno Pump	T. Oshima, H. Eitoku, M. Hirota and M. Suzuki	646 – 651
• Estimation of the Optimum Refractive Index by Laser Diffraction and Scattering Method – In the Raw Material of Fine Ceramics –	O. Hayakawa, K. Nakahira and J. Tsubaki	652 – 659
• Powder Flow-rate Control Through a Narrow Nozzle with Air Pressure	N. Terachi, J. Hidaka and S. Miwa	690 – 694
• Characteristics of a Closed-circuit Fine Grinding System Consisting of a Ring Roller-type Mill and a High Efficiency Vortex-type Classifier	N. Asai, O. Yamamoto, T. Makino T. Furukawa, M. Ito and H. Ninomiya	695 – 702
• Performance Evaluation of Dry Dispersers	H. Masuda and K. Gotoh	703 – 708
• The Effect of the Revolution Rate of a Pot Mill on the Preparation of Semiconductive SnO_2-Sb_2O_3 Fine Particle by Ball-milling	H. Shiomi, T. Fukuzaki and M. Nakamura	768 – 776
• Mechanoradicals of Quartz Produced by Grinding	M. Hasegawa, T. Ogata, M. Sato and Y. Kanda	777 – 781
• Data Reduction by Cascade Impactor	H. Yoshida, T. Fujioka and H. Makino	782 – 789

Title	Author(s)	Page
• The Effect of Wattability of a Surface-modified Powder on Granulation with a High-speed Mixer	K. Matsumoto and G. Hong	836 – 841
• The Low Temperature Phase Transition of Water on the Surface of Inorganic Powder Particles	M. Nakamura, H. Sakane and S. Tsujii	842 – 847
• Dispersion of Hydrophilic Particles in Non-aqueous Polymer Solutions	K. Osaka and T. Shimoda	848 – 853
• The Measurement and Evaluation of the Contact Potential Difference Between Various Powders and a Metal	H. Masuda, T. Itakura, K. Gotoh, T. Takahashi and T. Teshima	854 – 859

Kagaku Kogaku Ronbunshu Vol. 19 (1993)

Title	Autor(s)	Page
• Evaluation of Dispersion State of Electrically Conductive Resin with Fractal Dimension	Y. Mizuno, K. Terashita and K. Miyanami	21 – 29
• Analysis of Adhesion Force Arising from a Liquid Bridge Formed between Two Particles	Y. Endo, Y. Kousaka and Y. Nishie	55 – 61
• Removal of Fine Particles from Wafer Surface by Pulse Air Jets	Y. Otani, H. Emi and T. Morizane	114 – 119
• High-pressure Cold Isostatic Pressing of Ultra-fine Oxide Powders	H. Kamiya, C. Nakayama and G. Jimbo	220 – 229
• Formation of Wall Particle Layers by Simultaneous Deposition and Reentrainment of Fine Particles in Turbulent Aerosol Flows	S. Matsusaka, M. Simizu and H. Masuda	251 – 257
• Effects of Another Particulate Fraction for Elutriation	Z. Tanaka, H. Mitsuji and T. Takahashi	311 – 316
• Evaluation and Control of Equilibrium Moisture Contents in Powdery Materials	Y. Endo, Y. Kousaka and Y. Nishie	411 – 417
• Saturated and Unsaturated Water Movement Within Mesh-Type Wicks	H. Mori, M. Taguchi, M. Nakamura and S. Toyama	431 – 439
• Fine Particle Separation by Revised Type Air-Cyclone Classifier	H. Yoshida, T. Saeki, T. Fujioka, T. Ueda and T. Fuyuki	476 – 482
• Reduction of Iron Oxide Fine Particles from a Converter in a Powder-Particle Fluidized Bed	T. Takarada, H. Sakamoto, K. Maehara M. Ito, T. Tsutsui, N. Nakagawa and K. Kato	505 – 510
• Fluidization Characteristics of a Centrifugal Fluidized Bed	Z. Tanaka, T. Miya and T. Takahashi	605 – 609
• Parameters of Grinding Noise and Size Distribution of Fragments in Grinding of a Particle between Grinding Balls	J. Hidaka, H. Amita and A. Shimosaka	626 – 632
• Removal of Small Particles Deposited on Solid Surfaces by a Freezing Method	Y. Kousaka, T. Horiuchi, Y. Endo and T. Niida	655 – 662

Title	Author (s)	Page
• S-Potential of PSL Particles in Alcohol-Water Solutions	A. Kage and E. Arao	1031 – 1037
• Automatic Measurement of Concentrated Spherical Particles by Use of Image Processing	F. Koizumi and H. Nishitani	1120 – 1127
• Analysis of Liquid Bridge Formation and Adhesion Force between Two Particles of Different Sizes	Y. Endo, Y. Kousaka and M. Ishii	1128 – 1135
• Analysis of Separation between Two Particles Adhering by a Liquid Bridge	Y. Endo, Y. Kousaka	1136 – 1142
• Effect of Fine Particles on Behavior of Bubbles in Gas-Solid Fluidized Bed at Elevated Temperature	K. Ijichi, Y. Uemura, Y. Tanaka and Y. Hatate	1143 – 1148

Funsai (The Micromeritics) No. 37 (1993)

Title	Autor (s)	Page
• Measurement of Descending Velocity of Particles within Two-dimensional Conical Moving Bed	K. Shinohara, T. Murase	4 – 11
• On the Mechanism and the Performance of a Spouted-bed-air-filter	K. Ushiki, H. Miki, H. Ota, W. Eguchi and T. Sato	12 – 21
• Electroless Plating on Powder	M. Hirota, Y. Kuriyama, M. Suzuki and T. Oshima	22 – 27

New Product News

Hosokawa Micron Group introduces two new products.

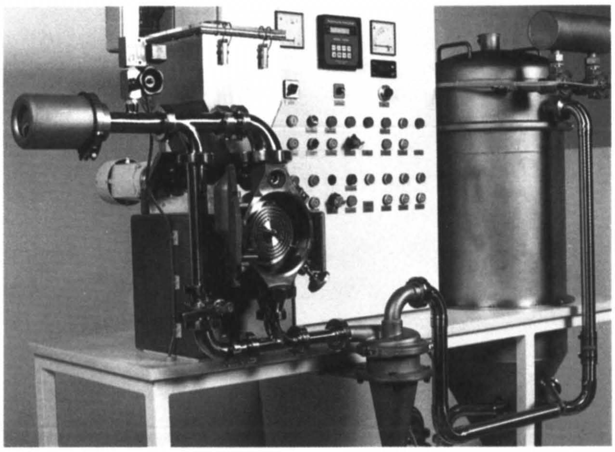

Fine-Impact-Mill UPZ Pharma-Design

UPZ fine-impact mills can be equipped with a variety of exchangeable, rotating or stationary grinding elements.

A wide range of finenesses is covered, with d_{97} values of approx. 20 to 700μm. The pharma machine sizes are suitable for the standard throughput rates.

Pharma-Design features

- Welded design free from dead spaces with tangential product discharge.
- Design limits: explosion-pressure-shock-resistant to 10 bar (g).
- Product-contact surfaces ground to Ra = 0.4μm; electropolishing to order.
- Pin discs in pharma design; plate beater unit, grinding tracks, etc. in one-piece construction. No dead spaces caused by bolted fittings.

UPZ Model		100 UPZ*	160 UPZ	250 UPZ	315 UPZ
Pin disc grinding media	(ϕmm)	100	160	250	315
Drive	(kw)	1.1~1.5	5.5	7.5~11	11~18.5
Grinding element speed	(rpm)	17,500	14,000	11,000	8,150

*Laboratory mill for small-scale production and pilot plant operation

For more information contact: **Hosokawa Alpine Aktiengesellschaft**
Petr-Dörfler-Straße 13-25, Postfach 10 11 09, D-86001 Augsburg 1, GERMANY
Telephone: 49-821-5906-0 Facsimile: 49-821-573839

AGGROBOT

AGGROBOT realizes completely automatic characterization of compressive and tensile properties of dry and wet powder beds with high accuracy.

Features

- The stress and the displacement are measured simultaneously in three thypes of measurements, namely compressive-tensile continuous test, compressive or tensile single test conducted full-automatically.
- From their relations, various analytical factors such as breaking energy and cohesive force between two particles are obtained.
- Owing to wide range of measurable tensile strength, wet powders with binder can be handled as a sample.
- Measurement at a constant temperature (between 0 to 70 deg C) is possible (option).
- The device is simple in structure, easy to operate and to clean.

For more information contact; **HOSOKAWA MICRON CORPORATION**
No. 9, 1-chome, Shoudai Tajika, Hirakata-shi, Osaka 573 JAPAN
Telephone: 81-720-55-2220 Facsimile: 81-720-55-3288